Resolving gradients in an ammonia oxidation reactor under industrial conditions

Vom Promotionsausschuss der
Technischen Universität Hamburg

zur Erlangung des akademischen Grades
Doktor-Ingenieur (Dr.-Ing.)

genehmigte Dissertation

von
Jan Pottbacker

aus
Hamburg

2022

1. Gutachter: Prof. Dr. rer. nat. Raimund Horn
2. Gutachter: Prof. Dr.-Ing. Michael Schlüter
Tag der mündlichen Prüfung: 06. Juli 2022
https://doi.org/10.15480/882.4465

Abstract

Since more than a century oxidation of ammonia to nitric oxide is used as first step of the Ostwald process to produce the commodity chemical nitric acid. A major side product of industrial ammonia oxidation is nitrous oxide, a strong greenhouse gas with a CO_2 equivalency factor of 298. In the light of the pressing need to reduce global greenhouse gas emissions, an ecological and economical improvement of ammonia oxidation is essential. However, the development and validation of ammonia oxidation models, that can be used for a systematic, knowledge-based improvement of the process, is limited by the lack of detailed, high quality experimental data measured in the reactions mass transfer controlled regime at industrial conditions.

In this work a new bench-scale setup is presented that enables studies of the underlying processes of ammonia oxidation under industrial, mass transfer controlled conditions by spatially resolved profile measurements. The spatial resolution achieved with the profile measurement technique is sufficient to resolve the influence of single catalyst wires. Platinum alloy gauze catalysts, the industry standard for ammonia oxidation, undergo considerable surface reconstruction in operation. Strategies are presented to minimize the influence of the reconstruction process on the measured profiles. Furthermore, the aptitude to measure gas phase temperature profiles using thermocouples and to measure the catalyst gauze temperature using pyrometry are analyzed. Measurements in the profile reactor are compared with computational fluid dynamics simulations of ammonia oxidation to explain the measured phenomena and to validate the surface kinetic model used in the simulations. All in all, the developed approach presented in this work allows to spatially resolve the processes in ammonia oxidation under industrial conditions providing a wealth of data for future process optimization.

Acknowledgments

I would like to express my gratitude to all the people who supported me during my time at the Institute of Chemical Reaction Engineering at TUHH:

First of all, I would like to thank Prof. Raimund Horn who gave me the opportunity to work on this interesting project in the last five years. Thank you for the guidance and support all the way during my time as a Ph.D. student and for all the creative input and good ideas.

I would like to thank Yara International ASA for funding the project and the great cooperation. No matter how the project was progressing, or which problems were holding up the schedule, there was nothing but great ideas, positive thinking, and support coming from all of our partners at Yara, contributing enormously to the success of the project. Especially, I would express my gratitude to the project managers of our collaboration with Yara, Maximilian Warner, Mohan Menon, and Jakub Bujalski for all their great support over the long project time. I would also like to thank Stian Sannes, Torgeir Lunde, David Waller, Bent Vigeland, and all other partners from Yara for creating such a great, productive atmosphere in our project meetings, making the meetings absolute highlights of my Ph.D. time. I was really fortunate, that I had the opportunity to discuss my research with so many experienced scientists.

I would like to thank Dr. Ing Sven Jakobtorweihen and his student Anna-Sophia Behnecke for providing the CFD results discussed in this thesis. Thank you Sven for all your valuable input and help that you contributed. It was a pleasure to work with you.

I would like to thank Prof. Dr.-Ing. Michael Schlüter for examining my thesis and Prof. Dr. Alexander Penn for taking the chair of the examination board.

I would like to thank all my colleagues from the Institute of Chemical Reaction Engineering at TUHH for the great time I had at the institute. I would like to thank

Dr. Oliver Korup for his guidance in developing and building the reactor setup and I would like to thank Klaus Mandel for his great work with the electronics and the reactor control system. My thanks go out to my research colleagues Ying Dong, Bahne Sosna, Stephan Bendt, Birte Wollak, Sebastian Sichert, Diego Espinoza, Viktor Berg, Filip Vrljic, and Andrés Aquino for the helping hands in times of need, the interesting discussions, proofreading and the fun times we had together. Thank you Christina Laarmann for the assistance in the labs and thanks go out to Hermine Oppelaar, Eleni Poultoutzidou, and Meike Lerdon for organizational support. I would also like to thank the former staff at the institute Dr. Ludwig Scharfenberg, Prof. Dr. Dr. h. c. Frerich Keil and Dr. Achim Bartsch for their scientific input. I would also like to thank Michael Schmidt and his colleagues at Reacnostics for the help they provided and the good working atmosphere in our shared labs.

I would like to thank my students Sven Brauer, Adnan Abdullah, and Melis Özdemir for their great work and support in the project. I was really fortunate, that I had the assistance of such motivated, creative, positive thinking, and nice students. I enjoyed the work with the three of you a lot.

I would like to thank Dirk Manning and his team at the workshop of the TUHH for the helping hands in the construction process and for borrowing us so many tools.

I would like to thank Dr. rer. nat. Tobias Krekeler for his assistance in the gauze aging project and for providing such nice SEM images for my thesis. I would also like to thank Thomas Sheppard, Srashtasrita Das, and the staff at DESY for the great cooperation in our gauze aging project.

Finally, and most importantly, I would like to thank my parents, family, and friends for their unconditional love and support.

Contents

1 Introduction

Nitric acid (HNO_3) is one of the most important commodity chemicals in the world. Annually more than 60 million tonnes of nitric acid are produced in approximately 500 plants with annual production capacities totaling 80 million tonnes [1]. The production of nitrogen containing fertilizers, mainly ammonium nitrate and calcium ammonium nitrate, accounted for almost 80 % of the global nitric acid consumption in 2020 [2]. Other large markets for nitric acid are the production of explosives and chemicals like adipic acid, toluene diisocyanate, nitrochlorobenzenes, and nitrobenzene. Nitric acid is also used industrially in the purification and treatment processes of metals as well as for the processing of uranium [2]. Since more than a century, nitric acid is produced in industry via the Ostwald process that is divided into three main steps: (i) the catalytic oxidation of ammonia (NH_3) by oxygen (O_2) to nitric oxide (NO), (ii) the oxidation of nitric oxide by oxygen to nitrogen dioxide (NO_2), and (iii) the reactive absorption of nitrogen dioxide in water (H_2O) producing nitric acid. This work focuses on the first step of the Ostwald process, the oxidation of ammonia.

Nowadays, industrial ammonia oxidation is catalyzed by stacks of up to 50 knitted gauzes composed of platinum-rhodium wires with rhodium contents of $5 - 10$ wt.% and wire diameters in the range of $60 - 80$ μm [3–5]. Under typical industrial reaction conditions with temperatures between $800 - 950$ °C and pressures between $1 - 12$ bar ammonia oxidation is a mass transfer limited process. Full ammonia conversion and selectivities of the target product nitric oxide of $92 - 98$ % are reached at the end of the few millimeters high catalyst beds [3]. Besides the target product nitric oxide, the side products nitrogen (N_2) and nitrous oxide (N_2O) are formed in ammonia oxidation according to the following equations [3, 6, 7].

$$\mathrm{NH_3} + \frac{5}{4}\,\mathrm{O_2} \longrightarrow \mathrm{NO} + \frac{3}{2}\,\mathrm{H_2O} \qquad \Delta H^0_{\mathrm{R},\,298} = -227\frac{\mathrm{kJ}}{\mathrm{mol}}$$

$$\mathrm{NH_3} + \frac{3}{4}\,\mathrm{O_2} \longrightarrow \frac{1}{2}\,\mathrm{N_2} + \frac{3}{2}\,\mathrm{H_2O} \qquad \Delta H^0_{\mathrm{R},\,298} = -317\frac{\mathrm{kJ}}{\mathrm{mol}}$$

$$\mathrm{NH_3} + \mathrm{O_2} \longrightarrow \frac{1}{2}\,\mathrm{N_2O} + \frac{3}{2}\,\mathrm{H_2O} \qquad \Delta H^0_{\mathrm{R},\,298} = -276\frac{\mathrm{kJ}}{\mathrm{mol}}$$

The educt ammonia is produced industrially in the energy intensive Haber-Bosch process. Thus, any losses in nitric oxide yield have a strong negative influence on both the economical and ecological performance of the overall nitric acid production process. The formation of nitrous oxide adds another downside to the process since nitrous oxide is a potent greenhouse gas with a CO_2 equivalency factor of 298 on a 100 year basis [8]. Today, nitrous oxide emissions are reduced using costly additional downstream abatement strategies and remainder emissions have to be compensated by the purchase of emission certificates, rendering reductions in nitrous oxide emissions lucrative, not only under ecological aspects. Direct primary abatement by reducing nitrous oxide formation during ammonia oxidation is hence a promising way to improve the overall performance of ammonia oxidation, especially since reduced nitrous oxide formation comes along with improved nitric oxide selectivity. However, optimization of industrial ammonia oxidation requires an in-depth understanding of the underlying processes.

Despite its long established industrial use in the Ostwald process the reaction paths leading to side product formation in ammonia oxidation are still not fully understood [3]. Simulation and experimental studies agree that the key to the product selectivities are the surface coverages of the platinum gauze catalyst, which are controlled by external mass transfer to the catalyst surface [9–13]. Low $\mathrm{NH_x}$ (with x= $0, 1, 2, 3$) species surface coverages and high oxygen surface coverages, and thus lower ammonia concentrations, higher oxygen concentrations, higher temperatures, lower pressures as well as reduced flow velocities are beneficial for high nitric oxide selectivities [3, 10–17]. Nitric oxide selectivity is however not the only factor worth considering for process optimization, but also the burner throughput, as well as the corrosion rate of the costly platinum gauze catalyst, need to be factored in. In operation, the platinum alloy gauze catalysts reconstruct con-

siderably from smooth wires at the beginning of a campaign to heavily corroded wires covered with fractal structures in the shape of cauliflowers at the end of a campaign. The reconstruction process, which is enhanced by high temperatures and high oxygen concentrations, is accompanied by significant losses of expensive platinum [3]. These complex, interconnected, and contradicting relations between operation parameters, product selectivities, burner throughput, and corrosion rate calls for systematic, knowledge-based optimization of the process.

In the last decades, the increasing processing power of modern computers facilitated process optimization of heterogeneously catalyzed reactions using digital twins, in which Computational Fluid Dynamics (CFD) simulations are used to model the interplay between transport processes and surface reactions. For ammonia oxidation first pioneering CFD studies were carried out by Jantzen et al. [18] and Nien [19]. Recently CFD simulations were used to validate microkinetic models of ammonia oxidation [15] and to investigate the influence of various catalyst gauze properties on the reaction performance [11, 14, 19]. While CFD simulations helped to deepen the understanding of the influencing factors of ammonia oxidation, their explanatory power is currently limited by the lack of a kinetic model that predicts ammonia oxidation accurately at industrial conditions. Qualitative trends are determined correctly by some existing kinetic models, but no existing model enables precise quantitative predictions over the entire industrially relevant range of operation conditions [11, 17]. The development of improved kinetic models is hindered by the lack of detailed experimental data under industrial conditions that can be used for validation and optimization of the models. Experimental studies of ammonia oxidation under industrial conditions are challenging due to the reactions mass transfer limitation and the extreme industrial process conditions with high temperatures, elevated pressures, strongly corrosive gas atmospheres, and high gas flow rates. Therefore, ammonia oxidation is often studied at kinetic controlled conditions in ultra high vacuum or at reduced temperatures [9, 13, 20–31], alternatively end of pipe measurements at industrial, mass transfer limited conditions are conducted [10, 14, 17], keeping the actual processes inside the reactor hidden. Furthermore, end of pipe measurements in laboratory sized reactors are distorted due to heat losses over the reactor walls that lead to lower nitric oxide selectivities than observed in industrial reactors [11]. The revelation of the actual processes

inside ammonia oxidation reactors requires resolving the steep concentration and temperature gradients around the platinum alloy gauze stacks with heights of only a few millimeters. A promising approach to tackle this problem are profile measurements adopting the spatial profile measurement technique, developed by Horn et al. [32]. In profile measurements a small sampling capillary equipped with additional analytical sensors is moved through a catalyst bed, allowing to measure concentration, temperature, and spectroscopic profiles to resolve the processes in catalytic reactors [32–40].

The aim of this work is the development and testing of an experimental setup that allows resolving the steep gradients around platinum gauze catalysts in ammonia oxidation under industrial conditions. For this purpose, the spatial profile measurement technique by Horn et al. is adopted for high spatial resolution measurements in a new setup tailored to cope with the demands of ammonia oxidation under industrial conditions. Separate, independent control of all relevant operation conditions is required to allow for systematic parametric studies over a wide range of industrially relevant operation conditions bridging the gap of experimental data needed for model development and validation.

The results presented in this work demonstrate that profile measurements with a spatial resolution sufficient to resolve the gradients in ammonia oxidation are feasible in the newly developed setup. Potential pitfalls specific for profile measurements in ammonia oxidation, like complications resulting from the catalyst restructuring, are shown and strategies to avoid them are presented. First systematic parametric studies are compared with detailed CFD simulations to validate the surface kinetic model by Kraehnert and Baerns [41]. All in all, a new approach is presented to gain deeper experimental insight into ammonia oxidation under industrial conditions for future process optimization.

2 Theoretical Background

This chapter gives an overview of the fundamentals of industrial ammonia oxidation and the methods utilized in this thesis. Firstly, an introduction to the historical development of industrial nitric acid production processes is given, followed by a description of the setup of modern nitric acid plants. Subsequently, the state of the art of ammonia oxidation as the first step of the Ostwald process is reviewed, including the reaction mechanism, consequences of the mass transfer limitation, CFD studies of the reaction, and finally, presenting some answers to the question: How do the operation conditions influence the reaction performance? Subsequently, the progress in the development and understanding of industrial ammonia oxidation catalysts over the last century is presented, concluding the introduction to the reaction studied in this work, industrial ammonia oxidation. In the following sections, the theoretical backgrounds of the methods used in this work are explained. Firstly, an overview of spatially resolved measurement techniques with a focus on spatial profile measurements via physical probing is given. Thereafter, the fundamentals of mass spectrometry, infrared spectroscopy, and computational fluid dynamics are briefly explained.

2.1 The History of the Industrial Nitric Acid Production

With an annular worldwide production of more than 60 million tons, nitric acid is one of the ten most produced industrial chemicals [1, 3]. However, there is only a small direct market for nitric acid as a product. Industrially produced nitric acid is mainly consumed directly on the plant. The largest fraction of nitric acid is utilized for the production of nitrate containing fertilizers e.g. ammonium nitrate

and calcium ammonium nitrate. The production of fertilizers accounts for more than 80 % of the total nitric acid consumption [1]. Nitric acid is also used in large quantities for the production of explosives. Further fields of application include the etching of steel, the synthesis of pharmaceuticals, dyes, adipic acid, and organic intermediates such as nitro-aromatics as well as nitro-alkanes [3, 4, 17].

Already in the middle ages, nitric acid was produced and used on a small scale, for example, for the production of explosives and the purification of gold with aqua regia. Until the beginning of the 20th century, nitric acid was mainly produced using natural nitrates and sulfuric acid or other mineral acids [42].

$$NaNO_3 + H_2SO_4 \longrightarrow NaHSO_4 + HNO_3 \tag{2.1}$$

Due to the low availability of natural nitrates in Europe, nitrates were produced in saltpeter plantations. In these plantations organic matter mixed with lime mortar and wood ashes decayed, allowing extraction of small amounts of potassium nitrate. At the beginning of the 19th century, an estimated annular nitrate production of 1250 tons was realized in such plantations in France [42, 43].

In the 19th century, a new source of nitrates was discovered: huge deposits of sodium nitrates in South America, known today as chile saltpeter. The new supply source of cheap nitrates led to a sharp increase in the availability of nitrates and thus, enabled the mass production of explosives and the usage of nitrates as fertilizers. In 1850 an estimated nitrate production of about 25 kilotons was achieved, in 1914 already 2.5 megatons of chile saltpeter were produced [5, 42]. However, at the end of the 19th century, it was clear that the chile nitrate supply may be exhausted in a foreseeable future. This could have led to famine, due to the important role of nitrate fertilizers in the provision of food for the growing population in the western world. Therefore, the development of industrial synthesis routes for nitrates and nitric acid was tackled by multiple chemists. Another accelerating factor for the development of a synthetic nitric acid source was the realization that in an event of war in Europe the nitrate supply of some countries may have been cut of, stopping the production of explosives in these countries [42].

One possibility to fixate atmospheric nitrogen is the direct oxidation of nitrogen in electric arc processes. In the 19th century, multiple chemists experimented with electric arc processes and thereby, found a way to oxidize nitrogen to nitric oxide using electric energy according to the Reaction 2.2.

$$N_2 + O_2 \rightleftharpoons 2\,NO \tag{2.2}$$

The nitric oxide produced in electric arc processes can be utilized in further process steps to produce nitric acid. The second step of this process is to cool down the nitric oxide and oxidize it to nitric dioxide. In the last process step nitric dioxide is absorbed in water forming nitric acid. In 1903 Kristian Birkeland and Sam Eyde started to plan an industrial electric arc process, later called the Birkeland-Eyde process. After a development period of two years, they founded the company Norsk-Hydro that operated the Birkeland-Eyde process in industrial plants on a large scale until 1929. Other direct nitric acid production processes besides the Birkeland-Eyde process did not gain wide acceptance in the industry. The main disadvantage of the direct processes is the low energy efficiency. High temperatures are needed to allow the production of nitric oxide at appreciable rates according to the equilibrium of Reaction 2.2. [3, 42, 44]

Another alternative nitric oxide synthesis process for the production of nitric acid is the catalytic oxidation of ammonia. In 1789 Rev. Isaac Milner reported for the first time the successful conversion of ammonia to nitric oxide by passing ammonia over a heated magnesium oxide catalyst [45]. William Henry [46] achieved similar results using platinum wires. In 1838 Frédéric Kuhlmann [47] filed a patent for a process to oxidize ammonia to nitric oxide using platinum sponges as well as copper and iron wires heated to 300 °C. Wilhelm Ostwald started to work on an industrial nitric acid production process based on the findings of Kuhlmann in 1900. In his first experiments, Ostwald used platinized asbestos as a catalyst. Later the catalyst was replaced by short platinum ribbons in most experiments. Furthermore, Ostwald also analyzed the influence of the temperature, the contact time, different catalyst shapes and materials such as platinum, iridium, palladium as well as oxides of nickel, cobalt, manganese, lead, silver, molybdenum, vanadium, copper, and chrome. In 1901, after his first successful experiments, Ostwald started

to work with Wilhelm Will and Friedrich Uhde on building the first plant for experiments on a technical scale. The construction was finalized in 1904. Already two years later, in 1906, the first industrial plant was built in Gerthe, Germany, allowing the production of up to 300 kg of nitric acid per day with a concentration of 53 % [17,45,48–50]. Ostwald's work established the foundation of modern nitric acid plants. The Ostwald process used in most modern nitric acid plants can be divided into three main steps [3]:

1. The catalytic oxidation of ammonia by atmospheric oxygen to nitric oxide:

$$\mathrm{NH_3} + \frac{5}{4}\,\mathrm{O_2} \longrightarrow \mathrm{NO} + \frac{3}{2}\,\mathrm{H_2O} \tag{2.3}$$

2. The oxidation of nitric oxide by atmospheric oxygen to give nitrogen dioxide:

$$\mathrm{NO} + \frac{1}{2}\,\mathrm{O_2} \longrightarrow \mathrm{NO_2} \tag{2.4}$$

3. The absorption of nitrogen dioxide in water to give nitric acid:

$$\mathrm{NO_2} + \frac{1}{3}\,\mathrm{H_2O} \longrightarrow \frac{2}{3}\,\mathrm{HNO_3} + \frac{1}{3}\,\mathrm{NO} \tag{2.5}$$

In the first plant in Gerthe corrugated platinum ribbons were used as a catalyst for the ammonia oxidation step [45, 51]. Before entering the reactor, the inlet gas mixture was preheated to 300 °C. Short contact times of 0.004 s were used to reduce consecutive reactions. The efficiency of the first plant has been estimated to lie between $75 - 85$ % [17, 52].

In 1909 Karl Kaiser patented the first process with major improvements compared to the original Ostwald process. Instead of preheating the complete inlet gas mixture, Kaiser just preheated the inlet air. This way the risk of thermal decomposition of ammonia before contacting the catalyst is reduced. However, the most significant modification of Kaiser was to change the catalyst to a platinum gauze catalyst with 1050 meshes per cm^2 woven out of wires with diameters of 0.06 mm. Woven platinum and platinum alloy catalysts of this type were the standard ammonia oxidation catalysts till they were replaced in the 1990s by knitted platinum and platinum alloy catalysts [45, 50, 53, 54].

Further progress in the nitric acid industry was closely linked to the development of the Haber-Bosch process for the production of ammonia. In 1913 the first pilot plant for ammonia production using the Haber-Bosch process was built. In the following years, the increasing supply with high quality ammonia from the Haber-Bosch process enabled the construction of new nitric acid plants with growing production capacities [5, 17].

The next game-changer for the nitric acid industry was the availability of stainless, austenitic chromium-nickel steels in the early 1920s. In absorbers build of stainless steel the operation pressure could be increased from atmospheric pressure to higher pressures in the range of 10 bar. This allowed a distinct reduction in equipment size and hence, a major cut in investment costs. Two different approaches were developed to allow higher absorption pressures: On the one hand the development of a single pressure process with high pressure in the absorption as well as in the combustion step, and on the other hand a dual-pressure process with atmospheric combustion and pressurized absorption. The single pressure process was developed in the United States of America by the company DuPont, whereas the dual-pressure process was developed by Giacomo Fauser in Europe [5, 17, 55–57]. Today single pressure processes are still the dominant nitric acid production processes in the US, in contrast, dual-pressure processes are often preferred in Europe [3, 17].

The flow sheets of modern nitric acid plants are still based either on Fausers dual-pressure or DuPonts single-pressure plants. In the last decades, changes to industrial plants were mainly limited to raising the production capacity of single plants to 2000 tonnes of nitric acid per day, achieving a high degree of energy integration and introducing different solutions to reduce the NO_x and N_2O concentrations in the exhaust gas [3, 17].

2.2 Modern Nitric Acid Production Plants

These days nitric acid is mainly produced in plants utilizing the Ostwald process. Modern single plant capacities reach up to 2000 tonnes per day of 100 % nitric acid [58] . With overall nitric acid yields in the range between $92-96$ %, depending

on the operation conditions chosen, the process is one of the most efficient bulk chemical processes [3, 17, 59].

In general, modern plants can be classified by their operation pressures. They can be divided into single-pressure plants with constant pressure in the absorption as well as in the combustion step, and dual-pressure processes with lower pressures in the combustion step and higher pressures in the absorption step. The processes can be further divided by their absolute pressures into low, medium and high pressure processes [3]. Nowadays, almost all industrial nitric acid plants are operated either as dual-pressure plants with medium pressure combustion and high pressure absorption or as single-pressure plants with medium or high pressures. Low pressure combustion plants are very capital cost intensive, which restricts this plant type to smaller units and already existing older plants [60].

In the following chapter, the production steps of modern nitric acid plants will be explained based on the example of a single-pressure nitric acid plant. A simplified process flow diagram of a single-pressure nitric acid plant is shown in Figure 2.1.

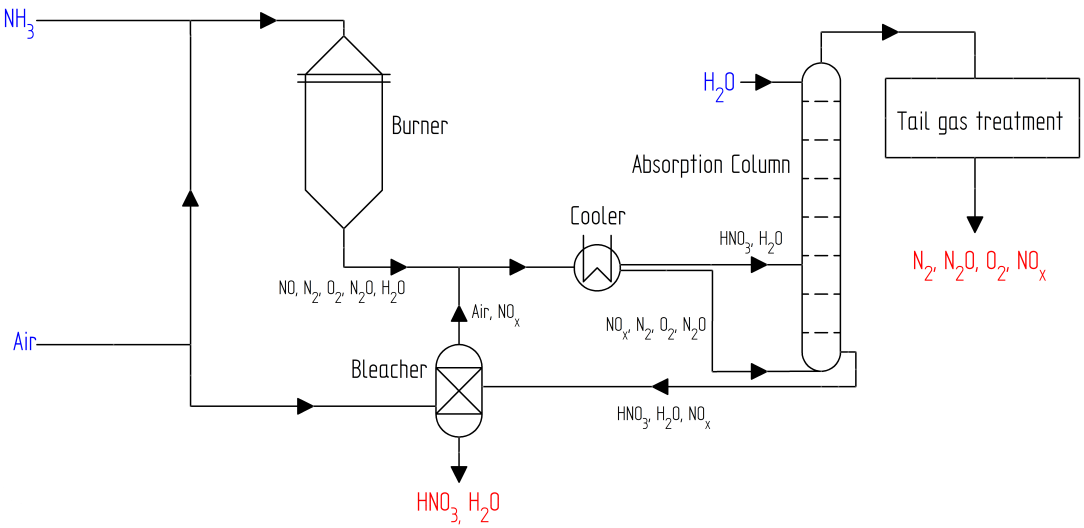

Figure 2.1: Simplified process flow diagram of a single-pressure nitric acid plant

The process can be divided into the following steps: Feed preparation, ammonia combustion, nitric oxide oxidation, absorption, bleaching, and emission abatement [60].

2.2.1 Feed Preparation

Prior to the first reaction step, the oxidation of ammonia to nitric oxide, the raw materials have to be delivered to the burner. The main objective of the feed preparation step is to provide the target process conditions for the subsequent ammonia oxidation like pressure, temperature, mixture homogeneity, and oxygen as well as ammonia concentration. In addition, the raw materials are purified by removing contamination preventing catalyst poisoning [60].

The process air is usually filtered in multistage filters with two or three filtration steps allowing to eliminate particles larger than 0.5 μm with an efficiency of 99.9 %. Typical filter materials are plastic fabrics and fiberglass. In some cases of high air pollution levels at the site of the plant additional water scrubbing processes may be necessary, in order to supply air with a satisfying purity. After the purification step the air is compressed to the target process pressure and the air temperature is adjusted to the target value in a heat exchanger [3, 60].

In modern nitric acid plants, synthetic ammonia produced in the Harber-Bosch process is used. The ammonia feed stock should guarantee purities of at least 99.8 % ammonia, less than 10 ppm oil, and less than 0.2 % water. However, ammonia can contain impurities like iron oxides, oils, volatile organics, and water. Especially iron oxide particles can act as serious catalyst poison in the ammonia oxidation step. Therefore, iron oxides are usually eliminated from the ammonia feed in magnetic separators. Subsequently, the ammonia is evaporated and filtered. Ammonia filters are usually constructed of Teflon, sintered metal, polypropylene, fiberglass, or ceramics [3, 60].

Once the raw materials are brought to the wanted purity, temperature, and pressure they can be mixed. In order to minimize the possibility of preliminary reactions of ammonia with oxygen before contacting the catalyst, the mixing is usually performed immediately in front of the burner or at the burner inlet using static mixers. Care has to be taken, in order to exclude the possibility of local high ammonia concentrations, which can present a safety risk due to the usually small margin of the ammonia concentration to the explosive limit. Additionally, inhomogeneities in the concentrations can result in reduced nitric oxide yields. A final filtration step is often placed directly behind the mixer [3, 60].

2.2.2 Ammonia Oxidation

The ammonia-air mixture is usually channeled through a perforated plate at the burner inlet assuring an even flow distribution over the catalyst [3]. Additionally, layers of Raschig rings are sometimes placed in front of the catalyst to improve the flow distribution [60]. At the surface of the catalyst, ammonia is oxidized. Three different main reactions can proceed. The wanted reaction is the oxidation of ammonia to nitric oxide. Two unwanted side reactions can occur: The oxidation of ammonia to molecular nitrogen as well as the oxidation of ammonia to nitrous oxide [17, 61].

$$\mathrm{NH_3} + \frac{5}{4}\,\mathrm{O_2} \longrightarrow \mathrm{NO} + \frac{3}{2}\,\mathrm{H_2O} \qquad \Delta H^0_{\mathrm{R},\,298} = -227\frac{\mathrm{kJ}}{\mathrm{mol_{NH_3}}} \tag{2.6}$$

$$\mathrm{NH_3} + \frac{3}{4}\,\mathrm{O_2} \longrightarrow \frac{1}{2}\,\mathrm{N_2} + \frac{3}{2}\,\mathrm{H_2O} \qquad \Delta H^0_{\mathrm{R},\,298} = -317\frac{\mathrm{kJ}}{\mathrm{mol_{NH_3}}} \tag{2.7}$$

$$\mathrm{NH_3} + \mathrm{O_2} \longrightarrow \frac{1}{2}\,\mathrm{N_2O} + \frac{3}{2}\,\mathrm{H_2O} \qquad \Delta H^0_{\mathrm{R},\,298} = -276\frac{\mathrm{kJ}}{\mathrm{mol_{NH_3}}} \tag{2.8}$$

Thermodynamically the formation of nitrogen is favored at industrial reaction conditions of $800 - 950$ °C and pressures of $1 - 12$ bar. However, by catalyzing the reaction with suitable catalysts, nitric oxide selectivities of $92 - 98$ % at full ammonia conversion can be achieved [3]. The catalyst used for this process are gauzes made of platinum or platinum-rhodium alloys with rhodium contents of up to 10 wt.%. Depending on the process conditions layers of $3 - 50$ gauzes are used. The gauzes are usually deposited in a basket, which is held in place by an annular flange [3]. Ammonia oxidation using platinum gauzes is a mass transfer limited process at industrial conditions [3, 17]. During the start-up phase of the reaction, the gauzes are ignited in most industrial burners using a hydrogen torch that rotates over the gauze surface. Once the gauzes are ignited, the reaction runs autothermally [3].

One major problem of modern nitric acid plants is the fast degradation of the catalyst gauzes. During their operation life the gauzes are constantly loosing platinum and to a smaller extent rhodium in the form of volatile oxides. These losses are a major cost factor of modern nitric acid plants. Depending on the

operation conditions, mainly the pressure, temperature, and ammonia loading, the gauzes need to be exchanged after $1.5 - 12$ months. Besides damaging the structural integrity of the gauzes, the platinum losses also lead to a loss in nitric oxide selectivity due to the morphological changes of the catalyst surface [3].

Since this project focuses on ammonia oxidation, the main aspects of this process step are reviewed in more detail in the Sections 2.3 and 2.4.

2.2.3 Nitric Oxide Oxidation

The hot combustion gases, that leave the burner, are cooled in the next process step [61]. A first heat exchanger is often placed directly behind the gauzes, allowing to generate steam, which can be utilized in other parts of the plant. The total number of heat exchangers, used for cooling the combustion gases, depends strongly on the level of energy integration of the plant [60]. In these coolers and condensers starts the second reaction step of the Ostwald process: The oxidation of nitric oxide to nitric dioxide [17, 61].

$$\mathrm{NO} + \frac{1}{2}\,\mathrm{O_2} \longrightarrow \mathrm{NO_2} \tag{2.9}$$

The oxidation of nitric oxide to nitric dioxide is a quite uncommon reaction since it is a rare example of reactions, whose reaction rate decreases with increasing temperature, and is in some mechanisms described as termolecular reaction. This information is especially important because the oxidation of nitric oxide is the rate limiting step of the total nitric acid production process. The rate law of the reaction can be described by Equation 2.10 [5, 17, 62].

$$r = k \cdot p_{\mathrm{NO}}^2 \cdot p_{\mathrm{O_2}} \tag{2.10}$$

Hence, at a constant combustion gas composition the reaction rate changes with $r \propto p^3$. Considering the inverse proportionality of the volume flow rate in pressure, gives an overall quadratic dependency of the residence time for nitric oxide oxidation in pressure, allowing a tremendous reduction of the required oxidation space by increasing the process pressure. For instance, a pressure increase from one to eight atmospheres would reduce the required residence time for nitric ox-

ide oxidation by a factor of 64. Therefore, the usage of high pressure systems allows reducing the capital costs for oxidation space extremely [5]. A high degree of nitric oxide oxidation in the gas stream entering the downstream absorber is wanted because it allows producing a product with a high acid strength. Thus, in most nitric acid plants additional oxidation space beside the heat exchangers and piping is provided. Typical additional oxidizer vessels are free spaces with indirect cooling surfaces or tray towers [60].

In order to supply a sufficient amount of oxygen for the oxidation processes downstream of the burner, additional air is added in most nitric acid plants. This secondary air is either added before a cooling heat exchanger or alternatively before the absorber, in which the nitric oxide oxidation process continues.

Besides the oxidation of nitric oxide, further reactions and processes take place in the coolers downstream of the burner. The first additional process is the equilibrium dimerization of nitrogen dioxide to dinitrogen tetroxide.

$$\mathrm{NO_2} \rightleftharpoons \frac{1}{2}\,\mathrm{N_2O_4} \tag{2.11}$$

Additionally, water formed in the ammonia oxidation step condenses in the coolers. Nitric oxides start to absorb in the liquid aqueous phase and start to form a weak nitric acid with a concentration of up to 40 wt.% (reactions see Section 2.2.4). The liquid and the gas phase leaving the condenser are divided in a splitter, before entering the absorber separately at different stages [4, 60].

Compared to a single pressure plant, the cooler/condenser section of a dual-pressure plant is a little bit more complex. The gas stream that leaves the burner is compressed after a heat exchanger to the target pressure of the absorption step. A large share of the nitric oxide oxidation processes as well as of the condensation occurs in the compressor itself [60].

2.2.4 Absorption

The third and final step of the Ostwald process mainly proceeds in one or multiple absorption columns. The cooled nitrous gas enters the absorption column at the bottom and is absorbed reactively in water that flows downwards in countercurrent. The weak nitric acid, that is condensed in the previous cooling steps, enters the

column at the stage which has the same nitric acid concentration. Good mass and heat transfer between the liquid and gaseous phase must be guaranteed in the absorber to enhance the formation of nitric acid. The overall reaction of the absorption process can be described with the following reaction [4, 5, 62].

$$NO_2 + \frac{1}{3}H_2O \longrightarrow \frac{2}{3}HNO_3 + \frac{1}{3}NO \tag{2.12}$$

However, the real processes in a nitric acid cooling and absorption section, leading to the formation of nitric acid, are not as simple as indicated with the three main equations of the Ostwald process. In reality, many side reactions and different species participate in the oxidation and absorption process. First of all, as already mentioned in the previous section, nitric dioxide is in equilibrium with its dimer dinitrogen tetroxide (see Reaction 2.11). The dinitrogen tetroxide can also absorb in water forming nitric acid and nitrous acid [4].

$$N_2O_4 + H_2O \longrightarrow HNO_3 + HNO_2 \tag{2.13}$$

This reaction contributes a large share of the total nitric acid formation due to the high solubility of dinitrogen tetroxide in water. Hence, the grade of dimerization of nitric dioxide is an important parameter of the absorption process. The nitrous acid formed in the reactive absorption of dinitrogen tetroxide dissociates to nitric acid, water, and nitrogen monoxide, which is transported back to the boundary layer [4, 63].

$$3\,HNO_2 \longrightarrow HNO_3 + H_2O + 2\,NO \tag{2.14}$$

The nitric oxide is oxidized to nitrogen dioxide in the boundary layer (see Reaction 2.9 in the previous section). Additionally to the presented side reactions, further processes such as reactions of dinitrogen trioxide, which is formed of nitric oxide and nitrogen dioxide, as well as the mass transport between the liquid and gas phase complicate the absorption process even more [4]. Since the focus of this work is the ammonia oxidation step, the absorption and oxidation mechanism will not be explained in more detail as a part of this review. More details on the

oxidation and absorption mechanism can be found for example in the following literature [4, 62, 63].

Nowadays, absorption columns used in industry for nitric acid production are built of stainless steel [3, 60]. Depending on the size of the plant, absorption columns with diameters of up to four meters and seventy meters height are constructed [5, 17]. In some plants multiple smaller absorption columns are utilized. The first medium pressure absorption plants were often built as packed columns. However, in modern medium and high pressure absorption processes tray towers with bubble caps or sieve trays are used. In tray columns the heat of absorption is removed from the process using tube coils placed in the liquid on the trays [60]. The operation pressure of industrial nitric acid absorption towers usually lies in the range of $4 - 14$ bar [3, 17]. Higher pressures allow to reduce the size of the absorber tremendously due to the high pressure dependency of the oxidation as well as absorption rates on the pressure (see Section 2.2.3) [3, 5]. Additionally, higher pressures facilitate the production of acids with a high strength [64]. In modern high pressure absorption systems efficiencies of 99 % and acid concentrations between $55 - 65$ % can be achieved [60].

2.2.5 Bleaching

Before nitric acid can be further processed, bleaching is necessary as a final process step. The nitric acid, which is taken from the bottom of the absorber, contains high amounts of dissolved nitric oxides such as nitric dioxide, nitric oxide, dinitrogen tetroxide, and dinitrogen trioxide [62]. Due to the high amounts of dissolved nitric dioxide, the nitric acid has a brownish color, when it leaves the absorber. The brown color is undesired in nitric acid, which is directly marketed and also, the high amounts of nitric oxides are unwanted in downstream processes, that utilize the nitric acid to produce for example fertilizers. Therefore, these nitric oxides are stripped from the nitric acid product stream in the bleaching process [17].

The bleaching process is carried out in small packed or tray towers. Secondary air is used as a carrier gas to extract nitric oxides from the liquid phase. Bleachers are usually operated in a counter-current setup [62]. The bleaching process is facilitated by heating the nitric acid stream, before entering the bleacher. This

way the solubility of nitric oxides in the liquid phase is reduced. The secondary air, that is used for stripping, is mixed with the gas stream that leaves the burner (see Section 2.2.3). Nitric oxides dissolved in the bleaching process are reintroduced into the nitric oxide oxidation and absorption section. Thereby, the losses of nitric oxides are minimized and the overall plant efficiency is optimized [60].

2.2.6 Emission Abatement Strategies

In the last decades, nitric oxide and nitrous oxide emissions of industrial plants had to be reduced drastically, due to the enactment of various administrative regulations to protect the climate and the environment. Several emission abatement strategies enable reduction of the pollutant levels of nitric acid plants below the strict emission limits of most western countries [3].

In most western countries the emission of nitric oxides is regulated since a couple of decades. Already in the early 1980s, the first administrative regulations to reduce nitric oxide emissions were enacted in Germany [3]. Nitric oxide emissions result from incomplete absorption of nitric oxides in water in the absorption section of nitric acid plants. Residual concentrations of nitric oxides inside the gas stream leaving the absorption section usually lie in the range of $100 - 400$ ppm [58]. High nitrogen oxide concentrations in the atmosphere can lead to the formation of acidic rain. Furthermore, high nitric dioxide concentrations give the plant exhaust gases a brownish color and an unwanted pungent odor. The strategies to reduce nitric oxide emissions can be divided into four groups: improved absorption, chemical scrubbing, adsorption, and catalytic reduction [3].

The absorption efficiency of a nitric acid plant can be increased by changing the operation conditions. An effective method to increase the absorption efficiency is the utilization of higher pressures. Compared to atmospheric absorption towers constructed in the early twentieth century, the absorption efficiency in modern high pressure nitric acid plants is considerably higher. In existing plants it is usually not possible to increase the absorption pressure without building an entirely new absorption column. Hence, this option is often not economically favorable for existing plants. The absorption efficiency also benefits from low temperatures. Thus, the installation of additional cooling in the last trays of an absorption column

is an effective method to increase the absorption efficiency. Finally, the absorption efficiency can be increased by installing additional absorption steps [3, 4, 60]. However, upgrading an existing plant using these strategies can be very expensive and is often technically hard to realize. Therefore, upgrading existing plants with improved absorption sections is often not economically profitable [3].

The second strategy to reduce nitric oxide emissions is the installation of an additional chemical scrubbing step. In chemical scrubbers the tail gases are scrubbed in liquors such as urea, ammonia solutions, and hydrogen peroxide. However, this method is often ruled out because of the high costs for the constantly consumed scrubbing liquor [3, 60].

The third strategy is the adsorption of nitric oxides in adsorbers based on molecular sieves and carbon based adsorbents. This method never gained popularity in industry due to high investment costs and problems in the process operation [3,60].

The fourth method, the catalytic reduction, can be divided into two subgroups: Unselective catalytic reduction and selective catalytic reduction [3, 60].

The unselective catalytic reduction is the oldest nitric oxide abatement strategy, firstly patented in 1924 by Giacomo Fauser. In unselective catalytic reduction processes a fuel such as methane, hydrogen, natural gas, or propane is combusted in the tail gas of the plant. The fuel reacts with molecular oxygen as well as with oxygen atoms of nitric oxide compounds reducing the nitric oxides to nitrogen. Various catalysts based on Pt, V_2O_5, Fe_2O_3, and TiO_2 can be used to catalyze the reaction. However, the process has a by far higher selectivity to reduce molecular oxygen instead of nitric oxides. Therefore, high amounts of fuel are required to reduce the molecular oxygen as well as the nitric oxides. This reduces the cost-effectiveness of the process. Furthermore, unwanted side products such as CO_2 and HCN can be produced depending on the selected fuel [3, 60, 65].

Nowadays, nitric oxide emissions of most modern nitric acid plants are minimized using a combination of improved absorption and selective catalytic reduction. In selective catalytic reduction the reducing agent has a higher selectivity to reduce nitric oxides than molecular oxygen. The higher selectivity can be achieved by using ammonia as a reducing agent and suitable catalysts. Selective catalytic reduction catalysts usually consist of a ceramic carrier and a catalytic active com-

pound such as base metal oxides or precious metals. The total reaction of the selective catalytic reduction can be described with Reaction 2.15 [3].

$$2\,NH_3 + NO + NO_2 \longrightarrow 2\,N_2 + 3\,H_2O \qquad \Delta\Delta H^0_{R,\,298} = -758\frac{kJ}{mol_{NO}} \tag{2.15}$$

Due to the higher selectivity less fuel is required in selective catalytic reduction compared to unselective alternatives and fewer unwanted side products are produced. Another advantage of the selective process compared to most unselective processes are lower operation temperatures, which allows usage of cheaper construction materials and hence, lowers the investment costs. However, on the downside ammonia has comparatively high caloric costs and additional monitoring is necessary to prevent ammonia breakthrough [3].

In addition to nitric oxides also the emission of nitrous oxide is administratively regulated in many western countries since the beginning of the century. Administrative regulations of nitrous oxide emissions have been enacted as a result of the Kyoto Protocol. Nitrous oxide is a potent greenhouse gas, whose contribution to the anthropogenic greenhouse effect is estimated to lie between $5 - 6$ % [66, 67]. Even though far less nitrous oxide is emitted to the atmosphere than CO_2, nitrous oxide affects the greenhouse effect strongly. The emission of one tonne of nitrous oxide is regarded equivalent to the emission of 298 tonnes of carbon dioxide on a 100 year basis [8]. Furthermore, nitrous oxide has a long average retention time of 114 years in the atmosphere and is considered to be one of the major stratospheric ozone-depleting substances [66, 68]. Hence, multiple processes have been developed in this century to reduce nitrous oxide emissions from nitric acid plants. The nitrous oxide abatement strategies can be divided into three groups: primary, secondary, and ternary abatement methods [3].

Primary abatement strategies have the goal to reduce the direct formation of nitrous oxide inside nitric acid plants. Nitrous oxide is a side product of the ammonia combustion step (see Section 2.2.2). By changing the operation parameters such as temperature, pressure as well as ammonia, and oxygen concentration inside the ammonia burner, the selectivity of the three products nitrogen, nitric oxide, and nitrous oxide can be influenced. Another factor that influences the selectivi-

ties are the properties of the catalyst like elemental composition and morphology. For example, catalysts based on metal oxides have about 80 % lower nitrous oxide selectivity than platinum based catalysts. However, metal oxide catalysts are not economically competitive due to lower nitric oxide selectivities (see Section 2.4.4). Since the exact reaction mechanism of ammonia combustion is still not completely understood, a systematic approach to optimize the nitrous oxide as well as nitric oxide selectivity is hard to establish. Therefore, additional downstream abatement strategies are necessary to fulfill the strict emission levels [3, 17].

Secondary nitrous oxide abatement strategies have the goal to decompose nitrous oxide directly after its formation in the burner before the nitrous gas reaches the absorption section of the plant. One secondary abatement method is to increase the extent of thermal decomposition of nitrous oxide to molecular nitrogen and oxygen in homogeneous phase. This can be achieved by increasing the residence time of the hot combustion gases in an extended reaction chamber. An increase of the residence time of two seconds leads to thermal decomposition ratios of up to 95 % [69]. However, due to the high volumetric throughput of modern nitric acid plants, the required space for such an extended reaction chamber increases the investment costs noticeably and also requires a lot of space. This rules out this method for many existing as well as new nitric acid plants. A space-saving alternative secondary approach is the catalyzed heterogeneous decomposition of nitrous oxide using specialized decomposition catalysts placed directly behind the platinum gauzes or possible platinum catchment gauzes [66]. Catalysts based on oxides of copper, iron, aluminum, or cobalt show the desired properties to decompose nitrous oxide and being inert towards nitric oxide [3]. One example of such catalysts is the YARA 58-Y1 catalyst, which consists of cobalt aluminate supported on cerium oxide [70]. Modern catalytic secondary abatement allows reducing the nitrous oxide concentration by more than 90 % [3, 66].

In ternary nitrous oxide abatement strategies, the nitrous oxide concentration is reduced at the tail end of a plant. One example of a ternary abatement process is a combined de-NO_x/de-N_2O process with nitrous oxide conversion efficiencies of 98 % developed by UHDE. In the first step of this process, nitrous oxide is catalytically decomposed to nitrogen and oxygen using ion-exchange zeolites. Subsequently, NO_x is decomposed catalytically. Ternary processes have high investment costs

due to the need for expensive equipment such as pressure reactors, additional heat management, tail-gas expander, and steam turbines [3].

All in all, a wide variety of methods can be used to regulate the emissions of nitric acids plants. However, the best method considering nitrous oxide emissions would be an improved ammonia oxidation step with lower nitrous oxide selectivities as well as higher nitric oxide selectivities. This way costs for additional abatement could be reduced and the efficiency of the process could be improved. To design an improved ammonia oxidation process systematically, a detailed, systematic understanding of the reaction mechanism and processes inside ammonia burners is inevitable.

2.3 The Ammonia Oxidation Process

Since ammonia oxidation plays a key role in the economic as well as ecologic efficiency of the Ostwald process, many researchers studied this process step, contributing to a growing understanding of its underlying mechanisms. Several hundred articles have been published in the last century presenting new insights into different aspects of the process. An all-encompassing review of all these articles is beyond the scope of this thesis. Hence, this chapter focuses on giving an overview of five major aspects: The reaction mechanism of ammonia oxidation, proposed microkinetic models of the reaction, the influence of the mass transport limitation, recent developments in CFD studies of the process, and how the performance of the process is influenced by the operation conditions.

2.3.1 The Reaction Mechanism of Ammonia Oxidation

The oxidation of ammonia to produce nitric oxide is an extremely fast, mass-transfer limited reaction that is catalyzed by gauzes made of platinum or platinum alloys. In industrial burners nitric oxide selectivities of $92-98$ % at full conversion are achieved. The reaction is usually operated at temperatures in the range of $800-950$ °C and pressures of $1-12$ bar [3, 61]. Besides the main product, nitric oxide, two side products, nitrogen and nitrous oxide, are formed in nitric acid

plants under industrial conditions. The three main reactions can be described according to the Equations 2.16 - 2.18 [3, 17].

$$\mathrm{NH_3} + \frac{5}{4}\,\mathrm{O_2} \longrightarrow \mathrm{NO} + \frac{3}{2}\,\mathrm{H_2O} \qquad \Delta H^0_{\mathrm{R,\,298}} = -227\frac{\mathrm{kJ}}{\mathrm{mol_{NH_3}}} \tag{2.16}$$

$$\mathrm{NH_3} + \frac{3}{4}\,\mathrm{O_2} \longrightarrow \frac{1}{2}\,\mathrm{N_2} + \frac{3}{2}\,\mathrm{H_2O} \qquad \Delta H^0_{\mathrm{R,\,298}} = -317\frac{\mathrm{kJ}}{\mathrm{mol_{NH_3}}} \tag{2.17}$$

$$\mathrm{NH_3} + \mathrm{O_2} \longrightarrow \frac{1}{2}\,\mathrm{N_2O} + \frac{3}{2}\,\mathrm{H_2O} \qquad \Delta H^0_{\mathrm{R,\,298}} = -276\frac{\mathrm{kJ}}{\mathrm{mol_{NH_3}}} \tag{2.18}$$

Besides these main reactions further subsequent reactions are discussed to influence the selectivities of the three different products. Examples for such subsequent reactions are the reaction of ammonia with nitric oxide in the gas phase forming nitrogen and water and the thermal decomposition of nitric oxide on the catalyst forming nitrogen and oxygen [3].

$$\mathrm{NH_3} + \frac{3}{2}\,\mathrm{NO} \longrightarrow \frac{5}{4}\,\mathrm{N_2} + \frac{3}{2}\,\mathrm{H_2O} \qquad \Delta H^0_{\mathrm{R,\,298}} = -452\frac{\mathrm{kJ}}{\mathrm{mol_{NH_3}}} \tag{2.19}$$

$$\mathrm{NO} \longrightarrow \frac{1}{2}\,\mathrm{N_2} + \frac{1}{2}\,\mathrm{O_2} \qquad \Delta H^0_{\mathrm{R,\,298}} = -45\frac{\mathrm{kJ}}{\mathrm{mol_{NO}}} \tag{2.20}$$

Even though many groups studied ammonia oxidation in the past, no generally accepted reaction mechanism exists that accurately describes the process over the entire range of industrial operation conditions [11, 17]. The development of reaction mechanisms is hindered by a lack of reliable experimental data. Due to extreme process conditions, constantly changing catalyst surfaces as well as the mass-transfer limitation of the reaction at industrial conditions, it is challenging to obtain experimental insight into the processes at the gauze surface [3, 17, 71]. Therefore, most mechanistic studies are limited to Density Functional Theory (DFT) simulations [16, 25, 31, 41, 72–74], are based on low pressure, Ultra-high Vacuum (UHV) [9, 20–25, 75, 76] or low temperature experiments [20–24, 26–28] carried out often with single crystals using various surface science methods [9, 20–22, 77–79], TAP setups [22, 29–31, 80, 81] or also synchrotron based methods [13, 28]. At low temperatures and vacuum conditions ammonia oxidation is kinetically

controlled facilitating the determination of kinetic data. However, the product selectivities differ strongly from industrial results [3]. Under UHV conditions, for example, no nitrous oxide is formed [9]. Hence, although valuable information can be obtained from low pressure and low temperature experiments, an extrapolation to industrial conditions cannot truly display the real processes inside industrial burners.

Despite the many challenges complicating ammonia oxidation studies, the understanding of the reaction mechanism has changed considerably over the years. In the 1920s and 1930s, first theories have been presented, which suggest that a key step in the reaction mechanism is the formation of molecular intermediates [61]. At this time researchers debated whether ammonia oxidation proceeds via the formation of nitroxyl, imides, or hydroxylamine as intermediates [6, 82–84]. Later those mechanisms have lost popularity since none of the suggested species have been measured in spectroscopic studies at UHV [9, 75–79]. The application of various surface science methods for in-situ analysis of surface species at low temperatures and pressures changed the mechanistic view on ammonia oxidation drastically. Nowadays, it is agreed that the reaction proceeds via the interaction of adsorbed surface species like adsorbed NH_x (with x = 0, 1, 2, 3) and adsorbed atomic oxygen. The selectivities of the process are mainly controlled by the surface coverages of the catalyst [9–13]. Generally, reduced surface coverage with NH_x (with x = 0, 1, 2, 3) species and increased coverage of the surface with atomic oxygen favor the formation of the wanted product nitric oxide [10–13, 15, 16, 29, 30, 74]. At temperatures below 300 °C nitrogen is the main product due to high surface coverage with atomic nitrogen [3, 12]. Nitrogen is also the main product at pressures below 10^{-4} mbar [12] compromising the explanatory power of studies at UHV. At higher temperatures in the range of $300 - 500$ °C nitrogen as well as nitric oxide have high surface coverage leading to high nitrous oxide formation rates. Between $500 - 600$ °C the reaction starts to become mass-transfer limited and the surface coverage of atomic oxygen dominates, making nitric oxide the main product [3, 12, 85, 86]. At temperatures above 1200 °C nitrogen becomes again the main product [3]. Additionally to the operation conditions, the reaction mechanism and the resulting selectivities are also influenced by the properties of the catalyst. DFT studies show that the kinetic parameters of the involved reaction steps highly de-

viate for different alloys and crystallographic planes [10, 16, 17, 25, 31, 41, 72–74]. Furthermore, the geometrical structure like wire diameter, orientation of wires to each other and the flow direction, etc. have a strong impact on the mass transfer processes and hence, influence the surface coverages and the resulting selectivities as well [11, 14, 19].

The results of in-situ analyses of surface species at low temperatures and pressures as well as the rapid increase of computer power enabled the description of industrial ammonia oxidation via complex microkinetic models at the turn of the century. Since then many groups have tackled the task of developing a suitable microkinetic model to describe the ammonia oxidation process. Even though the microkinetic models of different groups vary, for example, in their underlying assumptions, kinetic parameters, and area of operation conditions, all models are based on a comparable general process. On the following pages the mechanism of ammonia oxidation is explained step by step using exemplarily the Traversac mechanism [86]. The mechanism of Traversac is selected for this purpose since it was the first thermodynamically consistent model suggested in literature and includes all prominently discussed main elementary steps relevant under industrial conditions. Furthermore, the Traversac model is based on Pt(111) faces, which are at high temperatures the most thermodynamically stable faces of the face-centered cubic crystal structure of platinum [87] and hence, are most likely a good model surface for describing ammonia oxidation. In Section 2.3.2 various other microkinetic models postulated in the last two decades are reviewed.

In Figure 2.2 the main parts of the ammonia oxidation mechanism suggested by Traversac are illustrated. The according full set of reactions are shown in the Equations 2.21 − 2.42 and explained on the following pages. For a more detailed explanation of the model, kinetic parameters such as appropriate sticking coefficients, pre-exponential factors, activation and binding energies the reader is referred to Traversac's Ph.D. thesis [86].

The first step of the reaction mechanism is the chemisorption of ammonia on the surface.

$$\mathrm{NH_3\,(g) + Pt\,(s) \rightleftharpoons NH_3\,(s)} \tag{2.21}$$

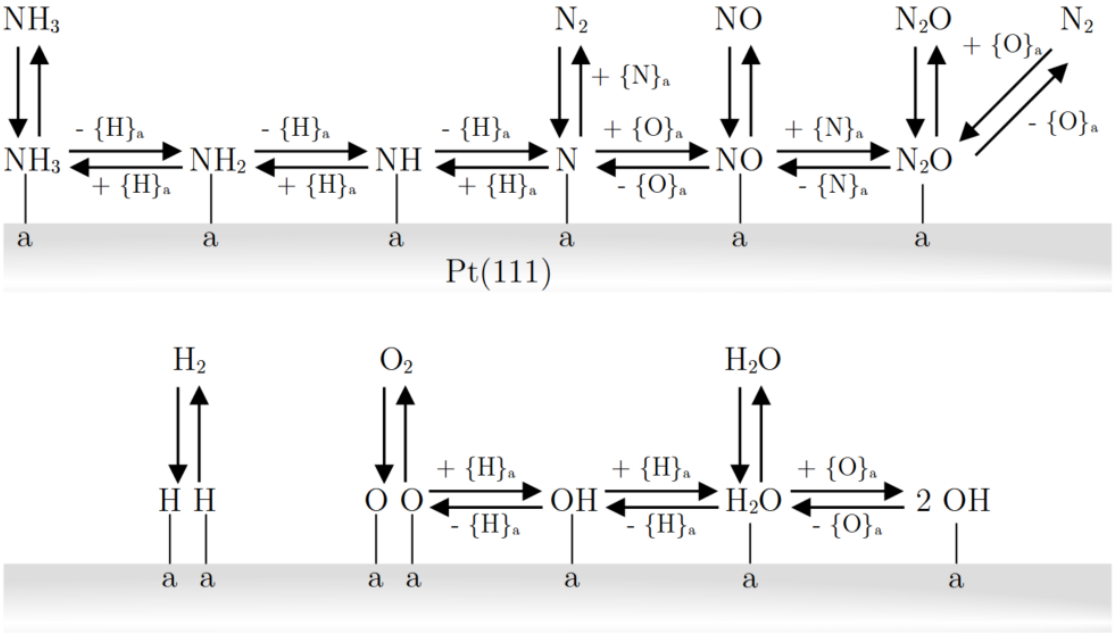

Figure 2.2: Scheme of the ammonia oxidation mechanism developed by Traversac with simplified hydrogen stripping

Usually, ammonia attaches to the surface with the nitrogen atom of ammonia molecules oriented to the surface and the hydrogen atoms pointing away from the surface [79, 88]. The chemisorption process is reported not to be blocked by adsorbed oxygen and the binding energy is reported to be not influenced strongly by different platinum faces (Pt(111), Pt(100), Pt(211), Pt(211)) [79,89]. At industrial conditions ammonia chemisorption is considered as the rate limiting step of the overall surface mechanism, due to the mass transfer limitation.

The second reactive feed component, oxygen, is adsorbed dissociatively, occupying preferentially hollow sites [90–92]. In contrast to ammonia adsorption, oxygen adsorption is reported to be strongly surface face dependent [71, 93].

$$\mathrm{O_2\,(g) + 2\,Pt\,(s) \rightleftharpoons 2\,O\,(s)} \tag{2.22}$$

Ammonia adsorbed at the surface is activated by stripping off hydrogen atoms. This step can be divided into three sub groups of reactions: Stripping by reactions with surface oxygen (Equations 2.23 – 2.25), stripping by reactions with

surface hydroxide (Equations 2.26 − 2.28) and self-activated hydrogen stripping (Equations 2.29 − 2.31) [94–96].

$$NH_3\,(s) + O\,(s) \rightleftharpoons NH_2\,(s) + OH\,(s) \tag{2.23}$$
$$NH_2\,(s) + O\,(s) \rightleftharpoons NH\,(s) + OH\,(s) \tag{2.24}$$
$$NH\,(s) + O\,(s) \rightleftharpoons N\,(s) + OH\,(s) \tag{2.25}$$
$$NH_3\,(s) + OH\,(s) \rightleftharpoons NH_2\,(s) + H_2O\,(s) \tag{2.26}$$
$$NH_2\,(s) + OH\,(s) \rightleftharpoons NH\,(s) + H_2O\,(s) \tag{2.27}$$
$$NH\,(s) + OH\,(s) \rightleftharpoons N\,(s) + H_2O\,(s) \tag{2.28}$$
$$NH_3\,(s) + Pt\,(s) \rightleftharpoons NH_2\,(s) + H\,(s) \tag{2.29}$$
$$NH_2\,(s) + Pt\,(s) \rightleftharpoons NH\,(s) + H\,(s) \tag{2.30}$$
$$NH\,(s) + Pt\,(s) \rightleftharpoons N\,(s) + H\,(s) \tag{2.31}$$

The theory that hydrogen stripping occurs during ammonia oxidation has been validated by in-situ measurements of OH, NH, and NH_2 molecules on the surface and is in agreement with DFT studies [22, 24, 72, 97]. Depending on the operation conditions the three different stripping mechanisms occur to a different extent. Self-activated stripping occurs preferentially at low oxygen to ammonia ratios, which result in low surface oxygen and hydroxide concentrations. In contrast at high oxygen contents stripping by surface oxygen and hydroxide dominates the overall stripping process [17]. The required activation by hydrogen stripping of ammonia by oxygen and hydroxide species favors chemisorption of ammonia on sites with neighboring oxygen atoms [71, 93]

Hydroxide and hydrogen species undergo a set of subsequent reactions that lead to the formation of the reaction product water. Surface hydrogen formed in the stripping of ammonia reacts with surface oxygen to hydroxide. Hydroxide is considered to be a mobile species that diffuses across the surface. In subsequent reactions hydroxide reacts with either hydrogen or a second hydroxide species leading to the formation of water. Finally, water desorbs leaving a free platinum site behind.

$$\mathrm{O\,(s) + H\,(s) \rightleftharpoons OH\,(s) + Pt\,(s)} \tag{2.32}$$

$$\mathrm{H_2O\,(s) + O\,(s) \rightleftharpoons 2\,OH\,(s)} \tag{2.33}$$

$$\mathrm{OH\,(s) + H\,(s) \rightleftharpoons H_2O\,(s) + Pt\,(s)} \tag{2.34}$$

$$\mathrm{H_2O\,(g) + Pt\,(s) \rightleftharpoons H_2O\,(s)} \tag{2.35}$$

Additionally, hydrogen can be formed by the combination of two surface hydrogen atoms and desorb into the gas phase.

$$\mathrm{H_2\,(g) + 2\,Pt\,(s) \rightleftharpoons 2\,H\,(s)} \tag{2.36}$$

The selectivities of the overall ammonia oxidation process are dominated by the reactions of surface nitrogen species. In general low surface coverage with NH_x (with x= $0, 1, 2, 3$) species and increased coverage of the surface with atomic oxygen favor the formation of the wanted product nitric oxide [10–13, 15, 16, 29, 30, 74]. Moreover, the binding energies of oxygen species are reported to influence product selectivities with reported high nitric oxide selectivities obtained for weakly bonded oxygen and high nitrogen and nitrous oxide selectivities resulting from strongly bonded oxygen [29, 30]. The formation of nitric oxide proceeds according to the Traversac mechanism by the reaction of surface nitrogen with surface oxygen, leading to the formation of surface nitric oxide. Subsequently, nitric oxide can desorb from the surface.

$$\mathrm{N\,(s) + O\,(s) \rightleftharpoons NO\,(s) + Pt\,(s)} \tag{2.37}$$

$$\mathrm{NO\,(s) \rightleftharpoons NO\,(g) + Pt\,(s)} \tag{2.38}$$

If two surface nitrogen atoms react, a nitrogen molecule is formed. Most microkinetic models assume that readsoprtion of nitrogen can be neglected, and only a few models like Traversac's include reversible desorption of nitrogen as shown in Equation 2.39.

$$2\,\mathrm{N\,(s)} \rightleftharpoons \mathrm{N_2\,(g)} + 2\,\mathrm{Pt\,(s)} \tag{2.39}$$

The formation pathway of the last product, nitrous oxide, is not well understood and many theories are suggested by different groups. In the most popular pathway, which is also used in Traversac's model, nitrous oxide is considered to form by the combination of surface nitric oxide and surface nitrogen. Finally, nitrous oxide desorbs into the gas phase.

$$\mathrm{NO\,(s)} + \mathrm{N\,(s)} \rightleftharpoons \mathrm{N_2O\,(s)} + \mathrm{Pt\,(s)} \tag{2.40}$$

$$\mathrm{N_2O\,(g)} + \mathrm{Pt\,(s)} \rightleftharpoons \mathrm{N_2O\,(s)} \tag{2.41}$$

Early experimental studies in the kinetically controlled regime indicate that nitrous oxide decomposes on platinum surfaces into nitrogen and oxygen. However, whether this decomposition reaction occurs to a noticeable extent at industrial conditions is controversially discussed [17, 86, 98].

$$\mathrm{N_2O\,(s)} \rightleftharpoons \mathrm{N_2\,(g)} + \mathrm{O\,(s)} \tag{2.42}$$

According to Temporal Analysis of Products (TAP) experiments conducted by Imbihl et al. [22] nitrogen is the end product of a reaction sequence in which firstly, nitrous oxide is formed from nitric oxide, and subsequently, nitrous oxide is decomposed to nitrogen. In recent studies carried out under industrial conditions nitrous oxide decomposition is reported to be negligible and not measurable as long as the temperature does not exceed 1100 K [98]. Above 1100 K nitrous oxide starts to be decomposed in homogeneous gas phase reactions at a noticeable rate [86]. Kondratenko et al. [23, 99] suggested that catalytic nitrous oxide decomposition is inhibited by site-blocking of adsorbed oxygen atoms. In contrast, Gonzalez et al. [72] stated that oxygen coverage at industrial conditions is not sufficient for site-blocking. Though, DFT studies of Gonzalez et al. indicate that nitrous oxide decomposes only on Pt(100) and Pt(110) facets and not on Pt(211), as well as Pt(111) facets at a considerable rate. Therefore, the group suggested that the catalyst is mainly composed of facets like Pt(111) and Pt(211) that do not favor the

decomposition process and the absence of measured nitrous oxide decomposition can be explained this way [72].

Besides the elemental steps included in Traversac's model, several other steps have been suggested in other models and studies. Especially the formation mechanism of nitrous oxide is still a matter of discussion. An alternative nitrous oxide formation route is via the dimerization of nitric oxide [22, 23].

$$\mathrm{NO\,(s) + NO\,(s) \rightleftharpoons (NO)_2\,(s) + Pt\,(s) \rightleftharpoons N_2O\,(g) + O\,(s) + Pt\,(s)} \tag{2.43}$$

DFT simulations show that nitrous oxide formation by nitric oxide dimerization is energetically favorable on Pt(211) surfaces compared to the formation by the combination of nitric oxide and surface nitrogen. However, the latter is kinetically favored at industrial conditions due to low surface concentrations of nitric oxide [72,100–102]. TAP experiments of Pérez-Ramírez et al. [30] also point towards the theory that nitrous oxide is primarily formed according to Equation 2.40.

For the formation of nitrogen a second formation route has to be considered at low temperatures. Hirano et al. [103] stated, that at temperatures below 330 °C nitrogen is primarily formed by the combination of surface nitric oxide and nitrogen. At higher temperatures the formation by the combination of two surface nitrogen species dominates the overall nitrogen formation [23].

$$\mathrm{N\,(s) + NO\,(s) \longrightarrow N_2\,(g) + O\,(s) + Pt\,(s)} \tag{2.44}$$

Another whole set of mechanistic steps are nitric oxide, nitrogen, as well as nitrous oxide formation steps by interactions of NH_x (x = 1 or 2) surface species with other surface species [30]. These steps are usually not included in most microkinetic models, since their contribution is considered negligible due to low surface coverages under industrial conditions. Therefore, these steps are not further considered in this short review.

A controversially discussed topic is the decomposition of nitric oxide. Until recently the optimal residence time theory has been widely spread. According to this theory, a maximum nitric oxide yield can be achieved if an optimal contact time between the gas mixture and the catalyst gauzes is guaranteed. Short

contact times lead to incomplete conversion. High contact times lead to decomposition of nitric oxide. However, several studies indicate that nitric oxide is not decomposed to a noticeable degree under industrial conditions [17, 98, 104–106]. One explanation for this lacking of decomposition is given by DFT studies. Due to high binding energies nitric oxide is decomposed on Pt(100) at a noticeable rate, while only negligible decomposition occurs on Pt(111) surfaces [89, 107, 108]. Since Pt(111) surface is the most stable and hence, dominant facet at high temperatures, insignificant nitric oxide decomposition rates can be explained by these results [86, 87, 109].

Another controversial aspect of industrial ammonia oxidation is the influence of homogeneous gas phase reactions. One example for these gas phase reactions is the decomposition of nitric oxide following Equation 2.19. Different theories have been presented claiming that this reaction proceeds by a radical-chain mechanism with many different intermediates [85,106,110]. However, most researchers assume that homogeneous gas phase reactions do not or only at a negligible degree participate in the overall reaction mechanism [3,17,98,111,112]. The only exception is the above mentioned decomposition of nitrous oxide at high temperatures above 1100 K [98]. This theory is also backed up experimentally, by tests at industrial conditions in which no decomposition of nitric oxide as well as nitrous oxide added into the feed of an ammonia oxidation test reactor has been measured [17, 72, 98].

Although microkinetic models like the Traversac mechanism are already way more sophisticated than older rate laws and Langmuir-Hinshelwood models, they cannot fully represent the true processes on the catalyst surface. One often made assumption is that the surface can be described as a homogeneous surface composed of only one facet. However, real catalysts are way more complex being composed not only of a variety of facets but also of different oxides [12]. Furthermore, the existing microkinetic models only consider platinum surfaces and neglect Pt-Rh alloy catalysts, which are mainly used in industrial ammonia oxidation. DFT studies, as well as experimental results, indicate that the kinetic parameters of the elementary steps of ammonia oxidation are highly surface dependent [25,113]. The catalyst surface is also undergoing a strong restructuring process during an industrial campaign length. A more comprehensive review on the catalyst and its restructuring is given in Chapter 2.4. A kinetic model that is supposed to fully

reflect all processes inside an ammonia burner needs also to consider these various, changing catalyst surfaces. To conclude, with the Traversac model a thermodynamic consistent model exists that includes all reaction steps that various research results indicate to be the main reaction pathways of ammonia oxidation under industrial conditions. However, the Traversac mechanism, like all surface mechanisms of ammonia oxidation, is not able to appropriately describe the reaction performance over the entire range of industrially relevant operation conditions on a quantitative basis. Hence, also other alternative reaction mechanisms proposed in the last decades are discussed in the following chapter.

2.3.2 Microkinetic Models of Industrial Ammonia Oxidation

In the last decades, several researchers contributed to the understanding of ammonia oxidation by developing microkinetic surface models. In this chapter, various microkinetic models are briefly introduced by comparing their main differences with the first thermodynamical consistent model by Traversac described in detail in the previous section. A detailed discussion of all models is beyond the scope of this work and for further details, the reader is referred to the original theses and articles in which the mechanisms are published.

In 2017 Gonzalez-Calderon [114] proposed a microkinetic model quite similar to the Traversac model. Both, the Traversac and Gonzalez-Calderon model were developed at the University of Sydney. In Figure 2.3 the microkinetic model proposed by Gonzalez-Calderon [114] is illustrated with a simplified water stripping mechanism.

Additionally to the steps shown in Figure 2.3, the complete water stripping mechanism following the Equations 2.23 - 2.31 is included in the mechanism by Gonzalez-Calderon. The only difference in the underlying reactions compared to Traversacs' model is in the treatment of nitrous oxide which is not formed as a surface adsorbed species, but instead directly desorbs into gas phase upon its formation. Gonzalez-Calderon parametrized the model for a stepped Pt(211) surface using kinetic parameters obtained by DFT calculations and sticking coefficients obtained from experiments [114].

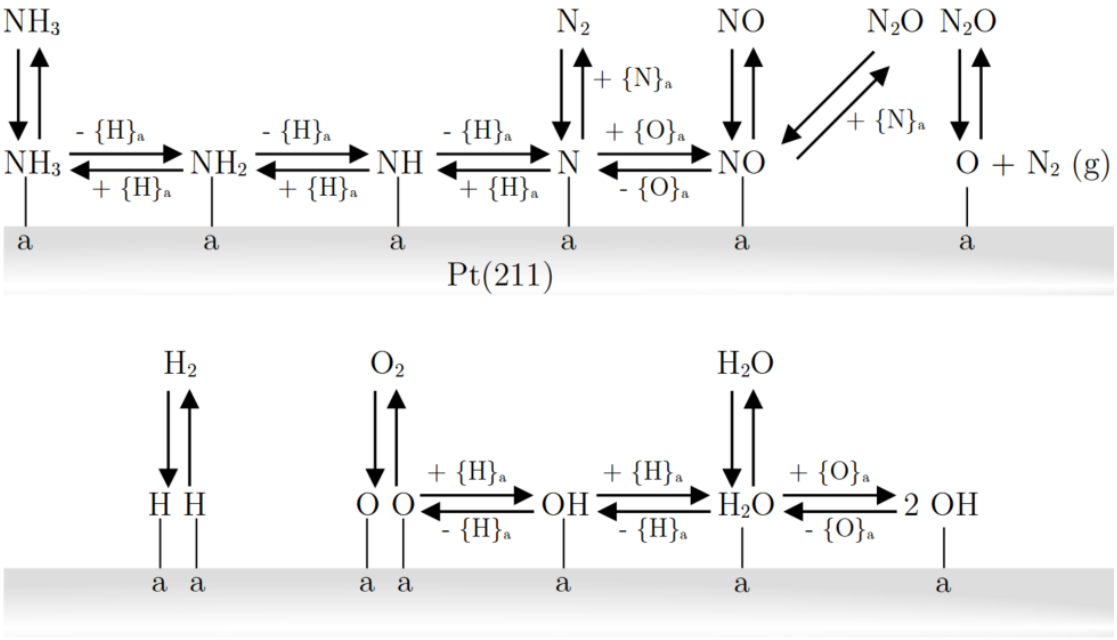

Figure 2.3: Scheme of the ammonia oxidation mechanism developed by Gonzalez-Calderon with simplified hydrogen stripping mechanism

Rebrov [115, 116] developed some of the first microkinetic models of ammonia oxidation in the early 2000s. The models by Rebrov are developed for multi crystalline platinum using a dual site mechanism that distinguishes between on top sites (a) and bridge sites (b). The latest version of the Rebrov model is shown in Figure 2.4.

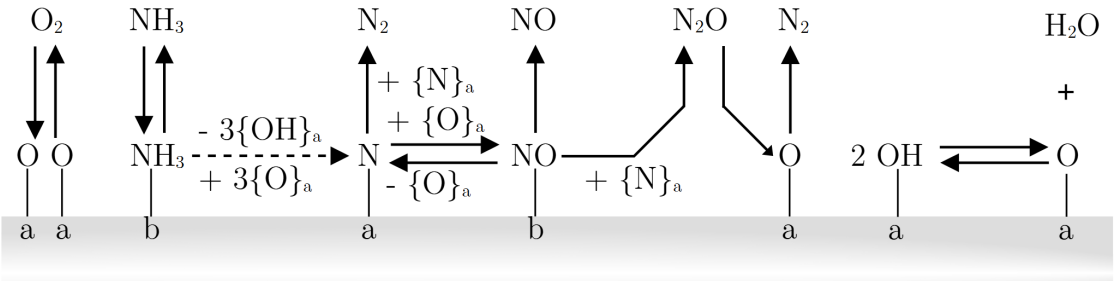

Figure 2.4: Kinetic surface mechanism suggested by Rebrov

Water stripping is lumped into a single reaction step in this latest version. Nitrous oxide desorbs directly upon formation but can readsorb under decomposition to nitrogen. The kinetic parameters used in the Rebrov model are based on sur-

face science methods from literature supplemented by DFT calculated parameters. The parameters were subsequently adjusted to fit experimental data [115,116]. The used experimental data was obtained outside of the mass-transfer limited range studying Pt supported on porous Al_2O_3 at temperatures of up to 400 °C and pressures of 1 bar in a microreactor setup [26, 27].

Krähnert and Baerns [41,117] developed another micro kinetic model for Pt(111) based on the Rebrov model shown in Figure 2.5.

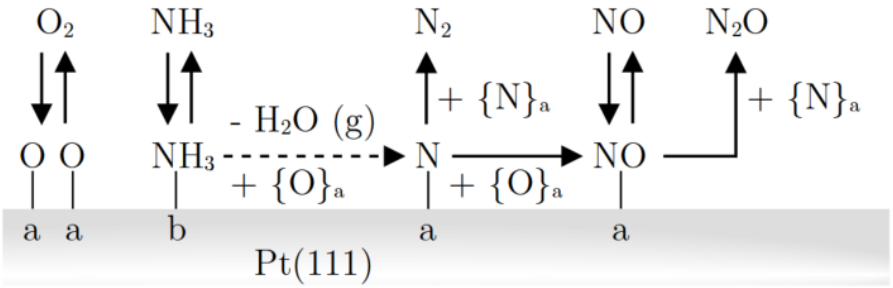

Figure 2.5: Ammonia oxidation mechanism proposed by Krähnert

In contrast to the Rebrov model, nitrous oxide decomposition is neglected but nitric oxide readsorption is included in the Krähnert model. The kinetic parameters used in the model are fitted to experimental data of the reaction measured using platinum foil catalysts at temperatures in the range of 286 − 385 °C and pressures between 1 and 6 bar in a micro-structured quartz reactor [41,117]. Even though the mechanism is not optimized for industrial conditions, it is widely used in CFD simulations of ammonia oxidation (see Section 2.3.4).

Besides its importance in the industrial process, ammonia oxidation is also important for selective catalytic reduction (SCR) applications. Therefore, several models exist that are parametrized for these applications like the re-parametrized version of the Krähnert mechanism by Scheuer [118]. Despite its parametrization for SCR applications, the Scheuer mechanism was also used in the past in CFD simulations of the industrial ammonia oxidation process (see Section 2.3.4). Further mechanisms developed for SCR applications are neglected in this review.

Scheibe et al. [20, 21, 119] proposed micro kinetic models based on experimental studies under UHV conditions. A schematic of the latest version developed for Pt(533) and Pt(443) sites is shown in Figure 2.6.

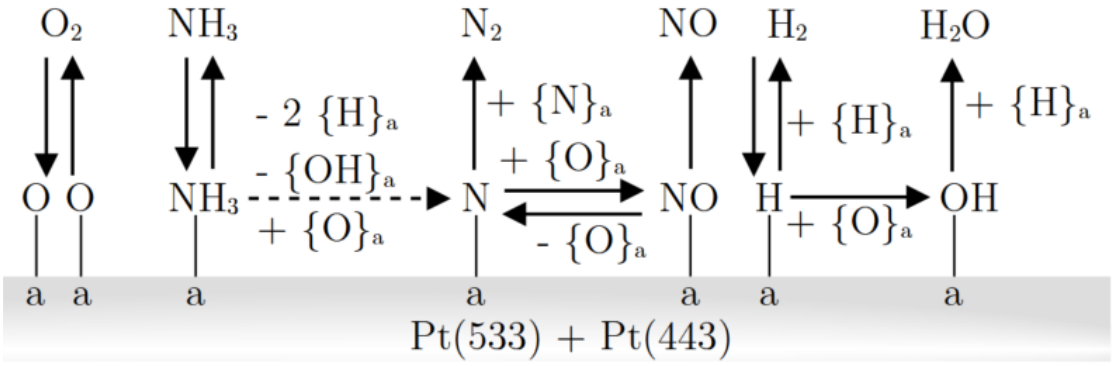

Figure 2.6: Schematic of the mechanism by Scheibe

A major drawback limiting the applicability of the Scheibe model for industrial ammonia oxidation is the missing nitrous oxide formation. The desorption steps of both nitrogen and nitric oxide are considered to be irreversible in the model. The kinetic parameters of the model are based on values reported in literature for various studies at UHV conditions. For four reaction steps the parameters were subsequently fitted to experimental data outside the mass transfer limited range, measured by Scheuer et al. using different techniques at UHV with pressures in the range of $10^{-5} - 10^{-4}$ mbar and temperatures of $200 - 700$ °C [20, 21, 119, 120].

Based on the Scheibe mechanism, Imbihl et al. [22] and Rafti et al. [25] developed improved mechanisms that also include nitrous oxide formation. One of the mechanisms proposed by Imbihl is illustrated in Figure 2.7

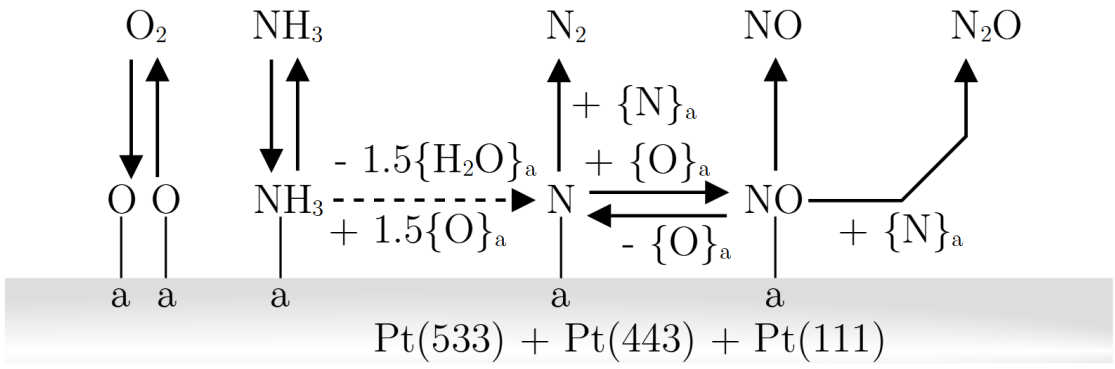

Figure 2.7: Surface mechanism according to Imbihl

The parameters of the mechanisms by Imbihl and Rafti are partly fitted to UHV, TAP and atmospheric experiments as well as partly based on DFT calculations [22, 25].

A schematic of the last mechanism presented in this short review, the mechanism proposed by Novell-Leruth [121], is depicted in Figure 2.8.

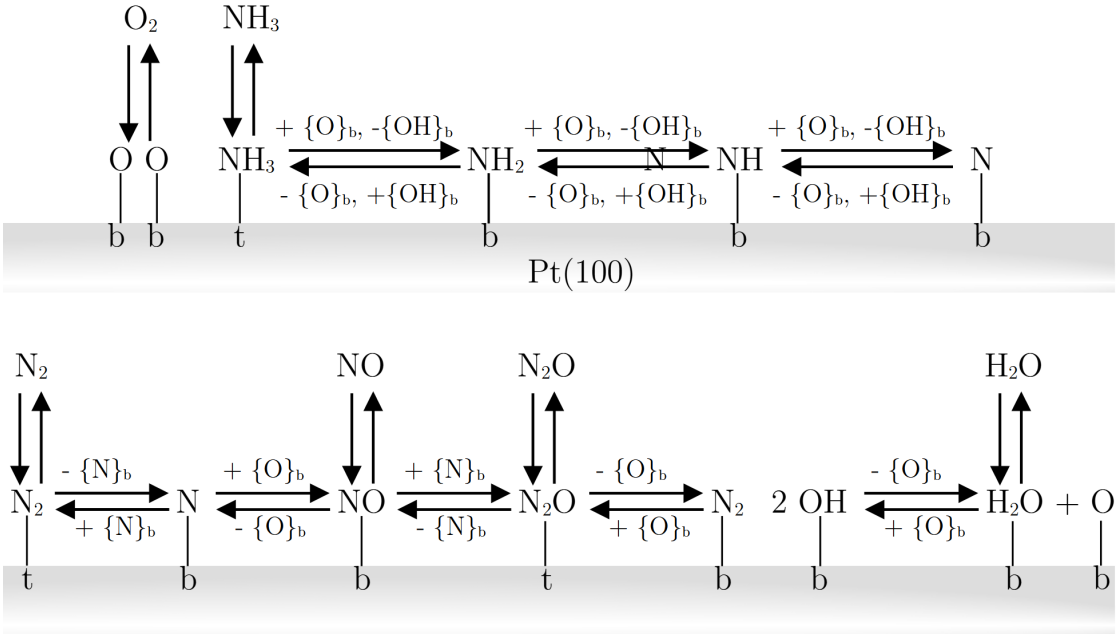

Figure 2.8: DFT calculated reaction network by Novell-Leruth

The Novell-Leruth mechanism is based entirely on DFT calculations for Pt(100) [121]. For additional information on the DFT calculations by Novel-Leruth the readers is referred to [95, 121, 122]. In the mechanism top and bridge surface sites are distinguished [121].

All in all, many different microkinetic models for ammonia oxidation were proposed in the last decades. Though, no mechanism exists to date, that allows an accurate quantitative prediction of the reaction performance over the entire range of industrial conditions and thus, is generally accepted. One reason for this gap of knowledge is the lack of reliable experimental data under the extreme industrial operation conditions that can be used for parameter fitting and validation. Most models are validated or even fitted to data obtained outside of the mass-transfer limited range of the reaction, even though totally different product selectivities

are obtained under these conditions. To accurately describe the processes inside ammonia oxidation burners not only an accurate surface mechanism but also accurate incorporation of the transport processes of the mass-transfer limited reaction is required.

2.3.3 The Industrial Ammonia Oxidation: A Mass-Transfer Limited Process

Early on in the history of ammonia oxidation studies, Andrussow [6, 7] discovered that ammonia oxidation is mass-transfer limited at industrial conditions. This observation has been confirmed by several studies in the following decades [17, 76, 105, 123–125]. Nevertheless, the mass-transfer limitation and its consequences have not been taken into account adequately by most researchers studying the reaction kinetics. The mass-transfer limitation does not only determine the reaction rate but also affects the selectivity of the nitrogen containing products. Therefore, the influence of the mass-transfer limitation on the reaction is a factor that has to be considered, if one tries to improve the overall process performance [17].

Besides many studies that neglect the importance of the mass-transfer limitation, several researchers have worked on the topic since Andrussow's time. Löffler et al. [126] and Flytzani-Stephanopoulos et al. [127] studied the influence of mass-transfer limitation and nonconstant reaction rates, resulting from surface heterogeneities, on platinum reconstruction processes and ammonia oxidation selectivities. The results of both groups agree that the combination of nonconstant reaction rates over the catalyst surface and the mass-transfer limitation strongly influence product selectivities as well as the extent of surface reconstruction [126, 127]. Oele [124] showed that the catalyst shape and surface structure influence the mass transfer of ammonia and oxygen and hence, the overall process performance. One major conclusion of his study is, that ammonia has a higher diffusion rate than oxygen.

First attempts of simulating the overall ammonia oxidation process considering both mass-transfer processes as well as surface reactions suffered under several strong simplifications [126, 128–130]. Studies published in the last century lack a detailed microkinetic surface mechanism and some even neglect the formation of

nitrous oxide. In addition, differences in the mass-transfer rate of reactants to the surface, as well as the complete transport process of products from the surface back to the gas phase, have often been neglected [17].

A first model including mass transport as well as a detailed microkinetic model was developed by Warner [17]. Surface reactions are described in Warner's model using the microkinetic model of Traversac (see Section 2.3.1) [17, 86]. Mass transport to and from the surface of individual species is described using the mass transfer correlation of Shah [17, 131]. Warner also considered other correlations like the correlation of Satterfield [132], but decided to use Shahs' correlation since it is validated over a wide range of Reynolds numbers and delivers good agreement with experimental results [17, 131, 132].

The correlation of Shah models the mass transfer along an infinite wire using a Chilton-Colburn j-factor analogy.

$$j_{\mathrm{D},\gamma} = \frac{Sh}{Re \cdot Sc^{\frac{1}{3}}} \tag{2.45}$$

With the Chilton-Colburn j-factor $j_{\mathrm{D},\gamma}$, the Sherwood number Sh and the Schmidt number Sc. The Reynolds number Re used in this model uses the superficial mass flux G corrected by the fractional open area of the gauze γ.

$$Re_{\mathrm{d},\gamma} = \frac{G \cdot d_{\mathrm{w}}}{\mu \cdot \gamma} \tag{2.46}$$

With the wire diameter d_w and the dynamic viscosity μ. The Chilton-Colburn j-factor is described by the following correlation [131, 133].

$$j_{\mathrm{D},\gamma} = 0.644 \cdot Re_{\mathrm{d},\gamma}^{-0.570} \qquad 5 < Re_{\mathrm{d},\gamma} < 245 \tag{2.47}$$

By comparing experimental results with the correlation, Warner showed that the correlation also gives good agreement outside of the range validated by Shah [17]. Combining Equations 2.45 and 2.47 as well as the definitions of the Sherwood number and the Schmidt number leads to the final correlation for the mass transport coefficient of a species $k_{\mathrm{g},s}$.

$$k_{\mathrm{g},s} = 0.644 \cdot \left(\frac{G \cdot d_{\mathrm{w}}}{\mu \cdot \gamma}\right)^{0.430} \cdot \frac{1}{d_{\mathrm{w}}} \cdot Sc^{\frac{1}{3}} \cdot D_{\mathrm{m},s} \tag{2.48}$$

Warner achieved good agreement between experimental results and simulation results using the mass-transfer correlation of Shah and the microkinetic model of Traversac in a pseudo-continuous approach. Warner's model describes how the selectivities of the three nitrogen containing products are influenced by mass transfer phenomena (see Chapter 2.3.5). However, several assumptions limit the accuracy of the model. First of all, the overall model is limited by the accuracy and application range of its underlying kinetic model and mass transfer model. Furthermore, the pseudo-continuous approach of the model neglects several effects such as changing gas phase concentrations and temperature along a gauze stack [17]. An alternative more detailed approach that can overcome these limitations are fully three-dimensional CFD simulations.

2.3.4 Computational Fluid Dynamics Studies on Ammonia Oxidation

In the last decades, the increasing processing power of modern computers and the development of fast algorithms facilitated CFD simulations of heterogeneously catalyzed reactions. CFD simulations are an optimal tool to study mass transfer limited processes like ammonia oxidation since they allow to take into account the complex interplay between surface reactions and mass transport processes and thus, the influence of the resulting complex concentration and temperature fields inside ammonia burners. Nevertheless, only a few studies on CFD simulations of ammonia oxidation have been published to date.

In 2002 Rebrov et al. [115] carried out first CFD simulations of ammonia oxidation over a catalyst of Pt supported on Al_2O_3 in a microreactor [27,115]. However, the used operation temperature of the microreactor of 325 °C is outside the relevant range of the industrial process and only few details of the simulations are given in the study.

In industry CFD simulations are used to optimize the ammonia burner design and geometry under the aspects of ideal flow distribution and temperature development along a gauze stack, as shown in a talk at the Uhde Fertilizer Symposium 2006 by Jantzen et al [18].

Nien [19] published first publicly accessible results of detailed CFD simulations of ammonia oxidation under industrial conditions for single and multiple wire setups in 2D as well as 3D using the reaction mechanism by Scheuer et al.. To speed up the computation time, Nien integrated precomputed reaction rates in his simulations using a so-called look-up table with the four dimensions ammonia concentration, nitric oxide concentration, oxygen concentration, and temperature. Using this approach the computation time is reduced for 2D simulations by a factor of $60-100$ and even higher speed up factors are achieved for full 3D simulations [19]. Nien showed that product selectivities vary both around the perimeter of a wire as well as from wire to wire along a gauze stack. The highest nitric oxide selectivities are achieved at the backside of a wire and the end of a stack, while the highest nitrous oxide selectivities are obtained at the front side of a wire and the beginning of a gauze stack [19].

Klingenberger [15] carried out CFD simulations of ammonia oxidation over gauze stacks using both the Krähnert mechanism and the mechanism by Novell-Leruth. He showed that the mechanism of Novell-Leruth overestimates nitrous oxide selectivities considerably and thus, is not suitable to quantitatively predict ammonia oxidation under industrial conditions. Using a rate control approach Klingenberger identified the most sensitive steps of the reaction network that lead to production of the respective products. While the diffusion of ammonia towards the catalyst surface is the overall rate determining step for nitric oxide formation also higher transport rates of nitric oxide favor its production considerably. The formation of the unwanted side products nitrogen and nitrous oxide is favored by reduced oxygen transport to the catalyst and transport of the products away from the catalyst [15].

In a recent PhD thesis, Wiser [11] published new CFD simulations of ammonia oxidation using the Krähnert model. Wiser showed that the influence of radiation in CFD simulations is negligible for qualitative studies since the gauze surface temperature only decreases by $10-12$ °C, but computation times triple if radiation is taken into account [11]. However, for more accurate quantitative studies radiation should still be included since the reduced surface temperatures lead to slightly decreased nitric oxide selectivities and increased nitrous oxide selectivities, as can be seen in Wisers simulations. Wiser also studied the influence of the wire orientation

towards the impinging gas flow by changing the attack angle of the gas. In this study, the different wire rotations relative to the flow direction between $0 - 70°$ were analyzed. Wires oblique to the flow direction showed reduced nitrous oxide selectivities [11]. However, it should be mentioned that a wide variety of other parameters that are known to influence the selectivities like the conversion, gauze temperature, etc. changed as well for the different wire rotations in Wisers studies.

Wiser also showed first publicly accessible CFD simulations of a knitted gauze stack and compared the performance with woven gauzes. The simulations showed that the formation sites of nitrous oxide strongly correlate with sites with increased mass transfer of educts towards the catalyst surface. In the simulations the knitted gauzes yielded a worse performance compared to the woven gauzes with reduced nitric oxide selectivities and increased nitrous oxide selectivities [11]. Furthermore, Wiser simulated ammonia oxidation over an aged, corroded catalyst wire obtained from a 3D tomography scan. The simulations with the corroded wire showed that at the tips of cauliflowers the highest nitrous oxide selectivities are reached. Since these cauliflower tips impinge the flow field, they contribute significantly to the total conversion, while catalyst regions below the cauliflower structures are obstructed by the cauliflowers and thus, contribute less to the overall conversion. The cauliflowers lead to an increase in the effective wire diameter. Since 3D tomography scans of corroded gauzes are still hard to obtain and the inclusion of cauliflowers leads to more complex meshing as well as increased computation times, Wiser showed an alternative approach to take the influence of cauliflowers into account. The performance obtained with a cauliflower covered gauze can be replicated in simulations using smooth wires with an adapted increased diameter and an adjusted averaged reaction rate, that results from the uneven contribution of cauliflowers tips compared to the underlying areas to the overall reaction rate [11]. Finally, Wiser showed that decreasing temperatures resulting from heat losses over the reaction walls in small lab reactors distort the measured selectivities if an integral end of pipe analysis is carried out [11].

Even though CFD simulations improved the understanding of industrial ammonia oxidation considerably, the shortcomings of the underlying microkinetic models still limit the explanatory power of CFD simulations on a quantitative basis.

2.3.5 The Influence of the Operation Conditions

The performance of industrial ammonia oxidation is influenced by several operation parameters. Since about 90 % of the nitric acid production costs result from the cost of ammonia, optimal nitric oxide yields are wanted. Besides the nitric oxide yield, other factors have to be considered to fulfill the requirements of modern nitric acid plants. Administrative environmental regulations led to a growing interest to reduce the amount of produced nitrous oxide. Another major cost factor is platinum loss of the ammonia oxidation catalyst and hence, these costs are intended to be minimized. Finally, high plant capacities are wanted at small investment costs for the construction of new plants and upgrades of existing plants. The question, which plant designs and operation conditions fulfill these requirements, is very complex. Only a few studies have been published that systematically tackle this question and study the influence of individual operation parameters independently. In this chapter today's understanding of how the temperature, the pressure, the feed composition, the burner loading, and the catalyst influence the performance of industrial ammonia oxidation is reviewed.

The temperature, strictly speaking the gauze temperature, of ammonia oxidation is considered to influence the product selectivities strongly. By increasing the temperature within the usual industrial range leads to improved nitric oxide selectivities. The nitrogen as well as the nitrous oxide selectivity decrease at higher temperatures. It has to be noted, that the gauze temperature is not constant along the surface. The first gauze of a stack has the highest temperature. Furthermore, locally varying activities due to differences in the composition as well as structures of a wire can lead to local temperature differences (for further details see Chapter 2.4). A limiting factor for the temperature selection is its influence on the durability of platinum catalyst gauzes. Higher temperatures lead to increased platinum losses, leading to shorter campaign lengths as well as higher catalyst costs [3, 17, 98].

Contrary to higher temperatures, higher pressures are thought to reduce the nitric oxide yield. Historically this was explained by Le Chatelier's principle. The formation of nitric oxide results in a volume increase and hence, higher pressures have a negative influence on this reaction. However, the formation of nitrogen

leads to an even higher volume increase and should therefore be influenced even more. Furthermore, the equilibrium of the three reactions is far on the product side and hence, using Le Chatelier's principle is the wrong approach to explain the pressure dependency. Instead, the pressure dependency can be explained by changing oxygen and especially ammonia partial pressures influencing the catalyst surface coverages. Higher ammonia partial pressures lead to higher surface nitrogen coverages accelerating surface reactions that ultimately lead to increased nitrous oxide formation. According to Warner [17], the nitrogen selectivity is not influenced by higher pressures since negative influences of higher concentrations are canceled out by higher mass transfer rates. For nitrous oxide Warner found a dependency of $S_{\mathrm{N_2O}} \sim \sqrt{p}$ [17]. Despite the negative influence on the product selectivities, modern ammonia burners are designed as medium or high pressure units. The main reason for this trend is that higher pressures allow higher throughputs. The selectivity losses due to higher pressures are often partially compensated by operating at higher temperatures. This strategy comes at the cost of increased platinum losses [3].

Given that the concentrations of the surface species play a crucial role for the product selectivities, it is not surprising that the feed composition strongly influences the selectivities as well. The feed composition of combustion with nitrogen as ballast media can be described by two variables: The absolute ammonia fraction and the ratio of ammonia to oxygen concentration. According to Warner [17], the nitrogen selectivity is not influenced by increasing ammonia to oxygen ratios but is negatively influenced by increasing absolute ammonia concentrations. Nitrous oxide formation is promoted by increasing ammonia to oxygen concentration ratios and by increased ammonia concentrations [17]. Accordingly nitric oxide selectivities can be maximized by decreasing the absolute ammonia concentration and the ammonia to oxygen concentration ratio [3, 17, 31, 134]. Usually, the absolute ammonia concentration and the ratio of ammonia to oxygen concentration are not varied independently. In industry ammonia is combusted in air. Both feed composition variables are varied by changing the absolute ammonia concentration. The ammonia to oxygen concentration ratio is not adjusted any further, which could be done by changing the oxygen content in the feed air.

In industry the choice of the absolute ammonia concentration is influenced by several factors. The stoichiometric ammonia to oxygen ratio of 0.8 for nitric oxide formation is achieved at a volumetric ammonia inlet fraction of 14.4 vol.%. Due to the different mass transfer rates of ammonia and oxygen, a lower ammonia to oxygen ratio of 0.7 is needed to guarantee a stoichiometric concentration ratio at the catalyst surface [124]. This ratio corresponds to an ammonia inlet concentration of 12.7 vol.%. To determine the economical optimal ammonia inlet fraction it is necessary to find a compromise between a high throughput, favoring high ammonia inlet fractions, and high selectivity, favoring low ammonia inlet fractions. Another factor that has to be considered is the explosive range of ammonia/air mixtures. Depending on the temperature, pressure, and flow velocity the explosive range of ammonia/air mixtures varies [3, 135, 136]. In the pressure range of $1 - 10$ bar the lower flammability limit is at an ammonia inlet concentration of about 15 vol.% at room temperature. To exclude safety risks resulting from incomplete mixing usually a safety margin of 2 vol.% is used. At higher inlet gas temperatures the ammonia inlet fraction has to be further reduced due to a reduced lower flammability limit. The dependency between the inlet gas temperature T_{in} in $^{\circ}C$ and the maximum ammonia inlet fraction $x_{\mathrm{NH_3,max}}$ that should be used, is described by the following equation [128].

$$x_{\mathrm{NH_3,max}} = 0.13 - 0.00011 \cdot T_{\mathrm{in}} \tag{2.49}$$

The understanding of the influence of the burner loading on the process performance has long been dominated by the assumption of an optimal contact time (see Chapter 2.3.1) [3]. Nowadays, the influence of burner loading is explained by its influence on mass transport rates. Side reactions that lead to a reduction of nitric oxide selectivity are enhanced by increasing ammonia partial pressures at the gauze surface. Increasing the burner loading, at otherwise constant operation conditions, leads to increased gas velocities, intensified mass transfer, and finally, increased surface coverage with NH_x species. This effect can be attenuated by increasing the gauze temperature and thereby, the reaction and desorption rates at the cost of higher catalyst decomposition rates. The mass transfer rates can also be controlled by adjusting the shape of the gauze and its wire diameter [17].

The catalyst itself does not only influence the mass transfer rate but also influences the economical performance of the process in a complex way. Depending on the chosen operation conditions, platinum-rhodium alloy gauze catalysts with varying rhodium contents are used in industry. In general, a good compromise between nitric oxide selectivity, catalyst loss rates, and material costs has to be found when it comes to the choice of a catalyst. The characteristics, especially the platinum losses, of ammonia oxidation catalysts are a very complex topic. Therefore, this topic is reviewed in detail in the following section.

2.4 Ammonia Oxidation Catalysts

One of the most important aspects of ammonia oxidation is the catalyst. The morphology and the composition of platinum gauze catalysts influence the nitric oxide selectivity strongly and hence, have a big impact on the efficiency of the overall process. Furthermore, high platinum losses of platinum gauzes are the second biggest cost factor of nitric acid production. The total platinum losses can reach up to 40 wt.% during the operation life of a gauze and account for $3-10$ % of the overall production costs [3, 60]. Therefore, strategies to reduce these costs and to optimize the nitric oxide selectivity by modifying the catalyst are an important field of research, that promises considerable economical profits. Despite the high research effort, only a few improvements of ammonia oxidation catalysts have been made since the first technical scale experiments of Ostwald. In the first section of this chapter, the improvements of platinum gauze catalysts since their introduction in 1909 are reviewed. Subsequently, the changes of the catalyst morphology during a campaign are described and different theories, how the processes can be explained, are presented. In the third section, multiple methods to reduce the platinum losses in modern nitric acid plants are shown. Finally, the current state of research to replace platinum gauze catalysts with cheaper alternatives is reviewed.

2.4.1 Historical Development of Platinum Gauze Catalysts

Already in the 19th century, Wilhelm Henry [46] and Frédéric Kuhlmann [47] showed the big potential of platinum as an ammonia oxidation catalyst. These results were supported by the work of Wilhelm Ostwald, who achieved good results using platinum based catalysts at the beginning of the 20th century. Therefore, platinum ribbons were used as catalysts in the first technical and industrial scale plants designed by Ostwald and his coworkers [45, 48, 50, 51]. In 1909 Karl Kaiser [54] introduced platinum gauze catalysts with 1050 meshes per cm^2 woven of wires with diameters of 0.06 mm [45, 50, 53, 54]. Kaiser established with his gauze catalysts a new standard defining the shape of ammonia oxidation catalysts for more than 80 years, which are sometimes still used today. In Figure 2.9 an image of a fresh, woven platinum gauze catalyst is shown [17].

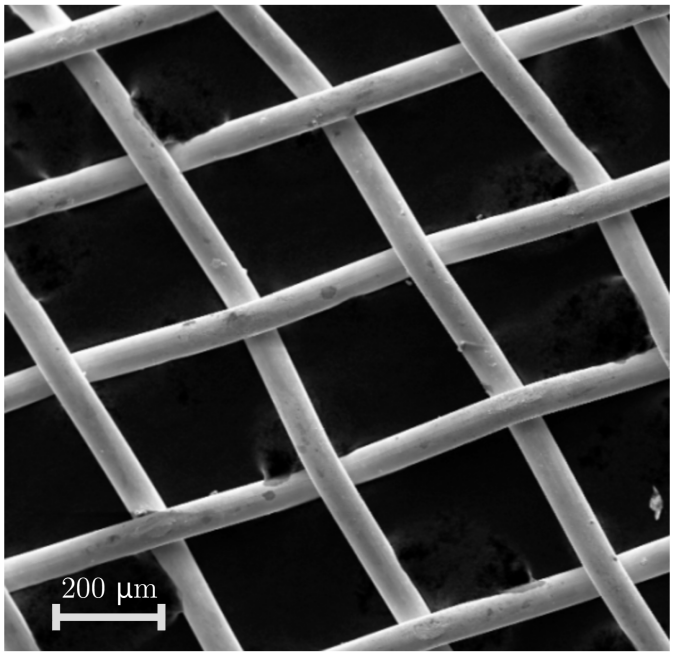

Figure 2.9: SEM picture of a fresh, woven platinum gauze with a wire diameter of 60 μm taken from [17], modified

Depending on the throughput, pressure, and flow velocity, gauze stacks made of $3 - 50$ gauzes are used in modern nitric acid plants. In low pressure combustion processes typically $3 - 5$ gauzes, in medium pressure plants $6 - 10$ gauzes, and in high pressure plants $20 - 50$ gauzes are used [3]. Gauzes used in high pressure

plants are often made of wires with a diameter of 0.076 mm instead of the 0.06 mm diameter established by Kaiser [3, 61].

Like many other catalysts, platinum gauze catalysts change their morphology dynamically during operation. Before the reaction is started, platinum gauze catalysts usually have a smooth homogeneous surface. Within a few days of operation the surface roughens considerably and growths in the shape of cauliflowers are formed on top of the wires [3, 137]. A secondary electron microscopy (SEM) image of a used platinum gauze catalyst is shown in Figure 2.10 [138].

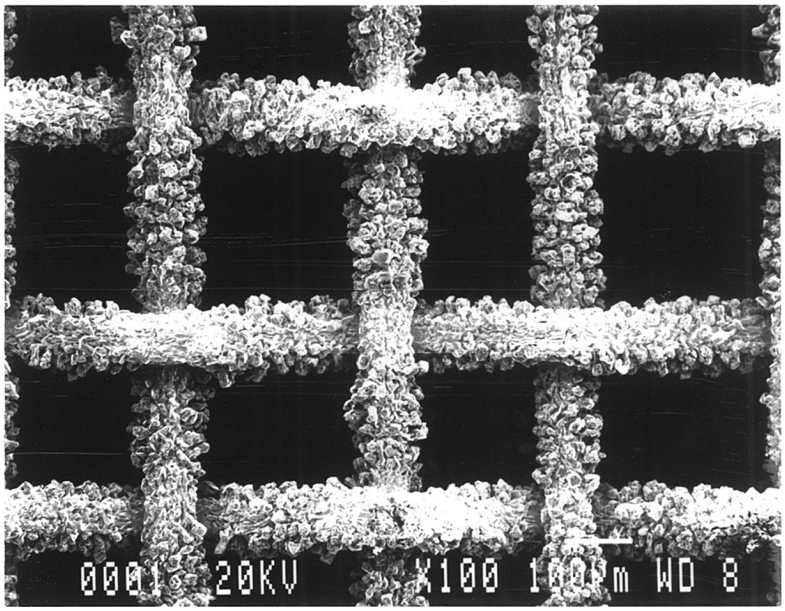

Figure 2.10: SEM picture of a used platinum gauze [138]

During the operation lifetime, platinum is constantly lost from the gauzes in the form of volatile platinum oxides. This can lead to selectivity losses and finally to mechanical degradation. Therefore, the gauzes have to be replaced after several months of operation [3, 139]. Reaction-induced morphology changes like this are called catalytic etching and are also known from other processes such as the oxidation of hydrogen, ethane, and propane [137, 140]. The rate, at which the platinum is lost, depends on many factors such as the temperature, pressure, catalyst composition, catalyst shape, loading, oxygen concentration, and gas velocity [138,139,141,142]. Depending on the chosen operation conditions the campaign length of a gauze stack varies strongly. In low pressure combustion processes the

gauzes usually have to be replaced after $7-12$ months, in medium pressure plants after $6-8$ months and in high pressure plants after $1.5-3$ months [3].

In 1928 the first major improvement of platinum gauze catalysts has been reported. By using an alloy made of platinum and up to 10 weight percent of rhodium the properties of the gauze are improved significantly. A detailed analysis of the influence of rhodium on the performance of platinum gauze catalysts in ammonia oxidation was published by Handforth and Tilley in 1934 [143]. In their experiments, Handforth and Tilley found out that Pt-Rh alloy catalysts have an improved nitric oxide selectivity, have improved mechanical stability, lose platinum at a lower rate, and therefore, have an extended operation lifetime. The results from Handforth and Tilly on the influence of the rhodium content on the platinum loss rate as well as on the nitric oxide selectivity are shown in Figure 2.11 [143].

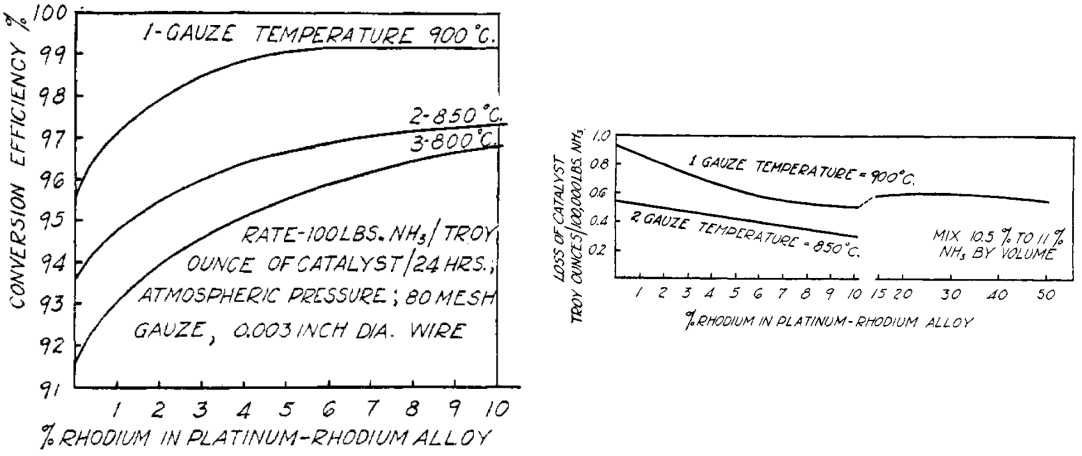

Figure 2.11: Results of Handforth and Tilley for the influence of the rhodium content on the nitric oxide selectivity as well as on the platinum loss rate [143]

The results of Handforth and Tilley show that the conversion efficiency is improved and the catalyst loss is reduced with increasing rhodium contents. The conversion efficiency reaches a plateau at rhodium contents between $5-10$ wt.% depending on the gauze temperature. At these rhodium contents increasing the rhodium content further does not improve the conversion efficiency noticeably. For a gauze temperature of 900 °C the conversion efficiency is increased up to rhodium contents of 6 wt.%. At lower temperatures higher rhodium contents are needed

to reach the optimal conversion efficiency [143]. Therefore, gauzes with varying rhodium contents are used in industrial nitric acid plants depending on the process temperature. In high pressure plants, which are usually operated at high temperatures, gauzes with rhodium contents of 5 wt.% are used. On the contrary in medium and low pressure plants, which are usually operated at lower temperatures, higher rhodium contents of 10 wt.% are often used. Since platinum and rhodium prices change constantly, the economical benefits of different gauze compositions have to be evaluated permanently. Even though the results of Handforth and Tilley were confirmed qualitatively in industrial plants, it has to be mentioned, that the experiments of Handforth and Tilley were not standardized. Parameters, that are today known to influence the ammonia oxidation process like the burner design and burner loading, were varied in the experiments. Therefore, the shown data should only be considered as a qualitative guideline. Nevertheless, Pt-Rh alloy catalysts gained wide acceptance in industry, after the results of Handforth and Tilley were published [3, 17].

After the introduction of Pt-Rh alloy catalysts in the 1930s, ammonia oxidation catalysts did basically not change until the early 1990s. In 1991 the company Johnson Matthey introduced a new kind of platinum gauze catalysts. By changing the fabrication process from weaving to knitting several improvements of the catalyst properties were achieved [144–146]. These days, knitted platinum gauze catalysts replaced woven platinum catalysts in most nitric acid plants with a market share of more than 90 % [67].

The list of claimed advantages of knitted gauze catalysts compared to woven gauze catalysts is long. The first advantage of knitted gauzes is their higher mechanical strength. Tensile tests conducted by Johnson Matthey show that knitted gauzes are able to stretch considerably, allowing them to absorb much more energy than woven gauzes, before the wires tear apart. These results can be compared to the higher mechanical strength of knitted clothes compared to woven clothes. The better stretchability of knitted gauzes is also advantageous considering the stability against thermal shocks. Fast changes in the temperature lead to thermal expansion or contraction of gauze wires, which can lead to fractures in woven gauzes. Due to the higher stretchability of knitted gauzes the risk of damaging gauzes by changing the temperature in the reactor is lowered [144, 146].

Another advantage of knitted gauzes is the higher available surface compared to woven gauzes due to the changed geometrical arrangement. In woven gauze catalyst about 17 % of the surface is not available because of the high number of intersections. For knitted gauzes only about 7 % of the surface is not available [144, 146].

Differences in the knitting process compared to the weaving process render another advantage possible. For setting up a loom for knitting only 5 kg of wire are required compared to $50 - 100$ kg of wire needed for the loom of a weaving process. The lower required loom stock levels allow to produce small quantities of non standard gauzes with varying compositions for research [144, 146].

The different, three-dimensional arrangement of knitted gauzes influences the flow distribution over the wires. Knitted gauzes are said to lead to more uniform flow distributions, which minimize the formation of hot spots. Since higher temperatures lead to increased platinum losses (see Figure 2.11 as well as the next section) a reduced formation of hot spots minimizes the platinum losses and hence, increases the operation life of a gauze. In experiments conducted by Johnson Matthey, it was shown that changing the gauze from woven to knitted structures allows extending the operation lifetime from 180 to 240 days in low pressure combustion, from 120 to 200 days in medium pressure combustion, and from 50 to 80 days in high pressure combustion. Furthermore, knitted gauzes are also said to have improved, more stable selectivities. The increase in selectivity is explained with lower Rh_2O_3 formation rates due to reduced hot spot formation. Because high Rh_2O_3 concentrations on the surface decrease the selectivity, knitted gauzes can be longer operated in higher selectivity ranges, without changing other operation parameters like the temperature [146].

Since the introduction of knitted platinum gauze catalysts different knitted structures have been developed. In general two kinds of knitting patterns, weft and warp knitted gauzes, can be distinguished [3]. The properties of gauzes with different knitting patterns differ in their mechanical properties as well as in the platinum loss rate and nitric oxide selectivity, due to the different flow distributions achieved with different patterns. Besides warp and weft knitted gauzes also special gauzes in which both knitting styles are combined are produced [3].

Nowadays, new multi-layer knitting structures with incorporated platinum getting gauzes (see Section 2.4.3) and many different knitting patterns are produced. The flow distribution of the gauzes is optimized for different burner types using CFD simulations [17, 18]. First surface mechanistic attempts to explain the improved selectivity of knitted compared to woven gauzes using CFD simulations are reviewed in Section 2.3.4. To date no detailed scientific model is reported, that describes the influence of the gauze shape on the platinum loss rate mechanistically. However, some theories aiming to explain the overall morphological changes of the catalyst have been postulated in the last decades.

2.4.2 Morphological Changes of Platinum Gauze Catalysts

The morphology of platinum and platinum-alloy gauze catalysts changes dynamically during an ammonia oxidation campaign. These morphological changes come with advantages such as increased surface areas as well as activities, but also with disadvantages like reduced selectivities and costly platinum losses. To design optimized catalysts systematically a deep understanding of the underlying mechanisms is necessary. Even though several researchers studied the morphological changes in the past, no generally agreed on theory exists that allows explaining all observed phenomena.

At the beginning of an operation campaign, new gauzes have a smooth homogeneous surface. To start the reaction, that runs autothermally in steady state, the cold gauzes need to be ignited. In the ignition phase first morphological changes start to occur. The cold gauzes can be ignited using multiple methods. The most commonly used method in industrial burners is the ignition using a hydrogen torch. At hot spots, heated by the torch, high temperatures are achieved, enhancing the reaction rate. After a while the reaction runs autothermal in steady state; the heated spot is ignited. From these hot spots the high reaction rate zone propagates radially across the gauze. During the ignition process the surface starts to roughen, increasing the available surface and hence, enhancing the reaction rate of the mass transfer limited process further. Alternative ignition techniques are the usage of electrically heated resistance wires incorporated into the gauze pack and using high pre-heating temperatures of up to 400 °C [3, 61, 147]. The

last method has the advantage that it can be utilized in small test reactors with limited space [147].

In the first days of an ammonia oxidation campaign the specific surface area of the catalyst increases constantly leading to enhanced activities. The time, until the maximum nitric oxide yield is achieved in industrial burners, varies between $3-8$ days depending on the chosen operation conditions as well as the size and the design of the burner [3, 61, 106]. In small pilot plants and test reactors the maximum nitric oxide yield can be achieved after only a few hours. The faster activation of smaller gauzes is attributed to more uniform flow fields and resulting fast temperature propagation [147]. After the activation period, the nitric oxide yield stays virtually constant during the months of operation. This is achieved by equalizing selectivity losses from the gauze aging process by varying the operation conditions, in general, the pre-heating temperature, during the campaign. During the whole operation time the surface of the catalyst still changes dynamically [3, 139, 148].

While the gauzes are ignited and activated a noticeable amount of ammonia passes unreacted over the gauzes decreasing the overall yield. These losses in yield result in considerable economical losses [147]. Therefore, the ignition protocols of industrial burners are optimized to achieve fast activation with high activities. The ignition behavior is influenced by many factors such as the ammonia concentration, the pre-heating temperature, the oxygen concentration, the loading, and especially, the available specific surface area [147]. By increasing the specific surface area of a gauze at the beginning of the process the light off dynamics can be improved significantly. Increased specific surface areas can be achieved by scattering platinum dust on the gauzes, using slightly roughened but mechanical stable gauzes of previous campaigns, and by using gauzes coated with dispersed small platinum particles [61, 147].

During the ignition and activation phase of an ammonia oxidation campaign the specific surface area of the gauzes increases by a factor of $2-20$ [138, 147]. The first gauze of a stack that is in direct contact with the fresh air-ammonia mixture is roughened the most. Gauzes placed at positions at the end of a stack roughen only slightly [3, 149]. In Figure 7.6 scanning electron microscopy (SEM) pictures

of the front sides of the first, second, and third gauze of a gauze stack composed of three gauzes are shown [149].

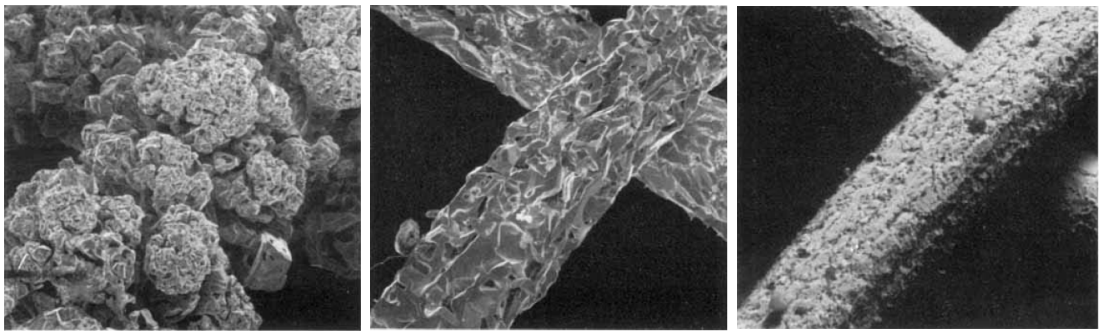

(a) First gauze **(b)** Second gauze **(c)** Third gauze

Figure 2.12: Front sides of platinum-rhodium gauzes of a stack after operation at atmospheric pressure for twelve months [149].

The gauze stack was used in an industrial ammonia burner for twelve months at atmospheric pressure with operation temperatures between $810 - 850$ °C. The pictures were taken after the campaign with an electron microscope [149]. On the first gauze typical growths in the shape of cauliflowers are visible. The second gauze has deep cavities while the last gauze is only slightly roughened.

Another factor that influences the restructuring processes is the elemental composition of the gauze. Hannevold et al. [71] carried out a systematic study to show this influence for single wires made of pure platinum and rhodium as well as for Pt-Rh alloys with rhodium contents of up to 40 wt.%. All experiments of the group were carried out at the same operation conditions. The group showed that on Pt, Pt/5%-Rh, Pt/10%-Rh, and Pt/13%-Rh wires cauliflowers are formed on the surface at the chosen operation conditions. On platinum wires plate-like shaped, big cauliflowers with relatively uniform sizes are formed. With increasing rhodium content in the alloy more bulky and smaller cauliflowers are formed. On wires with a rhodium content of 13 wt.% only a few cauliflowers are formed, preferably at grain boundaries. On Pt/20%-Rh, Pt/30%-Rh, and Pt/40%-Rh wires no cauliflowers are formed, but deep grooves and cracks along grain boundaries, pits, and well defined facets are visible. However, on pure rhodium wires bulky cauliflowers with strongly varying sizes are formed. Interestingly, the elemental composition of the cauliflowers formed on the different Pt-Rh alloy wires is comparable for all alloy

compositions. In general, the cauliflowers have a higher rhodium content than the solid bulk structure of the wires. Inside the cauliflowers a gradient with high rhodium contents of $31 - 33$ wt.% at the surface and lower rhodium contents at the middle is developed [71]. It should be mentioned, that these observations are only valid for the operation conditions chosen by the group [71]. However, the systematic study of Hannevold et al. demonstrates the importance of the alloy composition as an influencing factor of the restructuring process and its underlying mechanisms.

Besides the position and the composition of the gauze other parameters such as the temperature, the ammonia loading, and the pressure, in particular the oxygen partial pressure, affect the surface restructuring processes. In general, higher temperatures and higher pressures enhance the restructuring processes and therefore, shorten the operation time. Typical industrial operation conditions and the resulting catalyst changes are listed in Table 2.1 [3].

Table 2.1: Typical operation conditions of industrial nitric acid plants [3].

Plant type	**Low pressure**	**Medium pres.**	**High pres.**
Pressure [bar]	$1 - 2$	$3 - 7$	>8
NH_3 concentration [vol.%]	$12.0 - 12.5$	$10.5 - 11.5$	$10.0 - 10.5$
Gauze temperature [°C]	$800 - 850$	$880 - 900$	$900 - 950$
Gauze loading $\left[\frac{\text{t NH}_3}{\text{m}^2\text{d}}\right]$	$2 - 4.5$	$10 - 40$	$30 - 70$
Number of Gauzes	$3 - 5$	$6 - 10$	$20 - 50$
Catalyst loss $\left[\frac{\text{g}}{\text{t N in NH}_3}\right]$	$0.2 - 0.4$	$0.7 - 0.9$	$1.1 - 2.2$
Operating time [months]	$7 - 12$	$6 - 8$	$1.5 - 3$

Even though many scientists worked in the field of catalytic etching of platinum gauze catalysts, the detailed mechanisms of the surface reconstruction are still not completely understood. One problem, that hinders the progress, is the fact that in-situ analyses of the restructuring process are difficult to carry out due to the demanding industrial process conditions with pressures of up to 14 bar and temperatures of up to 1000 °C. Therefore, several groups, which suggested possible mechanisms for the restructuring process, had to base their mechanisms on studies that were carried out either at lower pressures and temperatures or on results of ex-situ analyses. The suggested mechanisms include mechanical effects,

simple thermal etching processes, surface, boundary layer as well as bulk diffusion mechanisms and theories based on the gas phase transport of volatile platinum oxides.

Studies of several groups indicate that at the typical process conditions inside an industrial ammonia burner gas phase transport of volatile platinum species is the dominating transport mechanism of the surface reconstruction processes [71, 150–153]. Physical properties like the low vapor pressure and the high melting point of platinum indicate that the species, which accounts for the major part of the gas phase platinum transport, is not elemental platinum. Instead of elemental platinum PtO_2 has been identified as the main gas phase transport species. The vapor pressure of PtO_2 is about 10000 times higher than the vapor pressure of elemental platinum at typical conditions inside an ammonia burner of $800 - 1000$ °C and $1 - 14$ bar [148, 153]. Hence, if the reaction conditions favor the formation of platinum oxides, the transport of platinum containing species is highly promoted [150, 154]. In fact, experimental results confirm that platinum species are transported in the gas phase during ammonia oxidation. Nilsen et al. [139, 151] observed the formation and gas phase transport of PtO_2 and at lower levels of PtO as well as of Pt(0) during ammonia oxidation using in-situ mass spectroscopy [139, 151].

Rhodium, the second component of most industrially used gauze catalysts, is also presumably transported mainly in vapor phase in the form of RhO_2 and other simple rhodium species such as Rh and RhO. However, the RhO_2 formation, as well as transport rates, are much lower than the rates of PtO_2. During the months of operation this inequality leads to slowly increasing total rhodium contents of Pt-Rh alloy gauzes because more of the volatile platinum is lost than the less volatile rhodium species [139, 146]. The changing composition with locally high rhodium contents leads to a decrease in the nitric oxide selectivity at otherwise constant reaction conditions over time. Due to these selectivity losses and the reduction of mechanical stability the gauzes need to be exchanged after a few months of operation (see Table 2.1) [3].

Even though it is generally agreed that PtO_2 plays an important role in the reconstruction process, the detailed mechanism of how the PtO_2 is formed and transported is still a matter of discussion. Experiments of several groups, in which

platinum and platinum-alloy gauzes were treated at typical reaction conditions in atmospheres of either oxygen, nitrogen, or ammonia, show only minor reconstruction effects without the formation of cauliflowers [139, 151]. These results indicate that the main factors that drive the reconstruction processes are not simple thermodynamic equilibrium processes but rather processes that result from the ammonia oxidation reaction. Multiple groups suggested that local differences in the PtO_2 formation rates play a key role in the transport process [151, 152].

One of the groups that proposed such mechanisms is the group of McCabe et al. [142, 152]. They suggested that diffusion of excess oxygen into fissures at grain boundaries leads to the formation of areas with a high oxidizing potential, which results in increased PtO_2 formation rates in these areas. The PtO_2 formed at these spots is transported over short distances until it is reduced at positions with lower oxidizing potentials. Once the PtO_2 is reduced, it is deposited again on the surface of the catalyst. By this mechanism, reconstructed structures spread out over the surface of the gauzes [142, 152].

Hannevold et al. [71] attributed local differences in the PtO_2 formation rate to the formation of hot spots [71]. The reaction rate of the ammonia oxidation is not constant along the whole surface of a gauze due to varying activation and adsorption energies at different crystal facets, defects, edge dislocations, steps et cetera. Furthermore, the rhodium and platinum content is not uniformly distributed over the surface of Pt-Rh alloy gauzes, which also leads to nonuniform reaction rates. A high frequency of successive reaction events of the fast and highly exothermic ammonia oxidation reaction may result in the formation of hot spots at positions with favorable reaction conditions. On these hot spots the surface temperature may exceed the average surface temperature by several hundred degrees. These high temperatures enhance the PtO_2 formation rate considerably. No experimental results resolve whether the PtO_2 is formed from solid, a molten surface, or in the vapor phase. The formed PtO_2 is transported in the vapor phase until it decomposes in lower temperature areas and is deposited on the surface of the catalyst, leading to the growth of the characteristic structures that can be seen on used platinum gauzes [71, 139].

Lyubovsky and Barelko [155] also suggested a mechanism based on local heat generation at active centers. The high heat generation rates at active centers

supposedly cause rapid sublimation of platinum, which is transported in vapor phase inside the boundary layer over the surface. The platinum is then deposited in a vapor-liquid-solid process in the shape of small wool-like needles that build the basis for further growth processes [155].

In contrast to the above mentioned groups, the group of Phillips et al. [156–158] suggested that radicals play an important role in restructuring processes of platinum catalysts. Upon the interaction of O_2H^* radicals with the catalyst surface, PtO_2H^* radicals are formed and transported into the gas phase. In the next step, small platinum containing clusters are formed by a homogeneous nucleation process in the gas phase and in a final step, the clusters are deposited on the catalyst surface [156–158]. The group based their mechanism on studies of hydrogen and ethene oxidation catalyzed by platinum catalysts. In these reactions comparable restructuring processes occur like in ammonia oxidation.

Many other theories besides the above mentioned vapor phase transport theories were suggested in the last decades. It is assumed that at industrial operation conditions vapor phase transport dominates the restructuring process. However, studies conducted at lower pressures and temperatures indicate that additional processes occur complementing the vapor phase processes.

Krähnert et al. [137] studied the restructuring process in a temperature range between $286-374$ °C. In this temperature range a noticeable contribution of vapor phase transport is regarded as unlikely because the provided energy at these temperatures is not sufficient to enable high phase transition rates from solid platinum into the vapor phase. Nevertheless, experiments at low temperatures also show surface restructuring to a certain extent. At these temperatures the formation of structures such as facets and pits can be observed. In contrast, cauliflowers and other structures with high surface areas are not formed in this temperature range. Krähnert et al. suggested that platinum transport is dominated at low temperatures by an adsorbate-related mobility enhancement of surface platinum atoms. One indication for this theory is, that simple temperature treatment experiments in absence of reactants showed no noticeable reconstruction of the surface. In presence of reactants the above mentioned facet formation occurs. The theory, that the mobility of surface platinum is enhanced by the presence of certain gases, is supported by observations of other groups [137, 151, 159]. Therefore, Krähnert et

al. ruled out that surface or bulk diffusion plays an important role in the surface reconstruction process in the low temperature range. At higher temperatures surface and bulk diffusion processes supposedly have a higher influence on the surface reconstruction process, but are dominated by vapor phase processes at industrial conditions. One common argument is that the high rhodium concentration gradients inside cauliflowers would be more smoothened out if bulk and surface diffusion processes would play a bigger role in the reconstruction mechanism [137].

Additionally to catalytic etching processes, mechanical losses accelerate the gauze aging process. The mechanical integrity is reduced over time due to the surface reconstruction. With advancing time in a campaign parts of the gauze can break off due to the reduced stability. Therefore, the catalyst gauzes are exchanged before the mechanical stability is reduced to such an extent that the risk of high mechanical loss rates exceeds the profitable range. Early surface reconstruction theories attributed the major part of the platinum losses to such mechanical losses. A widespread theory from the 1970s is that mechanical losses enabled by the penetration of hydrogen into the metal-crystal lattices lead to the surface reconstruction [160]. However, no experimental results support this theory.

The second factor, besides the reduction of the mechanical stability, that limits the campaign length are selectivity losses that come along with the changing surface composition and structure. One phenomenon that is known to reduce the selectivity drastically is the formation of small Rh_2O_3 needles [71,152,161,162]. In Figure 2.13 SEM pictures of a gauze covered with Rh_2O_3 needles is shown [149].

The formation of Rh_2O_3 is thermodynamically only favored in a certain temperature and oxygen partial pressure range [71, 163]. Normally industrial ammonia oxidation reactors are operated in a temperature range exceeding the maximum temperature until which Rh_2O_3 is formed. However, if the local temperature of a gauze drops due to catalyst poisoning the formation of Rh_2O_3 starts. Since Rh_2O_3 has a reduced activity for ammonia oxidation the reaction rate at the spots is further reduced, increasing the Rh_2O_3 formation rate. This snowball effect can lead to fast formation of high amounts of crystalline Rh_2O_3 needles with reduced activity as well as nitric oxide selectivity to a point where the gauze is not profitable and needs to be exchanged [71].

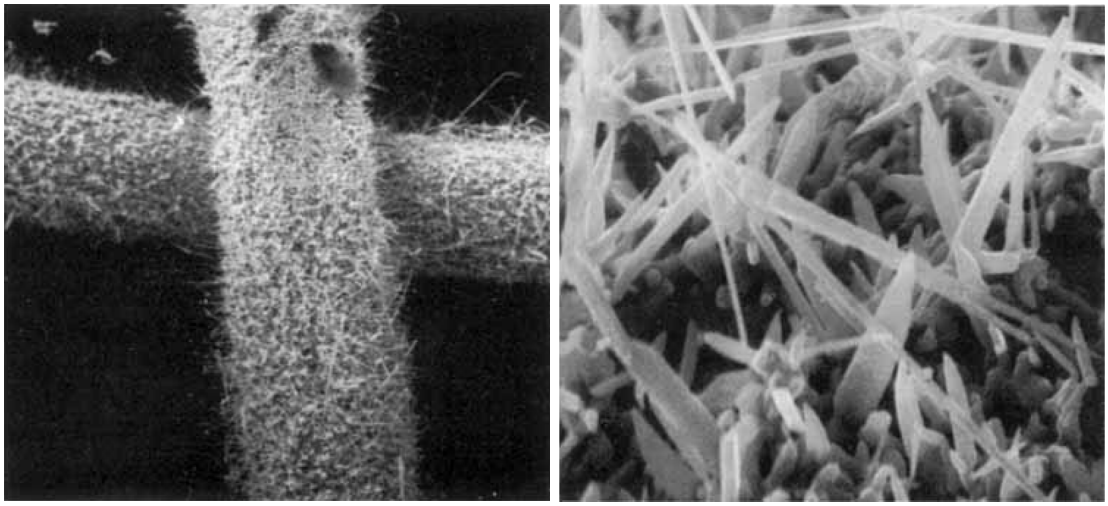

Figure 2.13: Platinum-rhodium gauze covered with Rh_2O_3 needles [149].

The example above shows the importance of preventing poisoning of the catalyst gauzes. A study carried out by Degussa [61] showed that contamination with gold, manganese, nickel, copper, beryllium, calcium, aluminum, and barium act as serious catalyst poisons. In industrial plants, iron oxides present a potential risk for catalyst poisoning [128]. Therefore, several filters are installed in nitric acid plants to minimize the risk of contamination (see Chapter 4.2). Contamination of the gauzes with phosphorus, arsenic, antimony, lead, zinc, tin, cadmium, aluminum, bismuth, and silicon present a special risk because they form low melting eutectics with platinum at the grain boundaries leading to reduced mechanical strength [61].

2.4.3 Reducing the Platinum Losses

The platinum and rhodium losses that result from the surface reconstruction have a distinct impact on the overall nitric acid production costs. The platinum losses contribute between $3 - 10$ % of the total production costs, depending on the chosen operation conditions as well as on the constantly changing prices of ammonia, platinum, and rhodium [60]. Therefore, early on in the history of the Ostwald process researchers studied ways to reduce the costly platinum losses. The possibilities, how different operation parameters and changing the shape as well as the composition of the catalyst affect the platinum losses, are explained in the previous

sections. In this section, the focus lies on additional platinum catchment installations and strategies to reduce the platinum losses by using combined platinum gauze/metal oxide catalysts.

Already during the Second World War first experiments with downstream platinum catchment installations were carried out in Germany [164]. Due to the war, the platinum supply in Germany was limited. Hence, strategies were needed to reduce the platinum losses to a minimum to keep the crucial production of nitric acid running. The solution developed at that time is to place gold plated Raschig rings downstream of the burner in low pressure plants. On the surface of the gold up to two thirds of the lost platinum could be retained. However, the process had high costs. Therefore, its usage was ended after the war. After the war, gold plated oxidation resistant steel installations were tested as downstream platinum catchment installations. In low pressure plants recovery efficiencies of up to 50 % can be achieved using these catchment installations. Though, at high temperatures used in modern high pressure plants these installations lose their mechanical integrity fast [164].

In the late 1950s layers of granular marble were tested as platinum catchment installation [165]. At temperatures of $700 - 800$ °C marble forms CaO, which can uptake up to 90 % of the lost platinum. However, marble layers have a high flow resistance and lead to high pressure drops, which excludes this method for most plants [3]. The problem of high pressure drops also makes mechanical filter solutions constructed of quartz or glass and metal wools uneconomical, even though retention rates of up to 40 % can be achieved [3, 60, 164].

In the late 1960s the company Degussa introduced platinum catchment installations based on Pd-Au alloy gauze packs [164]. The shape of the gauzes is similar to the shape of ammonia oxidation catalyst gauzes. Typically the gauzes have wire diameters of $0.06 - 0.09$ mm and 1024 meshes per cm^2. The gauzes are placed directly downstream of the ammonia oxidation catalyst with usually a few support Megapyr gauzes placed in between. A large fraction of the volatile platinum oxides lost from the catalyst gauzes dissociates directly downstream of the catalyst. The platinum is then adsorbed on the catchment gauze and is further absorbed as an alloy constituent. Besides platinum oxides also low quantities of rhodium oxides can be recovered using Pd-Au catchment gauzes. Palladium is a very effective col-

lector material for this mechanism. However, palladium can poorly be processed to wires. Therefore, gold is often used as an additional component of the catchment gauzes, increasing the mechanical strength but slightly decreasing the catchment efficiencies. Besides gold cheaper components such as nickel, copper, manganese, chromium, and boron can also be used to enhance the mechanical properties, but come at the cost of bigger collection efficiency reductions [3,60]. These days, getter gauzes composed of nickel-palladium alloys are often the best compromise between material costs and collection efficiency [166]. The collection efficiency depends on the number of used gauzes as well as the process conditions and ranges between $60 - 90$ %. The economic efficiency of this method is drastically reduced by the fact that high amounts of palladium are lost during operation. Palladium losses lie typically at about one third of the weight of collected platinum. Hence, the economic efficiency of this method depends strongly on platinum, palladium, gold, and other metal prices. If palladium based catchment gauzes are used, the gauzes are replaced usually together with the catalyst gauzes after every campaign [106, 167].

Another strategy to reduce platinum losses, which can be combined with getter gauzes, is the reduction of the platinum loading inside the burner. The main reason, why platinum is still used in ammonia oxidation burners despite its high costs, is the excellent nitric oxide selectivity achieved with platinum gauze catalysts. However, ammonia is mainly combusted on the first few gauzes of a stack. Nevertheless, the last gauzes of a stack cannot simply be removed as the selectivity drops for example from 95 % to $85 - 90$ % if the last gauzes with low activities are removed [168]. These observations made by the group of Gillepsie [168] can be explained with the influence of the last gauzes on the flow distribution and the pressure drop of the gauze pack. A solution for this problem is to replace the last gauzes with gauzes made of cheaper material like nichrome or to use a combination of platinum gauzes and metal oxide catalysts. The second method, the usage of a combined platinum gauze and metal oxide pellet catalyst bed, is often utilized in countries of the former USSR. By replacing the last gauzes with alternative catalysts platinum losses can be reduced by up to 30 %, while nitric oxide selectivities are only slightly reduced or stay constant [106].

2.4.4 Alternative Ammonia Oxidation Catalysts

Despite the high platinum costs and loss rates, ammonia oxidation is one of the few large-scale processes in the chemical industry in which no cheaper alternatives replaced platinum based catalysts. Many different alternative catalysts based on other platinum group metals, metal oxides, and mixed metal oxides have been tested for ammonia oxidation in the last decades.

The first group of alternative catalysts is based on other platinum group metals. The replacement of platinum or alloying platinum with iridium, ruthenium, and osmium increases the yield slightly, but also leads to increased weight losses and reduces the maximum campaign length significantly. In some eastern European countries platinum gauze catalysts with up to 20 weight percent of palladium were used in the past, to reduce the investment costs [61]. However, palladium prices spiked in the last decade, rendering such approaches unprofitable nowadays.

Already in 1902, Wilhelm Ostwald filed a patent for the usage of the second group of alternative catalysts: Metal oxide catalysts. Metal oxide catalysts based on oxides of iron, nickel, manganese, cobalt, molybdenum, or vanadium have lower nitric oxide selectivities than platinum gauze catalysts. However, metal oxide catalysts also have lower nitrous oxide selectivities but increased nitrogen selectivities, which makes them interesting under environmental aspects. During the First World War metal oxide based catalysts were used in industrial nitric acid plants in Germany. Due to the war, the platinum supply of Germany was cut of. As an alternative catalyst the so called "brown oxide catalyst" was used. The brown oxide catalyst is composed of 90 % Fe_2O_3, 5 % Mn_2O_3 and 5 % Bi_2O_3. In industrial plants nitric oxide yields of $92 - 94$ % were achieved during the First World War using brown oxide catalysts. However, these high yields could only be achieved when low ammonia concentrations between $7.1 - 7.3$ vol.% and low loadings of $0.6\ \frac{\mathrm{t\,N}}{\mathrm{m^2 \cdot d}}$ were used. After the war, brown oxide catalysts were replaced again by platinum gauze catalysts [3, 61].

Starting in the 1960s metal oxide catalysts based on cobalt oxides were used in some plants as ammonia oxidation catalysts. In order to achieve good selectivities cobalt oxide catalysts must operate in the form of Co_3O_4 [85,128,169]. Since cobalt oxide changes its configuration at high temperatures the operation temperature of

cobalt oxide based systems is limited to a range of about $660 - 750$ °C. Therefore, ammonia concentrations lower than 10.5 vol% are used in cobalt oxide systems. Furthermore, cobalt oxide catalysts are more susceptible to poisoning and lead to higher pressure drops than platinum gauze catalysts. These disadvantages render cobalt oxide catalysts less economical than platinum gauze catalysts, even though the catalyst is considerably cheaper and allows yields of $93 - 94$ % and campaign lengths of up to one year [3, 128]. Recent attempts using Co_3O_4 spinels as catalysts showed promising nitric oxide selectivities but still suffered from fast catalyst deactivation by reduction to CoO [106, 170, 171]

In countries of the former USSR a different approach is used in most industrial burners since the early 1960s [106, 172, 173]. In order to reduce the catalyst costs as well as the platinum losses two-bed ammonia oxidation systems are used [106, 174, 175]. In two-bed ammonia oxidation systems platinum gauze catalysts are combined with metal oxide catalysts reducing the needed number of gauzes. Usually, the utilized metal oxide catalysts are based on iron oxides that are modified with chromium, aluminum, or other oxides. Until the 1990s the metal oxides were used in the form of small pellets, till they were mainly replaced by honeycomb shaped catalysts [106, 176]. The honeycomb catalysts have multiple advantages compared to pellet shaped catalysts such as a reduced pressure drop, a more uniform flow distribution, and a higher mechanical strength. Since ammonia is mainly combusted on the platinum gauzes in front of the metal oxide catalyst, the demands of metal oxide catalysts used in two-bed systems vary from the demands of metal oxides in single-bed systems. The metal oxide catalysts are optimized for high nitric oxide selectivities, while the activity plays only a secondary role [106]. The achieved nitric oxide yield of ammonia burners operated with two-bed systems is reported to be equivalent to the yield of comparable conventional platinum gauze catalyst processes and the platinum losses can be reduced by up to 30 % [177].

In 2005 promising results were reported achieved with a new type of catalyst that is based on membranes of perovskites such as $La_{1-x}CaFeO_{3-\delta}$ and $La_{1-x}SrFeO_{3-\delta}$ (with x in the range of $0.1 - 0.2$). Ammonia and oxygen are supplied on opposing sides of the oxygen conducting membrane allowing to reach nitric oxide selectivities of up to 98 % at ammonia conversions of $80 - 95$ %. However, the membranes

suffer from fast physical degradation making it not yet worthwhile for industrial applications [178, 179].

Most recently Ruan et al. [180] claimed to have reached nitric oxide selectivities of 99.8 % at ammonia conversion of 97 % using a V_2O_5 catalyst in a chemical looping reactor. In the reactor 30 consecutive low volume (765 μL) pulses of 5 vol.% ammonia in argon are fed to 200 mg of V_2O_5 catalyst followed by a 30 minute long catalyst regeneration using a feed of 30 vol.% oxygen in argon as ballast medium at flow rates of 30 mL/min. The main origin of the achieved high nitric oxide yields is attributed to the chemical looping operation and not to the superior performance of the catalyst itself. In a conventional co-feed operation of the catalyst system only nitric oxide selectivities of 59.1 % at ammonia conversions of 75.1 % were obtained [180]. Since ammonia oxidation burners are operated at high throughputs in the dimension of several thousand tons of gas burned per day, a chemical looping process is to date more of academic interest but not feasible in industry. Nevertheless, the presented results demonstrate that high nitric oxide yields can also be achieved using alternative catalysts and creative improvements of the reactor operation modes may allow replacing the expensive platinum based catalysts in the future.

All in all, many different types of catalysts have been tested in the past. Nevertheless, to date, no alternative catalyst yet exists that out-performs platinum alloy gauze catalysts in industry.

2.5 Spatially Resolved Measurement Techniques

A knowledge-based improvement of catalytic reactors requires a deep understanding of the underlying processes. In the traditional approach heterogeneously catalyzed reactions are experimentally studied in kinetic test setups that treat the reactor as a black box. The operating conditions inside the test reactor e.g. inlet concentrations, space velocity, temperature, and pressure are controlled and the respective variables of interest can be measured at the reactor outlet. However, using this approach no information about the state of the catalyst, the concentrations, and temperature along the catalytic bed are obtained. Thus, only a general understanding of the process can be gained, but the actual most interesting pro-

cesses inside a catalytic fixed bed, like the formation sites of intermediates and byproducts, possible hot spots, changes in the catalyst structure among others remain hidden. To bridge this gap of knowledge spatially resolved measurement techniques are required [39].
In general, spatially resolved measurement techniques can be divided into two groups. On the one hand measurement techniques utilizing physical probes inserted inside the catalyst bed and on the other hand, electromagnetic techniques like optical spectroscopy, synchrotron-based and magnetic resonance techniques that utilize probes positioned outside the reactor [39]. In the last two decades a wide field of techniques was reported, all having unique strengths and limitations. Hence, the choice of an appropriate measurement technique strongly depends on the goals and requirements of the study as well as the operation conditions of the process. Magnetic resonance techniques for example are mostly limited to liquid phase reactions, while optical spectroscopy and synchrotron-based techniques require highly specialized reactor setups with optical access windows [39]. An important requirement in the selection of a suitable measurement technique is that it should be minimally invasive. Therefore, electromagnetic techniques with probes positioned outside of the reactor are often preferred over techniques with physical probing [39]. However, physical probing is still the only adequate technique for many applications, enabling for example measurements of gas phase concentrations with high accuracy by gas sampling.
A first step in the development of minimal invasive spatially resolved measurement techniques using physical probes was the development of the spatially resolved capillary-inlet mass spectrometer (Spaci-MS) by Partridge et al. [181]. In Spaci-MS a thin fused silica capillary with an open end is used as inlet of a MS. The capillary is placed inside a catalyst bed sampling gas at low flow rates rendering the technique minimally invasive. Using this technique Partridge et al. enabled studying highly dynamic, transient processes thanks to the high temporal resolution of the technique [181]. In the following years the group further improved the technique [182, 183]. By placing multiple sampling capillaries at fixed positions inside a catalyst bed first spatially resolved measurements were enabled [182].
The final evolution towards fully spatially resolved physical probing was then en-

abled by the profile measurement technique developed by Horn et al. [32, 33]. In Figure 2.14 a schematic explaining the setup used by Horn et al. is shown.

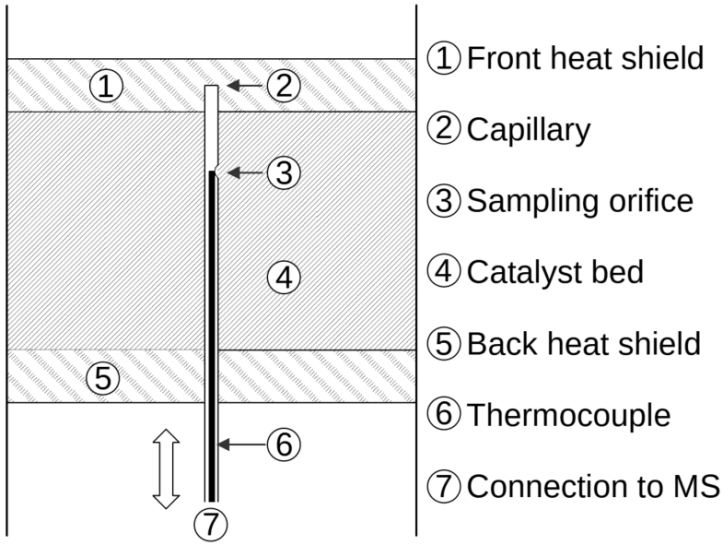

Figure 2.14: Schematic of the setup used for the first profile measurements by Horn et al. adopted from [32] (modified)

In profile measurements a thin quartz sampling capillary is connected to a linear translation stage which allows positioning of the sampling capillary at any axial position inside a catalyst bed. Gas is sampled through a small side sampling orifice that is drilled into the capillary. A thermocouple aligned with the sampling orifice allows parallel measurements of temperature profiles [32]. The spatial resolution of the profile measurement technique is only limited by the diameter of the sampling orifice and the accuracy of the linear translation stage. Capillary positioning using translation stages was also adopted in further development steps of the Spaci-MS technique, first for a single capillary setup [183] and subsequently, for a multi capillary setup [184].

In the following years, the possible range of operation conditions of the profile measurement technique was further extended. The original study from Horn et al. reported measurements at up to 1300 °C and atmospheric pressure [32]. The pressure range was further extended in later setups enabling measurements at pressures of first 11 bar [185, 186] and subsequently, up to 45 bar [34]. Full 360° rotation of the capillary is enabled by using an additional rotational stage [34].

By placing spectroscopy fibers inside the sampling capillary multiple spectroscopy techniques have been coupled with the profile measurement technique to date including pyrometry [34, 35], Raman spectroscopy [36] and laser-induced fluorescence spectroscopy [38]. The sampled gas can be analyzed by different analytical devices like MS [32], gas chromatography [35] and Fourier-transform infrared spectroscopy [37].
Recently, the profile measurement technique was adopted for measuring concentration profiles inside single catalyst pellets, enabling to resolve phenomena resulting from the interplay between diffusion and reaction, like boundary layers, for the first time experimentally. The invasiveness of the technique was assessed using combined experiments and CFD simulations, showing the technique to be minimally invasive under the right conditions [40]. The profile measurement technique was also already successfully adopted to study the external mass transfer limited reaction of methane combustion over platinum gauzes. Combined experiments and CFD simulations showed that the high gradients over the platinum gauze catalyst can be resolved using the profile measurement technique. The requirement for this is that a proper setup with a narrow sampling region is used [38]. In conclusion, performing spatially resolved measurements using the profile measurement technique by Horn et al. is a promising approach to study and resolve the processes inside an ammonia burner.

2.6 Mass Spectrometry

The quantitative analysis of the composition of sampling streams is a task that needs to be tackled frequently in chemistry and process engineering research. Various analytical techniques are established to analyze gas samples and the choice of the respective technique highly depends on the requirements of the given application. One of the most commonly used methods is mass spectrometry thanks to its high flexibility, sensitivity, and comparatively fast scan speeds (eg. compared with chromatographic methods like gas chromatography). In a mass spectrometer, the analyte is first brought into the gas phase, then ionized, subsequently, the various compounds of the analyte mixture are separated according to their resulting mass-to-charge ratio (m/z, with z the number of elemental charges of the result-

ing ions), and finally, a signal proportional to the stream of the separated ions is generated using an ion detector. The field of mass spectrometry can be further subdivided according to the components used in every step of a mass spectrometer and the utilized underlying physical principles [187]. A comprehensive overview of all existing aspects of mass spectrometry is beyond the scope of this work. Hence, the reader is referred to [187–189] for more detailed information on the wide field of mass spectrometry. This chapter focuses only on the working principles of the components of the HAL 4 EPIC Low Energy mass spectrometer with a molecular beam inlet system that was used for the experiments presented in this work.
A sketch of the molecular beam mass spectrometer (MBMS) used in this work is shown in Figure 2.15.

The MBMS can be divided into four main components. The working principles of each component are explained in detail in the following sections. First of all, the fundamentals of the inlet of the MBMS using a molecular beam (I in Figure 2.15) are explained. Subsequently, the reader is introduced to the basics of ion generation using electron impact ionization (II in Figure 2.15) and near threshold ionization. In the third subsection the physical backgrounds of quadrupole mass filters are explained, which are utilized in this setup for mass separation (III in Figure 2.15). Finally, a brief overview of ion detection using secondary electron multipliers is given (IV in Figure 2.15).

2.6.1 Gas Inlet by Molecular Beams

The inlet system of a mass spectrometer needs to fulfill several requirements depending on the application. In the used experimental setup a high pressure drop between the target reactor pressure p_r of up to 30 bar and the pressure in the mass spectrometer high vacuum chamber p_det (max. $5 \cdot 10^{-6}$ mbar) needs to be realized in a controlled fashion. Only comparatively low flow rates should enter the high vacuum chamber of the mass spectrometer to maintain the required vacuum levels. Furthermore, a fast response time in the overall sampling system is required to enable fast measurements of spatial concentration profiles in comparatively short time periods. In addition, the inlet system needs to be heated to 180 °C to prevent the formation of ammonium nitrate by the reaction of ammonia with nitric oxides.

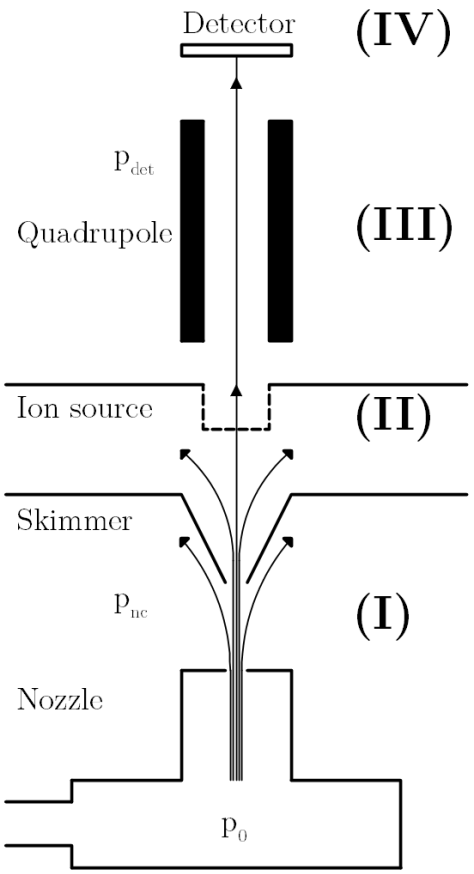

Figure 2.15: Sketch showing the components of the differentially pumped MBMS setup used in this work

These requirements can be fulfilled using a heated molecular beam inlet system. A molecular beam is a stream of particles that moves with only marginal inter-particular collisions through vacuum [190]. Molecular beams are usually formed by expanding gas from a high pressure source through a small orifice (nozzle in Figure 2.15 with the pressure p_0) into a low pressure chamber (first vacuum stage of the MBMS with the pressure p_{nc}). The flow regimes formed in molecular beams have distinct physical properties and characteristics making molecular beams an interesting tool for applications such as studying chemical reaction dynamics, spectroscopy of jet cooled molecules, collision experiments in molecular physics, and the continuous sampling of dynamic systems. Molecular beams can be classified by

the dominating type of particle interactions in the orifice that is used to form the molecular beam. If collisions between particles and the orifice walls dominate, an effusive beam is formed. In effusive beams a molecular flow is formed that can be described using gas kinetics. If inter-particular collisions dominate, a supersonic beam is formed. In supersonic beams a continuous, viscous flow is formed that can be described by gas dynamics [190]. The beam type can be classified using the Knudsen number Kn which is defined as the ratio of the mean free path length of the particles in the high pressure source $\bar{l}$ to the orifice diameter d_{n}.

$$Kn = \frac{\bar{l}}{d_{\mathrm{n}}} \tag{2.50}$$

The Maxwell mean free path length of the particles in the high pressure source $\bar{l}$ can be calculated assuming ideal gas behavior using the Boltzmann constant k_{B}, the gas phase temperature T, the pressure p as well as the collision cross section of the particles σ.

$$\bar{l} = \frac{k_{\mathrm{B}} T}{\pi \sqrt{2} p \sigma} \tag{2.51}$$

For $Kn > 0.5$ an effusive beam is formed, for $Kn < 10^{-2}$ a supersonic beam is formed and for $10^{-2} < Kn < 0.5$ a beam in the so called Knudsen flow regime is formed [191]. The nozzle used in the inlet system of the MBMS has a diameter of $d_{\mathrm{n}} = 100$ μm. The inlet is heated to $T = 200$ °C and operated at a a minimum pressure level of $p_{\mathrm{hps}} = 0.5$ bar. Assuming the collision cross section of the dominant molecule of the sampled gas mixture, nitrogen, $\sigma = 1.4 \cdot 10^{-19}$ m^2 [192] the highest Knudsen number obtained in the experiments can be estimated to be $Kn_{\mathrm{max}} = 2 \cdot 10^{-3}$. Thus, for all conditions studied in the experiments considered in this thesis a continuous, supersonic molecular beam is formed. Hence, only the characteristics of supersonic molecular beams are reviewed in the following.

Supersonic molecular beams are continuous, viscous flows that can be described by gas dynamics. The three-dimensional description of such a flow is a rather complex task on its own and beyond the scope of this work. Hence, the fundamentals are illustrated by considering the simplified one-dimensional case. Only

the most important steps of this case are shown here. For a more detailed treatment, including the derivation of all equations, the reader is referred to [191]. The force balance of a one dimensional volume element moving along a streamline is described by the Bernoulli equation.

$$\frac{1}{2}\left(u_{\mathrm{nc}}^2 - u_{\mathrm{hps}}^2\right) = -\int_{p_{\mathrm{hps}}}^{p_{\mathrm{nc}}} \frac{dp}{\rho} \tag{2.52}$$

The gas velocity at the high pressure side is labeled as u_{hps}, the velocity at the low pressure side in the nozzle chamber is labeled as u_{nc} and the density of the fluid is labeled as ρ. A relation between the pressure and the density is needed to solve the integral of Equation 2.52. Since the expansion in a supersonic beam is in good approximation an adiabatic process, the equation of state known as Poisson's law can be used to describe this relation using the isentropic expansion factor κ.

$$\left(\frac{p}{p_{\mathrm{hps}}}\right) = \left(\frac{T}{T_{\mathrm{hps}}}\right)^{\frac{\kappa}{\kappa-1}} = \left(\frac{\rho}{\rho_{\mathrm{hps}}}\right)^{\kappa} \rightarrow \frac{1}{\rho} = \frac{1}{\rho_{\mathrm{hps}}}\left(\frac{p_{\mathrm{hps}}}{p}\right)^{\frac{1}{\kappa}} \tag{2.53}$$

The gas phase velocity upstream the nozzle is several orders of magnitude lower than the velocity of the expanding beam in the nozzle chamber ($u_{\mathrm{hps}} << u_{\mathrm{nc}}$). Hence, the simplification is made, that the gas upstream the nozzle is at rest ($u_{\mathrm{hps}} = 0$). Using the ideal gas law $\left(\frac{p_{\mathrm{hps}}}{\rho_{\mathrm{hps}}} = \frac{R \cdot T_{\mathrm{hps}}}{M}\right)$, with the molecular weight of the molecules M, leads to an equation describing the velocity of the expanding particle stream in the nozzle chamber u_{nc}.

$$u_{\mathrm{nc}} = \sqrt{\frac{2\kappa}{\kappa-1}\frac{R \cdot T_{\mathrm{hps}}}{M}\left[1 - \left(\frac{p_{\mathrm{nc}}}{p_{\mathrm{hps}}}\right)^{\frac{\kappa-1}{\kappa}}\right]} \tag{2.54}$$

An important question for the characterization of the behavior of a molecular beam is, whether the particles are accelerated to the speed of sound. At the speed of sound a choked flow at the orifice is formed, limiting the mass flow through the orifice. The total flow rate through the orifice is then only a function of the isentropic expansion factor κ of the fluid, the nozzle diameter d_{n}, the pressure on the high pressure side p_{hps} and the gas temperature T. The speed of sound u_{ss} can be calculated according to Equation 2.55.

$$u_{\mathrm{ss}} = \sqrt{\frac{RT}{M}\kappa} \tag{2.55}$$

By using again Poisson's law (Equation 2.53) an expression for the speed of sound in dependence on the pressure ratio as the driving force of the expansion $\frac{p}{p_{\mathrm{hps}}}$ as well as the gas temperature before the gas is expanded T_{hps} can be formulated.

$$u_{\mathrm{ss}} = \sqrt{\frac{RT_{\mathrm{hps}}}{M}\kappa \left(\frac{p}{p_{\mathrm{hps}}}\right)^{\frac{\kappa-1}{\kappa}}} \tag{2.56}$$

By equating Equations 2.56 and 2.54 an expression for the critical pressure ratio, at which the particles are accelerated to the speed of sound, can be formulated.

$$\frac{p_{\mathrm{c}}}{p_{\mathrm{hps}}} = \left(\frac{2}{\kappa+1}\right)^{\frac{\kappa}{\kappa-1}} \tag{2.57}$$

The isentropic expansion factor κ of the main component of the sampled gas mixture, nitrogen, equals 1.4, corresponding to a critical pressure ratio of 0.53. This critical pressure ratio was always by far fulfilled in the conducted experiments with $p_{\mathrm{hps}} > 0.5$ bar and $p_{\mathrm{nc}} < 10^{-4}$ mbar. Thus, a supersonic molecular beam is formed under the investigated conditions and the sampled mass flow into the MS is limited due to the choked flow conditions at the nozzle. Furthermore, only a fraction of the gas inside the molecular beam passes through the skimmer (see Figure 2.15). Hence, by using a molecular beam inlet system the requirements of a controlled pressure drop of several orders of magnitude as well as a limited total mass flow rate into the mass spectrometer are fulfilled, without the necessity of any complex additional control systems. Furthermore, the chosen system has a short response time and allows measurements with high signal to noise ratios by directing the molecular beam directly into the ion source of the mass spectrometer (see Figure 2.15).

Even though molecular beams provide several advantages as an inlet system of a mass spectrometer, the operator has to understand and consider some characteristics of supersonic molecular beams, that can be potential sources of error, especially in quantitative measurements. If the expansion of the beam is not dis-

turbed by any geometries in the lower pressure chamber like walls etc. a typical axis-symmetric free-jet is formed, in which regions with different flow conditions are established. Figure 2.16 shows a schematic of the different regions formed in a supersonic continuum free-jet expansion [190].

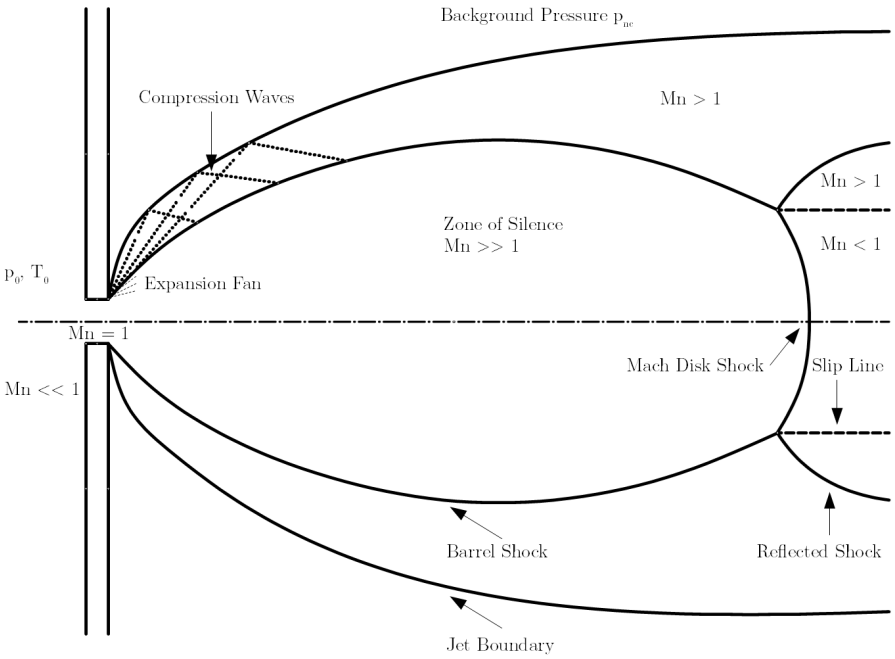

Figure 2.16: Schematic of a supersonic continuum free-jet expansion, adopted from [190] (modified)

During the expansion, the particles around the axis are accelerated above the speed of sound (indicated by Mach numbers $Mn = \frac{u}{u_{\mathrm{ss}}} > 1$) and the pressure drops significantly. The pressure drop also results in a steep decrease in the particle density as well as the collision frequency. A complex interplay of shock waves and sound waves, resulting from the interaction of the beam molecules with the surrounding background molecules, leads to the formation of regions in which an unstable, nonlinear flow field is established. At the edge of the jet the so called barrel shocks are formed and beyond the mach disk location x_{M} mach disk shocks are formed [193, 194]. To sample gas from a stable region, the position of the skimmer cone of the setup (see Figure 2.15) needs to be positioned inside the zone

of silence, in which no shock waves disturb the flow field [194]. The position of the mach disk location can be calculated according to Equation 2.58.

$$x_{\mathrm{M}} = 0.67 d_n \cdot \sqrt{\frac{p_{\mathrm{hps}}}{p_{\mathrm{nc}}}} \tag{2.58}$$

In the setup used in this thesis with $p_{\mathrm{hps}} > 0.5$ bar, $p_{\mathrm{nc}} < 10^{-3}$ mbar and $d_{\mathrm{n}} = 0.1$ mm the minimal mach disk position $x_{\mathrm{M,min}}$ is at 47 millimeters. The skimmer cone used in this setup is adjustable in all three room directions and is placed at a distance smaller than 47 mm away from the nozzle. Hence, mach disk shocks do not influence the sampled gas stream and by adjusting the position in the other two directions, the skimmer cone is placed outside of the barrel shock region.

However, another phenomenon can lead to systematic errors when molecular beams are used as inlet system for mass spectrometers. The expansion of the molecular beam and the extraction of a fraction of the beam using the skimmer influences the spatial distribution of the species. Several effects lead to this mass separation phenomenon [195].

The first one is the pressure separation effect. At a distance of only a few nozzle diameters away from the nozzle a steep drop in pressure occurs. Due to this pressure drop the particles are accelerated rapidly. Lighter species are accelerated stronger laterally than heavier species, leading to an enrichment of heavier species in the beam center.

Secondly, a free molecular diffusion effect occurs. Lighter molecules have a higher thermal velocity spread at the same mean velocity than heavier species in the free molecular region of the beam. Therefore, the diffusion perpendicular to the beam direction is higher for lighter species, again enriching heavier species in the beam center.

The third effect is mass separation induced by the skimmer. In front of the skimmer a shock wave can be formed that decelerates the particles. Lighter species are decelerated more strongly than heavier species and a higher fraction of heavier species passes this barrier induced by the skimmer shock wave. However, this effect is probably negligible in the used setup due to the usage of a well designed skimmer geometry as well as operating the nozzle chamber at low pressures, reducing the

chance of skimmer induced shock wave formation.
Finally, background gas can diffuse into the beam, leading to an enrichment of lighter species. At a progressed stage of the beam expansion the pressure inside the jet approaches the background pressure allowing diffusion of background molecules into the beam. Since lighter species have higher diffusion coefficients, this effect leads to enrichment of lighter species.
The influence of these effects can be minimized by using an appropriately designed setup, however, can not be prevented completely. Therefore a thorough calibration of the mass spectrometer at operation conditions needs to be carried out, to include the influence of the described effects on the measured compositions. This becomes especially important for quantitative data analysis.

2.6.2 Ion Generation using Electron Impact Ionization

In mass spectrometry the components of a sample are separated according to their mass-to-charge ratio m/z. Hence, to separate the different species of a sample, they first need to be ionized. Several options like photoionization, chemical ionization, and electron ionization can be used to generate ions from a gas sample [189]. A common ionization technique for low mass compounds with a weight below 600 amu is electron ionization. In electron ionization the sample is bombarded with electrons with defined kinetic energy. If the energy of the electron E exceeds the ionization energy of a species IE_s, the species is ionized with a probability P_i, that depends on the energy of the electron $P_\mathrm{i} = f(E)$. If the electron energy is smaller than the ionization energy IE_s no ionization occurs.

$$S + e^- \rightarrow S^+ + 2e^- \tag{2.59}$$
$$P_i(E < IE_s) = 0,\ P_\mathrm{i}(E \geq IE_s) = f_\mathrm{i}(E)$$

The ionization cross sections of most molecules have broad maxima in the range between 50 and 150 eV. Therefore, most mass spectrometers using electron impact ionization are operated in this range, typically at an electron energy of 70 eV [187]. Molecules that are ionized with electron energies exceeding the sum of the ioniza-

tion energy of the molecule IE_{XY} and the dissociation energy DI_{XY} of a bond between two parts of the molecule X-Y are fragmented with a certain probability P_{d}.

$$XY + e^- \rightarrow X^+ + Y + 2e^- \tag{2.60}$$
$$P_{\mathrm{d}}(E < IE_{\mathrm{XY}} + DI_{\mathrm{XY}}) = 0,\ P_{\mathrm{d}}(E \geq IE_{\mathrm{XY}} + DI_{\mathrm{XY}}) = f_{\mathrm{d}}(E)$$

A molecule can be identified by its characteristic fragmentation pattern (fingerprint) [187].
In the so called threshold ionization the ion source is operated near the ionization energy of a species. This way the contribution of two species to the signal intensity of a peak at a certain mass-to-charge ratio can be distinguished. In this work, for example, the contribution to the signal at m/z = 17 of ammonia NH_3^+ and OH^+ formed by water fragmentation needs to be distinguished to quantify the ammonia content of the sample. This can be done by operating the electron source between the ionization energy of ammonia (10.2 eV) [196, 197] and the electron energy needed for the fragmentation of water to OH^+ (18.2 eV) [198, 199]. In contrast to most mass spectrometers, which operate at a fixed electron energy of 70 eV, the electron energy of the HAL 4 EPIC low energy mass spectrometer used in this work is adjustable in a range from 4 to 150 eV. In Figure 2.17 the electrodes setup of the used mass spectrometer is shown, which allows tuning the operation parameters to match the requirements of complex applications like threshold ionization experiments.

A heated filament, typically made of rhenium, tungsten, or thoriated iridium, is used as cathode emitting electrons. The electrons are accelerated towards a wire cage that acts as an anode. By changing the potential between the cathode and the anode the kinetic energy of the electrons can be adjusted (IIa in Figure 2.17). The sample enters the ion source perpendicular to the electron beam. The positively charged ions are drawn out of the source by a focus electrode (IIb) and subsequently, decelerated by another electrode, the energy plate (IIIa), before they enter the quadrupole for mass separation (III).

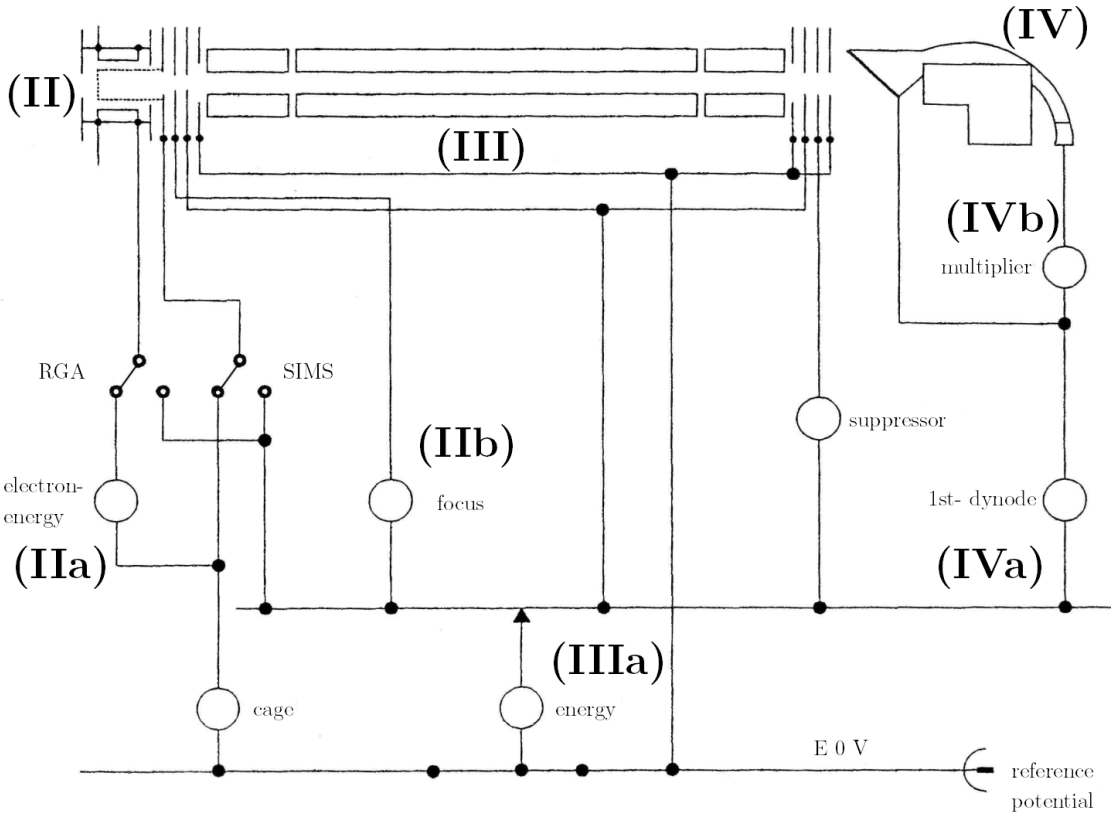

Figure 2.17: Electrodes setup of the HAL 4 EPIC low energy mass spectrometer used in this work, adopted from [200] (modified)

2.6.3 Mass Separation using Quadrupole Mass Filters

Nowadays, depending on the requirements of the application and the budget, operators can choose between various types of mass spectrometers using different mass separation principles like magnetic sector field, time of flight, quadrupole iron trap, orbit trap, and quadrupole mass filters [187]. The mass spectrometer used in this study is equipped with a quadrupole mass filter and thus, only the principles of quadrupole mass filters are considered in the following chapter.

A quadrupole mass filter consists of four hyperbolic or cylindrical rods that are arranged in a quadratic order [188]. A schematic of a linear quadrupole mass analyzer with cylindrical rods is shown in Figure 2.18.

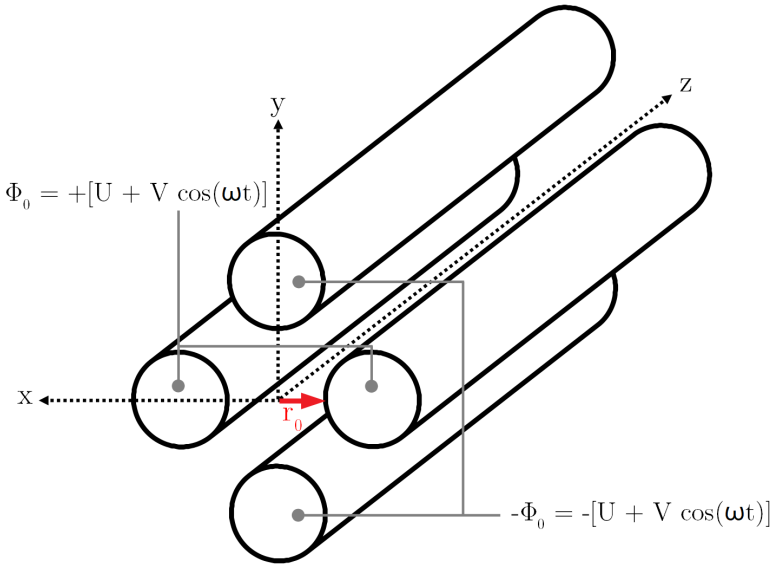

Figure 2.18: Schematic of a linear quadrupole mass analyzer with cylindrical rods, adopted from [187] (modified)

A potential $+\Phi_0$ is applied to the electrodes of one opposing rod pair and a potential $-\Phi_0$ is applied to the second rod pair. The potential Φ_0 consist of a direct current (DC) fraction U and a radio frequency (RF) fraction V with the angular frequency ω [187].

$$\Phi_0 = U + V\cos(\omega t) \tag{2.61}$$

It has to be mentioned that the following theoretical considerations are deducted for ideal hyperbolic rods with an infinite length generating a perfect, symmetrical field. Due to a cheaper and simpler manufacturing process, cylindrical rods are often used instead of hyperbolic rods, resulting in some imperfections in the field of the quadrupole. The oscillating field generated by quadrupoles composed of hyperbolic rods can be described by Equation 2.62 using the half distance between two rods r_0 and the distance from the center of the field in the respective direction x and y [188].

$$\Phi(x,y) = \Phi_0\frac{x^2-y^2}{r_0^2} = (U + V\cos(\omega t))\frac{x^2-y^2}{r_0^2} \tag{2.62}$$

The trajectory of a sample ion moving through the oscillating field of a quadrupole is described by the dimensionless Mathieu equation in the respective direction.

$$\frac{d^2x}{d\tau^2} + (a_\mathrm{x} + 2q_\mathrm{x}\cos(2\tau))\,x = 0 \tag{2.63}$$

$$\frac{d^2y}{d\tau^2} + (a_\mathrm{y} + 2q_\mathrm{y}\cos(2\tau))\,y = 0 \tag{2.64}$$

The dimensionless parameters of the Mathieu equation are given in the Equations 2.65 − 2.67 [188].

$$\tau = \frac{\omega t}{2} \tag{2.65}$$

$$a_\mathrm{x} = -a_\mathrm{y} = \frac{8zeU}{m\omega^2 r_0^2} \tag{2.66}$$

$$q_\mathrm{x} = -q_\mathrm{y} = \frac{4zeV}{m\omega^2 r_0^2} \tag{2.67}$$

While the ions pass through the quadrupole, they are not accelerated in z-direction and thus, their velocity in z-direction is constant. This velocity is set by an interplay of the potentials of the cage-, focus- and energy plate electrodes of the ion source (see the previous subsection). The Mathieu equations describe periodical motions in x- and y-direction which, combined with the constant motion in z-direction, result in a helical flight path of the ions through the quadrupole. Depending on the velocity in z-direction the ions perform a certain number of these periodical movements in x- and y-direction, named RF-cycles. If ions have high speeds in z-direction, they perform a low number of RF-cycles leading to high signal intensities coming along with a low mass resolution. Low z-velocities lead to a high number of RF-cycles resulting in low signal intensities and high mass resolutions. The mass filter characteristics of a quadrupole can be explained by the following considerations that are illustrated in Figure 2.19.

To the electrodes of one rod pair the potential $+\Phi_0$ is applied. The positive DC potential accelerates positively charged ions towards the central axis (1. in Figure 2.19a). Simultaneously, the ions are accelerated towards the rods due to the contribution of the negative half-cycle of the changing RF potential (2. in

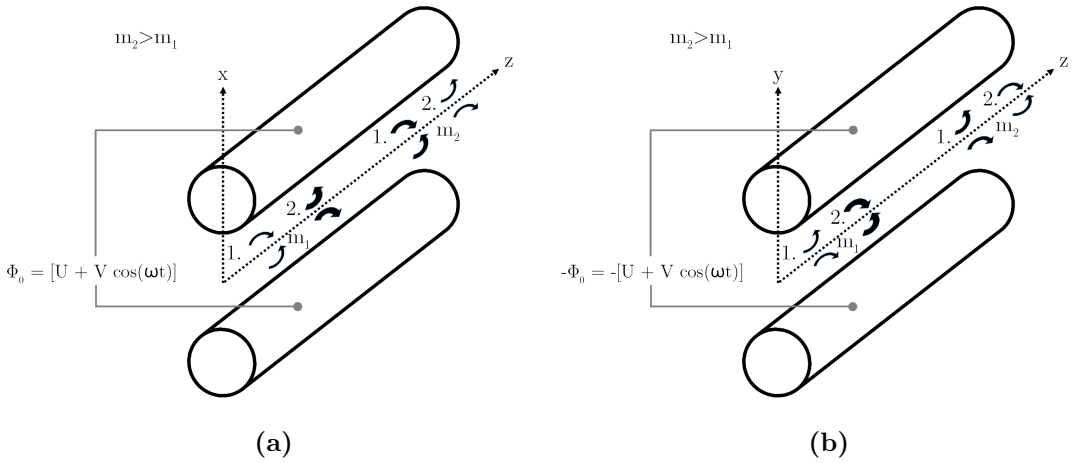

(a) **(b)**

Figure 2.19: Schematic of the operation principle of a quadrupole mass filter. (a) High-pass filter functionality of the rods in the xz-plane. (b) Low-pass filter functionality of the rods in the yz-plane, adopted from [188] (modified)

Figure 2.19a). Ions with low mass-to-charge ratios m/z are accelerated stronger towards the rods during the negative RF half-cycle. Hence, ions with low m/z are exiting the quadrupole explaining the high-pass filter functionality of the rod pair with a positive potential $+\Phi_0$. For the second rod pair the opposite effect is observed. A negative potential $-\Phi_0$ is applied to the electrodes of this rod pair. The negative DC potential accelerates positively charged ions towards the rods (1. in Figure 2.19b). Simultaneously, the ions are accelerated towards the central axis due to the contribution of the positive half-cycle of the changing RF potential (2. in Figure 2.19a). Ions with low mass-to-charge ratios m/z are stronger accelerated towards the central axis during the positive RF half-cycle while ions with high mass-to-charge ratios m/z are less affected. Therefore, ions with high m/z are exiting the quadrupole, due to the low-pass filter functionality of the rod pair with a negative potential $-\Phi_0$ [188]. The filtering performance, showing stable solutions of the Mathieu equation, is often illustrated by stability diagrams like the ones in Figure 2.20.

The trajectory of an ion is stable if the distances of the ion from the center axis $|x|$ and $|y|$ do not exceed r_0 at any time during its flight through the quadrupole. This stable region is located in the triangular regions of the stability diagrams. Beyond this region are combinations of a and q in which the trajectory of the

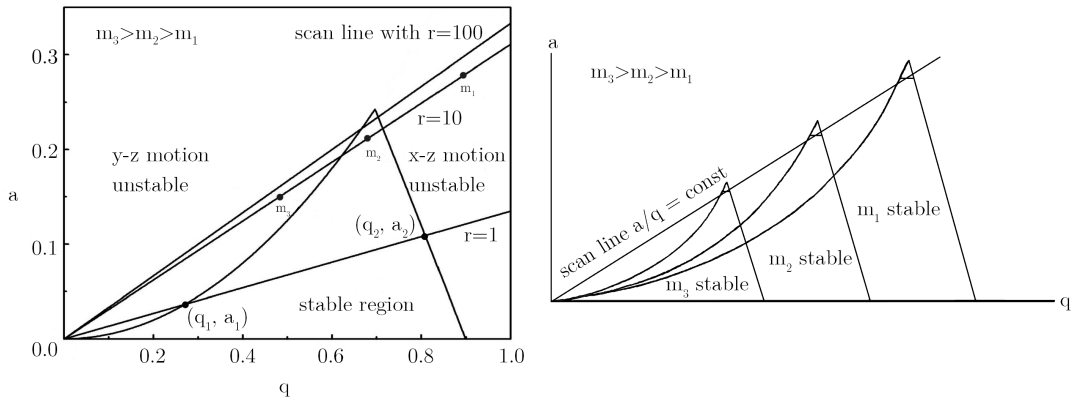

(a) **(b)**

Figure 2.20: Stability diagrams of a quadrupole mass filter: (a) Scan lines for different resolutions r. (b) Stability regions of varying masses, adopted from [187] (modified)

considered ion is either unstable in its y-z motion, x-z motion, or its motion in both directions. During a scan over a certain range of mass-to-charge ratios the ratio of the DC and RF voltage is kept constant. These scans are represented by straight lines with the slope s in the stability diagrams [201].

$$s = \frac{2U}{V} = \frac{a}{q} = \frac{\Delta a}{\Delta q} \tag{2.68}$$

The resolution re of a quadrupole mass filter is expressed by the ratio of the mean value of a in the stable region to the difference between the points of intersection of the scan line with the stability region $\Delta a = (a_2 - a_1)$ [201].

$$re = \frac{m}{\Delta m} = \frac{a}{\Delta a} = \frac{q}{\Delta q} \tag{2.69}$$

In Figure 2.20a it is illustrated that changing the slope of the scan line affects the achieved resolution of the quadrupole. The highest mass resolutions are achieved for scan lines that intersect the stable region close to the apex. During a mass scan over varying mass-to-charge ratios the total values of a and q are changed, while their ratio is kept constant. At low absolute values of a or q respectively first ions with high mass-to-charge ratios have a stable trajectory, while with increasing

absolute values of a and q ions with lower mass-to-charge ratios have a stable trajectory (see Figure 2.20b).

2.6.4 Ion Detection using Secondary Electron Multipliers

After separation according to their mass-to-charge ratio the ions are detected. The mass spectrometer used for this thesis is equipped with a secondary electron multiplier (IV in Figure 2.17). Secondary electron multipliers convert ion currents to electron currents while amplifying the current by several orders of magnitude.

A variety of different secondary electron multipliers designs exists but all have the same basic functional principle. In the first step, the high energetic ions that pass the quadrupole mass filter hit a first surface made of metal or a semiconductor. This first surface is named 1st-dynode or also conversion dynode. A negative potential is applied to this 1st-dynode (IVa in Figure 2.17) accelerating ions that pass the quadrupole mass filter in its direction. The impact of the ions on the 1st-dynode generates secondary electrons that are accelerated in a cascade to the surface of subsequent dynodes due to an increasing potential between every dynode. The impinging electrons generate a multiple of secondary electrons in each step of the cascade leading to high amplification of the current in the range of up to $10^6 - 10^8$ along a secondary electron multiplier [187]. In Figure 2.21 the working principle is illustrated based on a secondary electron multiplier with discrete dynodes.

Secondary electron multipliers with discrete dynodes are typically built with $12 - 18$ discrete dynodes and the potential is increasing from one dynode to the next by typically 100 V [187]. An alternative design is a continuous dynode made of lead-silicate glass tubes formed in a horn shape, so called channeltrons. The conducting surface emits the electrons while the increasing potential, that directs the electrons, is applied to a second underlying layer. The third popular secondary electron multiplier design is the usage of multi channel plates. Multi channel plates consist of an array of millions of short continuous dynodes each with a length in the μm range. The signal magnification of a single multi channel plate is typically in the range of $10^4 - 10^5$. Therefore, to achieve higher signal magnifications

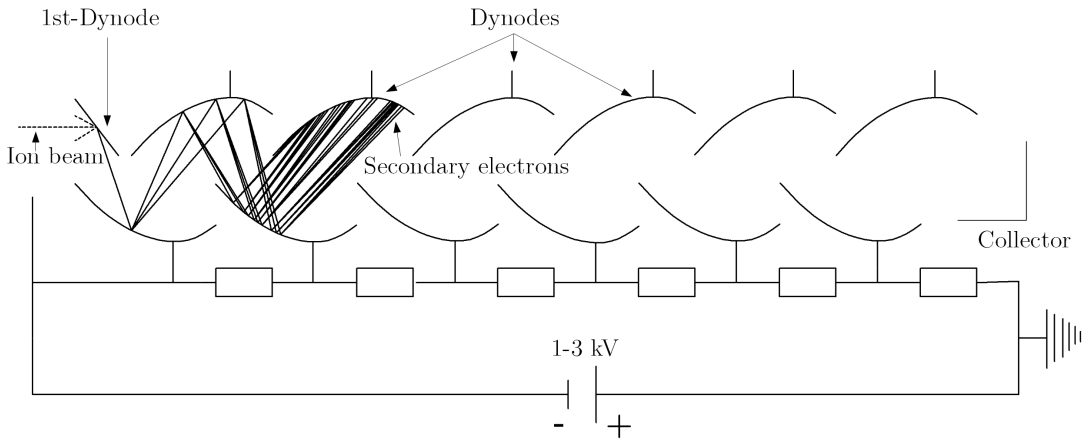

Figure 2.21: Working principle of a seondary electron multiplier with discrete dynodes adopted from [187] (modified)

sometimes two or three arrays are combined in a stack. Multi channel plates enable measurements with nanosecond resolution allowing single ion counting experiments [187].

Thanks to its cascade design secondary electron multipliers enable highly sensitive and fast measurements. However, one major drawback comes along with the technique. The number of electrons generated by the conversion dynode depends on the velocity, charge, electronic configuration, and mass of the impinging ion complicating direct quantification [187]. Hence, signal calibration with pure components at the same operation conditions is necessary to quantify the measured signals.

2.7 Infrared Thermography

A crucial parameter in industrial ammonia oxidation is the surface temperature of the platinum gauze catalyst. Not only the conversion and selectivities are strongly affected by changing surface temperatures (see Section 2.3.5), but also the speed of the catalyst surface restructuring process and the resulting platinum losses depend on the surface temperature (see Section 2.4.2). However, the extreme operation conditions in ammonia burners complicate accurate surface temperature measure-

ment in conventional industrial and lab reactors. This limitation can be overcome by infrared thermography measurements in profile reactors by coupling a pyrometer fiber with the sampling capillary (see Section 2.5).

A pyrometer allows measuring the temperature of an object in a contactless way. This is achieved by measuring the electromagnetic radiation, which every object with a temperature above the absolute zero of 0 K emits. For a perfect black body, a body that absorbs all incident electromagnetic radiation, the spectral radiation energy $E_{\lambda,\mathrm{b}}(T)$ is described by Planck's law [202].

$$E_{\lambda,\mathrm{b}}(T) = \frac{C_1}{\lambda^5 \left[\exp\left(\frac{C_2}{\lambda T}\right) - 1\right]} \tag{2.70}$$

In Equation 2.70 C_1 and C_2 label Planck's radiation constants, T the temperature of the body and λ the wavelength. For values of $\lambda \cdot T < 3125$ μm·K Wien's approximation can be applied with errors smaller than 1 % yielding the following expression [202]:

$$E_{\lambda,b}(T) = \frac{C_1}{\lambda^5 \exp\left(\frac{C_2}{\lambda T}\right)} \tag{2.71}$$

Real objects don't behave like perfect a black body but have a reduced spectral emissivity that is described by the ratio of the spectral radiation energy of the object $E_\lambda(T)$ to the spectral radiation energy of a black body $E_{\lambda,\mathrm{b}}(T)$.

$$\epsilon(\lambda, T) = \frac{E_\lambda(T)}{E_{\lambda,\mathrm{b}}(T)} \tag{2.72}$$

Factoring in the emissivity of a real object ϵ_λ the radiation signal measured with a monochromatic pyrometer $I_\lambda(T)$ is described by the following expression [202]:

$$I_\lambda(T) = \frac{K\epsilon_\lambda}{\lambda^5 \exp\left(\frac{C_2}{\lambda T}\right)} \tag{2.73}$$

K is a constant that is specific for the used pyrometer setup and depends on several design parameters such as the sensitivity of the detector, geometrical factors and the optics of the pyrometer [202]. By comparing the signal measured according to Equation 2.73 with the signal obtained during calibration of the pyrometer, an

equation for the temperature measured with the pyrometer, also called spectral radiance temperature T_{R}, can be derived [202].

$$\frac{1}{T_{\mathrm{R}}} = \frac{1}{T} + \frac{\lambda}{C_2} \ln \frac{\epsilon_{\mathrm{cal}}}{\epsilon} \tag{2.74}$$

To determine the actual temperature measured with a monochromatic pyrometer one of the following two scenarios needs to be fulfilled. Either it must be guaranteed that the emissivity of the body used for calibration ϵ_{cal} and the measured object ϵ are equal to cancel out the second term on the right hand side of Equation 2.74, alternatively, both emissivities need to be known precisely. For many applications, like ammonia oxidation, both of these options are hard to fulfill. The reason for this is that the emissivity of an object changes not only with different temperatures but also varies with changing surface structures, like the ones resulting from the oxidation and corrosion process in ammonia oxidation. A solution to this problem is the usage of a two-color pyrometer that allows measuring the signals at two monochromatic wavelengths.

$$I_{\lambda_1}(T) = \frac{K_1 \epsilon_1}{\lambda_1^5 \exp\left(\frac{C_2}{\lambda_1 \cdot T}\right)} \tag{2.75}$$

$$I_{\lambda_2}(T) = \frac{K_1 \epsilon_2}{\lambda_2^5 \exp\left(\frac{C_2}{\lambda_2 \cdot T}\right)} \tag{2.76}$$

By looking at the ratio of the two measured intensities an expression for the measured ratio temperature T_{R} can be derived [202].

$$T_{\mathrm{R}} = \left(\frac{1}{T} + \frac{\ln\left(\frac{\epsilon_1}{\epsilon_2}\right)}{C_2 \left(\lambda_2^{-1} - \lambda_1^{-1}\right)} \right)^{-1} \tag{2.77}$$

Two-color pyrometers measure typically at two narrow wavelengths λ_1 and λ_2 such that the difference in the emissivity of the analyzed body is negligible. In this case, the measured temperature T_{R} yields the actual temperature of the analyzed object, enabling the determination of surface temperatures also in challenging applications, like ammonia oxidation.

2.8 Fundamentals of Computational Fluid Dynamics

As already discussed in Section 2.3.4 CFD simulations are a powerful tool to gain a deep understanding of the complex interplay of mass transfer processes and reactions occurring in heterogeneous catalytic reactors, especially for mass transfer limited processes like ammonia oxidation. In this section, the underlying fundamental equations required for CFD simulations of heterogeneously catalyzed reactions are introduced. The combination of this set of equations with boundary and initial conditions allows the mathematical modeling of heterogeneous catalytic reactors.

The results of all CFD simulations presented in this thesis are obtained from steady state simulations of a laminar reaction flow that is treated as a compressible, continuous, thermally-perfect mixture of gases. Hence, the governing equations presented in this section are adopted to these assumptions. A gas flow is mathematically described by the conservation equations of mass, momentum, energy, and species. Heterogeneous catalytic reactions are then integrated into the model by coupling the obtained flow field with additional boundary conditions for the species conservation equations at the catalyst surface. In the following the required governing equations are presented, starting with the conservation of mass, also known as continuity equation [203].

$$\frac{\partial \left(\rho \cdot u_i\right)}{\partial x_i} = 0 \tag{2.78}$$

In the continuity equation, ρ represents the mass density, x_i the regarded direction in Cartesian coordinates and u_i the respective velocity component in this direction. Using the Navier-Stokes equations the conservation of momentum is given by Equation 2.79 [203].

$$\frac{\partial \left(\rho \cdot u_i \cdot u_j\right)}{\partial x_i} + \frac{\partial p}{\partial x_i} - \frac{\partial \tau_{ij}}{\partial x_j} - f_i = 0 \tag{2.79}$$

The only external volume force f_i in catalytic reactors, gravity, is also negligible and not considered in the simulations, while p is given by the static pressure and the stress tensor τ_{ij} is given for Newtonian fluids by:

$$\tau_{ij} = \mu \left(\frac{\partial u_i}{\partial x_j} + \frac{\partial u_j}{\partial x_i} \right) + \left(\kappa_\mu - \frac{2}{3}\mu \right) \delta_{ij} \frac{\partial u_k}{\partial x_k} \tag{2.80}$$

with the bulk viscosity κ_μ, which is zero at the given low flow velocities, and the Kronecker delta δ_{ij} [203]. The dynamic viscosity of the mixture μ is calculated according to Equation 2.81.

$$\mu = \sum_s \frac{X_s \mu_s}{\sum_t X_t \phi_{st}} \tag{2.81}$$

$$\text{with: } \phi_{st} = \frac{\left[1 + \left(\frac{\mu_s}{\mu_t} \right)^{1/2} \left(\frac{M_t}{M_s} \right)^{1/4} \right]^2}{\left[8 \left(1 + \frac{M_s}{M_t} \right) \right]^{1/2}} \tag{2.82}$$

The mole fraction of a species s is given by X_s and M_t denotes the molar mass of a species t. The dynamic viscosity of a species μ_s is given according to the kinetic theory of gases by Equation 2.83.

$$\mu_s = 2.67 \cdot 10^{-6} \frac{\sqrt{M_s T}}{\sigma^2 \Omega_{st}}. \tag{2.83}$$

Values for the collision integral Ω_{st} are tabulated [204] and depend on the reduced temperature T^*:

$$T^* = \frac{T k_\mathrm{B}}{\varepsilon} \tag{2.84}$$

with the temperature T and the Boltzmann constant k_B. The interaction well depth ε_{st} is calculated according to Equation 2.85.

$$\varepsilon_{st} = \sqrt{\varepsilon_s \varepsilon_t} \tag{2.85}$$

The interaction parameter that describes the collision cross section of two molecules σ_{st} in Equation 2.83 is given by the following expression [204]:

$$\sigma_{st} = \frac{1}{2} \left(\sigma_s + \sigma_t \right) \tag{2.86}$$

The conservation of species is defined according to Equation 2.87, adding a total of N_g conservation equations, one for each species [203].

$$\frac{\partial\left(\rho \cdot u_j \cdot w_s\right)}{\partial x_j} + \frac{\partial j_{s,j}}{\partial x_j} = 0 \tag{2.87}$$

w_s denotes the mass fraction of a species s and $j_{s,j}$ the mass flow of species s in the direction j according to the Maxwell-Stefan equation:

$$j_{s,j} = \sum_{t=1}^{N_\mathrm{g}-1} -\rho \frac{w_s}{X_s} \cdot D_{st} \frac{\partial X_s}{\partial x_j} + \frac{D_{\mathrm{T},s}}{T} \frac{\partial T}{\partial x_j}. \tag{2.88}$$

The relation between the molar fraction X_s and the mass fraction Y_s is given by Equation 2.89 [203].

$$X_s = \frac{1}{\sum_{t=1}^{N_\mathrm{g}} \frac{w_t}{M_t}} \frac{w_s}{M_s} \tag{2.89}$$

According to Chapman and Enskog the binary diffusion coefficient D_{st} used in Equation 2.88 is given by Equation 2.90 following the kinetic theory of gases [204].

$$D_{st} = 0.00186 \frac{\sqrt{T^3 \left(\frac{1}{M_s} + \frac{1}{M_t}\right)}}{p \sigma_{st}^2 \Omega_{st}} \tag{2.90}$$

The thermal diffusion coefficient $D_{\mathrm{T},s}$ can be calculated from the following empirical equation:

$$D_{\mathrm{T},s} = -2.59 \cdot 10^{-7} T^{0.659} \left[\frac{M_s^{0.511} X_t}{\sum_{t=1}^{N} M_s^{0.511} X_t} - w_t\right] \cdot \left[\frac{\sum_{t=1}^{N} M_s^{0.511} X_t}{\sum_{t=1}^{N} M_s^{0.489} X_t}\right] \tag{2.91}$$

Changes in the temperature along the reactor are taken into account by considering the conservation of energy [203].

$$\frac{\partial\left(\rho \cdot u_j \cdot h\right)}{\partial x_j} - u_j \frac{\partial p}{\partial x_j} - \frac{\partial}{\partial x_j}\left(\lambda_\mathrm{therm} \frac{\partial T}{\partial x_j}\right) + \frac{\partial}{\partial x_j} \sum_{s}^{N_\mathrm{g}} h_s \cdot j_{s,j} + \tau_{jk} \frac{\partial u_j}{\partial x_k} - HS = 0 \tag{2.92}$$

The specific enthalpy h of the gas mixture is obtained from the enthalpies of the single species according to the following two expressions:

$$h = \sum_{s}^{N_\mathrm{g}} w_s \cdot h_s(T) \tag{2.93}$$

$$h_s(T) = h_s\left(T_\mathrm{ref}\right) + \int_{T_\mathrm{ref}}^{T} c_{\mathrm{p},s}\ \mathrm{d}T \tag{2.94}$$

Since there are no absolute values for the enthalpy of a species, the changes relative to a reference state, in this case $T_\mathrm{ref} = 298.15$ K, are calculated using the specific heat capacities $c_{\mathrm{p},s}$. Typically the specific heat capacity of a species $c_{\mathrm{p},s}$ is calculated from a NASA polynomial function taken from the GRI-Mech 3.0 mechanism [205].

$$c_{\mathrm{p},s}(T) = A_1 + A_2 \cdot T + A_3 \cdot T^2 + A_4 \cdot T^3 + A_5 \cdot T^4 \tag{2.95}$$

By weighting the specific heat capacities according to their mass fractions, the heat capacity of the mixture c_p is determined.

$$c_\mathrm{p} = \sum_{s} w_s c_{\mathrm{p},s} \tag{2.96}$$

The thermal conductivity of the mixture λ_therm, required for solving Equation 2.92, is calculated according to the kinetic theory of gases from the thermal conductivities of the single species by the following equations using the universal gas constant R.

$$\lambda_\mathrm{therm} = \sum_{s} \frac{X_s \lambda_{\mathrm{therm},s}}{\sum_t X_t \phi_{st}} \tag{2.97}$$

$$\lambda_{\mathrm{therm},s} = \frac{15}{4}\frac{R}{M_s}\mu_s \left[\frac{4}{15}\frac{c_{\mathrm{p},s} M_s}{R} + \frac{1}{3}\right] \tag{2.98}$$

For solid phase regions only the heat transport by conduction and further heat sources HS, that include thermal radiation, are considered simplifying Equation 2.92 to the following expression:

$$-\frac{\partial}{\partial x_j}\left(\lambda_{\text{therm}}\frac{\partial T}{\partial x_j}\right) = HS. \tag{2.99}$$

Finally, the static pressure is calculated according to the ideal gas law [203].

$$p = \frac{\rho \cdot R \cdot T}{\sum_{s=1}^{N_\text{g}} X_s \cdot M_s} \tag{2.100}$$

The reactions at the catalyst surface are integrated into the model as boundary conditions of the species balances. The reaction rate R_s^{het} is given by the product of the molar weight M_i and the net production rate of a species $\dot{s}_s$.

$$R_s^{\text{het}} = M_s \dot{s}_s \tag{2.101}$$

$$\dot{s}_s = \sum_{k=1}^{K_\text{s}} \nu_{s,k} \cdot k_{\text{f}_k} \prod_{t=1}^{N_\text{g}+N_\text{s}} c_{s,t}^{\nu'_{tk}} \tag{2.102}$$

For the calculation of the net production rate of a species $\dot{s}_s$ the mean-field approximation is applied, viz. mean surface coverages and hence, mean surface concentrations of an adsorbate $c_{s,t}$ are used along a computational cell. The surface concentrations $c_{s,s}$ are calculated from the product of the total surface site density Γ and the surface coverage of a species θ_s.

$$c_s = \theta_s \Gamma \tag{2.103}$$

The reaction rate constant of a reaction k_{f_k} is calculated from the Arrhenius equation using the pre-exponential factor A_k, the temperature exponent β_k, the universal gas constant R and the activation energy of a reaction $E_{\text{a},k}$.

$$k_{\text{f}_k} = A_k T^{\beta_k} exp\left(\frac{-E_{\text{a},k}}{RT}\right) \tag{2.104}$$

The set of surface reactions and the required kinetic parameters are taken from the respective microkinetic model of the reaction, in this work the model by Krähnert and Baerns (see Section 2.3.2).

In steady state the molecules produced or consumed at the surface according to the reaction rate R_s^{het} need to be transported towards or away from the catalyst

surface, with $\vec{n}$ as the outward pointing unit vector that is normal to the catalyst surface.

$$\vec{n}\left(\vec{j}_{s,j}\right) = R_s^{\text{het}}. \tag{2.105}$$

This finishes the set of governing equations that form, together with boundary and inlet conditions, the mathematical model of the reactor. In CFD simulations a solution of this mathematical model is calculated. Since the model contains partial differential equations (PDE)s, for which analytical solutions are in most cases not available, a numerical approach is used to solve the equations [203]. The first step of the numerical approach is the discretization of the PDEs. In CFD simulations typically finite volumes are used in this discretization step, yielding a set of algebraic equations that approximate the PDEs at discrete points in space [206]. In the second step the geometric domain of the system, in this case the heterogeneous catalytic reactor, is divided into several control volumes, creating the numerical mesh. The discretized algebraic equations are defined in each specific point of this numerical mesh. Thirdly, finite approximations for surface and volume integrals in the finite volumes as well as gradients and interpolation between grid points are defined. Finally, the solution for the obtained set of algebraic equations is calculated in an iterative process until the convergence criteria are fulfilled [203, 206].

3 Materials and Methods

In this chapter, the material and methods used in this work are introduced. In the first section details on the measurements, conducted in the profile reactor, are presented. Secondly, the analytical procedure used for gas sample analysis via mass spectrometry is explained. In the final section the settings and models of the CFD simulations, used to validate the experimental results, are presented.

3.1 Experimental Details

In this work, a profile reactor was designed and built to study ammonia oxidation under industrial conditions (reactor details shown in Chapter 4). In the following section details on the experiments, conducted in the profile reactor, are presented.

A major influencing factor of industrial ammonia oxidation is the restructuring of the platinum gauze catalyst (see Section 2.4.2). The initially smooth wires reconstruct considerably forming fractal structures, shaped like cauliflowers, at the surface. Since the restructuring leads to a considerable change in available surface area and strongly influences the reaction performance, measurements should be conducted with a restructured catalyst. Thus, the restructuring behavior in the profile reactor was studied in an initial study to determine reaction conditions and aging times required to produce considerably restructured catalyst gauzes. In this catalyst aging campaign stacks of ten woven gauzes made of a platinum-rhodium alloy with a rhodium content of 5 wt.% were used. The gauzes were aged for five different aging times of 1, 10, 24, 50, and 100 hours. No profile measurements were performed during the aging campaign. The reactor was operated at an inlet temperature of $T_{in} = 300$ °C, a pressure of $p_r = 5$ bara, a feed gas composition of $x_{NH_3} = 0.10$, $x_{O_2} = 0.186$, nitrogen as ballast medium and an ammonia loading of 10 $\frac{\text{t N in NH}_3}{\text{m}^2\ \text{d}}$. After aging, SEM pictures of the gauzes were taken by Dr. rer.

nat. Tobias Krekeler at the Betriebseinheit Elektronenmikroskopie BEEM at the Hamburg University of Technology TUHH. The results of the aging campaign are discussed in Section 7.1.

In the first profile measurements another side effect of the catalyst restructuring was observed. The transport of volatile platinum species to the sampling capillary led to the formation of a catalytic active coating on and inside the sampling capillary. The influence of this capillary coating was analyzed by profile measurements at two different oxygen inlet molar fractions of $x_{O_2} = 0.15$ and $x_{O_2} = 0.40$. The reactor was operated at an inlet temperature of $T_{in} = 300$ °C, a pressure of $p_r = 1$ bara, an ammonia loading of 10 $\frac{\text{t N in NH}_3}{\text{m}^2\ \text{d}}$, with nitrogen as ballast medium, an ammonia molar fraction of $x_{NH_3} = 0.10$ and an argon molar fraction of $x_{Ar} = 0.02$. A single knitted gauze made of a platinum-rhodium alloy with a rhodium content of 5 wt.% was used as catalyst. The profile measurements were conducted with capillary movement in both axial directions starting with the sampling orifice upstream of the gauze. Subsequently, the sampling orifice was slowly moved downstream of the gauze and afterward, slowly back upstream of the gauze. The resulting temperature and concentration profiles are discussed in Section 7.2. The MBMS was operated using the first parameter set (see Section 3.2.3).

After characterizing the restructuring process and the capillary coating process, three profile measurement campaigns were conducted using the same single woven pure platinum gauze with wire diameters of $d_w = 90$ μm and wire spacings of 500 μm in all three campaigns. In the first measurement campaign, the influence of the oxygen concentration on the reaction performance was studied for five oxygen inlet molar fractions of $x_{O_2} = 0.10$, 0.15, 0.186, 0.25, 0.3, and 0.4. In the second and third measurement campaign the inlet temperature was varied from $T_{in} = 100$, 150, 200, 250, and 300 °C. A pyrometer fiber was tip aligned with the sampling orifice in the second campaign and a thermocouple was installed in the sampling capillary of the first and third campaigns. The platinum gauze was preaged in total for 48 hours prior to the first profile measurement campaign, 76 h prior to the second campaign and 90 hours prior to the third campaign. In all three measurement campaigns the reactor was operated at a pressure of $p_r = 5$ bara, with an ammonia inlet molar fraction of $x_{NH_3} = 0.10$ and an ammonia loading of 10 $\frac{\text{t N in NH}_3}{\text{m}^2\ \text{d}}$. Two volumetric percent of argon were dosed as internal standard. In

the oxygen influence campaign the inlet temperature was set to $T_{in} = 200$ °C and in the temperature influence campaigns oxygen inlet molar fractions of $x_{O_2} = 0.186$ were used. An altered procedure was applied in all three profile measurement campaigns to minimize the residence time of the orifice near the catalyst gauze and thus, to prevent capillary coating (see Section 7.2). The sampling orifice was positioned upstream of the catalyst gauze at the beginning of a measurement. Subsequently, the sampling orifice was moved relatively fast downstream of the gauze. The actual profile was recorded while moving the sampling orifice back up to the initial position upstream of the gauze. The MBMS was operated for all three campaigns using the second parameter set (see Table 3.2 in Section 3.2.3). To reach steady state, the reactor was operated at the first studied operation conditions for two hours before the first profile measurement of a campaign was started. After changing the oxygen concentration or the inlet temperature, respectively, the reactor was operated at constant conditions for one hour to reach steady state, before the next profile measurement was started.

3.2 Molecular Beam Mass Spectrometer

The gas phase composition of the sampled stream was analyzed using a mass spectrometer (MS) with a molecular beam inlet system. In this chapter, the components of the setup are presented first followed by details of the MS data analysis and calibration.

3.2.1 Molecular Beam Mass Spectrometer Setup

The setup used for gas analysis in this work consists of a HAL 4 EPIC low energy MS by Hiden Analytical (Warrington, United Kingdom) with an in-house designed and built heated molecular beam inlet system. A picture and a schematic sketch of the MBMS system are shown in Figure 3.1. The MBMS is composed of two ultra high vacuum chambers. In the first chamber the molecular beam inlet system is placed, while the second chamber houses the MS components like the electron impact ionizer, the quadrupole, and the secondary electron multiplier detector. A TC600 turbomolecular pump (Pfeiffer Vacuum GmbH, Asslar, Germany) is used

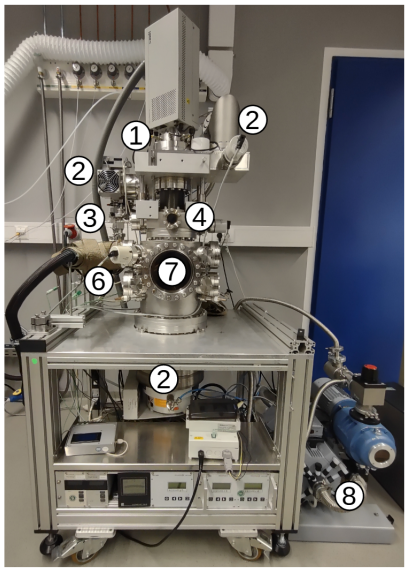

① Detector

② Turbomolecular pumps

③ Inlet ionization chamber

④ Ion source & quadrupole

⑤ Skimmer

⑥ Heated inlet

⑦ Molecular beam inlet

⑧ Roots pump

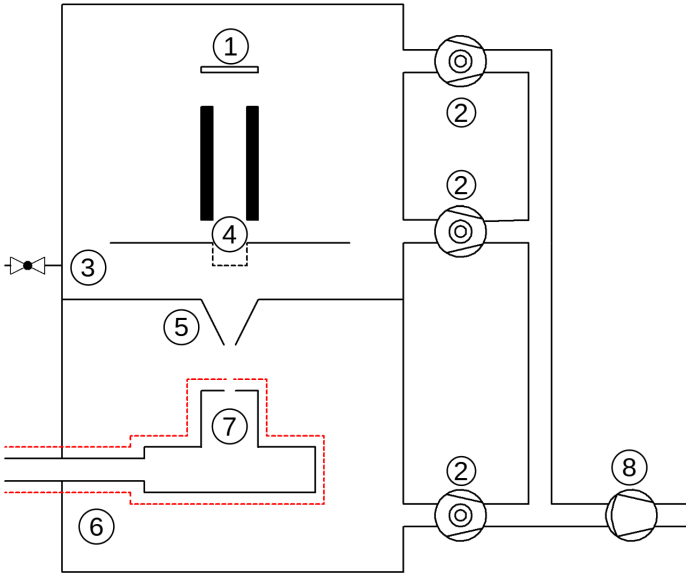

Figure 3.1: Picture and schematic sketch of the MBMS system used for gas sample analysis

to evacuate the molecular beam inlet vacuum chamber and two TMU 261 turbomolecular pumps (Pfeiffer Vacuum GmbH) are used to evacuate the ionization chamber. A corrosion resistant roots pump (RP 35C Vario by vacuubrand GmbH & Co. KG, Wertheim, Germany) is used as pre-vacuum pump.

The MBMS has two different gas inlet systems incorporated. Firstly, a molecular beam inlet system heatable to 200 °C, preventing the formation of ammonium nitrate and reducing the rate of nitric oxide oxidation to nitric dioxide. The molecular beam is generated using a nozzle with a diameter of 100 μm. Through a skimmer a fraction of the gas, that forms the molecular beam, is entering the second vacuum chamber in line of sight with the ion source. The molecular beam inlet was used for all profile measurements presented in this thesis. Alternatively to the molecular beam inlet, sampling streams with low flow rates can be directly dosed effusively into the ionization chamber. Detailed information on the theoretical background of molecular beams and mass spectrometry are given in Section 2.6.

3.2.2 Analysis of Mass Spectrometer Data

The molar flow rates of the gas samples were determined using a MBMS. A basic assumption for MS signal analysis is that the contribution of a species s to the measured peak intensity $I_{s,m/z}$ at the evaluated mass-to-charge ratio m/z is proportional to the molar flow of the ionized species hitting the MS detector and hence, proportional to the molar flow rate of the species entering the MS $I_{s,m/z} \propto \dot{n}_s$. Quantification of the peaks can then be achieved using an inert species with a known inlet concentration as an internal standard. In this project argon, having its main peak at $m/z = 40$, was used as the internal standard. The molar flow rates of all other species are quantified using calibration factors $CF_{s,m/z}$.

$$CF_{s,m/z} = \frac{I_{s,m/z} \cdot \dot{n}_{\mathrm{Ar}}}{I_{\mathrm{Ar},40} \cdot \dot{n}_s} \tag{3.1}$$

Details of the calibration process to determine the calibration factors $CF_{s,m/z}$ are described in Section 3.2.3. All measurements in this work were carried out in the analog scan mode of the MS and the measured peaks were integrated using the trapezoidal rule.

In the first step of the data evaluation, relative signals are calculated by determining the ratio of the measured signal intensities at a given m/z ratio and the signal intensity of argon $\frac{I_{s,m/z}}{I_{\mathrm{Ar},40}}$. At every axial position of a profile measurement at least two, usually three, analog scan cycles were measured and the averaged relative signals at the positions were calculated. In Table 3.1 the evaluated mass-to-charge ratios m/z of the quantified species are listed.

Table 3.1: Analyzed mass-to-charge ratios m/z used for the quantitative analysis of the sampling flow. Main m/z-ratio used for quantification of each species in bold letters

Species	Analyzed m/z-ratios
Ar	**40**
N_2	**28**
N_2O	**44**, 28, 30
NO_2	**46**, 30
NO	**30**
NH_3	**17**
O_2	**32**

For the quantification of NH_3 threshold ionization was utilized. An additional analog scan at an electron energy of 15 eV was carried out following the analog scan at the standard electron energy of 70 eV. At 15 eV only NH_3^+ but no OH^+, resulting from water dissociation, is formed (see Section 2.6.2), allowing to directly measure a pure NH_3 peak, that was used for quantification.
The fragmentation patterns of the species N_2O and NO_2 overlap with the main peaks used for quantification of N_2 at $m/z = 28$ and NO at $m/z = 30$. These fragmentation peak contributions were calculated according to Equation 3.2 and afterwards, subtracted from the total measured peak intensities yielding the corrected, averaged relative main signal peaks at $m/z = 28$ and $m/z = 30$.

$$I_{s,\mathrm{frag}} = I_{s,\mathrm{main}} \cdot \frac{CF_{s,\mathrm{frag}}}{CF_{s,\mathrm{main}}} \tag{3.2}$$

Furthermore, signal contributions of CO_2 from air were subtracted from the relative peaks at $m/z = 44$. For this firstly, an average of the relative peaks at $m/z = 44$ at the first three positions of each profile measurement (upstream of the

gauze) was determined, and subsequently, this relative contribution was subtracted from the measured relative signals at $m/z = 44$ at all positions of the analyzed profile measurement.
The molar flow rates of all analyzed species at all positions p were then calculated using the corrected, averaged relative main signal peaks obtained by factoring in the contributions of CO_2 and fragments of N_2O as well as NO_2.

$$\dot{n}_{s,p} = \dot{n}_{\mathrm{Ar}} \cdot \frac{I_{s,\mathrm{main},p}}{I_{\mathrm{Ar},40,p}} \cdot \frac{1}{CF_{s,\mathrm{main}}} \tag{3.3}$$

Using the molar flow rates of the species, the ammonia conversion $C_{\mathrm{NH_3},p}$, the nitric oxides selectivity $S_{\mathrm{NO_x},p}$ and yield $Y_{\mathrm{NO_x},p}$, as well as the nitrous oxide selectivity $S_{\mathrm{N_2O},p}$ and yield $Y_{\mathrm{N_2O},p}$ were calculated for all positions p according to the Equations 3.4 - 3.8.

$$C_{\mathrm{NH_3},p} = \frac{\dot{n}_{\mathrm{NH_3,inlet}} - \dot{n}_{\mathrm{NH_3},p}}{\dot{n}_{\mathrm{NH_3,inlet}}} \tag{3.4}$$

$$S_{\mathrm{NO_x},p} = \frac{\dot{n}_{\mathrm{NO},p} + \dot{n}_{\mathrm{NO_2},p}}{\dot{n}_{\mathrm{NH_3,inlet}} - \dot{n}_{\mathrm{NH_3},p}} \tag{3.5}$$

$$Y_{\mathrm{NO}_x,p} = \frac{\dot{n}_{\mathrm{NO},p} + \dot{n}_{\mathrm{NO_2},p}}{\dot{n}_{\mathrm{NH_3,inlet}}} \tag{3.6}$$

$$S_{\mathrm{N_2O},p} = \frac{2 \cdot \dot{n}_{\mathrm{N_2O,inlet}}}{\dot{n}_{\mathrm{NH_3,inlet}} - \dot{n}_{\mathrm{NH_3},p}} \tag{3.7}$$

$$Y_{\mathrm{N_2O},p} = \frac{2 \cdot \dot{n}_{\mathrm{N_2O,inlet}}}{\dot{n}_{\mathrm{NH_3,inlet}}} \tag{3.8}$$

For comparison with CFD simulations the conversion, yields, and selectivities were averaged over the last three positions downstream of the gauze.

3.2.3 Calibration of the Mass Spectrometer

The calibration factors $CF_{s,m/z}$ required for the quantitative analysis of the measured mass spectra were calculated according to Equation 3.1 for all characteristic fragmentation peaks of the analyzed species listed in Table 3.1.
The species nitrogen, oxygen, and ammonia were newly calibrated for every single profile measurement at the MS settings used also during the measurement. As

calibration mixture the inlet feed entering the profile reactor was used. By positioning the sampling orifice of the capillary upstream of the gauze the feed with known concentrations was sampled. The calibration factors of the three components were then calculated using the measured relative peaks averaged over the first three positions of each profile measurement and the molar flow rates $\dot{n}_{\mathrm{Ar}}$ and $\dot{n}_s$ entering the profile reactor.
Since the feed does not contain the products nitrous oxide, nitric oxide, and nitrogen dioxide these species were calibrated before the profile measurements. The gases were dosed through an additional sampling setup shown in Figure 3.2 using calibrated MFCs from Bronkhorst.

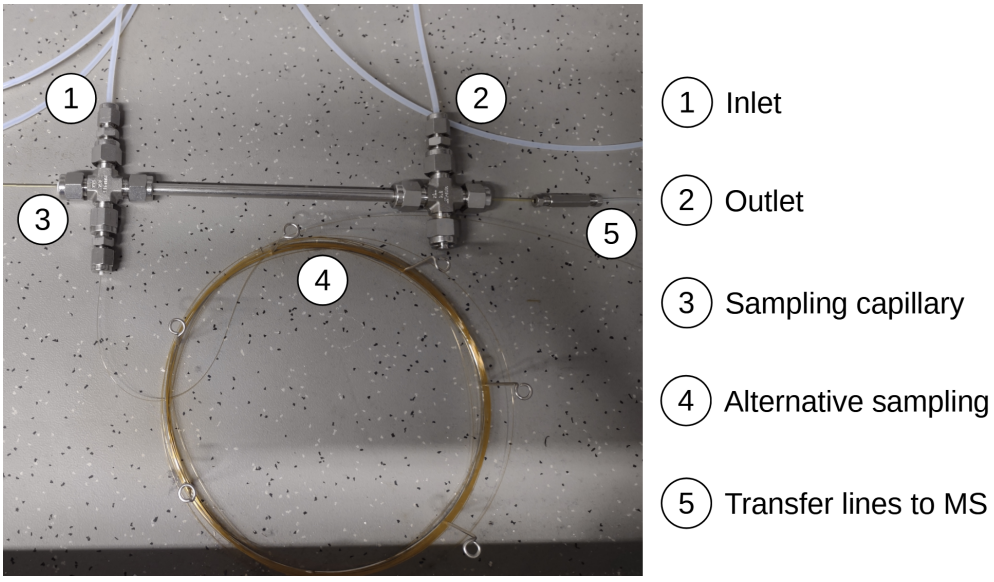

Figure 3.2: Sampling setup used for product calibration

The calibration setup allows calibration with significantly lower total flow rates compared to direct calibration inside the reactor. The sampling process was realized in the same way as in the profile reactor, utilizing a capillary with a 20 μm side sampling orifice. The MS was operated at two different sets of operation parameters (electrode setup see Figure 2.17) listed in Table 3.2 for the different measurements campaigns.

Table 3.2: The two sets of MS parameters used in this work

Parameter	First set	Second set
Mode-change-delay [ms]	50	50
Energy [V]	-2	-2
Focus [V]	-4	-200
Suppressor [V]	-200	-200
Cage [V]	1.6	3
Electron-energy [V]	70 & 15	70 & 15
Emission [μA]	160	10
1-st dynode [V]	-1200	-1200
multiplier [V]	2100	2100

Product calibrations were performed for both MS parameter sets individually. Nitrous oxide and nitric oxide were calibrated in binary mixtures with argon using the gases listed in Table 3.3.

Table 3.3: Purities of the gases used for MS calibration of nitrous oxide and nitric oxide

Species	Purity	Supplier
Nitric oxide	99.0 %	Westfalen
Nitrous oxide	99.999 %	Westfalen
Argon	99.996 %	Westfalen

Nitrogen dioxide was calibrated using a ternary mixture of nitrogen dioxide, nitrogen, and argon. A ternary mixture of nitrogen dioxide was required since nitrogen dioxide is a liquid at room temperature. Therefore, a bottle containing a mixture of 1.994 ± 0.04 vol.% nitrogen dioxide and 2.185 ± 0.044 vol.% argon in nitrogen (Air Liquide Deutschland GmbH, Düsseldorf, Germany) was used as nitrogen dioxide feedstock for the first calibrations. The calibration of nitrogen dioxide was carried out for the second set of MS parameters using a mixture composed of 5 vol.% nitrogen dioxide (purity 99 vol.%) in nitrogen (Westfalen AG). Both gas bottles were supplied at pressures excluding demixing over time allowing to dose nitrogen dioxide in gaseous state at room temperature. The inlet of the MS was heated to 180 °C for the calibration of nitrogen dioxide to prevent

dimerization to dinitrogen tetroxide.

In total at least six different gas compositions were measured in random order for the calibration of nitrous oxide, nitric oxide, and nitrogen dioxide. For every composition at least five scan cycles were measured. The relevant peaks of the measured mass spectra were integrated using the trapezoidal rule and averaged. Subsequently, linear regression of the measured relative signal intensities $\frac{I_{s,m/z}}{I_{\mathrm{Ar},40}}$ to the ratio of the dosed volume flows $\frac{\dot{V}_s}{\dot{V}_{\mathrm{Ar}}}$ was carried out yielding the calibration factors $CF_{s,m/z}$ as slopes of the regression fits. In Figure 3.3 the regression plot of nitric oxide is exemplarily shown for the second MS parameter set. The remaining calibration curves and details on the regression process are provided in Appendix A.1.

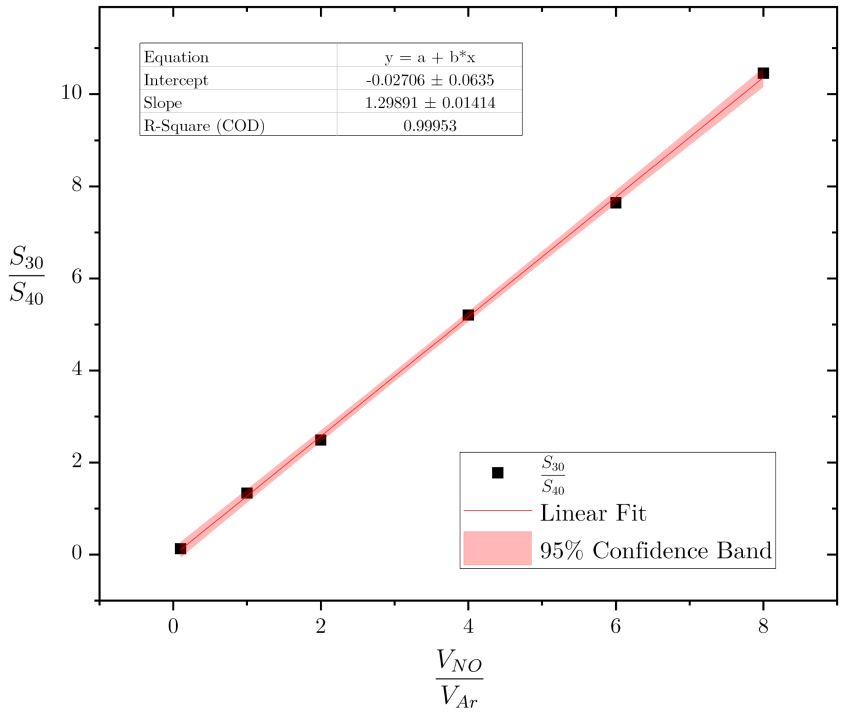

Figure 3.3: Regression plot of nitric oxide for the second MS parameter set. The calibration factor is determined by the regression slope $CF_{\mathrm{NO},30} = 1.29891$

3.3 Computation Fluid Dynamics Simulations

In this work ammonia oxidation is studied experimentally in a profile reactor. To understand the processes inside the profile reactor and to validate the most common surface mechanism of ammonia oxidation, the Kraehnert and Baerns mechanism, CFD simulations were conducted by Anna Sophia Behnecke and Dr. Sven Jakobtorweihen at the institute of chemical reaction engineering at TUHH. The simulations were designed to validate or supplement the conducted experiments in close cooperation by Anna Sophia Behnecke, Dr. Sven Jakobtorweihen, and the author. However, it should be stated clearly, that all CFD simulations shown in this work were performed by Anna Sophia Behnecke and Dr. Sven Jakobtorweihen. The methodology and settings used for the CFD simulations are described in the following section.

3.3.1 Model geometry

CFD simulations are used in this thesis to address two main questions. Firstly, how does the interplay of the sampling process and the steep local concentration gradients influence the measured profiles? Secondly, can the profiles measured in the profile reactor be described by existing microkinetic models of ammonia oxidation? Two different reactor models were designed for this task. In the first reactor model the actual profile reactor including capillary sampling was simulated (in the following "sampling model"), while secondly, an undisturbed reactor without capillary sampling was modeled in the "undisturbed model". In all presented CFD simulations woven pure platinum gauzes were used as catalyst. In a first approach the woven gauze was approximated by interpenetrating, hollow cylinders as gauze wires (in the following "interpenetrating wire model"). In a second more realistic approach the woven catalyst gauze is described by curved wires that run one upon the other ("curved wire model"). Both gauze models were used in both reactor models giving a total of four kinds of model geometries that are described in the following.

Sampling model with interpenetrating wires

To study, how the capillary sampling influences measured concentration profiles and to understand the influencing factors of the spatial resolution of the capillary sampling technique, a first simplified model system was used. In this model the flow domain of the reactor was reduced to a cylinder in the center of the reactor with a height of h_r =4 mm and a diameter of d_r = 5 mm compared to the actual profile reactor dimensions with diameters of $d_r = 12 - 18$ mm and maximum reaction zone lengths of up to $h_r = 60$ mm. A smaller flow domain was used to reduce the computational demand of the simulations. As shown in Figure 3.4 a woven gauze is positioned perpendicular to the flow direction at the mid height of the reactor.

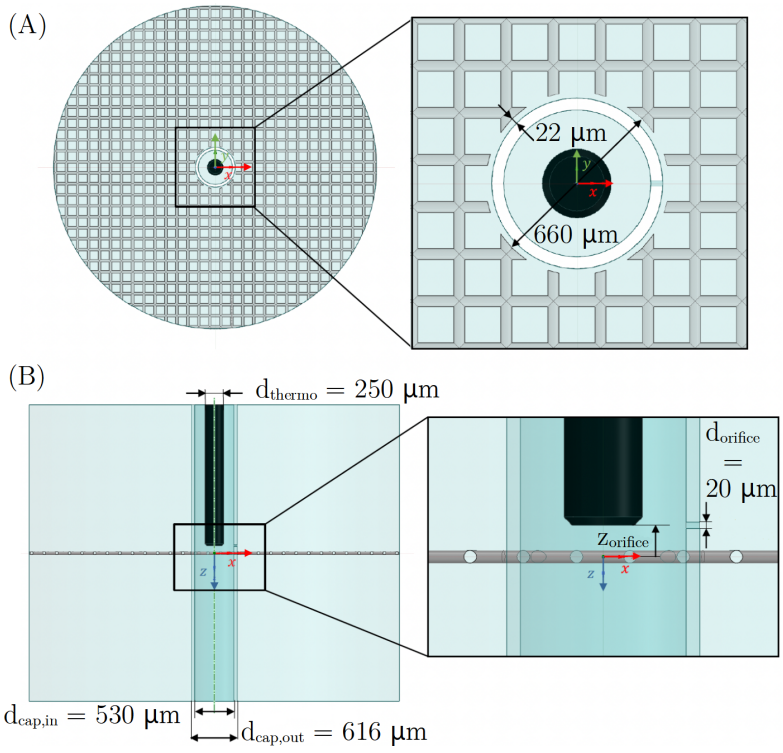

Figure 3.4: Cross sectional views of the xy-plane (A) and the xz-plane (B) of the sampling model geometry with interpenetrating wires for the orifice position $z = -0.1$ mm. On the right side a magnification of the center region including the sampling capillary is shown. Figure from [207]

In this first model the interpenetrating wire model was used. The wires of the gauze were modeled as interpenetrating, hollow cylinders with a Pt surface on the outside. Due to the hollow nature of the wires, heat transport inside the wires by conduction was neglected. The wires had a diameter of $d_{\mathrm{w}} = 40$ μm and a spacing between two wire centers of 170 μm. In the center of the gauze a hole with a diameter of 660 μm was extracted, allowing to fit the sampling capillary through the gauze. The sampling capillary ran through the center of the xy-plane over the whole height of the reactor domain. The capillary was dimensioned according to the sampling capillary used in the experiments with an outer diameter of $d_{\mathrm{cap,out}} = 616$ μm and an inner diameter of $d_{\mathrm{cap,inner}} = 530$ μm. In the utilized configuration the minimum distance between catalyst gauze and the sampling capillary was 22 μm. The capillary had a 20 μm sized orifice through which gas can be sampled. Tip-aligned with the orifice center a thermocouple with a diameter of $d_{\mathrm{thermo}} = 250$ μm was placed in the center of the sampling capillary. To reduce computational demand, the calculation domain was cut in half along the xz-plane as symmetry plane.

In a profile measurement the sampling capillary, and hence the sampling orifice, is moved up and down the reactor. To include the orifice movement, a total of eleven reactor geometries with varying axial orifice positions z_{orifice} were created with the sampling model with interpenetrating wires. The concentrations at the capillary outlet of these eleven orifice positions yield the simulated sampled concentration profiles.

Undisturbed reactor model with interpenetrating wires

Using the undisturbed reactor model with interpenetrating wires the axial concentration profiles inside a reactor with no capillary sampling were simulated. These profiles were used to validate the invasivity of the sampling process by comparing the undisturbed profiles with the sampled profiles simulated with the sampling model with interpenetrating wires. In contrast to the sampling model no sampling capillary was included in the undisturbed model, hence, also no hole was cut into the catalyst gauze. The catalyst wire diameter and spacing as well as the dimensions of the flow domain match the geometry of the sampling model with

interpenetrating wires as shown in the sketch of the undisturbed reactor geometry in Figure 3.5. To reduce computational effort, applying symmetry, only one fourth of the geometry was used.

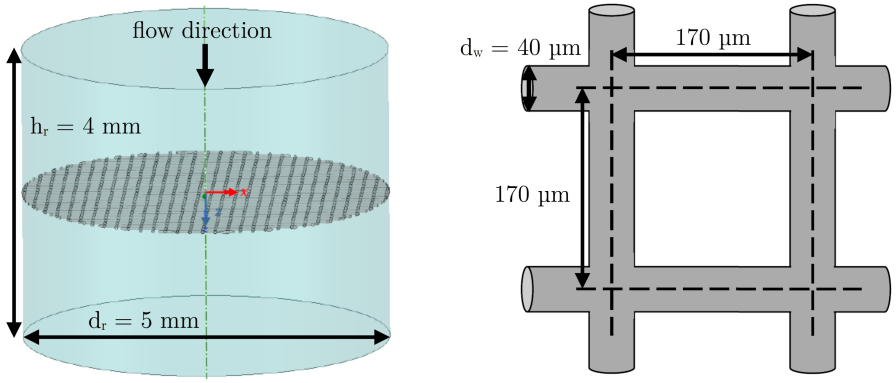

Figure 3.5: Geometry of the undisturbed reactor model with interpenetrating wires and sketch of the woven gauze made of interpenetrating wires. Adopted and changed from [208]

Undisturbed models with curved wires

The second set of reactor geometries was modeled using more realistic woven platinum gauzes composed of curved wires. The curved wires are modeled as solid platinum allowing to include heat transport phenomena in the wires. Since the crossing points of two wires are challenging to mesh, the gaps modification strategy according to [209] was used. The curvature of the wires was modified such that a gap of 2 μm was created in between two wires at the crossing points. In Figure 3.6 two detailed views of wires used in the curved wires model are shown.

Two different woven gauze geometries were modeled with the undisturbed model with curved wires. The first gauze had typical specifications of woven gauzes used in industry with wire diameters of $d_w = 76$ μm and wire spacings of 312.5 μm. The second gauze had the same specifications as the gauze used in the profile reactor measurements with wire diameters of $d_w = 90$ μm and wire spacings of 500 μm. To reduce the computational demand with the more complex gauze geometry, the reactor was modeled using a slightly smaller flow domain with a height of h_r =4 mm and a diameter of $d_r = 3.75$ mm. To simplify meshing, a gap of 20 μm was created

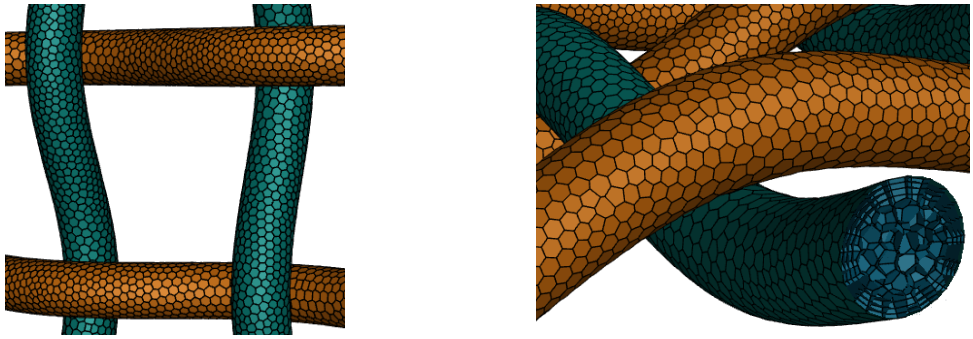

Figure 3.6: Detailed views of the curved wire gauze model. As shown in the cut on the right, the wires were modeled as solids composed of multiple cell layers. Figure from [207]

between the gauze and the outer edge of the flow domain. The resulting cut wire front ends were set inert. No symmetry was used in the simulations.

Sampling models with curved wires

To study the influence of the wire to gauze spacing and the influence of capillary coating a sampling model using a gauze made of curved wires was used. In this model a solid, woven gauze with wire diameters of $d_{\mathrm{w}} = 76$ μm and wire spacings of 312.5 μm was utilized. Two wire crosses were extracted from the gauze to fit the sampling capillary through, allowing to simulate profile measurements with large orifice to wire spacings. A sampling capillary with an outer diameter of $d_{\mathrm{cap,out}} = 520$ μm, an inner diameter of $d_{\mathrm{cap,inner}} = 434$ μm and a sampling orifice with a diameter of 20 μm was placed in direct contact with one wire cross as shown in Figure 3.7.

Two different azimuthal capillary rotation angles were used. In the first rotation the sampling orifice is directed towards the gauze (Figure 3.7a) and in the second rotation the sampling orifice is directed towards the gap, created by extracting a second wire cross (Figure 3.7b). To simulate the profile measurement process, geometries with varying axial orifice positions z_{orifice} were created. For the configuration with orifice rotation towards the gauze a total of eleven and for orifice rotation towards the gap a total of seven geometries were used. The dimensions of the flow domain matched the dimensions of the undisturbed curved wire model with a height of $h_{\mathrm{r}} =$4 mm and a diameter of $d_{\mathrm{r}} = 3.75$ mm.

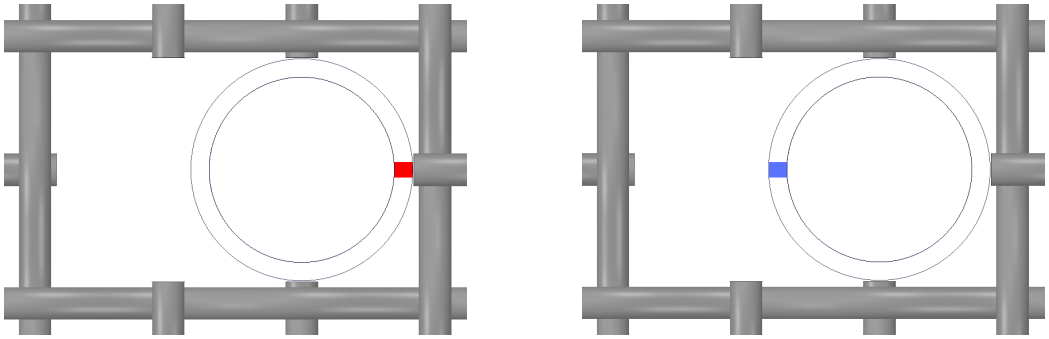

(a) Sampling orifice at the gauze **(b)** Sampling orifice at the gap

Figure 3.7: Sketch of the sampling capillary region of the sampling models with curved wires for two different azimuthal capillary rotation angles. Figures from [207]

3.3.2 Meshing

Both the fluid and solid regions of the domain were modeled using meshes made of polyhedral cells. To enable an accurate description of the transport processes in regions with steep gradients a locally refined mesh is required. This was achieved by manually defining bodies of influence (BOI)s in regions with steep gradients. For each BOI a predefined main mesh size, characterized by the edge length of a cell, was used. The first BOI was defined for the reaction zone around the catalyst gauze, with locally high concentration and temperature gradients, and multiple BOIs were defined in the vicinity of the sampling orifice, where drastic changes in the flow regime occur. At the interfaces between fluid and solid regions, as well as between fluid and walls of the flow domain, three layers of prism cells were used to ensure accurate resolution of near-wall gradients. The mesh was refined iteratively till mesh independence was achieved. Mesh independence studies of the interpenetrating wire models are documented in [208]. The final meshes of the interpenetrating wire models are composed of 1,914,115 cells for the undisturbed model and in the range of 2.7 million cells for the sampling models. The meshes of the undisturbed curved wire models are composed of 2,588,272 cells for the gauze with wire diameters of $d_w = 76$ μm and 1,95,814 cells for the gauze with wire diameters of $d_w = 90$ μm. The meshes of the sampling model with curved wires are composed of about 3.8 million cells.

3.3.3 Simulation Details

Prior to conducting CFD simulations, first the boundary conditions of the system need to be defined. In Figure 3.8 the used boundary conditions are shown exemplarily for the sampling model with interpenetrating wires.

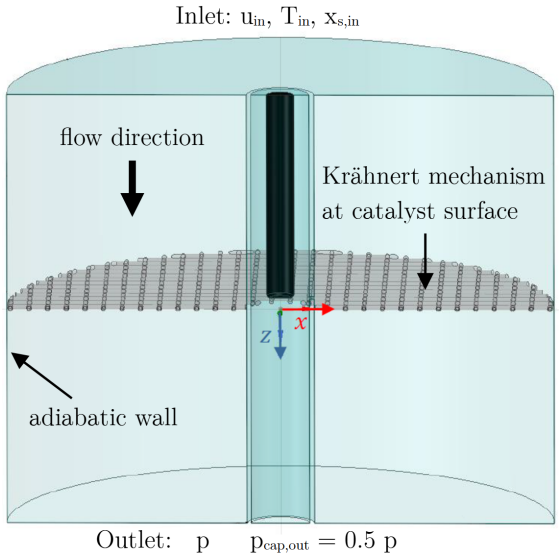

Figure 3.8: Boundary conditions defined in the sampling model. Adopted and changed from [208]

At the inlet of the flow domain the flow velocity in axial direction u_{in}, the temperature T_{in} and the molar fractions $x_{s,\text{in}}$ were defined. To model the heterogeneously catalyzed surface reactions the Kraehnert and Baerns mechanism (see Section 2.3.2) was implemented by means of boundary conditions for species fluxes at the gauze surface. For both surface sites in the Kraehnert and Baerns model a site density of $2.7063 \cdot 10^{-9}$ $\frac{\text{mol}}{\text{cm}^2}$ was used. Homogeneous reactions in the gas phase were neglected. At the reactor outlet the pressure p and at the sampling capillary outlet the pressure $p_{\text{cap,out}} = 0.5 \cdot p$ were defined, resulting in choked flow inside the sampling orifice (see Section 5.1). The no-slip boundary condition was applied to all solid walls (sampling capillary and catalyst gauze) in the modeling domain. No heat was transported through the virtual outer wall of the modeling domain making it adiabatic. At the symmetry planes, used in the interpenetrating wire models, all gradients normal to the symmetry plane were set to zero.

The sampling capillary was modeled as a solid hollow cylinder made of fused silica and the wires in the curved wire models were modeled as solid platinum. Heat transport via conduction in the solids and heat transfer from solid to fluid and vice versa were included using constant thermal properties (density of fused silica $\rho_{\text{silica}} = 2,201\,\text{kg/m}^3$, thermal conductivity of fused silica $\lambda_{\text{silica}} = 2.68\,\text{W/(m·K)}$, specific heat capacity of fused silica $c_{\text{p,silica}} = 1052\,\text{J/(kg·K)}$ [210], density of platinum $\rho_{\text{pt}} = 21,450\,\text{kg/m}^3$, thermal conductivity of platinum $\lambda_{\text{pt}} = 76.6\,\text{W/(m·K)}$ and specific heat capacity of platinum $c_{\text{p,pt}} = 148\,\text{J/(kg·K)}$ [41,211]). To calculate gas phase transport properties, physical parameters from the GRI-Mech 3.0 mechanism were used for the curved wire models [205]. For the interpenetrating wire models physical properties from the Chemkin thermochemistry database according to Table A.1 in the Appendix A.2 were used.

In all simulations, the reactor was simulated in steady state using laminar flow conditions. The utilized, underlying governing equations are presented in detail in Section 2.8. Heat transport via radiation was neglected since it was shown in literature, that radiation only has a minor impact on ammonia oxidation, but significantly increases computational demand [11].

Finite volume was used as the discretization method. The pressure-based pseudo-transient solver was used with a coupled-algorithm for pressure-velocity-coupling, due to its robust and efficient implementation in Fluent. The least squares cell-based method was used for discretization of gradients and the second-order upwind scheme was used for spatial discretization of pressure, momentum, and species. No explicit chemistry solver was used. After every simulation mass and atom balances were checked. A simulation was considered final as soon as all convergence criteria in the form of residuals were fulfilled. The residuals of the continuity and momentum balances in all three space directions, as well as all species transport equation, were set to 10^{-4}. The residual for conservation of energy was set to 10^{-6}. An additional convergence criterion for the nitric oxide flow at the outlet was defined with a residual of 10^{-5} to ensure that the overall mass and atom balances were fulfilled.

The actual simulations were divided into a two step process to improve the stability of the solution and to facilitate convergence. At first, the flow field through the reactor was calculated with disabled reactions and using constant catalyst

temperatures in the range of $650 - 1000$ K, depending on the simulation. In the second step, surface reactions were activated and the catalyst temperature was set as variable. Despite this two step process, reaching a converged solution is still challenging and time demanding, especially if capillary sampling is considered.

Meshing and simulations with the interpenetrating wire models were conducted using ANSYS Fluent 2019R1, while ANSYS Fluent 2021R2 was used for meshing and simulations with the curved wire models.

4 Profile Reactor for Ammonia Oxidation under Industrial Conditions

The aim of this thesis is the development of an experimental setup to study ammonia oxidation under industrial conditions that allows gaining a deeper understanding of the underlying processes and mechanisms of the reaction. For this purpose, a novel profile reactor was designed, built, and brought into operation as part of this work. In this chapter, the working principles of the profile reactor and the different units of the experimental setup are presented. Firstly, the conception of the profile reactor and its key feature, the profile measurement technique, are explained. Subsequently, all parts of the experimental setup are presented starting with the feed preparation, continuing with the profile reactor itself, and ending with the absorber used for emission abatement.

4.1 Reactor Conception

As the first step of the Ostwald process oxidation of ammonia is of major importance for the industrial production of the bulk chemical nitric acid. Despite its major economic importance the actual processes inside ammonia burners are not well understood. The detailed reaction mechanism is still a matter of debate, especially the reaction paths leading to the formation of the unwanted side products nitrous oxide and nitrogen. Furthermore, the influence of possible gas phase chemistry is still unclear and the processes leading to the corrosion of the expensive platinum alloy catalysts are not fully revealed. Under typical industrial conditions, with temperatures of up to 950 °C and pressures of up to 12 bar, the

oxidation of ammonia is a mass transfer-limited process. The high reaction rates are achieved using highly reactive stacks of platinum-alloy gauzes as catalysts. Full conversion is achieved within the catalyst bed, which typically only has a height of a few millimeters. Hence, to measure the actual processes inside an ammonia burner, a measurement technique with a high spatial resolution and a system that can cope with the extreme process conditions is required. Therefore, a novel profile reactor was developed, tailored to study ammonia oxidation by spatial profile measurements.

The key feature of the novel reactor is the integration of the spatial profile measurement technique developed by Horn et al. [32]. In Figure 4.1 a schematic sketch of the inside of the reaction zone is shown.

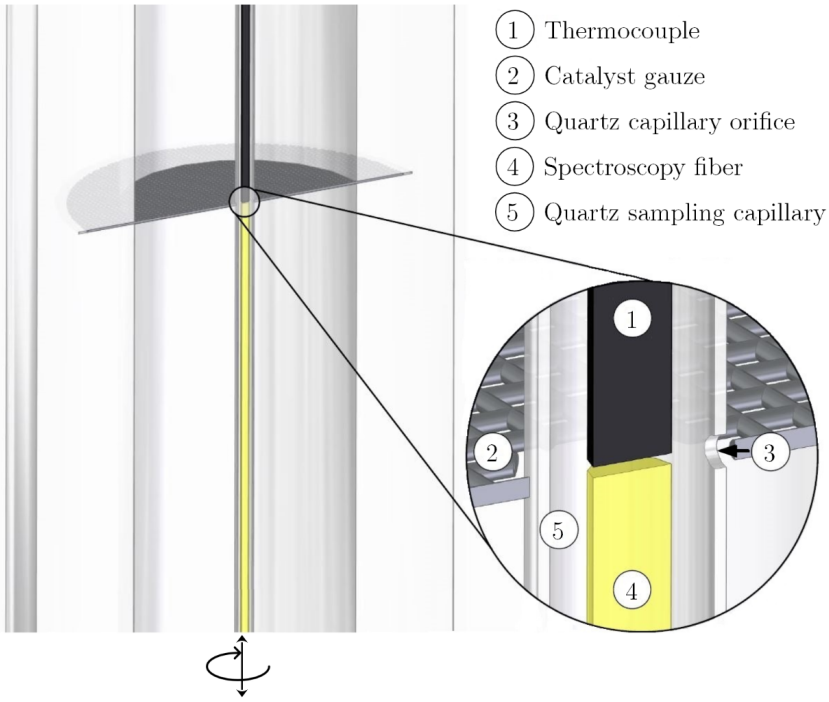

Figure 4.1: Schematic of the reaction zone of the novel profile reactor. Figure from [207]

The 6 cm long reaction zone consists out of an inert gauze holder in which one or multiple catalyst gauze stacks can be fixed at any arbitrary position. Using two stepper motors, one translation stage and one rotation stage, a thin quartz

sampling capillary can be positioned in the center of the reactor with μm resolution at varying angles and vertical positions. A small fraction of the gas stream is sampled through a side-sampling orifice inside the capillary. A transfer line to a MS is connected to one end of the capillary enabling analysis of the gas phase composition. Additionally, the quartz capillary can accommodate a thermocouple to measure the gas phase temperature. By coupling a pyrometer fiber inside the capillary, the catalyst surface temperature can be measured. In the future, further spectroscopic methods like Raman spectroscopy or laser-induced fluorescence could be coupled inside the capillary analogously to fiber pyrometer measurements.

Using the profile measurement technique detailed information about the processes inside the reactor can be obtained experimentally. The reactor is designed to be operated in a wide range of operation conditions listed in Table 4.1

Table 4.1: Designed operation condition range of the novel profile reactor

Parameter	**Minimum**	**Maximum**
Temperature [°C]	200	1000
Pressure [bar]	1	30
Gauze loading $\left[\frac{\text{t N in NH}_3}{\text{m}^2\text{d}}\right]$	1	20
NH_3 concentration [vol.%]	0.5	12
O_2 concentration [vol.%]	0	50
Total flow rate $\left[\frac{\text{sL}}{\text{min}}\right]$	1	63

The design parameters cover most of the parameter range used in commercial ammonia burners (see Table 2.1 in Section 2.4.2) and even exceed both the maximal temperature (950 °C) and pressure (12 bar) of typical industrial ammonia burners. For one parameter, the burner loading, the given parameter range does not cover the entire range of typical industrial values, since the reactor is not designed for very high ammonia loadings of up to 50 $\frac{\text{t N in NH}_3}{\text{m}^2\text{ d}}$ in the current setup. The values given in Table 4.1 refer to the loading range one obtains for using a gauze holder with an inner diameter of 12 mm. However, the gauze holder is exchangeable and could be easily replaced by a gauze holder with a smaller inner diameter, shifting the range of possible burner loadings to higher values in a cost effective way. Since

this comes at the price of stronger pronounced wall effects, an alternative approach would be the usage of an additional high flow range ammonia mass flow controller. The flow rates of all species and hence, the gas composition can be varied over a wide range. Details on this are given in the next section. Furthermore, the reactor is designed in a way that all operation parameters can be varied independently. This allows studying the direct influence of every parameter on the processes inside the reactor and the overall performance of the process. In the following sections, all parts of the experimental setup, shown in the simplified process flow diagram in Figure 4.2, are explained in detail.

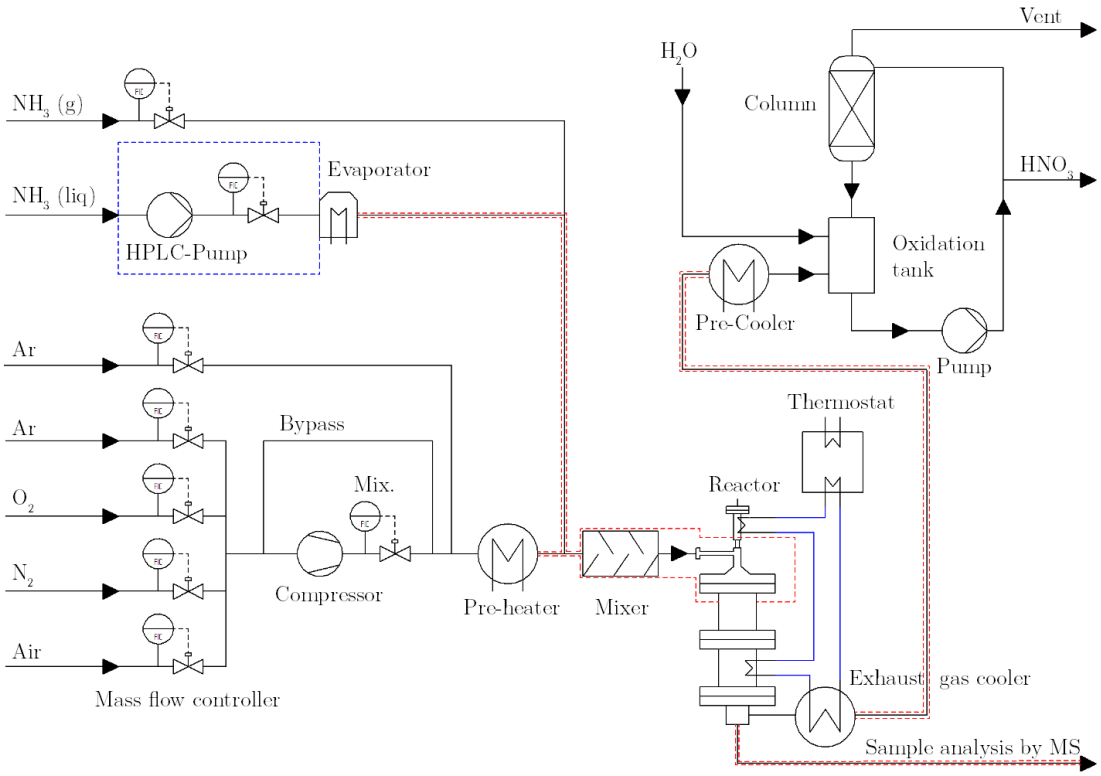

Figure 4.2: Simplified process flow diagram of the ammonia oxidation profile reactor

4.2 Feed Preparation

The novel profile reactor setup is designed to allow for independent variation of all operation conditions over a wide range (see Table 2.1). To fulfill this requirement, a complex feed preparation setup is used. Furthermore, the setup is designed in a modular approach, allowing for easy implementation of future upgrades, for example additional feed modules to dose water, nitrous oxide, or nitric oxides in the gas feed.

Since industrial ammonia oxidation is typically operated at high ammonia gas loadings, the reactants need to be supplied at quite significant flow rates for a bench scale reactor setup. The reactor is designed to be operated at a total feed flow rate of up to 65 sL/min. The flow rates of all species are controlled using mass flow controllers (MFC) (Bronkhorst High-Tech B.V., Ruurlo, Netherlands). A list of the MFC specifications is given in Table 4.2.

Table 4.2: Types and flow ranges of the utilized MFCs

Species	Flow Range	MFC Type
Ammonia (g.)	$0.04 - 2.14\ \frac{\text{g}}{\text{min}}$	F-201EV-RAD-22-K
Ammonia (liq.)	$0.04 - 2.14\ \frac{\text{g}}{\text{min}}$	ML120V00-RAD-11-0-S
Argon	$0.02 - 1\ \frac{\text{sL}}{\text{min}}$	F-201CV-500-RAD-11-V
Argon	$0.9 - 45\ \frac{\text{sL}}{\text{min}}$	F-201AV-50K-RAD-22-V
Oxygen	$0.2 - 10\ \frac{\text{sL}}{\text{min}}$	F-201CV-10K-RAD-22-V
Nitrogen	$0.5 - 25\ \frac{\text{sL}}{\text{min}}$	F-201CV-20K-RAD-22-V
Air	$0.5 - 25\ \frac{\text{sL}}{\text{min}}$	F-201CV-20K-RAD-22-V
Mixture	$1.2 - 60\ \frac{\text{sL}}{\text{min}}$	M14-RAD-22-0-S

The MFCs are installed in compact modules. A CAD model and a detailed flow chart of a MFC module are shown in Figure 4.3.

An inline filter (Ham-Let GmbH, Feldkirchen, Germany) is installed upstream of the MFC protecting it from particles. A normally closed magnetic valve (Christian Bürkert GmbH & Co. KG, Ingelfingen, Germany) is installed as a safety measure in front of the MFCs of the ammonia modules as well as all oxygen containing modules. In case of any malfunction or disturbance in the process an automatized process control system sets the flow rates of all MFCs to zero and

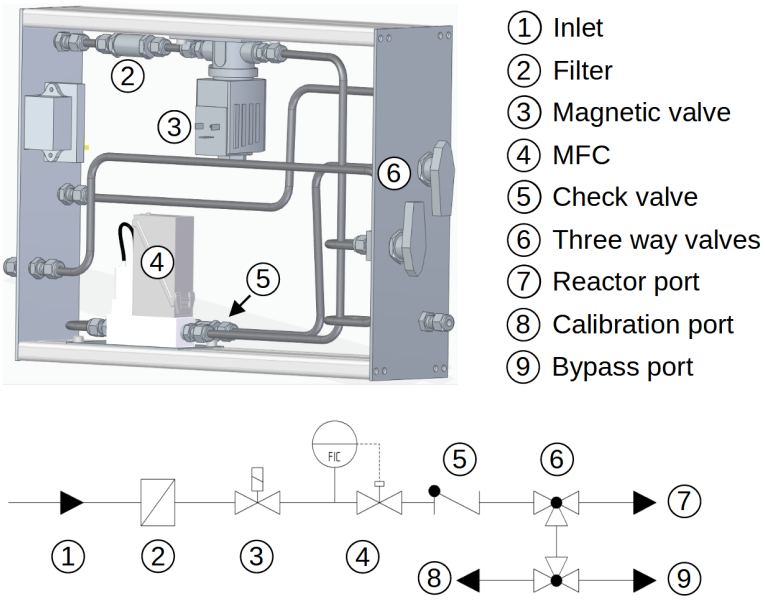

Figure 4.3: CAD model and flow chart of a MFC module

the magnetic valves are closed. A check valve (Ham-Let GmbH) downstream of the MFCs prevents any backward flow of the gases. Using two three-way valves (Swagelok / B.E.S.T. Fluidsysteme GmbH, Neuss, Germany) the gas flow can be either directed towards the reactor, a bypass line, or towards an additional port at the front side used to calibrate the MFCs.

The feed preparation setup can be divided into three sections: the combustion air section, the internal standard section, and the ammonia section. In the combustion air section the flow rates of the high flow nitrogen, oxygen, argon and air modules towards the reactor are controlled. By using three MFCs for pressurized air, nitrogen, and oxygen a wide range of concentrations and total flow rates of the combustion air can be adjusted. Furthermore, by using a high flow rate argon module the ballast medium of the reaction can be switched from nitrogen to argon. The four gases are supplied at pressures of 8 bar by the central gas supply installed in the technical hall of the TUHH. In Table 4.3 the purities and suppliers of the used educt gases are listed.

A pneumatic compressor (DLE 5-15 by Maximator GmbH, Nordhausen, Germany) is installed downstream of the modules allowing to increase the pressure

Table 4.3: Suppliers and purities of the used gases

Species	Purity	Supplier
Ammonia (g.)	99.98 %	Westfalen AG
Ammonia (liq.)	99.98 %	Westfalen AG
Argon	99.996 %	Westfalen AG
Argon	99.996 %	Westfalen AG
Oxygen	99.999 %	Westfalen AG
Nitrogen	99.8 %	Linde plc

of the combustion air up to 45 bar. The compressor is designed lubricant free in all gas contacting parts. Two 3.785 L sized storage tanks (Swagelok / B.E.S.T. Fluidsysteme GmbH) are installed in front and behind the compressor to buffer pressure fluctuations originating from the piston movements of the compressor (displacement volume of 373 cm^3). This way the control dynamics of the MFCs are minimally affected by the compressor. For reactor operation inside a pressure range of up to 5 bar, the compressor unit can be bypassed. In this case, the total flow rate of the combustion air entering the reactor is directly given by the flow rates set for the nitrogen, oxygen, argon, and air module. All above mentioned parts of the combustion air section are mounted inside a separated rack shown in Figure 4.4.

If the reaction is studied at pressures above 5 bar the total flow rate of the pressurized combustion air is controlled by an additional mixture MFC module. This is necessary since otherwise the flow rate would fluctuate with every movement of the compressor pistons. In the mixture module an additional pressure reducer (WIKA Alexander Wiegand SE & Co. KG, Klingenberg, Germany) is installed in front of the MFC, canceling out any pressure fluctuations upstream of the MFC. For example, at a reactor pressure of 30 bar the outlet pressure of the compressor is adjusted to 45 bar and consecutively reduced to 40 bar using the pressure reducer. The MFC used in the mixture module utilizes the Coriolis principle, allowing to measure directly the dosed mass flow and the density of the dosed mixture. Hence, this enables precise dosing of the combustion air with varying compositions without the necessity to calibrate the MFC for each new gas composition.

Figure 4.4: Combustion air section consisting of four MFCs modules, buffer cylinders and a pneumatic compressor

The second feed preparation section is the internal standard section. In all presented experiments 2 vol.% of Argon is used as internal standard. The comparatively low required flow rates can be sufficiently covered using a single high pressure argon bottle. Therefore, the argon used as internal standard can directly be dosed using a single MFC module without the need to increase the pressure using the compressor unit. Alternatively, helium can also be used as internal standard in the setup.

The last feed preparation section is used for dosing ammonia using two MFC modules. Ammonia has a vapor pressure of 8.57 bar at room temperature of 20 °C [212]. Hence, the ammonia section must be designed in a way that uncontrolled phase transitions of ammonia are excluded for the entire pressure range of $1 - 30$ bar. For reactor pressures up to 5 bar, ammonia is directly dosed in gas phase using one MFC module. At pressures above 5 bar, liquid ammonia is

extracted from a dip tube ammonia bottle. The pressure of the liquid ammonia is then increased by a high-performance liquid chromatography (HPLC) pump (WaDose-LITE-HP-10-SS-U-TU-C, FLUSYS GmbH, Offenbach, Germany). The flow rate of the pressurized ammonia is controlled with a Coriolis MFC and finally, the ammonia is evaporated using a low pulsation total evaporator developed by the ICVT at the University Stuttgart (Stuttgart, Germany). To prevent uncontrolled phase transitions in the system, the whole liquid ammonia section is cooled to 0 °C using an ethanol/water mixture cooled with a Lauda Microcool MC 350 chiller (Lauda GmbH, Lauda-Knigshofen, Germany). The cooling medium is used to cool the HPLC pump-head, the bottom part of the evaporator, and a box, in which the MFC, as well as the piping, are installed, to guarantee pulsation free evaporation. The piping downstream of the evaporator is trace heated to up to 100 °C with a heating wire (Type HST, Horst GmbH, Lorsch, Germany) preventing condensation of ammonia.

The combustion air and the internal standard are pre-heated in front of the reactor using a compact pre-heater developed by the Fraunhofer Institute for Microengineering and Microsystems (IMM) (Mainz, Germany). It is designed to heat up to 65 sL/min of gas from room temperature to up to 700 °C at pressures of up to 30 bar within a very compact device that consists of a 3D-printed pressure vessel contacted with a 2000 W cartridge heater. To withstand the combination of high temperatures, pressures, and corrosive atmosphere the pressure vessel is built of Inconel 718. In cooperation with the IMM a mixing area was designed and integrated behind the pre-heating zone allowing to mix the ammonia stream with the pre-heated gas mixture. The pre-heater and mixer are combined in a single compact device manufactured by IMM. The combined pre-heating and mixing device is directly attached to the pressure vessel of the novel profile reactor shown in Figure 4.5. In Figure 4.5 the ammonia section, the internal standard section, and the mix module are shown in the second zone.

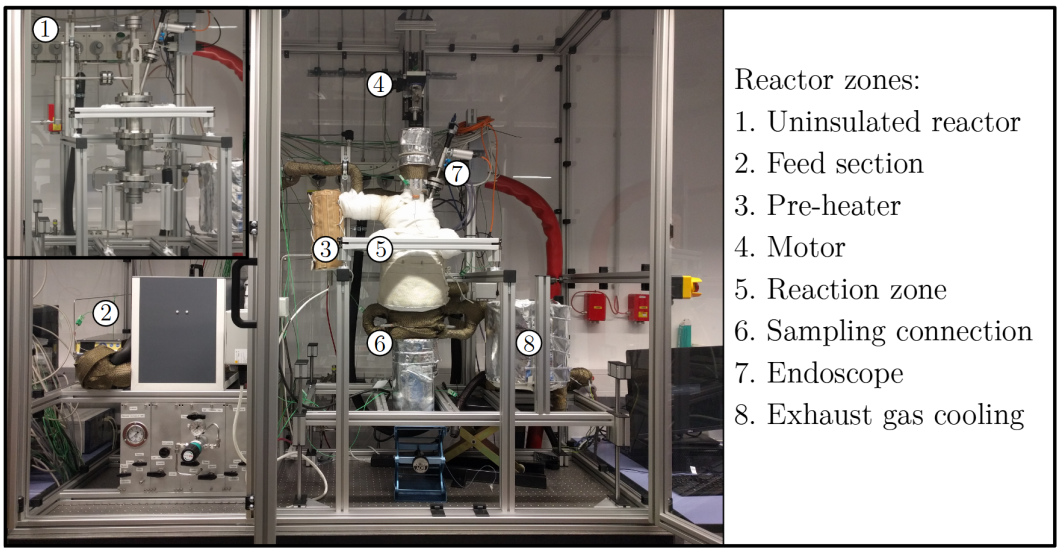

Figure 4.5: Zones of the novel profile reactor for ammonia oxidation under industrial conditions

4.3 Profile Reactor

The novel profile reactor consists of a pressure vessel designed in-house and manufactured by Halmosi GmbH (Heilbronn, Germany). To withstand the combination of high temperatures, pressures and corrosive gases the pressure vessel is built of the materials Inconel 617, Inconel 625, and V4A 1.4571. Inside the reaction zone an inert gauze holder is placed in which catalyst gauzes can be fixed at any arbitrary axial position.

A sampling capillary made of fused silica (MicroQuartz GmbH, München, Germany) is inserted in the center of the reactor. The sampling capillary has an outer diameter of 670 μm and an inner diameter of 530 μm. The polyimide coating of the capillary is burned off prior installation in the reactor at all parts that are in contact with gas temperatures above 250 °C reducing the outer diameter of the capillary to 616 μm. Using a M-403.6DG linear stage (Physik-Instrumente GmBH Co. KG, Karlsruhe, Germany) with a designed resolution of 0.2 μm, a minimum incremental motion of 0.2 μm, and an unidirectional repeatability of 1 μm the vertical position of the capillary can be adjusted. For rotation movements a M-060.DG rotation stage (Physik-Instrumente GmbH & Co. KG) with a

designed resolution of 2.1 μrad, a minimum incremental motion of 6.3 μrad, and an unidirectional repeatability of 50 μrad is utilized. Through a small laser drilled side sampling orifice (drilled by LaserMicronics GmbH, Garbsen, Germany) with a diameter of 20 μm gas is sampled from the reaction zone. The bottom end of the capillary is connected to a microvolume cross (Valco Instruments Company Inc., Houston, United States of America) housed inside a heated bag manufactured by Horst GmbH (Lorsch, Germany). A heated hose (Type: HMI300 TA/03 PFA, Hillesheim GmbH, Waghäusel, Germany) connects the microvolume cross to the MBMS used for gas sample analysis. Using this setup the temperature of the sampled gas is kept above 200 °C over the whole transport way reducing consecutive reactions and, especially important under safety aspects, preventing ammonium nitrate formation.

Additionally to gas phase concentration measurements, temperature profiles are measured by inserting thermocouples or pyrometer fibers into the sampling capillary. The tip of the thermocouple or pyrometer fiber is aligned with the sampling orifice. For gas phase temperature measurements a type-K thermocouple with an outer diameter of 250 μm (TMH GmbH, Maintal, Germany) is used. An IGAR 12-LO MB13 quotient pyrometer (IMPAC Infrared GmbH, Frankfurt a.M., Germany) measuring at a spectral range of 1.28 and 1.65 μm is used. The optical fiber attached to the pyrometer is a WF 400/440P (CeramOptec GmbH, Bonn, Germany) with an outer diameter of 440 μm and an in-house polished conical tip. The pyrometer setup was calibrated using a black body calibrator (TK600 by Teco Maritime ASA, Lysaker, Norway).

An endoscope of the type LPR.100.0300.00.05.HT with an integrated LED light source (Hinze OptoEngineering GmbH & Co. KG, Hamburg, Germany) is positioned at the inlet region of the reactor. Using the endoscope it is possible to continuously observe the front gauze inside the reaction zone under operation using a Sony IMX265 camera sensor (distributed by Hinze OptoEngineering GmbH & Co. KG).

The hot reaction gases are cooled in the cooling section of the pressure vessel directly downstream of the reaction zone and additionally, inside an additional pipe-in-pipe cooler (DTC-IN1/SSC-6-1-1, by Sentry Equipment distributed by Lambertz-Solutions GmbH, Lüdenscheid, Germany). The temperatures in the

cooling sections are controlled using Ultra 350 thermal oil tempered to 185 °C with an Integral XT 4 HW thermostat (Lauda GmbH). Additional electrical trace heating is installed around the pressure vessel to keep the feed stream tempered at the target inlet temperature behind the pre-heater. A back pressure regulator (DN-HF2SNN12B, Equilibar LLC, Fletcher, United States of America) is used to control the reactor pressure.

4.4 Absorber

The off-gas from the ammonia oxidation reactor contains several corrosive and toxic components like nitric oxides and residual ammonia. Hence, an absorber is used for emission abatement to absorb these corrosive and toxic compounds in water. The absorption process follows the second and third steps of the Ostwald process: The oxidation of nitrogen oxide to nitrogen dioxide and the absorption of nitrogen dioxide in water forming nitric acid (see Sections 2.2.3 & 2.2.4). In Figure 4.6 a CAD model of the absorber unit used in this study is shown.

The hot combustion gases are entering the absorber unit through a heated transfer line at a temperature of 200 °C and ambient pressure. In the first step, the hot gases are cooled down in a pre-cooler unit. Subsequently, the gases enter an 80 L sized storage tank partially filled with water. Here the oxidation of nitrogen oxide to nitrogen dioxide starts at a significant rate and first absorption processes start at the water surface. The absorption column is operated in a counter current flow arrangement with the gas flowing from bottom to top and water flowing from top to bottom. The absorption column has a diameter of 20 cm and is filled over its 1.9 m length with a Raschig ring packing providing a high surface area ensuring good gas liquid contact. A pump (RM PVDF-TGKKK-6/140-30S(18S) by Renner GmbH, Maulbronn-Schmie, Germany) is used to pump the water upwards. The amount of water flowing towards the water distribution system at the column head is controllable by a valve. A fraction of the upwards pumped water is continuously flowing out of the absorber towards the neutralization unit of the technical hall. This continuous extraction of water leads to a slowly falling water level in the storage tank. Once the water level falls below a defined threshold, a level indicator (VEGAPULS64, VEGA Grieshaber KG, Schiltach, Germany) gives

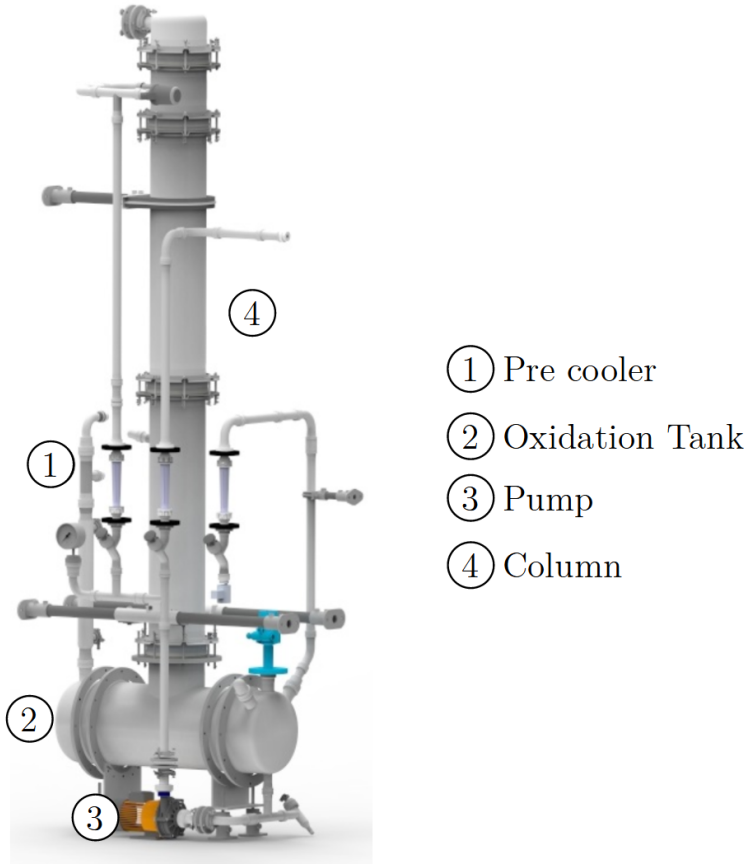

Figure 4.6: CAD Model of the absorber

a signal opening a magnetic valve (Christian Bürkert GmbH & Co. KG) and water refills the storage tank till an upper threshold level is reached. Using this simple setup continuous operation of the absorption column over many days is enabled without compromising the absorption efficiency due to rising nitric acid concentrations. The dimensioning of the absorption unit was carried out in a bachelor thesis by Sven Brauer [213]. The absorption column was manufactured and designed in cooperation with De Dietrich Process Systems GmbH (Mainz, Germany).

5 Spatial resolution of the capillary sampling technique

In the following chapter, the spatial resolution of concentration profile measurements via capillary sampling is analyzed for ammonia oxidation under industrial conditions. Parts of the chapter have been previously published in [207], while here, the chapter is extended by additional, complementary results. The simulations shown in Section 5.1 have been conducted by Anna Sophia Behnecke and have been published in her master thesis [208]. The simulations shown in Section 5.2 have been conducted by Dr. Sven Jakobtorweihen.

Ammonia oxidation is an extremely fast, mass transfer limited reaction with steep concentration gradients around the catalyst gauzes. Full ammonia conversion is achieved using gauze stacks which are only a few millimeters thick. A measuring technique with a high spatial resolution is required in order to resolve these steep gradients. Profile measurements via capillary sampling have a finite spatial resolution since gas samples are extracted from a certain sampling volume rather than from a specific point. For example, the gas phase concentration measured at a specific orifice position represents a gas mixture sampled from a defined volume around the orifice. This spatial averaging leads to smearing out of the measured concentration gradients, in mathematical terms described by a convolution integral. In order to understand and interpret the measured profiles appropriately, this signal convolution by the measurement technique and its influencing factors must be understood. To understand this sampling through a small orifice in a process with steep concentration gradients, we first investigate sampling at a fixed azimuthal orientation of the orifice with respect to the gauze by means of CFD simulations. In the second section the influence of the azimuthal angle between

orifice and wires is analyzed experimentally by profile measurements as well as by a second set of simulations, performed on a model with curved wires (see Figure 3.6).

5.1 CFD simulations on the influence of the sampling volume

The influence of the sampling process can be studied by means of CFD simulations by comparing sampled gas phase concentration profiles with radially averaged concentration profiles of an undisturbed reactor without capillary sampling. In Figure 5.1 simulated mole fraction profiles for the undisturbed reactor model and the sampling model with interpenetrating wires (see Figure 3.4) are compared.

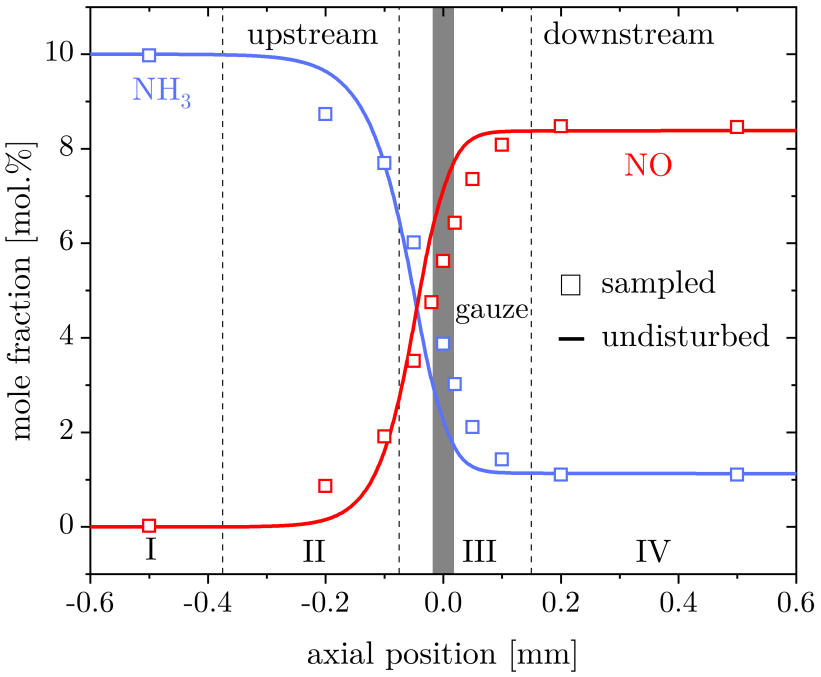

Figure 5.1: Comparison of simulated mole fraction profiles of nitric oxide and ammonia obtained from the sampling model (squares) and the undisturbed reactor model (solid lines). Operation conditions: T_{inlet} = 650 K, p = 10 bar, x_{NH_3} = 0.10, x_{O_2} = 0.19, u_{in} = 0.2 m/s; taken from [207]

Sampled and undisturbed profiles agree well, showing the expected steep concentration gradients around the catalyst gauze located at an axial position of zero

millimeters. Four distinct areas can be distinguished, indicated by the dotted lines in the figure. At orifice positions upstream 0.375 mm ($z \leq -0.375$ mm, Region I) and 0.15 mm downstream of the gauze ($z \geq 0.15$ mm, Region IV) the sampled and the undisturbed profiles match almost perfectly yielding the inlet and outlet mole fractions. In the vicinity of the gauze, where the concentration gradients are steepest, the sampled and the undisturbed profiles deviate. Upstream of the gauze in Region II higher product concentrations and lower educt concentrations are predicted by the sampling model compared to the undisturbed model. In the immediate vicinity but still upstream of the gauze this trend reverses showing lower product concentrations and higher educt concentrations of the sampling model compared to the undisturbed model (Region III). Differences are largest directly at the catalyst gauze.

The deviations between the sampled profiles and the undisturbed profiles can be explained by analyzing the interplay of the high local concentration differences and the gas sampling regions. The nitric oxide concentration fields inside the undisturbed reactor obtained at two different inlet velocities are visualized in surface contour plots in Figure 5.2.

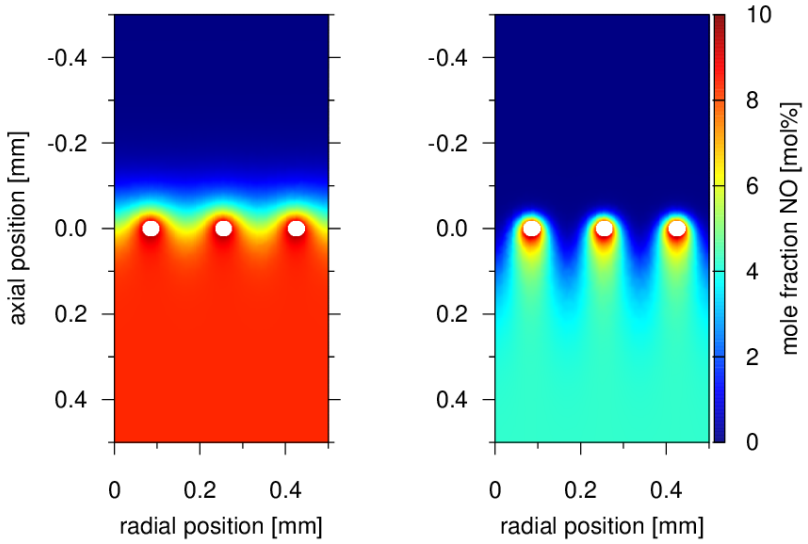

Figure 5.2: Surface contour plots of the local nitric oxide concentration through the mid-plane of an undisturbed reactor for inlet velocities of $u_{in} = 0.2$ m/s (left) and $u_{in} = 1$ m/s (right). Operation conditions: $T_{inlet} = 650$ K, p = 10 bar, $x_{NH_3} = 0.10$, $x_{O_2} = 0.19$; taken from [207]

For an inlet velocity of 0.2 m/s, the surface contour plots show that the nitric oxide concentration starts to rise about 0.1 mm upstream of the gauze, due to back diffusion from the reaction zone. Around the catalyst wires, represented by the light gray circles, the nitric oxide concentration increases strongly. Between the wires, nitric oxide concentrations are lower than close to the wires. Thus, pronounced radial concentration gradients are formed in addition to the gradients in axial direction. The radial concentration gradients are smoothened out downstream of the gauze by diffusion. At an inlet flow velocity of $u_{in} = 0.2$ m/s, the nitric oxide concentration is spatially uniform within about 0.075 mm downstream of the gauze. Both, the magnitude of the radial concentration gradients as well as their extension in axial direction depend on the ratio of the diffusive transport velocity of a respective species compared to the overall convective transport velocity in flow direction. At otherwise constant operation conditions, the magnitude of the gradients and their extension in axial direction increase with increasing flow velocities as shown exemplarily for an inlet velocity of 1 m/s in the contour surface at the right side of Figure 5.2.

In Figure 5.3 the interplay of gas sampling through the sampling capillary in a strongly varying concentration field is shown by means of streamlines flowing through the reactor on a 2D slice through the mid-plane of the sampling model at three different orifice positions for an inlet velocity of $u_{in} = 0.2$ m/s.

The streamlines, colored according to the local nitric oxide concentrations, indicate the convective transport of the sampled gas into the capillary orifice in the sampling model. The outermost streamline that still reaches the sampling orifice is included in all three plots. It is evident that gas is only sampled from a narrow region around the sampling orifice, which is represented by the channel in the dark gray colored capillary on the left side of the plots. For the illustrated case, the sampling area extends up to 0.22 mm downstream of the orifice and extends up to 0.3 mm in radial direction at the height of the wires, limiting the sampling region to the first two wires closest to the orifice. Despite this high spatial resolution of the technique, the sampled gas always represents a mixture of gas coming from regions down- and upstream of the sampling orifice. The streamlines are selected such that an equal amount of sampled gas originates from every region in between two plotted streamlines. If the orifice is positioned 0.1 mm upstream of the cat-

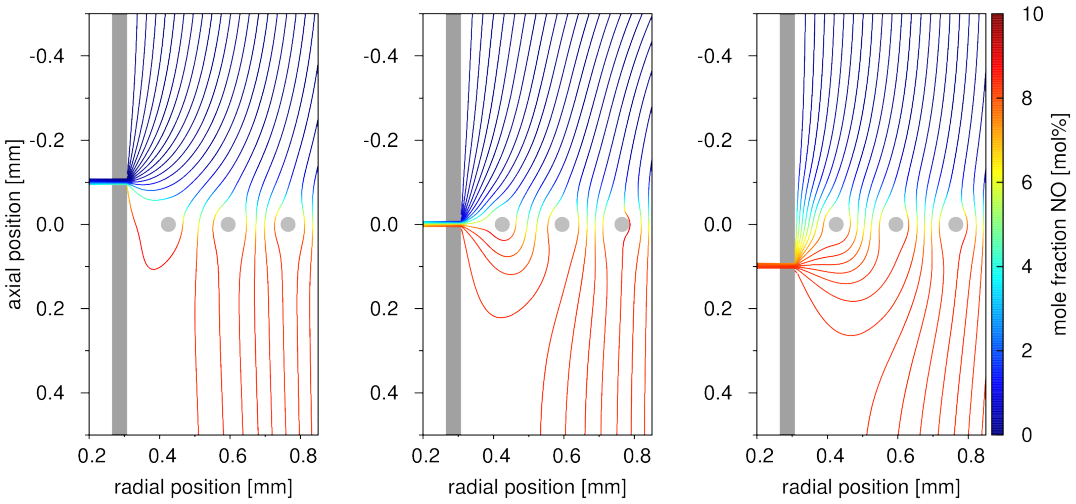

Figure 5.3: Gas streamlines through the mid-plane of the reactor for three axial orifice positions: 0.1 mm upstream of the gauze (left), at the gauze (middle) and 0.1 mm downstream of the gauze (right). The streamlines are colored according to the local nitric oxide concentration. Operation conditions: T_{inlet} = 650 K, p = 10 bar, x_{NH_3} = 0.10, x_{O_2} = 0.19, u_{in} = 0.2 m/s; taken from [207]

alyst gauze, a small fraction of the sampled gas has already passed through the reaction zone, mixing in a considerable amount of products to the sampled flow. In comparison, back diffusion of products only starts to be visible in the undisturbed case at this axial position. Hence, this extension of the sampling region downstream of the orifice explains the observed difference in concentrations between the sampled and the undisturbed profiles in Region II of Figure 5.1. Product species from the reaction zone are drawn into the orifice at earlier positions in the sampling model leading to an earlier rise in product concentration compared to the undisturbed model. For the same reason, educt concentrations are dropping earlier as in the undisturbed case. This trend reverses at orifice positions in direct vicinity of the gauze where gas from three different regions is sampled: Gas coming from upstream of the gauze with negligible product concentrations, gas coming from regions around the gauze with concentrations close to the respective radial average, and finally gas coming from downstream of the gauze with elevated product concentrations. The total number of streamlines reaching the sampling orifice, each representing the same amount of sampled gas, show that a significant

amount of sampled gas originates from upstream of the gauze and only a smaller fraction originates from regions around or downstream of the gauze. Thus, the sampled product concentrations are lower than the undisturbed average. Directly at the gauze, where the highest concentration gradients exist, deviations are most strongly pronounced. At positions downstream of the gauze still a larger fraction of gas is sampled from upstream of the orifice. However, due to the fast diffusion, the concentration gradients are less pronounced in the respective streamlines and the deviations between sampled and undisturbed profiles are reduced. Once the sampling orifice is positioned at regions where diffusion has smeared out any concentration gradients in between streamlines reaching the orifice, the sampled and the undisturbed profiles match again.

Several factors influence the spatial resolution of the capillary sampling technique and the resulting convolution of the measured concentration profiles. An important factor is the mass flow sampled through the orifice, which is determined by the diameter of the sampling orifice and the operation conditions of the setup. At a fixed reactor pressure, the mass flow rate sampled through the orifice increases with decreasing pressure inside the capillary until the gas flow reaches speed of sound inside the orifice (choked flow). At this point, the mass flow rate reaches a maximum. Even if the pressure inside the capillary is reduced below this critical pressure ratio

$$\frac{p_{\mathrm{crit}}}{p_{\mathrm{r}}} = \left(\frac{2}{\kappa+1}\right)^{\frac{\kappa}{\kappa-1}} \tag{5.1}$$

the mass flow rate through the orifice remains constant and is referred to as the the critical mass flow rate or the mass flow rate at choked conditions [214]. It can be calculated using the reactor temperature T_{r}, reactor pressure p_{r}, the isentropic exponent κ, the specific heat capacity c_{p}, the diameter of the orifice d_{orifice} and the mass-specific gas constant R_{spec} according to

$$\dot{m}_{\mathrm{choked}} = \left(\frac{2}{\kappa+1}\right)^{\frac{1}{\kappa-1}} \sqrt{\frac{\kappa-1}{\kappa+1}} \sqrt{\frac{2\ c_{\mathrm{p}}}{T_{\mathrm{r}}}} \frac{\pi\ p_{\mathrm{r}}\ d_{\mathrm{orifice}}^2}{4\ R_{\mathrm{spec}}}. \tag{5.2}$$

A more detailed description of choked flow inside small orifices and the resulting supersonic beams is given in Section 2.6.1. The critical pressure ratio required

for choked flow of, for example, air with an isentropic exponent κ of 1.4 accounts to 0.528. For the experiments in this work, the capillary outlet was connected to the vacuum pump system of the MBMS operated at 10^{-4} mbar pressure. Another small orifice, the MBMS inlet nozzle, is placed between the sampling orifice and the vacuum chamber. The MBMS inlet nozzle has a diameter of 100 μm and thus, is significantly larger than the sampling orifice of the capillary with a diameter of 20 μm, which is why the sampling orifice is the main flow restriction in the sampling system. The pressures inside the reactor were atmospheric or above for all conducted experiments and simulations. Therefore, choked flow can be anticipated inside the sampling orifice under all conditions. CFD simulations with varying capillary outlet pressure $p_{\mathrm{cap,out}}$ were performed (see [208]) confirming that choked flow was reached for $p_{\mathrm{cap,out}}/p_{\mathrm{r}} = 0.5$ which was used in all conducted simulations and reached in all experiments.

The spatial resolution of the capillary sampling technique can be defined as a hypothetical surface around the sampling orifice, having a surface area A_{samp}, through which all streamlines pass through which are ending inside the orifice. Along these streamlines gas with the mass flow rate $\dot{m}_{\mathrm{choked}}$ is transported. The area A_{samp} from which the sample is taken is related to the mass flux through the reactor G_{r} which equals the product of reactor inlet density ρ_{in} and inlet velocity u_{in} according to the following equation:

$$\begin{aligned} \dot{m}_{\mathrm{chocked}} &= G_{\mathrm{r}} \cdot A_{\mathrm{samp}} = \rho_{\mathrm{in}} \cdot u_{\mathrm{in}} \cdot A_{\mathrm{samp}} \\ &= \left(\frac{2}{\kappa+1}\right)^{\frac{1}{\kappa-1}} \sqrt{\frac{\kappa-1}{\kappa+1}} \sqrt{\frac{2\ c_{\mathrm{p}}}{T_{\mathrm{r}}}} \frac{\pi\ p_{\mathrm{r}}\ d_{\mathrm{orifice}}^2}{4\ R_{\mathrm{spec}}} \end{aligned} \tag{5.3}$$

The sampled mass flow rate $\dot{m}_{\mathrm{chocked}}$ depends on properties of the sampled gas (the isentropic exponent κ, the mass-specific gas constant $\mathrm{R_{spec}}$ and the specific heat capacity $\mathrm{c_p}$), the reactor pressure p_{r}, the reactor temperature T_{r} and the diameter of the sampling orifice $\mathrm{d_{orifice}}$. The latter enters quadratically, therefore, very small orifices of 20 μm were used in this work to achieve high spatial resolution.

Three simulation studies, each with different variable operation parameters, were conducted to answer the question: How does the spatial resolution of profile mea-

surements change at changing operation conditions? This question is of particular importance for data analysis of profiles measured during measurement campaigns in which an operation parameter, for example the inlet temperature, is varied. A change in spatial resolution results in changed convolution of the measured concentration profiles, which needs to be considered for data analysis and interpretation. In the three simulation studies, an inert flow of air through the sampling reactor was simulated.

In the first set of simulations, the reactor inlet velocity u_{in} and therewith, the reactor mass flux G_{r} was increased at otherwise constant conditions. The resulting extension of the sampling volumes, by means of the outer streamline still passing through the sampling orifice, are shown in Figure 5.4.

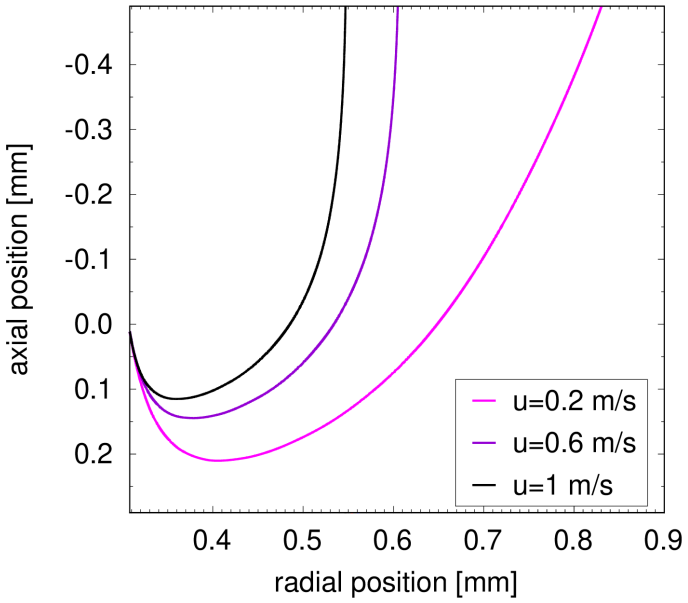

Figure 5.4: Outermost streamlines of the sampling gas flow for increasing inlet velocity and reactor mass flux; adopted and changed from [207]

In line with Equation 5.3, if G_{r} increases at constant sampled mass flow $\dot{m}_{\mathrm{chocked}}$, the sampling area decreases with increasing inlet velocity and therefore, the spatial resolution becomes better.

In a second set of simulations, the reactor inlet velocity u_{in} was kept constant and the reactor pressure p_{r} was increased translating into an increased reactor mass flux G_{r}. According to Equation 5.3, the sampling area will stay approximately

constant because also the sampled mass flow through the orifice $\dot{m}_{\text{chocked}}$ increases linearly with pressure such that both effects cancel, in line with the simulation results shown in Figure 5.5.

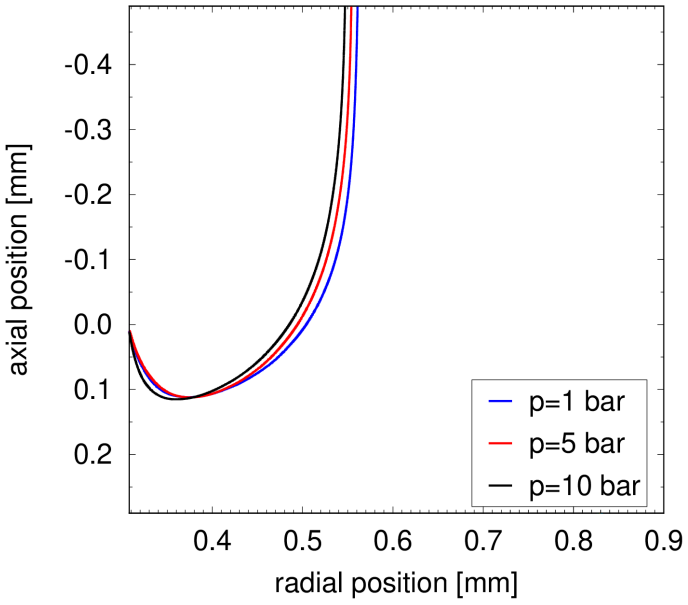

Figure 5.5: Outer streamlines of the sampling gas flow for increasing pressure and reactor mass flux; adopted and changed from [207]

On the contrary, the sampling area A_{samp} would change if the reactor pressure p_{r} is increased while keeping the mass flux G_{r} constant, corresponding into a decreasing inlet velocity u_{in}. The linear increase of the sampled mass flow $\dot{m}_{\text{chocked}}$ with increasing reactor pressure, is not canceled out in this scenario since the change in inlet velocity u_{in} is canceled by a change of the density ρ_{in} keeping the mass flux G_{r} constant according to Equation 5.3. In an experimental campaign in which the reactor pressure is changed at a constant mass flux G_{r}, translating to constant ammonia loading and molar fraction, and otherwise constant operation conditions the change in the sampling area needs to be considered for data analysis of the measured profiles.

In a third set of simulations the reactor temperature T_{r} was increased at constant reactor mass flux G_{r} and reactor pressure p_{r}. According to Equation 5.3, the sampled mass flow rate is on the one hand inversely proportional to the square root of the reactor temperature but depends on the other hand also on gas specific

properties such as c_p and κ. While κ changes only slightly ($\kappa = 1.4$ for an ideal diatomic gas), the heat capacity c_p increases with increasing temperature. As shown in Figure 5.6, these effects almost cancel keeping the sampling area virtually unchanged over the investigated temperature range.

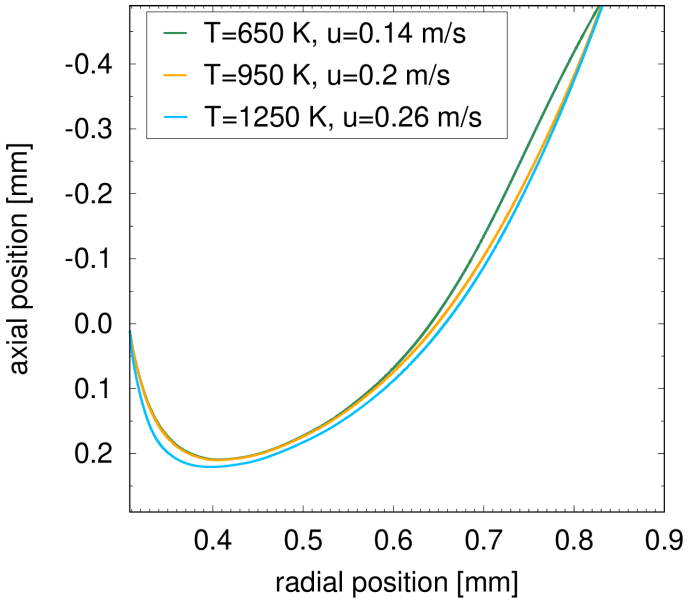

Figure 5.6: Outer streamlines of the sampling gas flow for increasing inlet temperature and inlet velocity; adopted and changed from [207]

The three selected temperatures represent typical temperatures in ammonia burners from the cold inlet to the hottest regions around the wires. This result, that the sampling area is not changing with varying temperatures at constant reactor pressure p_r and mass flux G_r, is of particular importance for the detailed study of the reactor inlet temperature influence on the reaction presented in Chapter 8.

As shown in the three sets of simulations above, the spatial resolution depends for certain parameter variations on the operation conditions inside the reactor and consequently, the convolution of the measured profiles should be affected by changing operation conditions as well. To illustrate this, the simulation shown in Figure 5.1 was repeated with a changed inlet velocity of 1 m/s instead of 0.2 m/s used in the first simulation. The mass flux was also increased by a factor of five and all other operation conditions were kept constant for the two simulations at $T_{inlet} = 650$ K, p = 10 bar, $x_{NH_3} = 0.10$ and $x_{O_2} = 0.19$. The resulting mole

fraction profiles of nitric oxide and ammonia obtained from the sampling model and the undisturbed reactor model are shown in Figure 5.7.

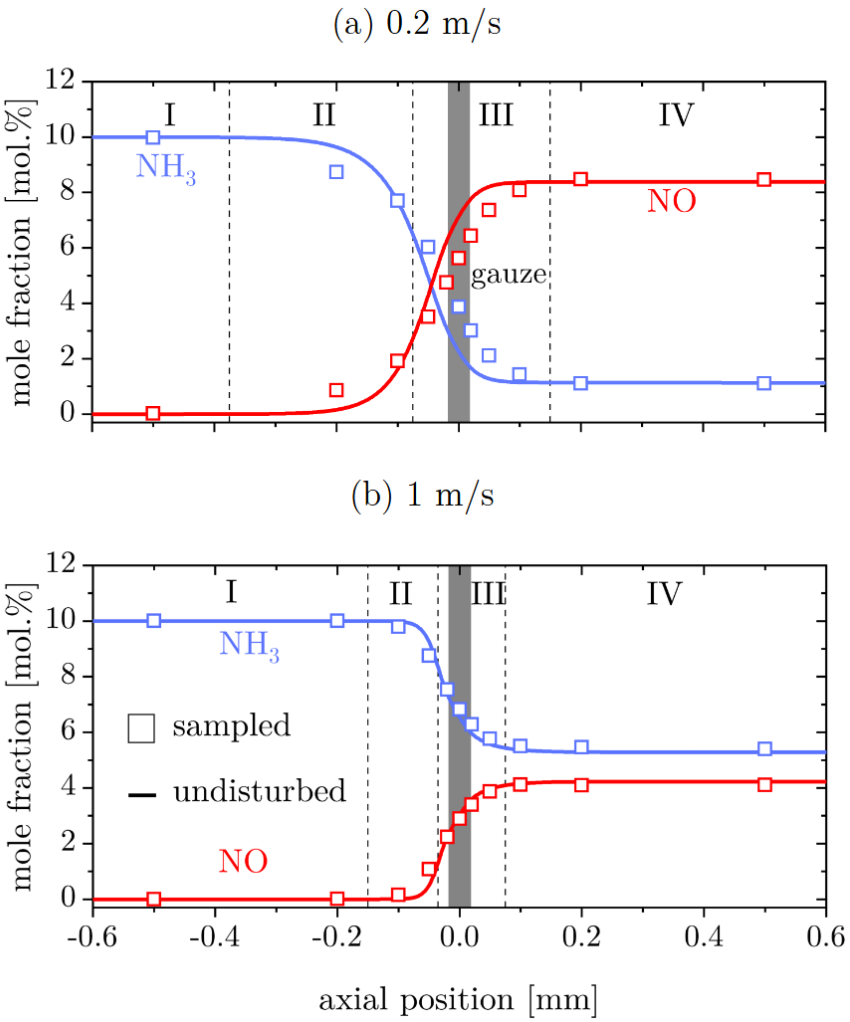

Figure 5.7: Comparison of simulated mole fraction profiles of nitric oxide and ammonia obtained from the sampling model (squares) and the undisturbed reactor model (solid lines) for two different inlet velocities of 0.2 m/s (top) and 1 m/s (bottom). Operation conditions: $T_{inlet} = 650$ K, $p = 10$ bar, $x_{NH_3} = 0.10$, $x_{O_2} = 0.19$; adopted and changed from [208]

Several differences are visible in the mole fraction profiles at the two different inlet velocities. At the higher inlet velocity of 1 m/s, which is inside the typical industrial range of mid pressure burners between $1 - 3$ m/s [3], significantly lower conversion of ammonia and lower production of nitric oxide is obtained, due to

the significantly reduced residence time at the gauze. For both flow velocities in Region I and Region IV the sampled and the undisturbed profiles match, while in Region II the nitric oxide mole fraction is overestimated and in Region III the nitric oxide mole fraction is underestimated. However, the extension of Region II and Region III is significantly smaller at the higher flow velocity of 1 m/s and also the relative deviations are significantly reduced. In Figure 5.8 the streamlines through the sampling reactor are shown for both velocities at an orifice position of 0.1 mm downstream of the gauze.

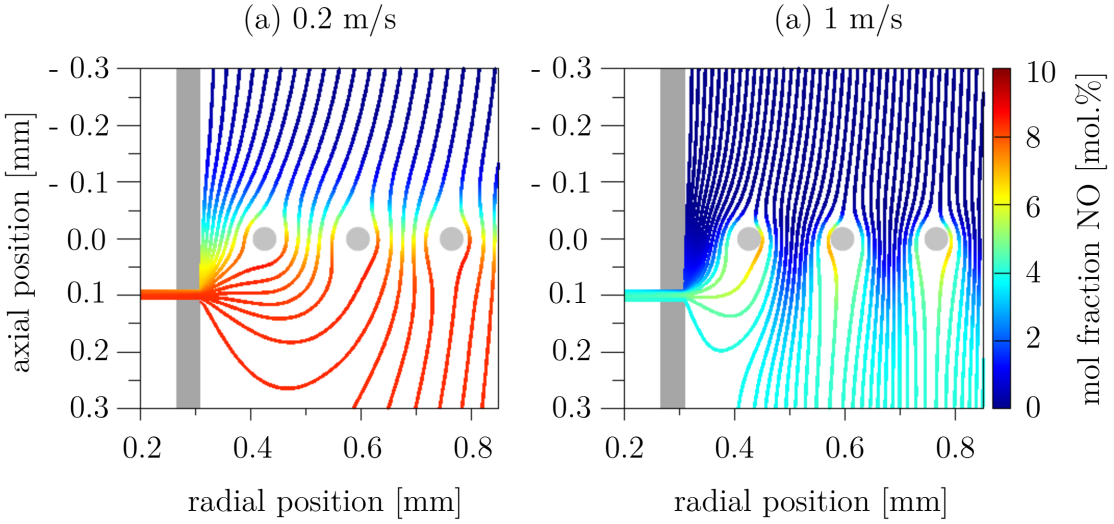

Figure 5.8: Gas streamlines through the mid-plane of the sampling reactor for inlet velocities of 0.2 m/s (left) and 1 m/s (right). The streamlines are colored according to the local nitric oxide concentration. Operation conditions: $T_{inlet} = 650$ K, p = 10 bar, $x_{NH_3} = 0.10$, $x_{O_2} = 0.19$; adopted and changed from [208]

In accordance with the results shown in Figure 5.4, the extension of the sampling region is reduced for the higher inlet velocity and mass flux used in the 1 m/s simulation. The reduced extension of the sampling region and the in consequence higher spatial resolution benefits a reduced convolution of the sampled profile. For example Region II, in which nitric oxide selectivities are overestimated, starts significantly closer to the gauze at a position of −0.15 mm at an inlet velocity of 1 m/s compared to −0.375 mm for an inlet velocity of 0.2 m/s, because the downstream extension of the sampling region is drastically reduced. However, no general statement about the influence of the operation conditions on the profile

convolution can be made, because not only does the size of the sampling volume influences the measured profiles, but also the relative positioning of the orifice to the gauze wires is of major importance, as demonstrated in the following section.

5.2 Influence of the sampling orifice positioning

As shown in the previous section, gas is sampled exclusively from a small region around the sampling orifice, ensuring a high spatial resolution of the capillary sampling technique in the used configuration. Only catalyst wires within the sampling area contribute to the measured profiles. Therefore, another factor determining the shape of the measured profiles is the relative position of the sampling orifice to the catalyst wires. This will be demonstrated in the following using CFD simulations and experiments.

In the CFD study a single woven gauze with a big gap created by extracting two wire crosses is used for the sampling model with curved wires (see Section 3.3.1). Two different cases are simulated in this study. In the first case, the sampling orifice is positioned directly close to a wire, and in the second case, the sampling orifice is positioned in the gap with no wire in close vicinity. Sketches of the corresponding simulation domains are illustrated in Figure 5.9. The resulting simulated molar flow rate profiles of ammonia and nitric oxide sampled at the two different capillary rotation arrangements are compared to undisturbed simulated profiles at the same conditions in Figure 5.9.

The undisturbed profiles show the typical steep gradients at the catalyst gauze. Upstream of the gauze the flow rate of ammonia is equal to the inlet flow rate and the nitric oxide flow rate is zero. In direct vicinity of the gauze the ammonia flow rate drops and the nitric oxide flow rate rises sharply. Axial diffusion causes a minor rounding of the otherwise sharp edges of the radially averaged profiles, but, compared to convection, the influence is small. In the simulated profiles where sampling was considered, deviations from the undisturbed case are observed depending on the orientation of the orifice and wires. When the sampling orifice is positioned next to a wire, the sampled ammonia profile has a pronounced minimum and the nitric oxide profile has a corresponding maximum at the axial position of the gauze. Downstream of the gauze the ammonia flow rate rises again and

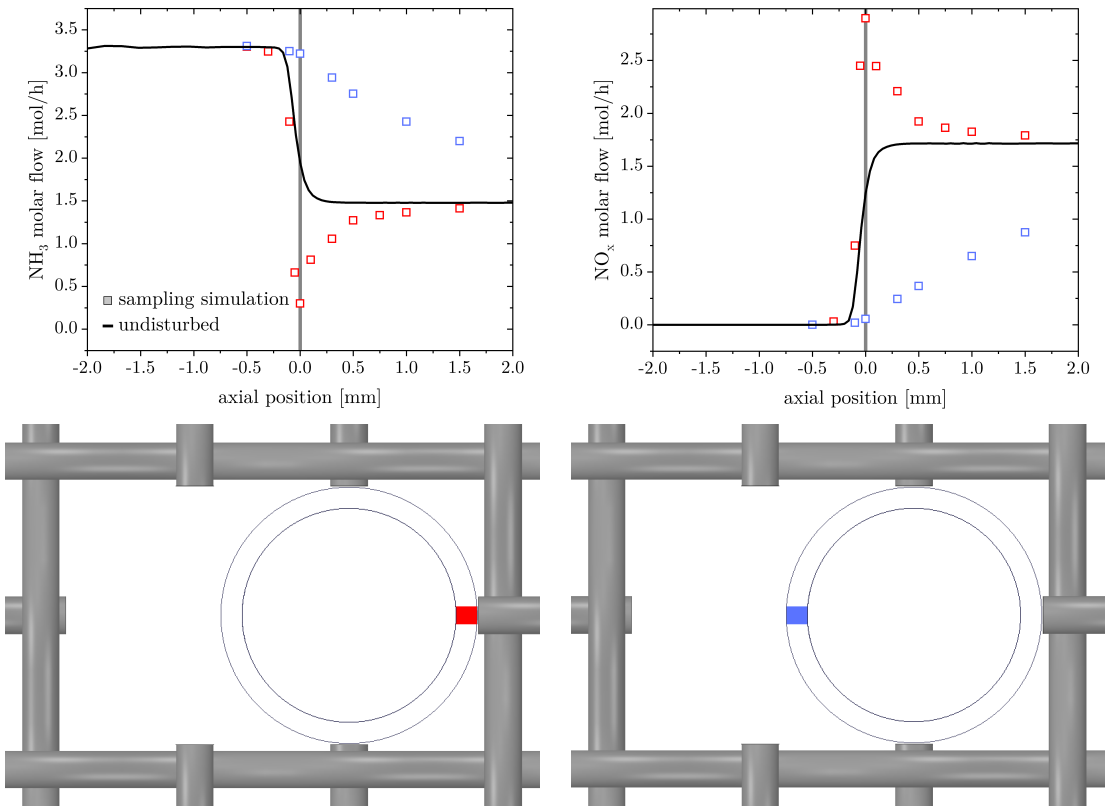

Figure 5.9: Comparison of simulated ammonia molar flow rate profiles (left) and nitric oxides molar flow rate profiles (right) for different sampling configurations: undisturbed profiles (solid lines), sampling close to wire (red squares), sampling in gap between wires (blue squares). Operation conditions: $T_{inlet} = 300$ °C, p = 5 bar, $x_{NH_3} = 0.10$, $x_{O_2} = 0.186$, NH_3 loading = 10 $\frac{\text{t N in } NH_3}{\text{m}^2\ \text{d}}$. Figure taken from [207]

the nitric oxide flow rate drops due to radial diffusion. The molar flow rates of both ammonia and nitric oxide almost reach the undisturbed flow rate at the last simulated position, 1.5 mm downstream of the gauze. A completely different profile is obtained when the sampling orifice is pointing away from a wire into a gap. Only a small initial drop in the educt concentrations and a small rise in the product concentrations are visible. Downstream of the gauze the ammonia flow rate drops and the nitric oxide flow rate increases slowly again due to radial diffusion. Even at the last simulated sampling position, 1.5 mm downstream of the gauze, the flow rates have still not reached the undisturbed values because the orifice is in this position quite far from the wire causing spatial gradients.

The different shapes of the measured profiles depend on which streamlines are sampled into the orifice. If streamlines are sampled which are passing close to the catalyst wires, viz. if the orifice is facing the gauze, ammonia conversion and nitric oxide formation in those streamlines are high. Downstream of the gauze, ammonia from streamlines bypassing the gauze at larger distances diffuses into the streamlines passing close to the gauze and vice versa for nitric oxide. This causes a rise in ammonia molar flow rate and a drop in nitric oxide flow rate until the radial concentration gradients vanish. If streamlines are sampled which are passing far away from the catalyst wires, viz. if the orifice is pointing to a gap or mesh center, the situation is exactly opposite.

The simulation results shown in Figure 5.9 illustrate the importance of how gauze and sampling orifice are positioned to each other. To confirm these predictions, experiments were conducted in which the sampling orifice was positioned at three distinct locations with respect to the wires. Endoscope pictures of how the sampling capillary is running through the gauze and simplified sketches, indicating the orifice-gauze orientation in each case are shown in Figure 5.10.

In the first arrangement the orifice is positioned as close as possible to a wire, while in the second arrangement the orifice is positioned as far away as possible from any wires by positioning the capillary into the center of a mesh, and finally, in the third case the orifice is arranged at a medium distance with the orifice pointing into a 90° corner of two crossing wires. For all three arrangements profile measurements were conducted at the same operation conditions of $T_{inlet} = 200$ °C, $p = 5$ bar, $x_{NH_3} = 0.10$, $x_{O_2} = 0.186$, NH_3 loading $= 10 \frac{\text{t N in } NH_3}{\text{m}^2 \text{ d}}$. The measured and the undisturbed simulated molar flow rate profiles of ammonia and nitric oxide for each arrangement are shown in Figure 5.11.

If the orifice is positioned directly at a gauze wire, profiles with a distinct ammonia minimum and nitric oxide maximum are measured as predicted by the CFD simulations shown in Figure 5.9. If the sampling orifice is positioned in the center of a mesh, viz. comparably far away from any wire, the initial slopes of the simulated undisturbed ammonia and nitric oxide flow rate profiles are captured well. In this arrangement, the sampling volume of the orifice does not extend into the reaction zone until the axial position of the orifice equals the gauze position. Downstream of the gauze a significant fraction of gas is sampled which

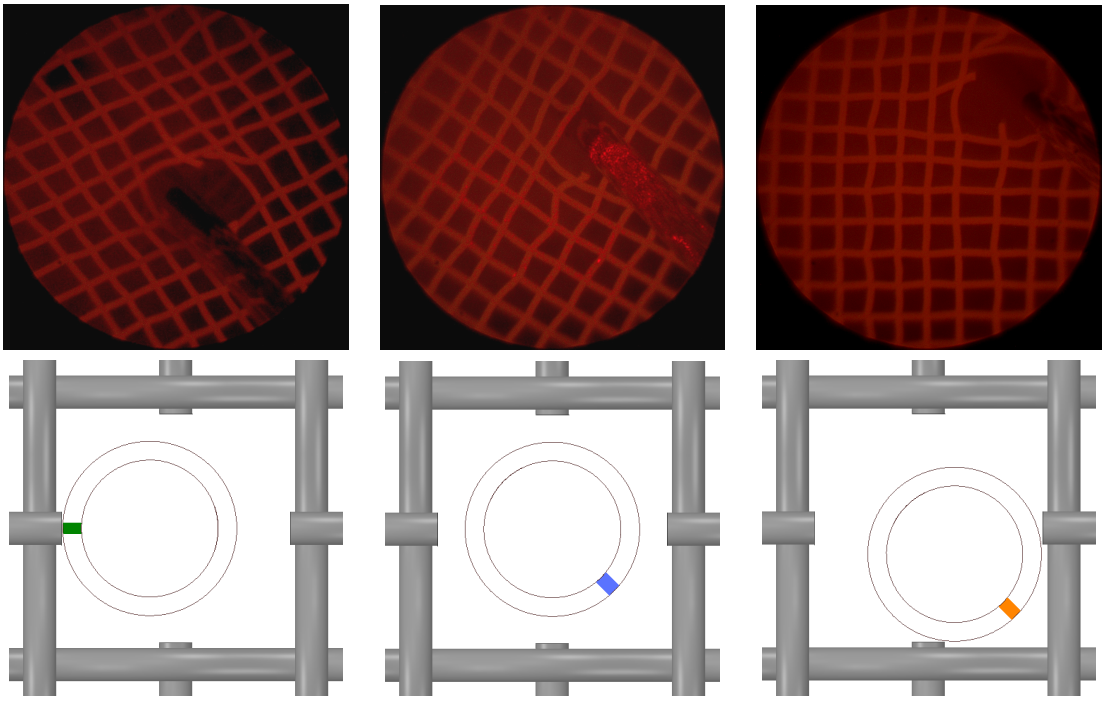

Figure 5.10: Top: Endoscope pictures of the experimental setup for three orifice to gauze arrangements. Bottom: Idealized sketches of the three orifice to gauze arrangements. Figure taken from [207]

has bypassed the wires, leading to considerable differences between the measured and undisturbed simulated profiles. With increasing distance from the gauze the molar flow rate profile of ammonia decreases and that of nitric oxide increases due to radial diffusion from high conversion streamlines approaching constant values.

If the capillary is positioned in a corner of two crossing wires and the orifice is rotated such that it is pointing right into the corner, it has a medium distance to the gauze compared to the first two cases. The sampling volume in this arrangement covers in a balanced way bypass flow, products formed at a wire crossing and products formed at a straight wire piece resulting in measured profile shapes that are close to the undisturbed simulated profiles both before and after the gauze.

The simulation and measurement results presented in Section 5.1 and Section 5.2 illustrate that the size of the orifice and the position of the orifice with respect to the gauze influence the shape of the molar flow rate profiles in a delicate manner. A smaller orifice translates on the one hand into a higher spatial resolution but

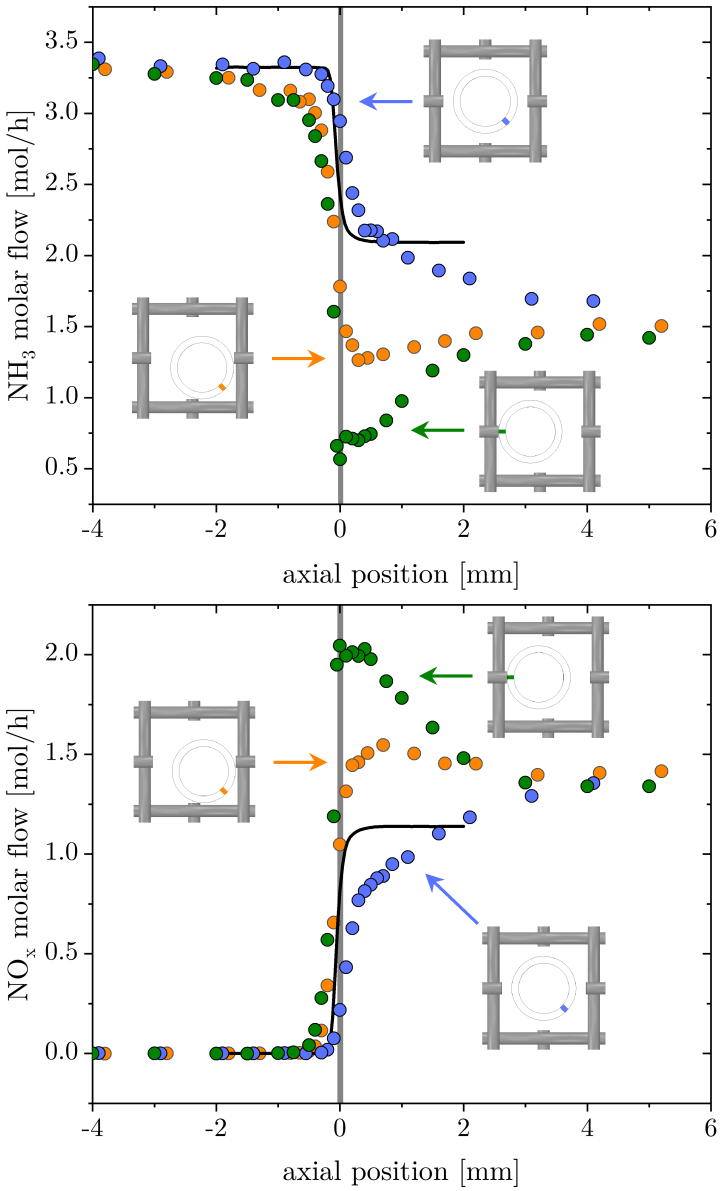

Figure 5.11: Comparison of the undisturbed simulated (solid line) and measured (circles) molar flow rate profiles for three varying orifice to gauze arrangements of ammonia in the top and nitric oxide in the bottom plot. Operation conditions: T_{inlet} = 200 °C, p = 5 bar, x_{NH_3} = 0.10, x_{O_2} = 0.186, NH_3 loading = 10 $\frac{\text{t N in NH}_3}{\text{m}^2\ \text{d}}$. Figure taken from [207]

requires on the other hand precise positioning with respect to the gauze to obtain well balanced profiles, which are close to radially averaged profiles in an undis-

turbed reactor. By choosing a sampling orifice of 20 μm or less and by positioning this orifice accurately in a gauze area of interest, e.g. by the help of an endoscope, even local phenomena like varying selectivities induced by different gauze geometries can be studied, for example straight wires vs. wire crossing points. Another possible application is to distinguish between reaction products formed in catalytic reactions at the gauze surface and reaction products formed in gas phase reactions. Such highly resolved reactor profile measurements should always be accompanied by CFD simulations to interpret the obtained profiles quantitatively. If it is just the goal to measure radially averaged profiles without that fine spatial details are of interest, larger sampling orifices of 50 μm or even 100 μm should be used. In no event should integral end of pipe measurements in laboratory sized reactors be compared to reactor simulations or industrial reactor data because the end of pipe concentration data measured in small laboratory reactors are distorted due to heat losses over the reactor walls that lead to lower nitric oxide selectivities than observed in industrial reactors of large diameter [11].

6 Temperature measurements with thermocouples

In the previous chapter, it was shown that profile measurements by capillary sampling are well suited to resolve the steep concentration gradients in ammonia oxidation reactors under industrial conditions. In most application examples, not only measurements of concentration profiles but also gas temperature profile measurements are of interest. Therefore, already in the first profile measurement setup by Horn et al. [32, 33] concentration measurements by capillary sampling were accompanied by gas temperature measurements via thermocouples. Since these first studies, gas temperature profile measurements via thermocouples were adopted in many setups and for various reaction systems [32, 33, 35, 36, 39, 40, 215–217]. Spatially resolved temperature profile measurements are enabled by inserting a thermocouple into the moveable sampling capillary and aligning the thermocouple tip with the sampling orifice. In this chapter, the suitability to resolve the steep gas temperature gradients around catalyst gauzes in ammonia oxidation reactors with thermocouples is analyzed. CFD simulations shown in this chapter have been conducted by Sven Jakobtorweihen.

In most profile measurements in the newly developed reactor setup, temperature profiles were measured along with concentration profiles using a type-K thermocouple. In this chapter, the data quality of the measured profiles is discussed exemplarily for five temperature profiles that were measured at varying reactor inlet temperatures and otherwise constant conditions. The measured thermocouple temperature profiles and corresponding simulated gas temperature profiles, obtained from CFD simulations using the undisturbed reactor model at the same operation conditions, are shown in Figure 6.1

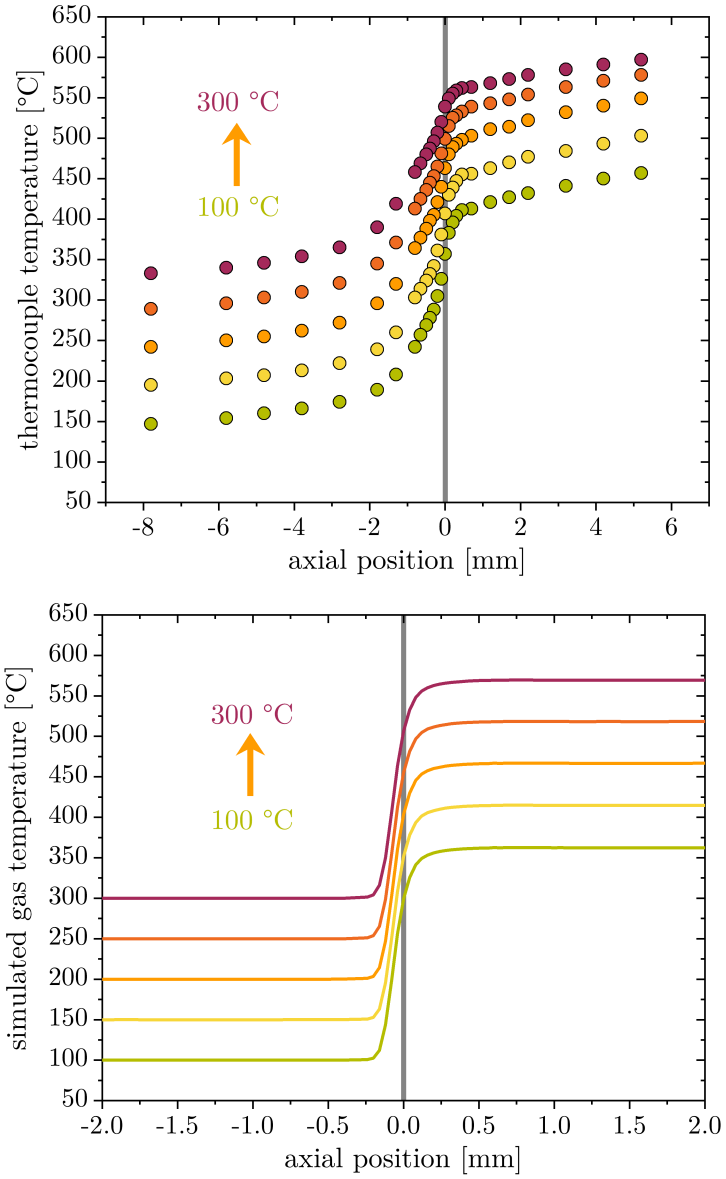

Figure 6.1: Comparison of temperature profiles measured with a type-K thermocouple (top) and simulated, radially averaged gas temperature profiles obtained from undisturbed reactor simulations (bottom) for varying inlet temperatures of 100 °C, 150 °C, 200 °C, 250 °C and 300 °C. Operation conditions: p = 5 bar, $x_{NH_3} = 0.10$, $x_{O_2} = 0.186$, NH_3 loading = 10 $\frac{\text{t N in } NH_3}{\text{m}^2 \text{ d}}$

The five temperature profile measurements and corresponding CFD simulations were conducted at varying inlet temperatures of 100 °C, 150 °C, 200 °C, 250 °C

and 300 °C with the sampling orifice arranged at a medium distance to the wires pointing into a corner of two crossing wires (see Figure 5.10, right). All five profile measurements and CFD simulations were conducted at the same operation conditions of p = 5 bar, $x_{NH_3} = 0.10$, $x_{O_2} = 0.186$ and NH_3 loading = 10 $\frac{\text{t N in } NH_3}{\text{m}^2 \text{ d}}$.

The measured thermocouple temperature profiles deviate considerably from the radially averaged gas temperature profiles obtained from CFD simulations with the undisturbed reactor model. The first distinct deviation between measured and simulated temperature profiles is the difference in the inlet temperature. In the simulated profiles the gas temperatures match the corresponding inlet temperatures till -0.25 mm upstream of the gauze. In contrast, the measured inlet temperatures deviate considerably from the targeted set-points at the first measured position -7.8 mm upstream of the gauze. Additionally to the mismatch in the obtained inlet temperatures, also the measured profile shapes deviate considerably. On the one hand, the simulated temperature profiles show steep gradients at the catalyst gauze region, analogously to the concentration profiles discussed in Chapter 5. Till -0.25 mm upstream of the gauze the gas temperatures match the inlet temperatures, followed by a sharp temperature rise in the direct vicinity of the gauze and constant temperatures towards the outlet. On the other hand, the measured thermocouple temperature profiles show a rise in temperature starting already at the first analyzed positions from -7.8 to -5.8 mm upstream of the gauze. The slopes of the temperature profiles increase, reaching the steepest gradients around the catalyst gauze position. In contrast to the simulated profiles, the measured temperatures continue to increase till the last analyzed position 5.2 mm downstream of the gauze.

To explain the measured temperature profiles multiple phenomena have to be taken into account. First of all, it should be noted that the measured temperature represents the temperature of the thermocouple tip. If the thermocouple is in thermal equilibrium with its surrounding medium, the measured temperature equals the temperature of the medium, in this application the temperature of the sampled gas. However, the thermocouple temperature is not only influenced by the surrounding gas, but also by thermal radiation originating from the gauzes. In a second measurement campaign, gauze surface temperatures were measured with a fiber pyrometer using the same catalyst gauze and operation conditions like in

the measurements shown in Figure 6.1. For an inlet temperature of 100 °C a gauze temperature of 836 °C was determined, while a temperature of 948 °C was measured at an inlet temperature of 300 °C. A detailed discussion of the gauze surface temperature measurements is given in Section 8.2. For thermocouple positions in close range but still upstream of the gauze heat is transported by radiation from the hot catalyst gauze surface towards the colder thermocouple tip, heating up the thermocouple. The inlet gas molecules are also heated up by radiation, but only to a small extent due to low residence times and lower thermal absorption of gas molecules. This results in a deviation between the measured thermocouple temperature and the gas temperature. It should be noted here, that radiation is neglected in the CFD simulations shown in Figure 6.1. First preliminary CFD simulation tests with activated radiation, conducted by Dr. Sven Jakobtorweihen, showed no strong change of the simulated temperature profile shape. This suggests the hypothesis that the actual gas temperature profiles inside ammonia oxidation reactors are close to the simulated profiles shown in Figure 6.1. For a final assessment, a more thorough investigation of the radiation influence in CFD simulations is required, including systematic testing of the various parameters that can be adjusted in radiation models.

Several characteristics of the measured temperature profiles can be attributed to the discussed influence of gauze radiation. The thermocouple is heated up by gauze radiation, resulting in the observed deviation between the inlet temperature set-points and the measured temperatures at a thermocouple position -7.8 mm upstream of the gauze. Erroneous inlet temperature control can be excluded as the possible origin of the deviation, since upon extinction of the reaction, by interrupting the ammonia flow, the measured thermocouple temperature dropped immediately until the set-point inlet temperature was reached. Depending on the thermocouple tip position and the corresponding previously measured temperature, the set-point inlet temperature was reached within seconds up to a few minutes. This shows that the inlet temperature control worked. The results from the CFD simulations indicate that the actual gas temperature equals the inlet temperature for positions more distant than -0.25 mm upstream of the gauze in the used configuration. The closer the thermocouple was moved in the experiments to the gauze, the stronger gets the radiation influence. Therefore, the measured ther-

mocouple temperature and the corresponding slope of the measured temperature profile increase for orifice positions closer to the gauze, explaining the mismatch between measured and simulated profile shape upstream of the gauze. In close vicinity to the gauze the actual temperature of the sampled gas flow increases as well, resulting in the steep temperature gradients measured in this region. Continuously increasing temperatures were measured with the thermocouple downstream of the analyzed single gauze. This can be explained by the influence of radiation originating from the afterburner gauze stack that was positioned ten millimeters downstream of the studied single gauze.

Another effect that complicates precise gas temperature measurements via thermocouples is the alignment of the thermocouple tip with the sampling orifice. The thermocouple tip is aligned in the capillary assembling process in cold state with the sampling orifice using the endoscope camera. The thermocouple and capillary expand due to thermal expansion induced by the high temperatures during operation. The silica capillary and the Inconel sheathed thermocouple have different thermal expansion coefficients, resulting in misalignment of the thermocouple tip with the sampling orifice. This effect can be avoided to a certain degree by realigning the thermocouple tip during operation using the endoscope camera and under consideration of the measured signals, as it was done in the measurements shown in this chapter.

Furthermore, gas temperature profiles measured with thermocouples might be influenced by the gas sampling process itself. In the sampling process the molecules are sampled through a small orifice into the low pressure environment inside the sampling capillary, resulting in the formation of a supersonic jet. The gas molecules might be cooled down to some extent in the expansion process, indicated also in first preliminary CFD studies. The exact influence of the expansion process on the gas temperatures measured with thermocouples was not analyzed yet in detail by CFD simulations, but might not be negligible, especially in regions with pronounced temperature gradients.

To sum up, the results in this chapter indicate that thermocouple measurements are not an optimal approach for precise measurements of gas temperatures in ammonia oxidation. Especially the influence of radiation, but also misalignment of the thermocouple tip due to thermal expansion and the unclear influence of the

sampling process on the gas sample temperature complicate the matter. However, thermocouple measurements could still prove to be a valuable tool for validation of CFD simulations, especially to adjust and validate the various parameters in radiation models. Lacking precise gas temperature measurements complicate the accurate validation of CFD models and the characterization of the heat losses in the reactor by conduction over the reactor walls. Therefore, the integration of a reliable method for precise gas temperature measurements should be of high priority in future studies of ammonia oxidation in the developed profile reactor. A promising approach to tackle this challenge is gas temperature measurement using Raman spectroscopy with spectroscopic fibers coupled into the sampling capillary, comparable with the pyrometer measurements discussed in Section 8.2. Raman measurements require though a considerably more complex setup than pyrometer measurements. A proof of principle of gas temperature measurements in profile reactors was already carried out by Sosna [218] using carbon monoxide oxidation as a test reaction system.

7 Influence of catalyst reconstruction

During an industrial ammonia oxidation campaign the morphology of the used platinum or platinum-rhodium alloy gauzes changes dynamically. Starting with smooth, homogeneous wires the gauzes restructure forming fractal structures, shaped like cauliflowers, at the surface. The cauliflower growth results in considerably increased surface areas by up to 20 times the initial values [138, 147]. Additionally, the local alloy composition of cauliflowers changes compared to the initial alloy composition, leading to rhodium enriched cauliflower tips [71]. The changing surface area and gauze composition lead to higher ammonia conversion for reconstructed gauzes compared to fresh gauzes and also influence the achieved nitric oxide selectivities. Maximum nitric oxide yields are obtained in an industrial campaign, depending on the operation conditions, after three to eight days, while in small lab reactors complete activation is typically achieved within a few hours [3, 61, 106, 147]. To provide comparable conditions within a measurement campaign, measurements should be conducted with an already restructured gauze, which is not changing its morphology considerably during a measurement campaign. Measurements with reconstructed gauzes also provide better comparability with typical industrial results for entire operation campaigns. Hence, in the first section of this chapter, the rates of the catalyst reconstruction process inside the profile reactor are illustrated by showing and discussing the catalyst morphologies of gauze stacks that were aged for different operation times in the profile reactor. Another phenomenon was observed as a side effect of the reconstruction process. The sampling capillary running through the center of the profile reactor got covered with a catalytically active coating over the course of a multiple day long measurement campaign. In the second section of this chapter negative examples

are shown, how capillary coating can influence measured profiles and strategies to detect as well as prevent such distortions are discussed.

7.1 Morphological changes at varying aging times and stack positions

The dynamics of the reconstruction process of platinum alloy gauzes in ammonia oxidation is reported to depend on the operation conditions but also scales with the dimensions of the reactor [3,61,106,147]. To get an impression of the dynamics of the reconstruction process in the profile reactor stacks of ten woven gauzes made of platinum-rhodium alloy with a rhodium content of 5 wt.% were aged for 1, 10, 24, 50, and 100 h. During aging the reactor was operated at an inlet temperature of $T_{in} = 300$ °C, a pressure of $p_r = 5$ bara, a feed gas composition of $x_{NH_3} = 0.10$, $x_{O_2} = 0.186$ and an ammonia loading of 10 $\frac{\text{t N in NH}_3}{\text{m}^2\ \text{d}}$. Assuming full ammonia conversion and a resulting adiabatic temperature rise of 67 °C for every vol.% ammonia in the feed mixture [3], reaction temperatures in the range of 970 °C can be anticipated under the selected operation conditions. The catalyst reconstruction rate is reported to be enhanced with increasing reaction temperatures [3]. Therefore, a high reaction temperature, at the upper end of the industrial range, was chosen to allow for significant catalyst reconstruction within a reasonable time period manageable concerning gas consumption and required manpower for the shifts. The goals of the experiments were to determine after which aging time the catalyst gauzes are considerably reconstructed, showing typical cauliflower structures observed in industry, and to resolve at which rate the reconstruction process continues for already reconstructed gauzes under high temperatures and resulting high corrosion rates. After aging, the single gauzes of a stack were carefully separated and subsequently, analyzed via SEM by Dr. Tobias Krekeler of the BEEM at TUHH. SEM pictures of the front sides of the first gauze of the stacks aged for 1, 10, 24, and 100 h respectively are shown in Figure 7.1.

For an aging time of only one hour the surface of the front side of the first gauze is already reconstructed noticeably (Figure 7.1 a and b). The gauze parts that are directly exposed to the gas stream are consistently covered with numerous small

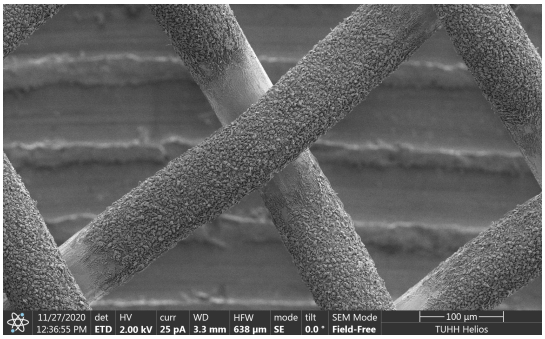

(a) 1 hour aging time

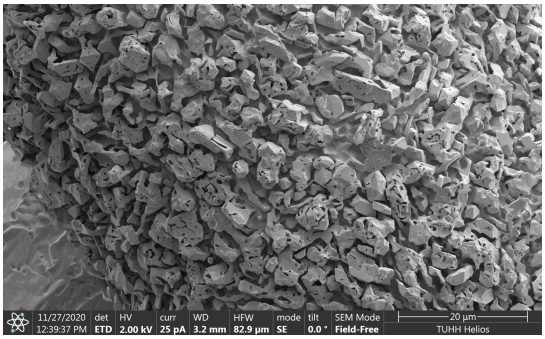

(b) 1 hour aging time detail view

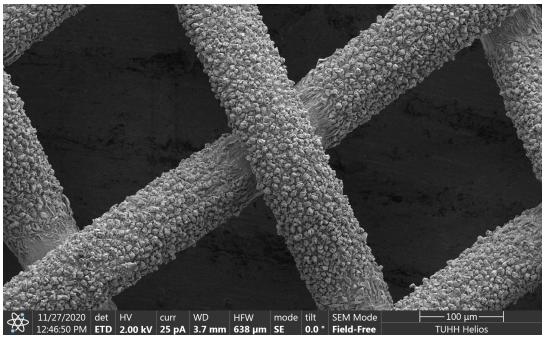

(c) 10 hour aging time

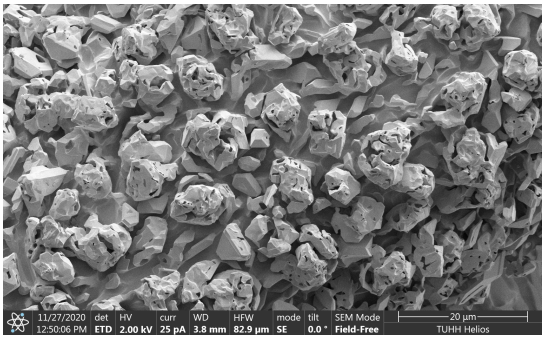

(d) 10 hour aging time detail view

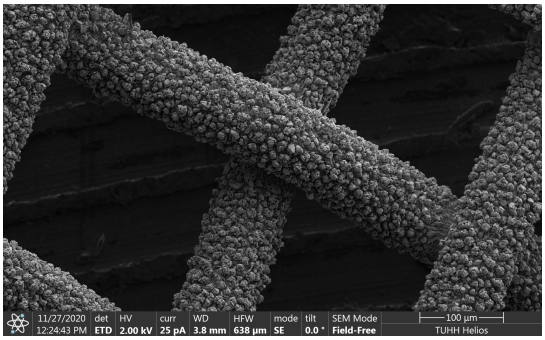

(e) 24 hour aging time

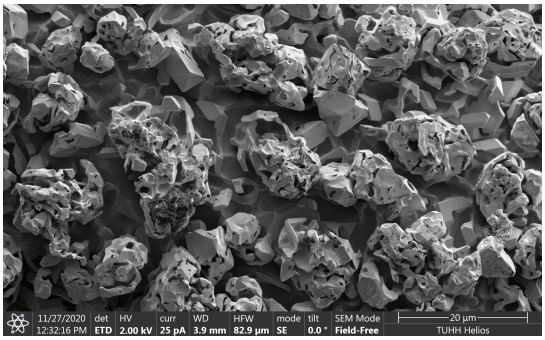

(f) 24 hour aging time detail view

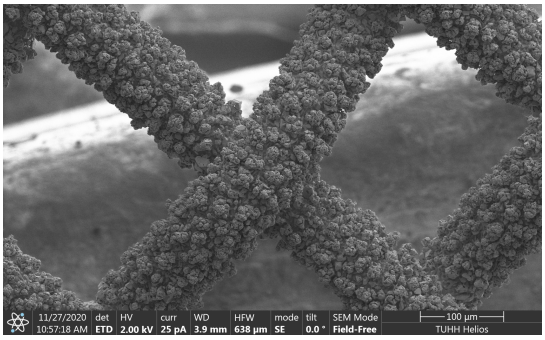

(g) 100 hour aging time

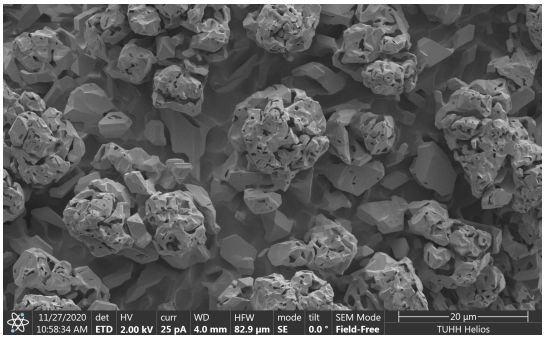

(h) 100 hour aging time detail view

Figure 7.1: SEM pictures of the first gauze of a stack aged for different time periods

cauliflower precursors in the size range of only a few micrometers. The parts of the gauze that are positioned in the slipstream of other wires, e.g. wire crossing points, are not considerably reconstructed after an aging time of one hour. The front side of the first gauze that was exposed to the reaction for ten hours is covered by cauliflowers with sizes of up to five micrometers. While the cauliflower size increased, the total number of cauliflowers is reduced compared to the one hour aged gauze. At the crossing point of two wires first morphological changes in the form of deep cavities are visible, but no cauliflower shaped protrusions are formed yet. On the gauze that was aged for 24 hours cauliflowers are also covering the wire crossing points. The cauliflower size increased to up to ten micrometers, while the total number of cauliflowers is further reduced compared to the ten hour aged gauze. The cauliflowers covering the 100 hours aged gauze have grown a bit in size compared to the 24 hours aged gauze, but the growth rate slowed down considerably.

Analysis of the front sides of the first gauzes in the stacks shows that the surface reconstruction starts initially with a high rate in the first hours under the used reaction conditions. Within 24 hours, the catalyst surface changes significantly from smooth wires to wires that are evenly covered with cauliflowers. Typical measurement campaigns with for example five profile measurements require typically at least ten hours. A measurement campaign conducted during the initial reconstruction phase would be significantly influenced by the considerable relative changes of the surface during the campaign, compromising the comparability of the measurements. The comparison of the gauzes aged for 24 hours and 100 hours shows that the rate of the relative changes of the catalyst surface slows down with increasing time on stream. Since aging times of 24 hours are also well feasible from a logistical point of view, gauzes should be aged for at least 24 hours before they are used in a profile measurement campaign. It should also be emphasized at this point, that the corrosion rate at the operation conditions chosen for the aging process are already at the upper limit of corrosion rates at which profile measurements with a sampling capillary are feasible at all without serious distortion of the profiles (see following Section 7.2). In the longest time periods of the profile measurement campaigns presented in the following chapters, the reactor was operated at lower temperatures, compared to the aging experiments presented in this

chapter, resulting in significantly reduced platinum loss rates. This way also the influence of catalyst reconstruction can be reduced in the measurement campaigns.

The performed aging experiments allow not only to analyze the degree of reconstruction of the first gauzes of a stack at different aging times but also allow to compare the different reconstruction degrees at varying relative positions within a gauze stack and the differences between the front and back sides of a gauze. Respective SEM pictures that were taken from the 100 hours aged gauze stack are shown in Figure 7.2.

In contrast to the front side of the first gauze (Figure 7.2 a and b) the back side of the first gauze (Figure 7.2 c and d) is not evenly covered with cauliflowers over the entire surface. At wire parts that are positioned in the slipstream, like the wire crossing shown in detail in Figure 7.2 d, the gauze is restructured but no complete cauliflowers are formed yet. The comparison of the front sides of the first, fifth, and tenth gauze of the stack shows that reconstruction mainly occurs at the top gauzes of a stack. While the front side of the first gauze is entirely covered with cauliflowers, the surface of the fifth gauze is significantly roughened and restructured but not covered with cauliflowers, while the tenth gauze is only slightly restructured.

The observed restructuring behavior, with a considerably restructured first gauze and only slightly restructured gauzes further downstream in the stack, is in line with results reported in literature [149]. The observation that wire parts positioned in the slipstream are less restructured supports those mechanistic theories that attribute reconstruction to surface reaction induced local differences in the PtO_2 formation rate. The most prominent of these theories is the hot spot theory. According to the hot spot theory, the reaction rate is not constant along the whole surface of a gauze due to varying activation and adsorption energies resulting from defects, edge dislocations, steps, or varying crystal facets as well as nonuniform elemental compositions. At positions favorable for the reaction high conversion rates of the strongly exothermic reaction result in the formation of hot spots several hundred degrees centigrade hotter than the average surface temperature. Volatile platinum components are transported from these hot spots to the vapor phase, where they decompose at lower temperatures and redeposit on the wire surface forming cauliflowers [71]. The comparison of back and front sides as well as the

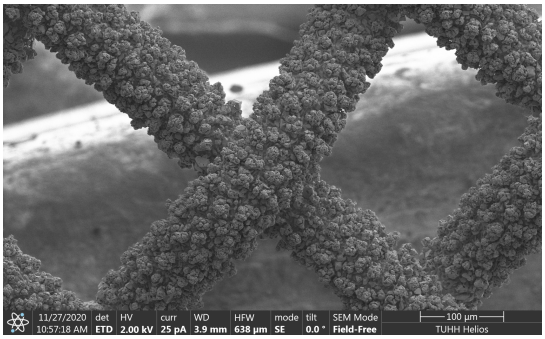

(a) First gauze, front side

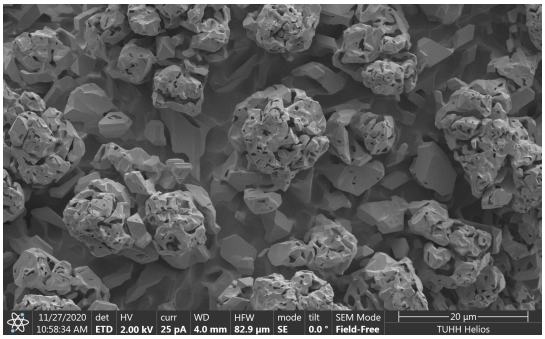

(b) First gauze, front side detail view

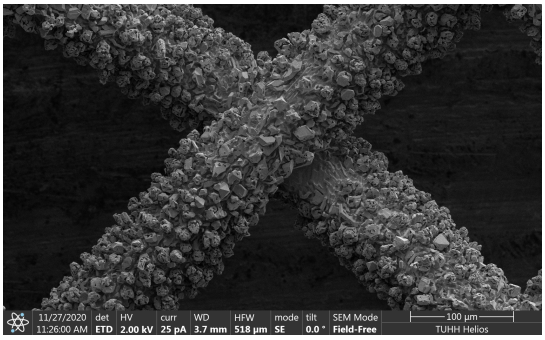

(c) First gauze, back side

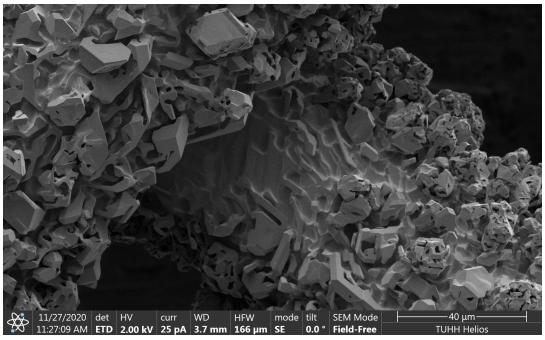

(d) First gauze, back side detail view

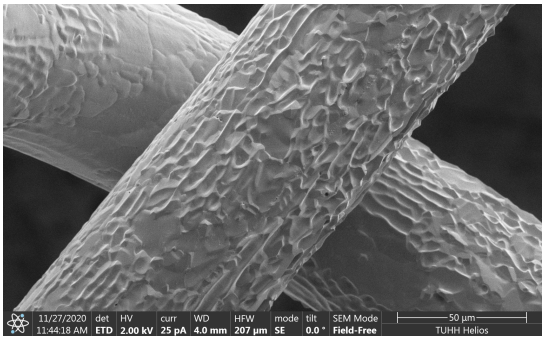

(e) Fifth gauze, front side

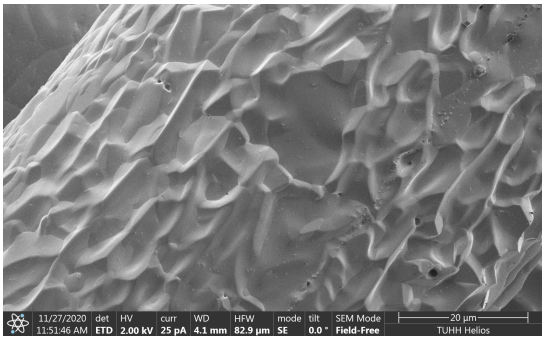

(f) Fifth gauze, front side detail view

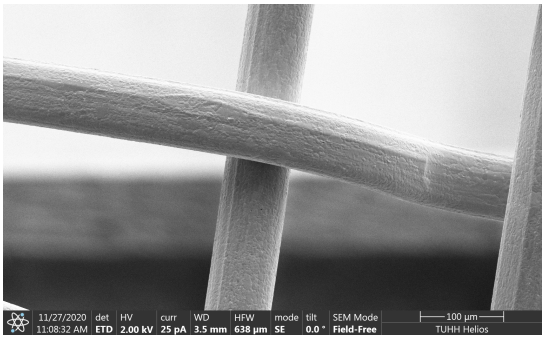

(g) Tenth gauze, front side

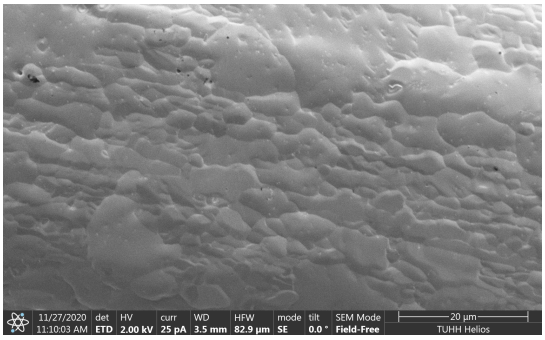

(h) Tenth gauze, front side detail view

Figure 7.2: SEM pictures of a 100 hours aged gauze stack. Comparison between the back and front side of the first gauze (a − d) as well as comparison between the front sides of different gauzes inside a stack (a,b,e − h)

generally less restructured wire parts positioned in slipstreams are in line with the hot spot theory. Mass transport rates of ammonia and oxygen are high towards wire parts that are directly exposed to the fresh educt gas stream resulting in high reaction rates, which may lead to the formation of hot spots. Gauze parts in the slipstream have significantly reduced mass transfer rates to their surface, leading to lower reaction rates that reduce the probability of hot spot formation and strong gauze restructuring. With increasing time on stream redeposition of volatile platinum, originated mainly from high reaction rate regions, also covers the low reaction rate regions of the gauzes. Thus, the catalyst restructuring observed in the aging experiments is in line with the popular hot spot theory. However, ex-situ analysis of aged gauzes is not providing any real new mechanistic insights into the restructuring process. For this more sophisticated operando experiments, analyzing the catalyst surface and the gas phase processes simultaneously with a high spatial and temporal resolution, would be a promising approach, but such experiments are out of the scope of this work.

7.2 Influence of sampling capillary coating

The restructuring of platinum alloy gauze catalysts in industrial ammonia oxidation and the associated influence on ammonia conversion as well as product selectivities are, at least phenomenologically, well described (see Section 2.4.2). Consequently, measurements of ammonia oxidation that claim comparability with industrial processes should be conducted with reconstructed gauzes. To provide comparability within a measurement campaign the gauzes should also not reconstruct considerably during a measurement campaign. However, another possible implication of the platinum losses needs to be considered as well: Are volatile platinum compounds transported and deposited in sampling lines used for gas phase product analysis in ammonia oxidation test reactors and if so, does deposited platinum influence the measurements? These two questions are of particular importance for profile measurements in which a sampling orifice is positioned in direct vicinity of catalyst wires increasing the risk of sampling volatile platinum species that can contaminate the sampling lines. As shown in this section, contamination of the sampling line with catalytically active deposits can in fact distort profile

measurements in ammonia oxidation reactors. Therefore, measures to detect and prevent the formation of catalytically active deposits in the sampling lines are presented.

In a first multiple days long profile measurement campaign an unexpected phenomenon was observed with increasing time on stream: In some measurements ammonia conversion and product formation were observed upstream of the gauze, even though the endoscope camera monitoring the reaction zone showed no reasonable explanation, like wires that got bent in upstream direction by the moving sampling capillary. The reaction was interrupted by stopping the ammonia flow to the reactor for 15 minutes. Upon reignition, no ammonia conversion was observed anymore at sampling orifice positions upstream of the gauze. However, once the next profile measurement was carried out, moving the sampling orifice downstream of the gauze and back up to its initial upstream position, ammonia conversion was again observed, while the orifice was translated upwards through the regions upstream of the catalyst gauze. The resulting molar flow rate profiles of ammonia, oxygen, nitric oxide, nitrous oxide, and nitrogen dioxide measured in consecutive profile measurements moving the sampling orifice first in downstream and secondly in upstream direction are shown in Figure 7.3.

The measurement was conducted at an inlet temperature of $T_{in} = 300$ °C, a pressure of $p_r = 1$ bara, an ammonia loading of 10 $\frac{\text{t N in NH}_3}{\text{m}^2\ \text{d}}$, with nitrogen as ballast medium and the following inlet molar fractions of oxygen $x_{O_2} = 0.15$, ammonia $x_{NH_3} = 0.10$ as well as argon $x_{Ar} = 0.02$. The azimuthal angle of the sampling orifice was kept constant throughout both measurements. Comparison between the molar flow rate profiles measured in downstream and upstream direction shows a hysteresis for all species. Upstream of the gauze, an ammonia molar flow rate of 3.3 mol/h was obtained for the downstream direction compared with a molar flow rate of 1.7 mol/h measured while moving the sampling orifice back upstream of the gauze. The profiles measured in upstream direction show significant product formation upstream of the gauze with molar flow rates of 0.025 mol/h for nitrous oxide, 0.30 mol/h for nitric oxide, and $0.01 - 0.02$ mol/h for nitrogen dioxide, while no products were formed upstream of the gauze in the profile measurement in downstream direction. Downstream of the gauze the profiles for both directions match.

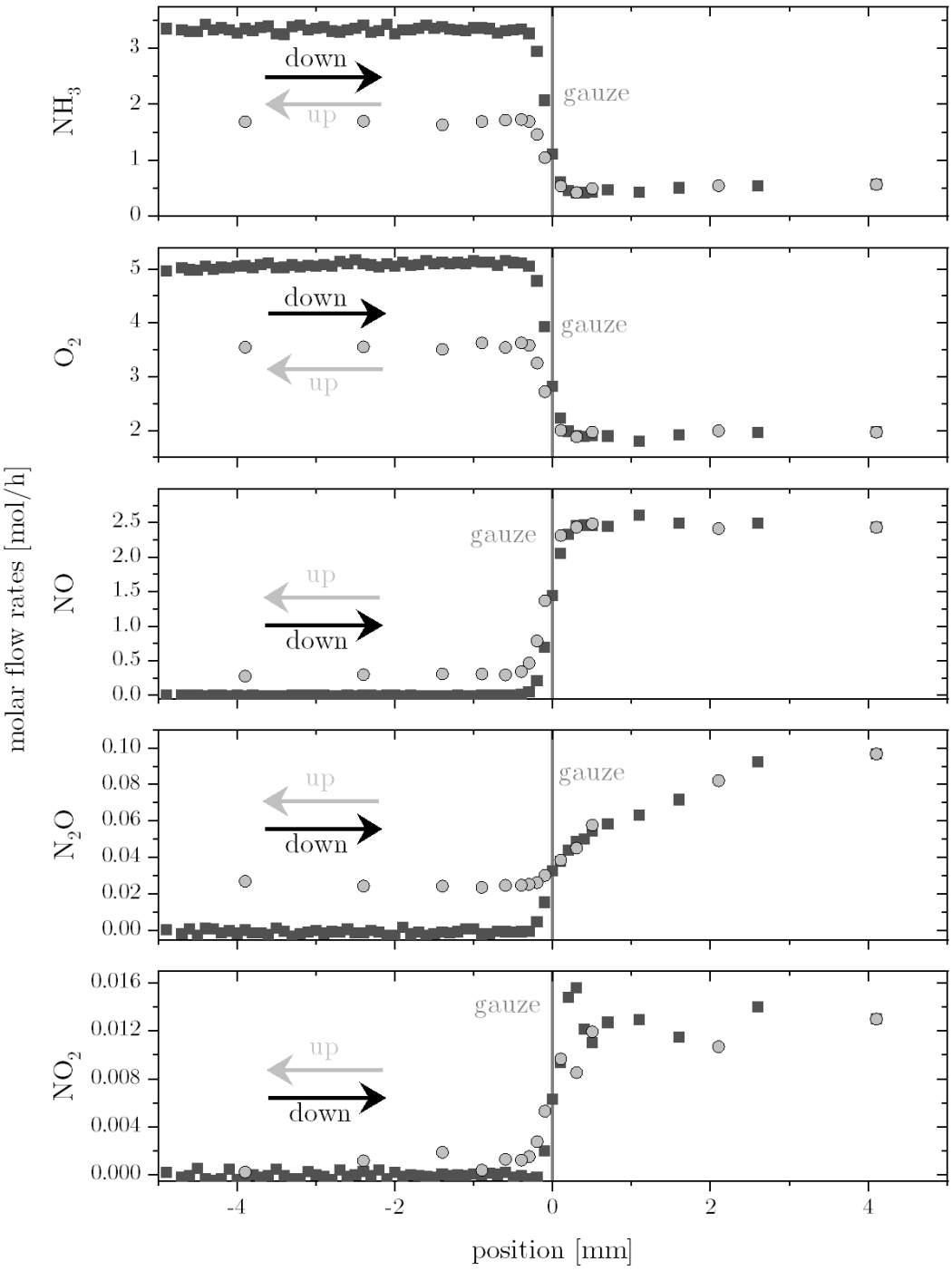

Figure 7.3: Comparison of molar flow rate profiles of ammonia, oxygen, nitric oxide, nitrous oxide and nitrogen dioxide measured in two opposing movement directions. First the sampling orifice was moved in downstream direction (black squares), subsequently the sampling orifice was moved back in upstream direction (grey circles). Operation conditions: $x_{O_2} = 0.15$, $T_{inlet} = 300$ °C, p = 1 bar, $x_{NH_3} = 0.10$, NH_3 loading = 10 $\frac{\text{t N in } NH_3}{\text{m}^2 \text{ d}}$

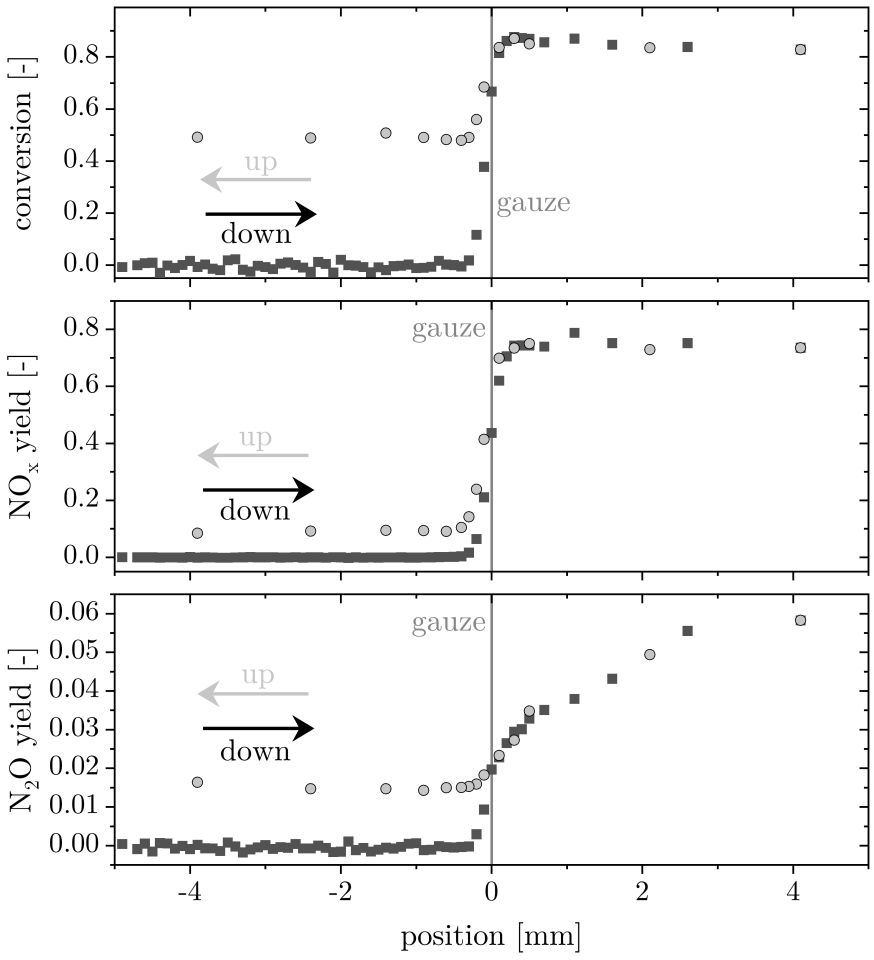

Figure 7.4: Comparison of ammonia conversion (top), nitric oxides yield (middle) and nitrous oxide yield (bottom) profiles for two opposing movement directions calculated from the molar flow rate profiles shown in Figure 7.3. Operation conditions: $x_{O_2} = 0.15$, $T_{inlet} = 300$ °C, p = 1 bar, $x_{NH_3} = 0.10$, NH_3 loading = 10 $\frac{\text{t N in } NH_3}{\text{m}^2 \text{ d}}$

The resulting ammonia conversions as well as nitric oxide and nitrous oxide yields, calculated from the molar flow rate profiles, are shown in Figure 7.4. The ammonia conversion as well as nitric oxide and nitrous oxide yield profiles show the same hysteresis trends as the molar flow rate profiles. Downstream of the gauze the profiles match. Upstream of the gauze conversions of $X_{NH_3} = 0.49$, nitric oxides yields of $Y_{NO_x} = 0.092$ and nitrous oxide yields of $Y_{N_2O} = 0.015$ are obtained for

the measurement in upstream direction compared to ammonia conversions and product yields of zero obtained for the measurement in downstream direction.

The origin of the profile hystereses was found when the quartz sampling capillary was removed from the profile reactor. A light gray coating was visible at the parts positioned in regions around the catalyst gauzes. Corresponding light microscope pictures of a capillary part positioned upstream of the gauzes, the capillary part around the sampling orifice, and a capillary part downstream of the orifice are shown in Figure 7.5.

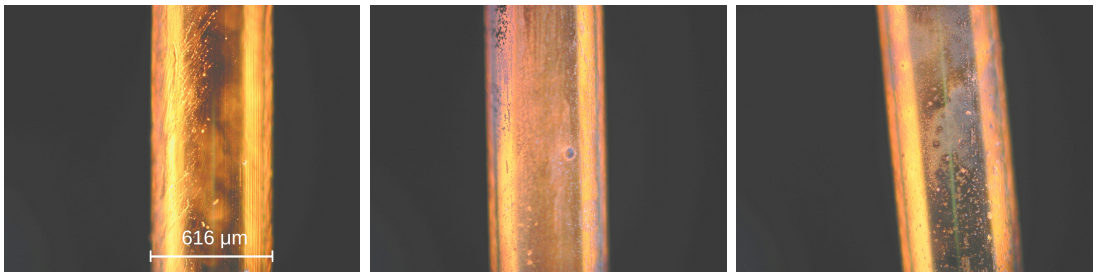

(a) Upstream **(b)** Orifice **(c)** Downstream

Figure 7.5: Light microscope pictures of different parts of the sampling capillary used in the profile measurements shown in Figures 7.3 – 7.7. (a) Capillary part that was positioned upstream of the gauzes over the entire measurement campaign. (b) Coated capillary part with the sampling orifice in the middle of the picture. (c) Capillary part that was positioned downstream of the gauze over the entire measurement campaign

The capillary part that was positioned upstream of the gauzes over the entire measurement campaign shows no signs of any coating or other contamination. Both the capillary region around the sampling orifice and the capillary part positioned downstream of the gauze show clear signs of a light gray coating on the capillary. Apparently, volatile platinum compounds formed during the reaction not only lead to restructuring of platinum gauzes, but are also deposited on and, more importantly, inside the sampling capillary, forming the thin gray capillary coating visible in Figures 7.5 b and c.

The coating growth process and the ignition process of the resulting inner capillary coating that lead to the hystereses in the profiles are schematically illustrated in Figure 7.6.

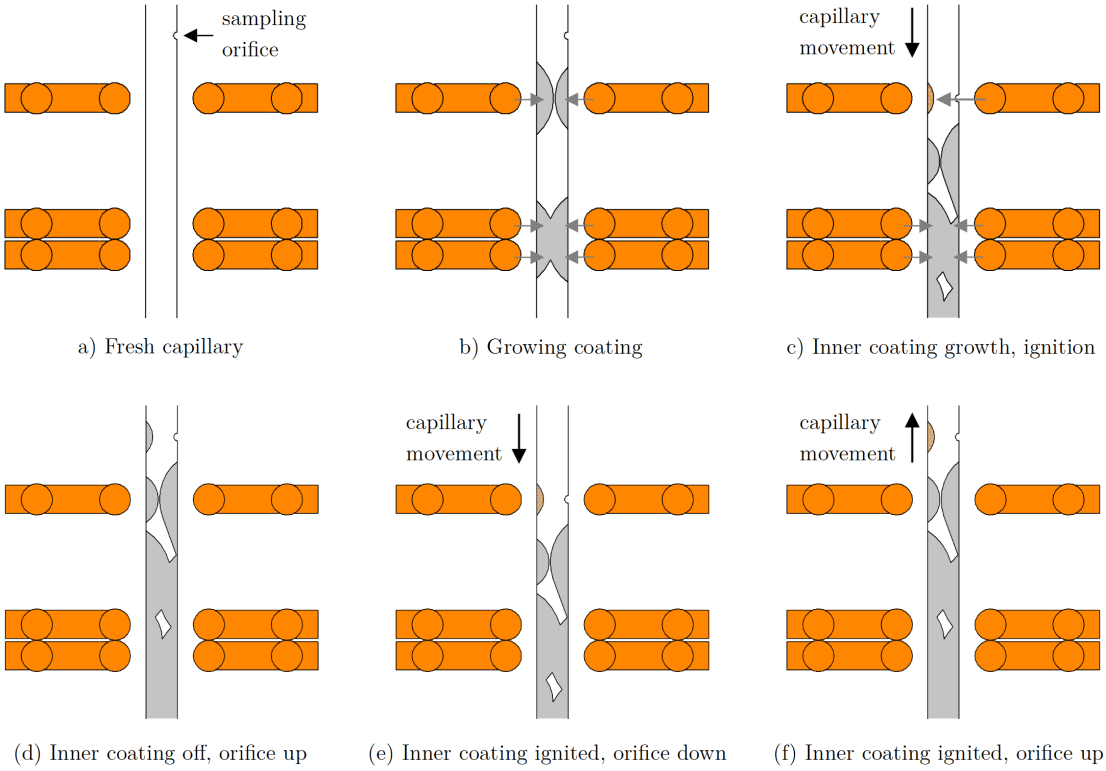

Figure 7.6: Sketch picturing the growth process of platinum coating on the capillary walls (a − c) and the ignition process of inner coating leading to the measured hysteresis in the molar flow rate profiles (d − f)

At the beginning of a measurement campaign a fresh, uncoated sampling capillary is installed inside the profile reactor (Figure 7.6 a). Upon ignition of the reaction volatile platinum compounds are formed at the gauze, transported towards, and subsequently deposited at the capillary walls, starting the coating growth process at the outside capillary walls (Figure 7.6 b). At this point the sampling orifice is usually positioned upstream of the catalyst gauzes so that no volatile platinum compounds are sampled, which could contaminate the sampling line. During a profile measurement the sampling orifice is moved in downstream direction passing the analyzed catalyst gauze and is finally positioned between the analyzed gauze and afterburner gauzes, which are usually positioned downstream of the analyzed gauze. As soon as the sampling orifice passes through regions in which products are sampled, viz. as soon as first sampled streamlines extend into

the region of a gauze (see Section 5.1), volatile platinum compounds are sampled through the sampling orifice. At the outlet of the sampling orifice a supersonic jet is formed directing the sampled molecule stream with high flow velocities against the inner capillary wall opposite of the sampling orifice. Starting with this first contact volatile platinum compounds are deposited also at the inside of the sampling capillary, most likely mainly directly opposite of the sampling orifice. The coating ignites and becomes catalytically active, resulting in a distortion of the measured profiles, if the coating is positioned in the hot regions around the gauze (Figure 7.6 c).

In the first measurement campaign the reactor system was tested for multiple days in a row while positioning the sampling orifice sometimes directly at the analyzed first catalyst gauze for periods longer than one hour. In some measurements the reactor was operated at extreme operation conditions with inlet temperatures of 300 °C and oxygen inlet molar fractions of up to $x_{O_2} = 0.40$, leading to high platinum loss rates. Thus, before starting the profile measurements shown in Figures 7.3 and 7.4 at the last day of the campaign, a significant coating layer was already formed inside the sampling capillary. Before the start of the profile measurement, the catalytic activity of the coating was extinguished by interrupting the ammonia feed to the reactor for 15 minutes. The cooled ammonia coating did not reignite after restarting the ammonia feed as long as the sampling orifice was still positioned upstream of the gauze (Figure 7.6 d). After one hour the profile measurement in downstream direction was started, moving the sampling orifice and the inner capillary coating in the hot vicinity of the analyzed gauze. In the vicinity of the gauze the inner coating got heated up by radiation of the gauze and was also bombarded with hot sampled molecules, igniting the coating. Therefore, the profile measurement in upstream direction was started with an already hot, ignited inner capillary coating (Figure 7.6 e). During the profile measurement in upstream direction the already ignited coating was bombarded with sampled hot reaction products or, at positions upstream of the gauze, bombarded with the sampled fresh educt stream. The resulting ammonia conversion at the coating provided enough heat to keep the coating ignited at upstream positions (Figure 7.6 f), resulting in the measured hystereses. Using a type-K thermocouple the tempera-

ture inside the sampling capillary was recorded. The corresponding temperature profiles measured in both directions are shown in Figure 7.7.

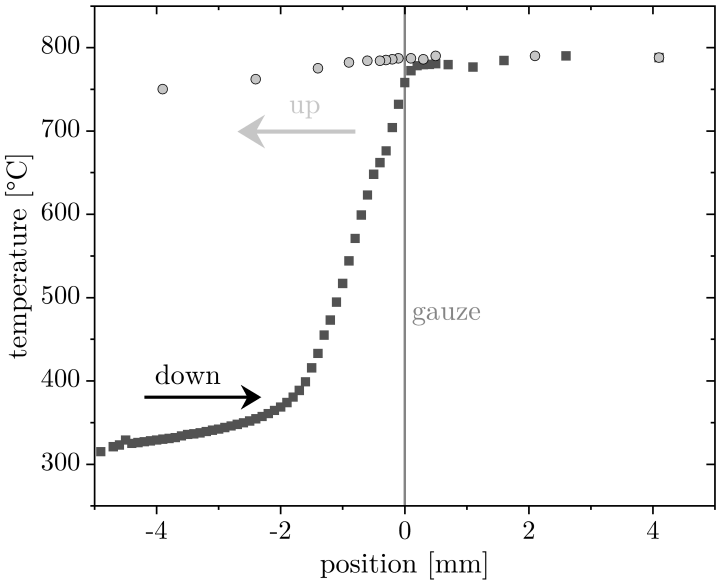

Figure 7.7: Comparison of temperature profiles measured with a type-K thermocouple in two opposing movement directions. Operation conditions: $x_{O_2} = 0.15$, $T_{inlet} = 300$ °C, p = 1 bar, $x_{NH_3} = 0.10$, NH_3 loading = 10 $\frac{\text{t N in } NH_3}{m^2\ d}$

The temperature profiles show a hysteresis as well, in line with the measured molar flow rate profiles. In downstream direction the thermocouple temperature increases first with a low slope and then with a higher slope for sampling orifice positions closer than 1.5 millimeters to the catalyst gauze. In upstream direction the temperature decreases only a bit starting with a temperature of 787 °C at the gauze and ending with a temperature of 750 °C 3.9 millimeters upstream of the gauze, due to the heat of reaction produced by the surface reactions at the capillary coating.

A second profile measurement was performed on the same day like the profile measurement discussed on the previous pages using identical operation conditions except for higher oxygen inlet molar fraction of $x_{O_2} = 0.40$ compared with $x_{O_2} = 0.15$ in the first measurement. The molar flow rate profiles measured at increased oxygen inlet molar fractions are shown in Figure 7.8.

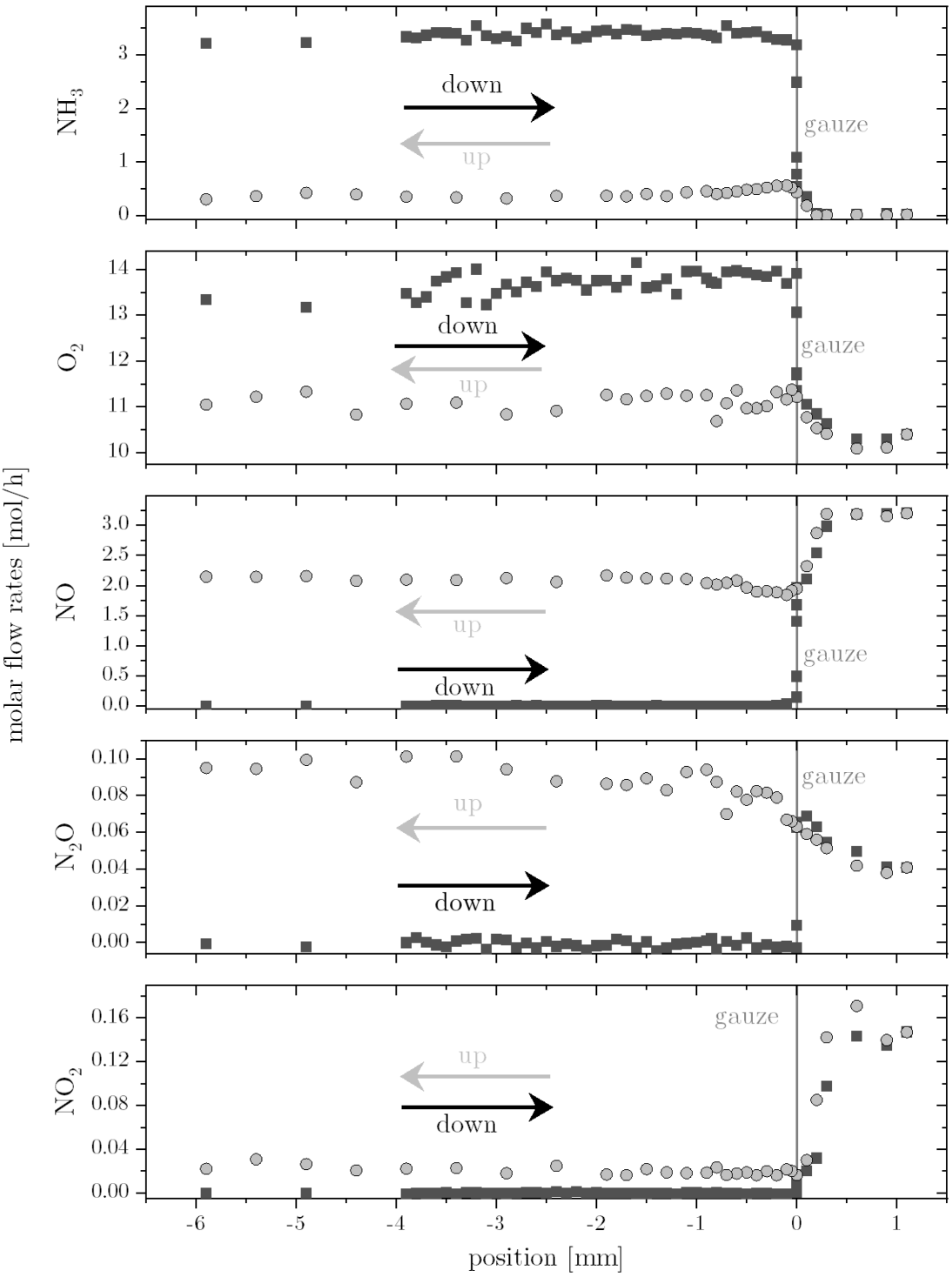

Figure 7.8: Comparison of molar flow rate profiles of ammonia, oxygen, nitric oxide, nitrous oxide and nitrogen dioxide measured in two opposing movement directions. Operation conditions: $x_{O_2} = 0.40$, $T_{inlet} = 300\ °C$, $p = 1$ bar, $x_{NH_3} = 0.10$, NH_3 loading $= 10\ \frac{\text{t N in } NH_3}{m^2\ d}$

All measured molar flow rate profiles show a hysteresis for the higher oxygen inlet molar fraction of $x_{O_2} = 0.40$ as well. High ammonia conversions were measured at upstream orifice positions in the profile measurement in upstream direction as shown in Figure 7.9.

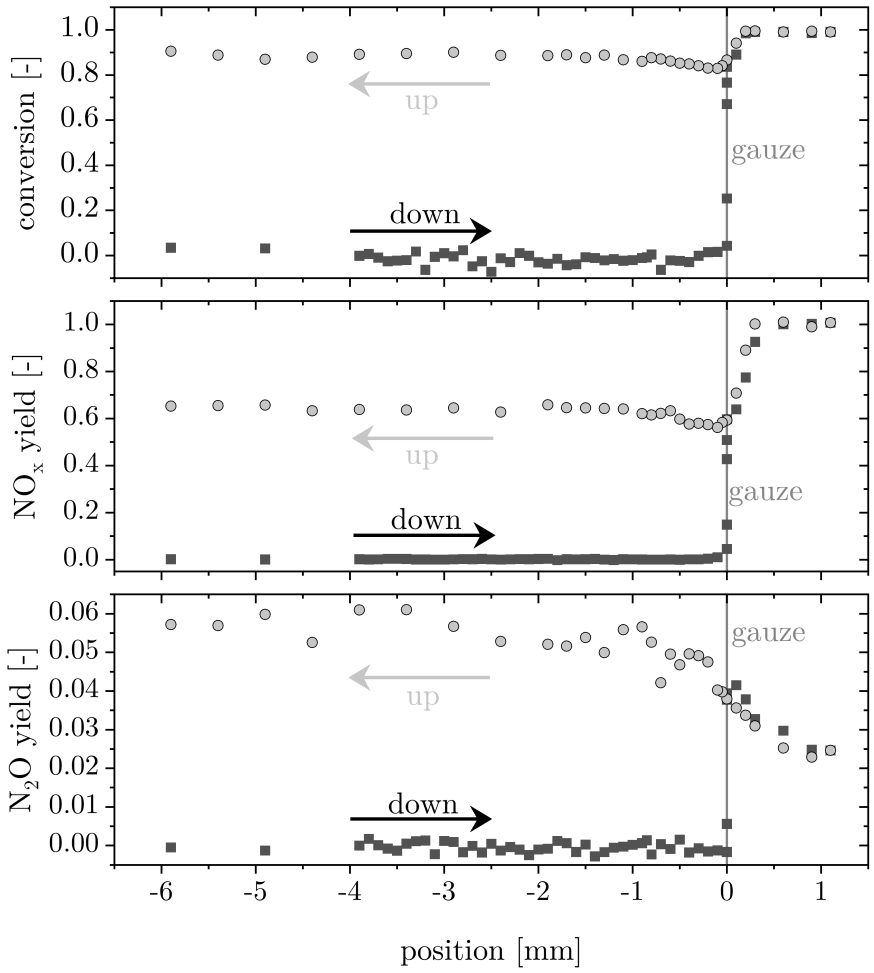

Figure 7.9: Comparison of ammonia conversion (top), nitric oxides yield (middle) and nitrous oxide yield (bottom) profiles for two opposing movement directions calculated from the molar flow rate profiles shown in Figure 7.8. Operation conditions: $x_{O_2} = 0.40$, $T_{inlet} = 300$ °C, p = 1 bar, $x_{NH_3} = 0.10$, NH_3 loading = 10 $\frac{\text{t N in } NH_3}{\text{m}^2 \text{ d}}$

The measured ammonia flow rates upstream of the gauze in upstream direction of about 0.4 mol/h correspond to ammonia conversions of $X_{NH_3} = 0.88$, significantly higher than ammonia conversions of $X_{NH_3} = 0.49$ obtained in the measure-

ment at an oxygen inlet molar fraction of $x_{O_2} = 0.15$. For nitric oxides a yield of approximately $Y_{NO_x} = 0.64$ and for nitrous oxide a yield of $Y_{N_2O} = 0.055$ was obtained upstream of the gauze in upstream direction at an oxygen inlet molar fraction of $x_{O_2} = 0.40$. This corresponds to nitric oxides selectivities of $S_{NO_x} = 0.73$ and nitrous oxide selectivities of $S_{N_2O} = 0.065$. Both selectivities were higher than the according selectivities of $S_{NO_x} = 0.19$ for nitric oxides and $S_{N_2O} = 0.03$ for nitrous oxide calculated for positions upstream of the gauze in upstream direction at an oxygen inlet molar fraction of $x_{O_2} = 0.15$.

The measured flow rates, corresponding ammonia conversion, product yields, and selectivities obtained upstream of the gauze in upstream direction for both oxygen inlet molar flow rates result from surface reactions at the capillary coating. Considerably different selectivities were obtained downstream of the gauze, for example a nitric oxides selectivity of $S_{NO_x} = 0.87$ corresponds to nitric oxides yields of $Y_{NO_x} = 0.74$ and ammonia conversions of $X_{NH_3} = 0.85$ measured downstream of the gauze at an oxygen inlet molar fraction of $x_{O_2} = 0.15$. The coating was thus not only highly catalytically active, as demonstrated by the high ammonia conversions measured upstream of the gauze in upstream direction, but surface reactions at the coating result also in different product selectivities than surface reactions at the catalyst gauze. Hence, it can be expected that the molar flow rate profiles, the corresponding ammonia conversion, and product selectivities measured around and downstream of the gauze were significantly distorted by the catalytically active coating.

To explain the large differences in selectivities obtained from surface reactions at the gauze compared to surface reactions at the coating, the surface coverages have to be considered. Recent simulation and experimental studies agree that the surface coverages of the catalyst are decisive for the product selectivities [9–13]. High surface coverage with NH_x (with x= $0, 1, 2, 3$) species result in high formation rates of nitrogen and nitrous oxide while higher surface coverage with oxygen favors nitric oxide formation [3,10–17]. The surface coverages at the gauze and the coating are strongly influenced by the different flow regimes around the respective catalytically active surface. On the one hand, a laminar gas flow evolves around the catalyst gauzes in the reactor, forming a defined boundary layer around the wires. The reaction rate is determined by diffusion of educt molecules through

the boundary layer to the catalyst surface, resulting in generally low surface coverages. On the other hand, the sampled gas stream is directed in a supersonic jet against the capillary wall located at the backside of the sampling orifice. If this capillary region is coated with a catalytically active coating, the sampled molecules are bombarding against this catalytically active surface with high flow velocities, resulting in a completely different flow regime compared with the laminar flow around the gauze wires. The bombardment with sampled molecules from the directed supersonic jet should result in considerably higher surface coverages of NH_x species and oxygen on the coating in comparison with the gauze surface coverages. This could explain why decreased nitric oxides selectivities were measured upstream of the gauze for both oxygen inlet concentrations compared with the respective selectivities obtained around the catalyst gauze. Both, the surface coverage with NH_x species and oxygen, were probably considerably higher on the coating surface compared with the gauze surface, but the negative influence of high NH_x species surface coverages dominated the positive effect of increased oxygen surface coverage with respect to nitric oxides formation rates.

Comparison of the measurements at the two different oxygen inlet molar fractions shows strongly differing selectivities at the ignited coating for positions upstream of the gauze. For an oxygen inlet molar fraction of $x_{O_2} = 0.40$ a nitric oxides selectivity of $S_{NO_x} = 0.73$ was obtained, compared with a nitric oxides selectivity of just $S_{NO_x} = 0.19$ at an oxygen inlet molar fraction of $x_{O_2} = 0.15$. The considerable increase in oxygen inlet molar flow rate results in considerably increased oxygen surface coverages, while the NH_x species surface coverages should stay in the same range for both measurements. The considerably higher oxygen surface coverages favor nitric oxide formation, due to the higher probability of recombination of NH_x surface species with adsorbed oxygen, and reduces the probability of recombination of two NH_x surface species, which leads to formation of the side product nitrogen. Nitrogen is the main product formed at the coating for an oxygen inlet molar fraction of $x_{O_2} = 0.15$. Especially interesting is the comparison of the nitrous oxide formation rates at the ignited coating for the two different oxygen inlet molar fractions. While for an oxygen inlet molar fraction of $x_{O_2} = 0.40$ the measured nitrous oxide molar flow rates and the corresponding nitrous oxide yield increased in upstream direction, the nitrous oxide molar

flow rates and yields decreased for an oxygen inlet molar fraction of $x_{O_2} = 0.15$ in upstream direction. These differences in nitrous oxide formation can also be explained based on the surface coverages. The main formation route for nitrous oxide is, according to most mechanistic models (see Sections 2.3.1 and 2.3.2), the surface reaction of adsorbed nitric oxide with adsorbed nitrogen atoms. Considerably higher nitric oxide formation rates were measured for the ignited coating at an oxygen inlet molar fraction of $x_{O_2} = 0.40$ compared to an oxygen inlet molar fraction of $x_{O_2} = 0.15$. Thus, considerably less adsorbed nitric oxide should cover the coating surface at low oxygen inlet molar fractions, reducing the probability of surface reactions between adsorbed nitric oxide and adsorbed nitrogen atoms. Therefore, considerably higher nitrous oxide formation rates are obtained at higher oxygen inlet molar fractions in the special flow regime around the ignited coating. Further factors that could influence the different selectivities obtained at the ignited coating and the catalyst gauzes could be varying elemental composition and different surface characteristics of the coating and the gauze, the lower pressures as well as the lower temperatures (see Figure 7.7) inside the sampling capillary. Even though capillary coating is an unwanted effect in ammonia oxidation profile measurements, some interesting characteristics were observed. Therefore, future studies of the matter might be of interest, for example CFD studies looking into the question, how a super sonic beam directed against the capillary coating influences the surface coverages on the coating and the product selectivities, to verify the hypotheses presented here.

All in all, the two measurements presented in this chapter show that volatile platinum compounds can be deposited in the sampling capillary and lead to the formation of a catalytically active coating, which distorts the measured profiles. Such a distortion is usually not wanted. Therefore, a methodology was developed to detect the formation of capillary coating in measurement campaigns, tests were conducted to determine at which operation conditions high coating rates significantly complicate measurements, and the measurement protocol was optimized to minimize the coating formation rate. After the first profile measurement campaign discussed in this chapter, the profile measurement protocol was optimized by minimizing the residence time of the sampling orifice in close vicinity and downstream of the catalyst gauzes. By keeping the sampling orifice upstream of the

gauze for the longest time periods of a measurement campaign, less volatile platinum compounds are sampled and deposited in the sampling capillary, reducing the influence of capillary coating on measured profiles. Furthermore, measurements in upstream and downstream direction are performed according to the new protocol with different movement speeds. A measurement is started by setting the respective operation conditions and waiting till steady state is reached. Over this time period the sampling orifice is positioned upstream of the gauze. Afterward, the sampling orifice is moved with comparably high movement speed downstream of the gauze. This is followed by a slower measurement in upstream direction, stopping at each analyzed position. The measured signal intensities in upstream and downstream direction are compared and checked for hysteresis, to determine if a catalytically active coating affected the measurements. If an active coating is detected, the measurement campaign needs to be stopped and a new sampling capillary needs to be installed, to guarantee that profile measurements are not affected by capillary coating. At combined high inlet temperatures of 300 °C and high oxygen inlet molar fractions of $x_{O_2} = 0.30 - 0.40$ only up to two profile measurements were possible before first profile hysteresis were detected. The measurement campaigns presented in detail in the following chapters were conducted for most experiments at milder conditions, with lower inlet temperatures and/or lower oxygen molar fractions. In these measurement campaigns no signs of profile hysteresis were observed and no signs of capillary coating were visible around the sampling capillary after disassembling the reactor at the end of the campaigns. The capillary coating rate is an important factor that should be considered in the planning process of a measurement campaign.

To resolve the steep gradients in ammonia oxidation a sampling probe needs to be positioned in direct close vicinity to the studied catalyst gauzes. Under typical industrial operation conditions formation of volatile platinum compounds is inevitable. Accordingly, volatile platinum compounds will be sampled and deposited in any sampling lines used in ammonia oxidation reactors. The short distances between sampling orifice and catalyst gauzes in profile measurements can result in the formation of coatings that strongly influence the measurements. However, the possibility to move the sampling orifice to positions upstream and downstream of the gauze allows for a constant inspection for active coatings, by

checking for profile hysteresis. Sampling capillaries can be exchanged, once measurements are affected by coating. In contrast, in setups with fixed sampling lines positioned permanently downstream of catalyst gauzes no easy check for catalytic active coatings by hysteresis checks can be performed. Fluctuations in measured signals, like slowly decreasing measured ammonia signals, might be wrongly attributed to, for example, errors in analytic systems. On the other hand, reduced coating rates can be anticipated in setups with sampling orifices positioned several millimeters or centimeters downstream of catalyst gauzes, since less volatile platinum compounds are transported and deposited inside sampling lines. Nevertheless, sampling lines used in such experimental setups should be checked regularly for catalytically active coatings. Otherwise, platinum might agglomerate in the sampling lines and distort the measurements. Also, coating rates should be taken into account for positioning of sampling orifices, e.g. a permanently installed sampling orifice should not be positioned in close vicinity to catalyst gauzes.

8 Influence of the Inlet Temperature

After establishing the basics of profile measurements in ammonia oxidation, by providing the required qualitative understanding of the measured profiles in Chapter 5 and introducing the importance of excluding capillary coating in experiments in Chapter 7, a quantitative comparison between the measured profiles and the simulated undisturbed profiles is drawn in this chapter. For this, the influence of the gas inlet temperature on the reactor performance is taken as an example. By comparing measured and simulated profiles the capability of a reaction mechanism to predict ammonia oxidation under industrial conditions can be analyzed, as demonstrated here for the Kraehnert and Baerns mechanism [41]. Furthermore the possibilities to couple additional analytical techniques with the sampling capillary are shown exemplarily for gauze temperature measurements by means of fiber pyrometry. This chapter is an extended version of Chapter 3.2 of the publication [207] providing additional data and a more detailed discussion of the results. The CFD simulations shown in this chapter have been conducted by Dr. Sven Jakobtorweihen.

8.1 Influence of the inlet temperature on educt conversion and product selectivity

The aim of this work was the development of an experimental setup that enables resolving the processes inside ammonia oxidation reactors under industrial conditions. Profile measurements can bridge the gap of experimental data required for validation of existing and the development of future ammonia oxidation reaction mechanisms. As a first step in this direction, a quantitative comparison of experimental and simulated species profiles for varying inlet temperatures is provided in

this section. The profile measurements were conducted using the orifice to gauze arrangement at medium distance with the orifice pointing into a 90° corner of two crossing wires shown on the right side of Figure 5.10 in Section 5.2. The inlet temperature was varied from 100 °C to 300 °C in steps of 50 °C, while keeping the reactor pressure and the inlet flow rates constant. As shown in Figure 5.6 and discussed in Section 5.1, the sampling volume does not change much if only the inlet gas temperature is varied and the orifice is translated along one and the same scan line. All changes observed in the profiles can be directly attributed to changing performance of the catalyzed reaction in the same region. The measured molar flow rate profiles of the most important species and the corresponding undisturbed simulated profiles for the five different inlet temperatures are shown in Figure 8.1.

While the shapes of the profiles do not change noticeably, a clear trend in the outlet flow rates is visible upon increasing the inlet temperature. The simulated outlet flow rates of ammonia and oxygen decrease with increasing inlet temperatures resulting in increasing ammonia conversions as shown in Figure 8.2.

Under the given reaction conditions, the rate of ammonia conversion is determined by the rate of transport of ammonia to the catalyst surface. The molar flux of a species s to the wire surface, $j_{\mathrm{surface},s}$ in mol/(m^2·s), is given by the product of the mass transfer coefficient $k_{\mathrm{c},s}$ and the driving force for diffusion, viz. the concentration gradient between the bulk phase and the wire surface $c_{\mathrm{bulk},s} - c_{\mathrm{surface},s}$.

$$j_{\mathrm{surface},s} = k_{\mathrm{c},s} \cdot (c_{\mathrm{bulk},s} - c_{\mathrm{surface},s}) \tag{8.1}$$

The mass transfer coefficient for flow around a gauze or a stack of gauzes can be described with the correlation by Shah et al. [133] using the Reynolds number Re, the Schmidt number Sc, the diffusion coefficient D_s and the wire diameter d_{w}.

$$k_{\mathrm{c},s} = 0.644 \; Re^{0.43} \; Sc^{\frac{1}{3}} \; \frac{D_s}{d_{\mathrm{w}}} \tag{8.2}$$

The Reynolds and Schmidt numbers are calculated from the superficial mass flux G_{r}, the wire diameter d_{w}, the viscosity μ, the fraction of the reactor cross section that is open to the flow γ, the density ρ and the diffusion coefficient D_s.

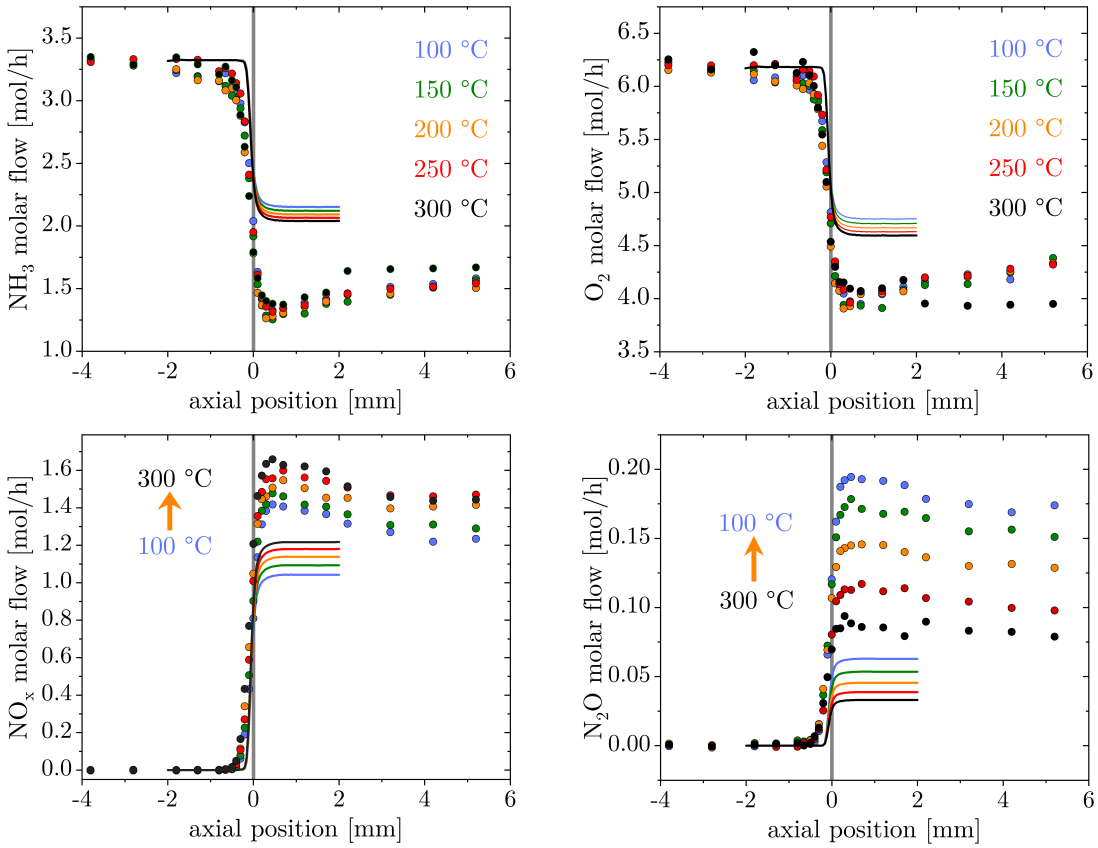

Figure 8.1: Undisturbed simulated (line) and measured sampled (circles) species molar flow profiles of NH_3, O_2, NO_x and N_2O at varying inlet temperatures of 100 °C, 150 °C, 200 °C, 250 °C and 300 °C. Operation conditions: p = 5 bar, $x_{NH_3} = 0.10$, $x_{O_2} = 0.186$, NH_3 loading = 10 $\frac{\text{t N in } NH_3}{\text{m}^2\ \text{d}}$. Figure taken from [207]

$$k_{c,s} = 0.644 \left(\frac{G_r\ d_w}{\mu\ \gamma}\right)^{0.43} \left(\frac{\mu}{\rho D_s}\right)^{\frac{1}{3}} \frac{D_s}{d_w} \tag{8.3}$$

The correlation was successfully validated for industrial ammonia oxidation by Warner et al. [10,17] showing good agreement with their experimental results over a wide range of operation conditions. Factoring in the temperature dependence of all variables $\rho \propto \frac{1}{T}$, $\mu \propto \sqrt{T}$, $D_s \propto T^{1.5}$, $c_{\text{bulk},s} \propto \frac{1}{T}$ [219], yields that the molar flux of species s to the wire surface depends only mildly on temperature $j_{\text{surface},s} \propto T^{0.285}$. In consequence, increasing the reactor inlet temperature leads

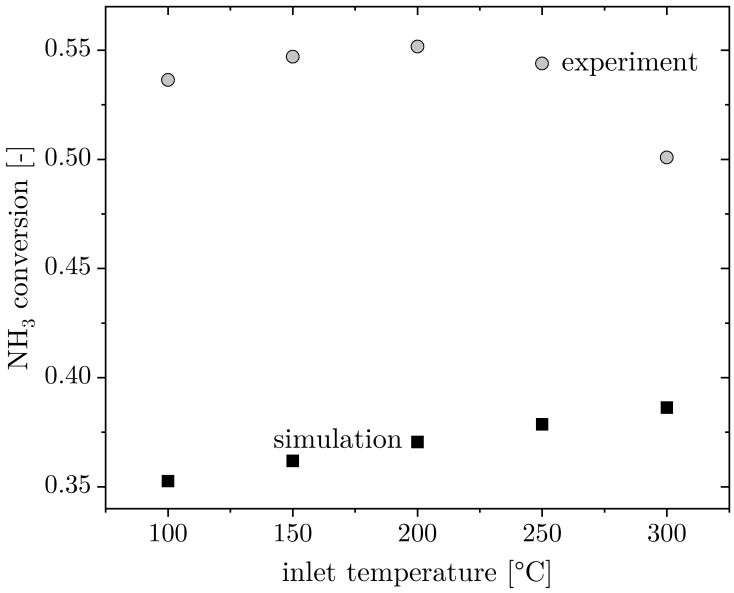

Figure 8.2: Simulated (squares) as well as experimental (circles) NH_3 conversions obtained for varying inlet temperatures of 100 °C, 150 °C, 200 °C, 250 °C and 300 °C. Operation conditions: p = 5 bar, $x_{NH_3} = 0.10$, $x_{O_2} = 0.186$, NH_3 loading = 10 $\frac{\text{t N in } NH_3}{\text{m}^2 \text{ d}}$. Figure taken from [207]

to a small increase in ammonia conversion as predicted by simulation (solid lines in Figure 8.1).

The experimental educt flow rates (full circles in Figure 8.1) and the corresponding ammonia conversion (Figure 8.2) do not show such a clear trend. At a temperature of 100 °C, 150 °C, and 200 °C the expected trend of increasing ammonia conversion is observed. At 250 °C ammonia conversion does not increase further and at 300 °C ammonia conversion is significantly lower than for the other temperatures. This behavior cannot be explained by theory and could be due to turbulences, gauze changes, or instabilities in the MS product analysis. Evidence for the latter are the distinct steps visible in the species profiles of ammonia, oxygen, and nitrous oxide at a position of 2.2 mm downstream of the gauze occurring only in the measurement at 300°C. Analysis of the MS raw data shows that at this position a distinct reduction of all signal intensities was measured. The origin of this reduction in signal intensities could not be identified, for example, the recorded pressure inside the vacuum chamber of the mass spectrometer was stable,

the recordings of reactor pressure, temperature, gas flow rates, and also the video recordings of the endoscope camera showed no abnormalities.

One important factor that leads to systematic deviations between simulations and experiments is the corrosion state of the gauze. With increasing time on stream the catalyst gauzes undergo considerable reconstruction during which the initially smooth wires transform into highly corroded wires exposing cauliflower shaped protrusions (see Chapter 7). The resulting increase in catalyst surface area is virtually increasing the wire diameter having a positive effect on the overall mass transfer rate [11]. Hence, gauze corrosion leads to increased ammonia conversion [3, 11]. The gauze used in the measurement campaign shown in Figure 8.1 was aged for 92 hours on stream before measurements were begun, to ensure a well developed and stationary cauliflower coverage during the measurements. In the model smooth wires were used which is probably the reason that higher ammonia conversion is observed experimentally compared to simulations (Figure 8.2).

For the products nitric oxide and nitrous oxide opposing trends are predicted by simulations. With increasing inlet temperatures, the simulated nitric oxide flow rates increase while the nitrous oxide flow rates decrease (Figure 8.1). These trends are also observed in the experiments. If the flow rates at the end of the measurement domain are converted into nitric oxide as well as nitrous oxide yields and selectivities the data shown in Figure 8.3 are obtained.

Qualitatively, the trends that higher reactor inlet temperatures lead to higher nitric oxide and reduced nitrous oxide selectivities are observed both in experiments and simulations, in agreement with results reported by other groups in literature [3, 14, 17]. Especially significantly lower nitrous oxide selectivities at higher temperatures are of particular importance for optimizing the process under economical as well as ecological aspects considering the fact that nitrous oxide is a potent green-house gas. However, increased inlet temperatures come along with significantly increased platinum loss rates as discussed in Section 2.4.2 and also observed by increased capillary coating rates in our experiments (see Section 7.2). Quantitatively, the experimental nitrous oxide as well as the nitric oxide molar flow rate profiles, selectivities, and yields deviate significantly from the simulated values. In the simulations, the nitric oxide yield and selectivity are generally overestimated, while the nitrous oxide yield and selectivity are strongly under-

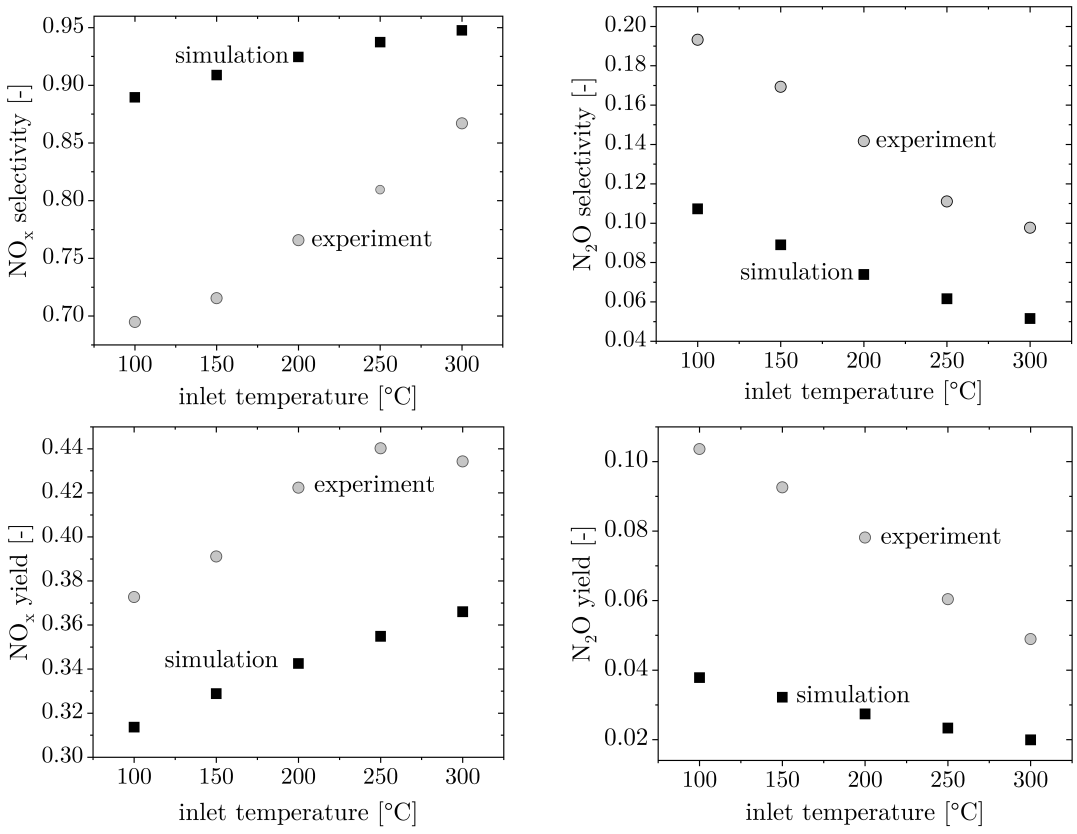

Figure 8.3: Simulated (squares) as well as experimental (circles) NO_x selectivities and yields as well as N_2O selectivities and yields obtained for varying inlet temperatures of 100 °C, 150 °C, 200 °C, 250 °C and 300 °C. Operation conditions: p = 5 bar, $x_{NH_3} = 0.10$, $x_{O_2} = 0.186$, NH_3 loading = 10 $\frac{\text{t N in } NH_3}{\text{m}^2 \text{ d}}$. Selectivity plots taken from [207].

estimated. This is because, in lack of better alternatives, the kinetic model for ammonia oxidation on platinum developed by Kraehnert and Baerns [41] was used for the simulations, which was not established for industrial reactor conditions. The mechanism by Kraehnert and Baerns is based on experimental data measured at temperature and pressure conditions at which the reaction is kinetically controlled (286 °C − 385 °C, 1 − 6 bar). In the present work, the reactor pressure is at 5 bar, similar to the pressures used by Kraehnert and Baerns, but the catalyst operates in mass transfer control with gauze temperatures at industrial conditions between 800 °C and 1000 °C (see following section). Considering this strong extrapolation of the Kraehnert and Baerns model to industrial conditions,

the observed deviations between simulated and experimental conversion and selectivities are still reasonable but there is no quantitative match. Most importantly, the Kraehnert and Baerns model captures the experimental trends correctly which enables to screen the parameter space of the process for more favorable conditions than currently applied in industry. However, a systematic, knowledge-based optimization of the process using the Kraehnert and Baerns model is limited by the quantitative inaccuracies under industrial conditions, especially under ecological aspects considering the strong underestimation of nitrous oxide selectivities. To date, the Kraehnert and Baerns mechanism is the most widely used mechanism for simulating industrial ammonia oxidation because of its robustness, easy implementation, and reduced computing times compared to simulations with more complex mechanisms. Several other, much more complex established kinetic models for ammonia oxidation on platinum were scrutinized by Dr. Sven Jakobtorweihen before the Krähnert model was chosen, but none provided better agreement despite increasing numerical complexity and longer computation times. It can be stated that currently no kinetic model exists that captures ammonia oxidation at industrial conditions correctly in line with reports by other groups [11, 15].

It should also be noted here that measured and simulated selectivities to the target product nitric oxide are lower in the present work than nitric oxide selectivities of $92 - 98$ % achieved in industrial reactors [3]. This can be explained since the performance of a single, woven pure platinum gauze was investigated here, while in industrial reactors stacks of up to 50 geometry-optimized knitted gauzes are used composed of platinum-rhodium alloy wires. Both, the knitting pattern as well as alloying of platinum with rhodium have a positive effect on the nitric oxide selectivity [3]. Probably the most significant difference between the studies presented in this paper and industrial reactors is that the reaction is studied on a single gauze only, resulting in incomplete ammonia conversion. CFD simulations suggest that nitrous oxide and also nitrogen are mainly produced on the first gauzes in a gauze stack at high ammonia concentrations [11, 19]. At the first gauze, ammonia fluxes to the platinum surface are high leading to high NH_x coverages (with $x = 0, 1, 2, 3$) which in turn favor the formation of the nitrogen rich side products nitrous oxide and nitrogen.

8.2 Influence on catalyst temperature

In addition to measuring the gas phase composition profiles, further information can be measured in spatial profile reactors by coupling additional analytical techniques with the sampling capillary. Fiber-based spectroscopic methods like Raman spectroscopy, pyrometry, or laser-induced fluorescence spectroscopy are promising techniques that can be coupled with spatial profile reactors as shown in other articles by Horn et al. [34–36, 38]. As a first step in this direction, a pyrometer fiber was inserted in the sampling capillary, tip-aligned with the orifice, to measure the gauze temperature as function of the reactor inlet temperature. A sketch of the utilized experimental setup is shown in Figure 8.4.

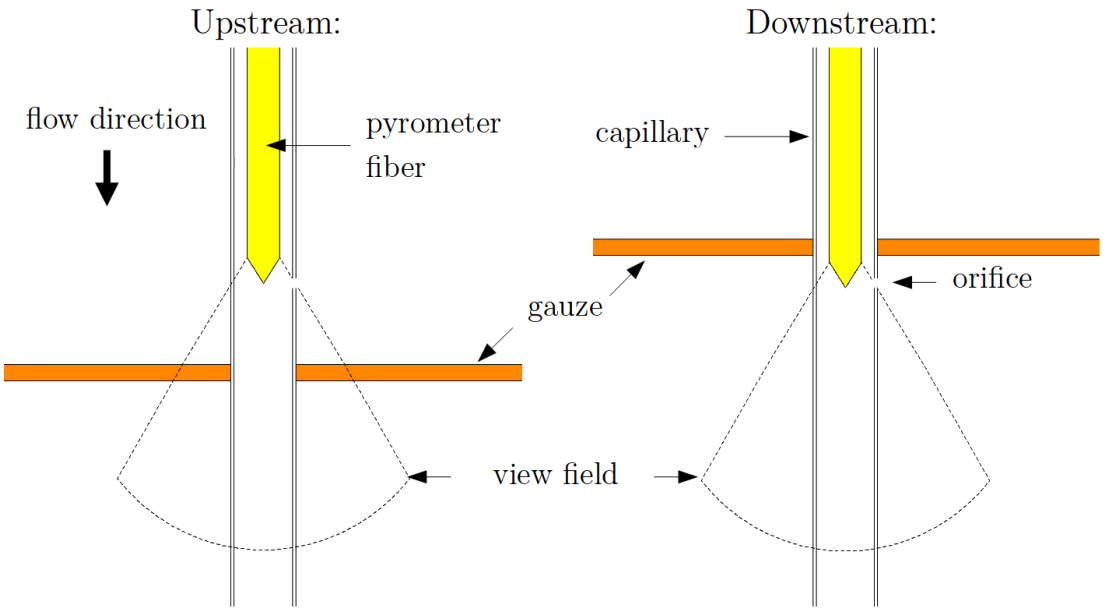

Figure 8.4: Sketch of the experimental setup and view field used in the pyrometer gauze temperature measurements. Figure taken from [207]

The measurements were performed with the capillary running through the center of a mesh (configuration shown in Figure 5.10, middle, in Section 5.2). The measurements were conducted with the same operation conditions as the species profile measurements shown in the previous section, varying the inlet temperature from 100 °C − 300 °C in steps of 50 °C. The temperature profiles measured by the fiber pyrometer are shown in Figure 8.5.

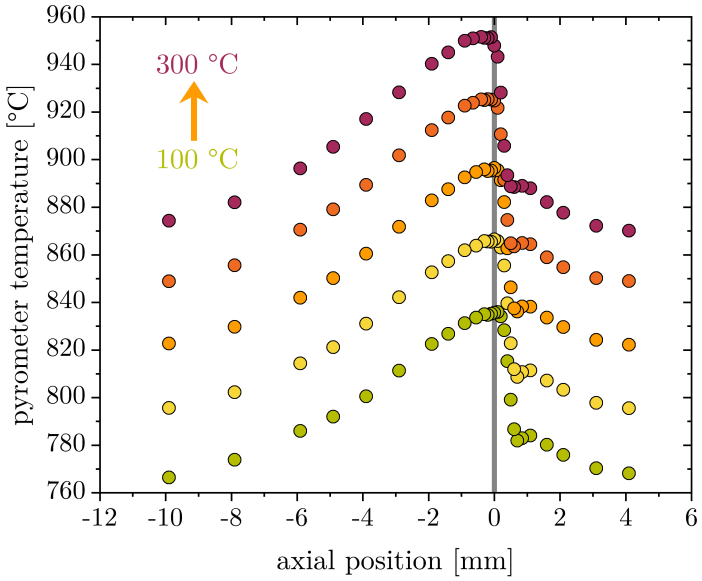

Figure 8.5: Catalyst temperature profiles measured with a fiber pyrometer at inlet temperatures of 100 °C, 150 °C, 200 °C, 250 °C and 300 °C. Operation conditions: p = 5 bar, x_{NH_3} = 0.10, x_{O_2} = 0.186, NH_3 loading = 10 $\frac{\text{t N in } NH_3}{\text{m}^2 \text{ d}}$. Figure taken from [207]

At all inlet temperatures, the temperature profiles measured with the pyrometer have the same shape. In contrast to the concentration profiles presented in previous sections, temperature profiles measured with a pyrometer fiber cannot be interpreted as spatial temperature profiles through the reactor. As the fiber tip is approaching the gauze, the view field of the fiber captures more and more thermal radiation from the gauze and the temperature increases until it reaches a maximum value at the position of the catalyst gauze. This maximum temperature corresponds to the gauze temperature and is the only temperature value from the profile that should be interpreted. Upon translating the capillary further, the measured temperature drops sharply, since the gauze leaves the view field of the fiber tip. Downstream of the gauze, the fiber tip collects only thermal radiation from the gauze holders, from the reactor walls, and from a stack of gauzes placed 10 mm downstream of the measurement gauze to ensure full ammonia conversion and prevent ammonium nitrate formation in transfer lines and the nitric oxide scrubber downstream of the reactor.

A comparison of the measured and simulated gauze temperatures is shown in Figure 8.6.

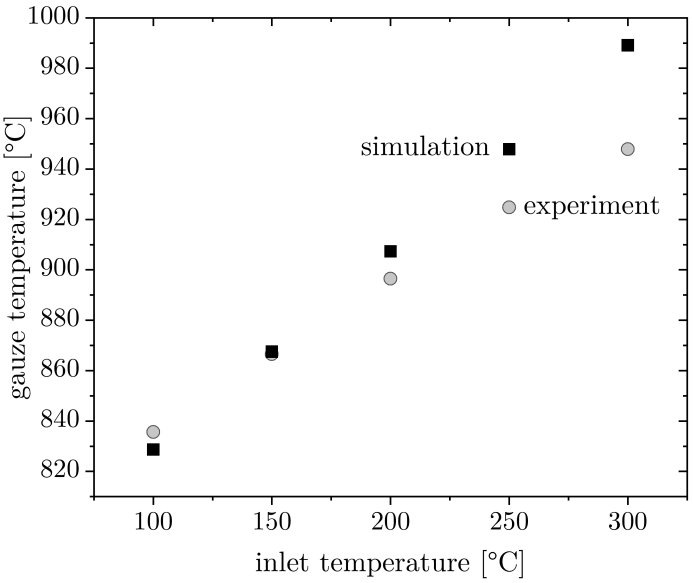

Figure 8.6: Comparison of measured gauze temperatures (circles) to averaged simulated gauze temperatures (squares). Operation conditions: p = 5 bar, $x_{NH_3} = 0.10$, $x_{O_2} = 0.186$, NH_3 loading = 10 $\frac{\text{t N in } NH_3}{\text{m}^2 \text{ d}}$. Figure taken from [207]

.

Experimental and simulated gauze temperatures are in good agreement. At an inlet temperature of 100 °C, the experimental gauze temperature is a few degrees centigrade higher than the simulated gauze temperature. For higher reactor inlet temperatures, the simulated gauze temperatures are higher than the measured values. This may, at least in parts, be attributed to the fact that heat losses by radiation were not yet included in the model used in this work. However, in CFD studies by Wiser [11], it is reported that the influence of radiation is negligible, decreasing the gauze temperature only by about 10 °C. Another reason that the simulated temperatures are higher than the corresponding experimental values might be, that the modeling domain was assumed to be adiabatic, while in the real reactor, heat is lost not only by radiation from the gauze but also by radial conduction of heat in the gauze to the reactor wall. In either way, measurements and simulations show clearly that increasing the reactor inlet temperature translates in first approximation into an almost linear increase of the gauze temperature.

The gauze surface temperature is reported to be a crucial parameter that strongly influences the product selectivities of industrial ammonia oxidation [3, 17]. To our best knowledge, no other experimental laboratory setup for ammonia oxidation is reported in literature in which the surface temperature can be directly measured by pyrometry.

The gauze temperature measurements by pyrometry demonstrate the value of coupling additional analytical techniques with the sampling capillary. Possible other applications of this principle are coupling Raman spectroscopy to determine gas phase temperatures from rotational and vibrational bands, as established by Sosna [218] for CO oxidation, or to search for indicators of gas phase reactions using laser-induced fluorescence spectroscopy, as carried out by Schwarz [38].

9 Influence of the Oxygen Molar Inlet Fraction

In this chapter, the influence of the oxygen concentration on the molar flow rates, ammonia conversion, and product selectivities is analyzed by comparing profile measurements at five different oxygen inlet molar fractions with corresponding CFD simulations. The CFD simulations shown in this chapter have been conducted by Dr. Sven Jakobtorweihen.

Five profile measurements were conducted at oxygen inlet molar fractions of x_{O_2} = 0.15, 0.186, 0.25, 0.3 and 0.4. The inlet temperature, pressure, ammonia inlet molar fraction and ammonia loading were kept constant in all measurements at T_{inlet} = 200 °C, p = 5 bar, x_{NH_3} = 0.10, NH_3 loading = 10 $\frac{\text{t N in } NH_3}{m^2\ d}$. The sampling orifice was kept at a fixed azimuthal angle, positioned as close as possible to a wire (see Figure 5.10 left). The measured molar flow rate profiles and corresponding undisturbed simulated profiles of ammonia, oxygen, nitric oxides, and nitrous oxide are shown in Figure 9.1.

The simulated molar flow rate profiles show the trend that the nitric oxide molar flow rates increase and the nitrous oxide flow rates decrease with increasing oxygen inlet molar fraction. The ammonia molar flow rates and the resulting conversion is not affected in CFD simulations by changing the oxygen inlet molar fraction. In the measurements similar profile shapes are obtained in all five experiments with distinct product maxima and educt minima at the position of the gauze. The profile shapes with distinct product maxima and educt minima can be explained by the used orifice orientation close to a straight wire piece, as discussed in detail in Section 5.2. For higher oxygen inlet molar fractions higher ammonia molar flow rates, and correspondingly lower ammonia conversions, were measured. The

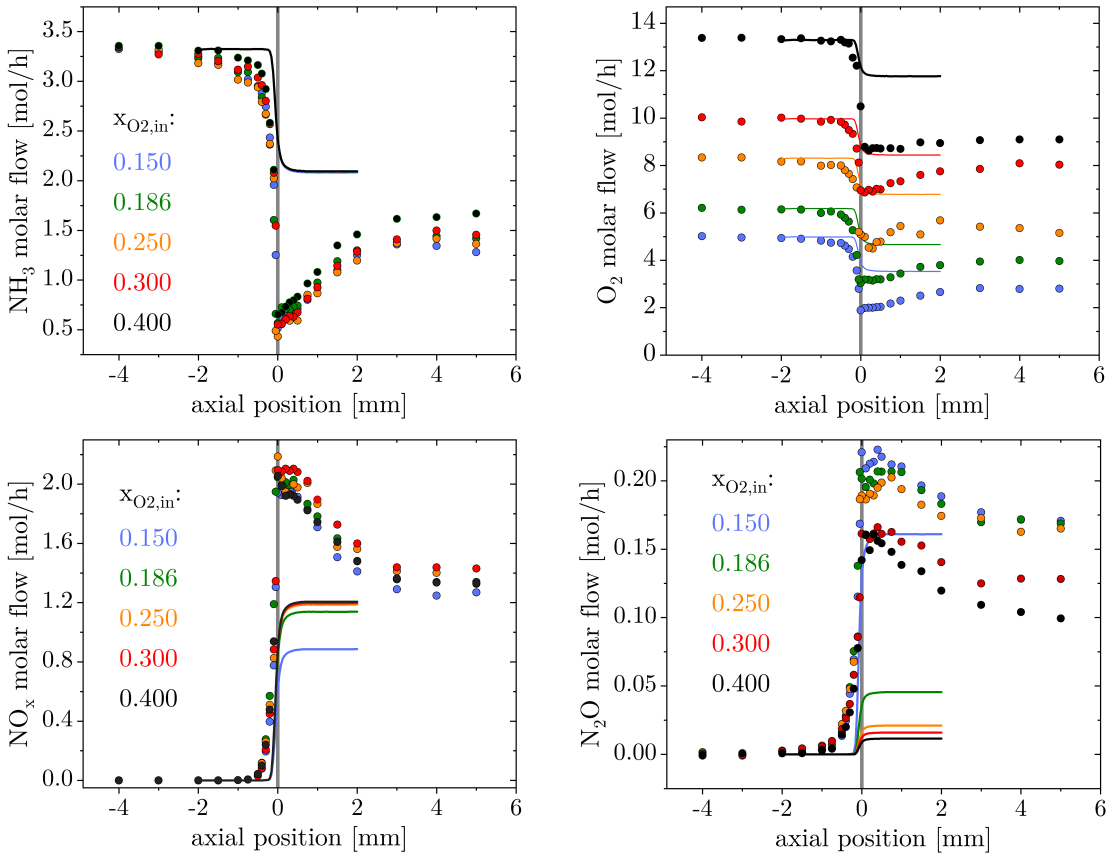

Figure 9.1: Undisturbed simulated (line) and measured sampled (circles) species molar flow profiles of NH_3, O_2, NO_x and N_2O at varying oxygen molar inlet fractions of x_{O_2} = 0.15, 0.186, 0.25, 0.3 and 0.4. Operation conditions: T_{inlet} = 200 °C, p = 5 bar, x_{NH_3} = 0.10, NH_3 loading = 10 $\frac{\text{t N in } NH_3}{\text{m}^2 \text{ d}}$

ammonia conversions, nitric oxides selectivities, and nitrous oxide selectivities, calculated from the molar flow rate profiles, are shown in Figure 9.2.

The origin of the decreasing ammonia conversion with increasing oxygen inlet molar fraction in the experiments is unclear and further experiments should be conducted to rule out any experimental errors. The simulated product selectivities show a strong decrease of the nitric oxide selectivity and a corresponding strong increase of the nitrous oxide selectivity for a reduction of the oxygen inlet molar fraction from x_{O_2} = 0.186 to x_{O_2} = 0.15. Increasing the oxygen inlet molar fraction from x_{O_2} = 0.186 to x_{O_2} = 0.25, 0.3 and 0.4 resulted in lower increases of the nitric oxide selectivity and lower decreases of the nitrous oxide selectivity with

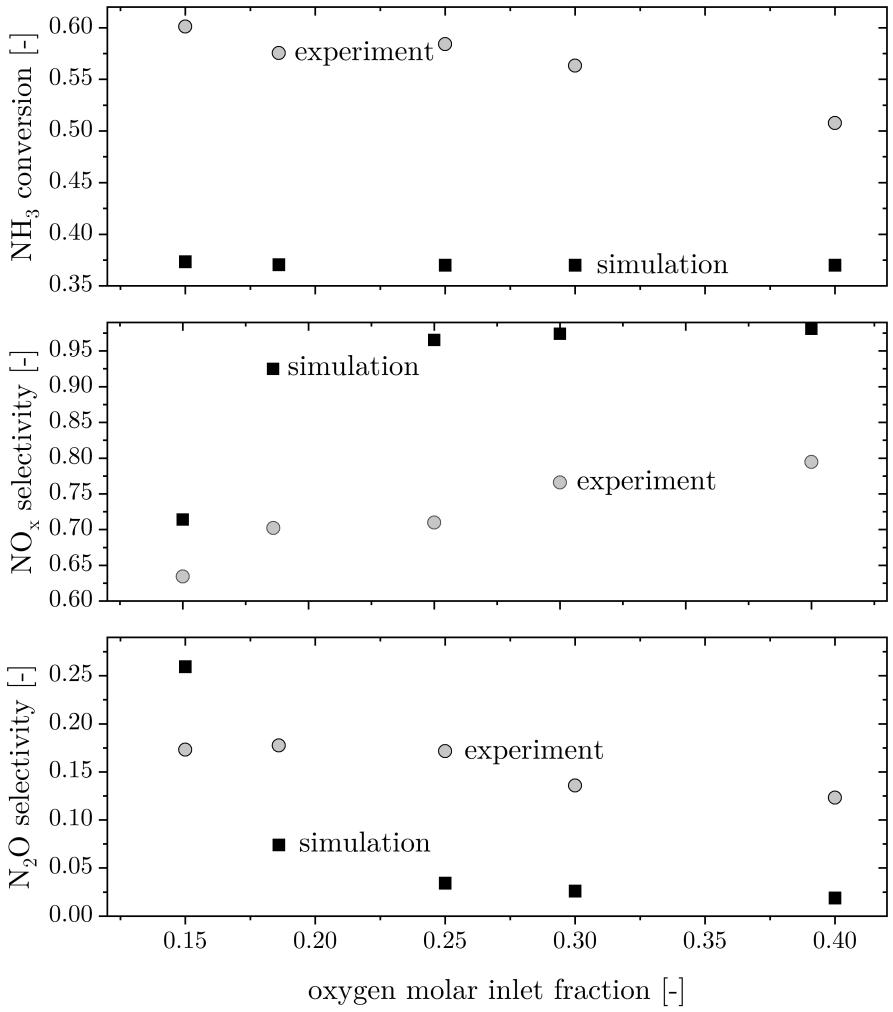

Figure 9.2: Simulated (squares) as well as experimental (circles) ammonia conversions, nitric oxide selectivities and nitrous oxide selectivities calculated from the species molar flow rate profiles at varying oxygen molar inlet fractions of $x_{O_2} = 0.15$, 0.186, 0.25, 0.3 and 0.4 shown in Figure 9.1. Operation conditions: $T_{inlet} = 200$ °C, p = 5 bar, $x_{NH_3} = 0.10$, NH_3 loading = 10 $\frac{\text{t N in } NH_3}{\text{m}^2 \text{ d}}$

every further increase in oxygen concentration. The simulated profiles indicate that the increase of nitric oxide selectivity with increasing oxygen inlet molar fraction is described by an asymptotic function, viz. the higher the oxygen molar inlet fraction the lower is the increase in nitric oxides selectivity and decrease in nitrous oxide selectivity upon increasing the oxygen molar inlet fraction further.

The experimental product selectivities do not show the same asymptotic trend observed in the simulations. The distinct sharp increase in nitric oxides selectivity and decrease in nitrous oxide selectivity observed in the simulations is not confirmed experimentally. The measured nitrous oxide selectivities do not change much for oxygen molar inlet fractions from $x_{O_2} = 0.15$ to $x_{O_2} = 0.25$. At higher oxygen inlet molar fractions of $x_{O_2} = 0.30$ and $x_{O_2} = 0.40$ lower nitrous oxide selectivities were measured. For an oxygen inlet molar fraction of $x_{O_2} = 0.15$ higher nitrous oxide selectivities were predicted in the CFD simulations by the Kraehnert and Baerns model compared with the profile measurements, while nitrous oxide selectivities were significantly underestimated by the Kraehnert and Baerns model for higher oxygen inlet molar fractions. The measured nitric oxides selectivities show a relatively linear increase with increasing oxygen inlet molar fractions. Simulated nitric oxide selectivities were overestimated by the Kraehnert and Baerns model in comparison with the measured profiles for all oxygen inlet molar fractions.

In general, simulations and experiments confirm that higher oxygen molar inlet fractions shift product selectivities towards lower nitrous oxide selectivities and higher nitric oxides selectivities in agreement with literature (see Section 2.3.5). In contrast with the temperature influence discussed in Section 8.1, experiments and simulations deviate not only quantitatively, but also the simulated asymptotic correlation between oxygen inlet molar fraction and product selectivities was not observed experimentally. A more precise understanding of the influence of the oxygen inlet molar fraction on the product distribution and the underlying reaction mechanisms is of particular interest since operating ammonia oxidation reactors at increased oxygen inlet molar fractions might be an appealing approach to increase nitric oxide selectivities and decrease nitrous oxide selectivities. To operate ammonia oxidation reactors with increased oxygen molar inlet fractions vast amounts of oxygen need to be added to the feed at an industrial scale. A potential new source of such excess oxygen might be the hydrolysis of water at an industrial scale for the production of green hydrogen or green ammonia, which could supply high amounts of off-gas with high oxygen contents in the future. Facilities producing green hydrogen, green ammonia, and in the next step greener nitric acid based products might profit from such a combined plant concept. To explore the

positive effects of increased oxygen concentrations in ammonia oxidation, further profile measurements should be conducted and also the influence of increased oxygen inlet molar fractions on the gauze corrosion rates should be studied in more detail.

10 Summary and Future Perspective

In this thesis, a new experimental setup was developed and tested that allows resolving the steep gradients around platinum gauze catalysts of ammonia oxidation under industrial conditions. The heart of the developed setup, the profile reactor, is composed of a pressure vessel build of Inconel 617, Inconel 625, and V4A 1.4571 in order to withstand temperatures of 1000 °C at 30 bar pressure in the highly corrosive gas atmosphere of ammonia oxidation. All operation conditions, namely the reactor temperature, pressure, feed gas composition, and ammonia loading, can be varied independently in the developed setup, enabling systematic parametric studies of ammonia oxidation over a wide range of industrially relevant operation conditions. The modular design of the setup allows the easy implementation of future upgrades, for example additional feed modules to dose water, nitrous oxide, or nitric oxides in the gas feed. Also, the inert gauze holder is designed in a modular approach, allowing the positioning of single gauzes or stacks of gauzes at any arbitrary axial position inside the six centimeter long reaction zone. The key feature of the setup is the implementation of the profile measurement technique developed by Horn et al. [32]. Gas samples are extracted from the reaction zone through a 20 μm sized sampling orifice drilled in a sampling capillary with an outer diameter of 616 μm.

The developed setup enables concentration profile measurements with a high spatial resolution. The spatial resolution of profile measurements is defined by the extension of the sampling region as demonstrated in CFD simulations. Gas that is sampled through the capillary orifice represents a mixture extracted from a defined volume around the orifice, introducing a spatial averaging that results in a minor mismatch between sampled and radially averaged concentration profiles, expressed in mathematical terms by a convolution integral. It was discussed that the sampling region and the resulting signal convolution is tunable by changing

the operation conditions and the sampling orifice diameter. In measurements and CFD studies, it was shown that the relative positioning of the sampling orifice with respect to the analyzed gauze wires is of essential importance due to the high spatial resolution of the used reactor configuration. For sampling orifice positions in close vicinity to a wire distinct product maxima and educt minima were obtained in the measured profiles, while for large orifice to wire spacings the slopes of the profile gradients were underrepresented in comparison with radially averaged profiles of an undisturbed reactor. Well balanced profiles, which are close to radially averaged profiles in an undisturbed reactor, were obtained for medium distances between the sampling orifice and the catalyst gauze. The endoscope camera that was integrated into the reactor setup proved to be crucial for the precise positioning of the sampling orifice with respect to the catalyst gauzes.

In the experiments, some specific characteristics of profile measurements in ammonia oxidation were identified. On the one hand the steep concentration gradients around the catalyst wires with diameters of $76-90$ μm can be resolved well by capillary sampling. On the other hand, thermocouples turned out to be a non-reliable probe to measure gas phase temperature profiles in ammonia oxidation, in contrast to being well suited for gas temperature measurements in kinetically controlled reactions as shown in literature [32, 33]. The steep temperature gradients could not be resolved accurately due to the strong influence of radiation, temperature gradients induced in the sampling process and misalignment of the thermocouple tip resulting from thermal expansion. Another factor that complicates profile measurements in ammonia oxidation is the formation of volatile platinum compounds in the gauze reconstruction process. For measurements at combined high temperature and high oxygen concentration volatile platinum compounds are formed at high rates around the gauzes. The volatile compounds are deposited at the outside and inside sampling capillary walls, forming a catalytically active coating. The coating affects the measured concentration profiles. Pronounced hystereses were observed in concentration profiles measured with strongly coated sampling capillaries. The coating also affects the measured conversion and product selectivities. Thus, the protocol of the profile measurements was adopted to exclude coating influences. By minimizing the residence time of the sampling orifice in direct vicinity or downstream of the gauzes, the inner capillary walls can be protected from coat-

ing formation over the longest time periods of a measurement campaign. After every profile measurement the signal intensities are checked for profile hysteresis, to verify that no active coating was formed. Once an active coating is detected, the measurement campaign needs to be stopped and a new sampling capillary needs to be installed, to guarantee profile measurements are not affected by capillary coating. Especially for measurements at extreme operation conditions with combined high temperatures and high oxygen molar fractions noticeable capillary coating was detected already after two to three profile measurements. At milder operation conditions, e.g. reduced temperatures, parametric studies were conducted without any signs of capillary coating visible after several profile measurements in a row. This shows that coating rates are an important factor that should be considered in the planning process of a measurement campaign.

By coupling a pyrometer fiber into the sampling capillary the catalyst gauze temperature, an essential process parameter inaccessible in conventional laboratory reactors, was measured for varying inlet temperatures. The catalyst gauze temperature is a crucial process parameter of industrial ammonia oxidation that influences the product selectivities and is decisive for the gauze corrosion rate. Comparison with CFD simulations showed a good agreement between simulated and measured gauze temperatures. The results show exemplarily how complementary valuable information can be gathered in the profile reactor by coupling additional analytical probes into the sampling capillary.

In a first systematic study, the influence of the reactor inlet temperature on ammonia conversion and product selectivities was analyzed and compared with results obtained from CFD simulations. In the CFD simulations the kinetic model by Kraehnert and Baerns [41] was used to model surface reactions at the catalyst gauze. In agreement with literature [3, 10], the measured molar flow rate profiles confirmed that increasing the reactor inlet temperature leads to decreasing nitrous oxide selectivity and increasing nitric oxide selectivity in the industrial relevant temperature range. The simulated molar flow rate profiles predicted the same trends as the measurements but deviated quantitatively from the measured results. Especially considerably lower nitrous oxide selectivities were predicted by the Kreahnert and Baerns model.

In a second combined simulative and experimental study the influence of the oxygen molar inlet fractions on the molar flow rate profiles, ammonia conversion as well as product selectivities was analyzed. The comparison showed stronger deviations between measured and simulated results than in the inlet temperature study. The simulated profiles showed a strong decrease of the nitric oxide selectivity and a corresponding strong increase of the nitrous oxide selectivity for a reduction of the oxygen molar inlet fraction from $x_{O_2} = 0.186$ to $x_{O_2} = 0.15$, while every increase of the oxygen molar inlet fraction from $x_{O_2} = 0.186$ to $x_{O_2} = 0.25,\ 0.3$ and 0.4 resulted only in a minor increase of the nitric oxide selectivity and a minor decrease of the nitrous oxide selectivity. The measured profiles confirmed the trend that increasing the oxygen molar inlet fraction results in decreased nitrous oxide selectivity and increased nitric oxide selectivity, but the distinct sharp decrease in nitric oxide selectivity for an oxygen molar inlet fraction of $x_{O_2} = 0.15$ was not confirmed experimentally.

The comparison of measured and simulated molar flow rate profiles for different operation conditions showed that the Kraehnert and Baerns model is well suited to predict qualitative trends of ammonia oxidation, also under mass transport controlled, industrially relevant operation conditions. However, the absolute values obtained from experiments and simulations, especially nitrous oxide formation rates, deviate considerably, limiting the value of the Kraehnert and Baerns model for systematic, knowledge-based optimization of ammonia oxidation.

The setup developed in this work allows resolving the gradients around the catalyst gauzes of ammonia oxidation over a wide range of industrially relevant operation conditions. In future studies the setup should be used to gather experimental data needed for validation and optimization of improved kinetic models of ammonia oxidation. In this work, the influence of the inlet temperature and oxygen molar inlet fraction on the reaction performance was studied using single woven platinum gauzes. Complementary data resolving the influence of all relevant operation conditions, namely the reactor pressure, the temperature, the ammonia loading, the oxygen concentration, and the ammonia concentration could be measured for various gauze arrangements including single catalyst gauzes of platinum but also platinum-rhodium alloy gauzes, gauze stacks and varying knitting patterns and weaves.

Additionally to measurements of well balanced profiles, viz. profiles close to the radial average in an undisturbed reactor, also local phenomena like varying selectivities induced by different gauze geometries could be studied. Such studies could be enabled by positioning smaller sampling orifices, compared with the 20 μm sized orifices used in this work, in respective gauze areas of interest. An interesting application example for such studies is a comparison between the selectivities measured at straight wire parts compared to wire crossing points. Furthermore, measurements with a higher spatial resolution might provide hints that allow distinguishing between catalytically formed reaction products and products formed in gas phase reactions. Another approach to finding indicators for gas phase reactions are laser-induced fluorescence spectroscopy measurements by coupling spectroscopy fibers into the sampling capillary as established by Schwarz [38].

Measurements of gas phase temperature profiles using thermocouples did not provide sufficiently accurate results in this work. A promising alternative for future studies of ammonia oxidation are gas phase temperature profile measurements using Raman spectroscopy as performed by Sosna for carbon monoxide oxidation [218].

All in all, for the first time in the history of the century old Ostwald process, the profile reactor developed and tested in this work enabled to resolve the steep concentration gradients around catalyst gauzes in ammonia oxidation under industrial conditions. The design of the setup allows conducting systematic studies over a wide range of industrially relevant operation conditions, making the profile reactor an ideal tool to bridge the gap of experimental data that hinders a better understanding of the process since the times of Wilhelm Ostwald. By coupling additional analytical probes into the sampling capillary, valuable new insights into the underlying processes of ammonia oxidation can be gained. The full potential of profile measurements can be realized in combination with CFD simulations for the validation of existing kinetic models and, on the next level, in combination with theoretical methods like DFT calculations, for the development of improved kinetic models that accurately predict ammonia oxidation over the entire range of industrially relevant operation conditions. Both, a better understanding of the underlying processes of ammonia oxidation and improved kinetic models are required for a future systematic, knowledge-based optimization of the century old

Ostwald process, targeting a more sustainable, ecological process with improved nitric oxide yields, reduced gauze corrosion rates, and minimized nitrous oxide emissions.

A Appendix

A.1 Linear Regression for MBMS Calibration

The calibration factors $CF_{s,m/z}$ of the species NO, N_2O and NO_2 are determined from the slope b of the linear regression of the measured relative signal intensities $\frac{I_{s,m/z}}{I_{Ar,40}}$ at the y-axis over the ratio of the dosed volume flows $\frac{\dot{V}_s}{\dot{V}_{Ar}}$ at the x-axis.

$$y = a + b \cdot x \tag{A.1}$$

The intercept and slope of the regression curve are calculated according to the Equations A.2 and A.3 using the center of mass for the determined y values $\overline{y}$ and x values $\overline{x}$.

$$b = \frac{\sum_{i=1}^{n} (x_i - \overline{x})(y_i - \overline{y})}{\sum_{i=1}^{n} (x_i - \overline{x})^2} \tag{A.2}$$

$$a = \overline{y} - b\overline{x} \tag{A.3}$$

$$\overline{y} = \frac{1}{n} \sum_{i=1}^{n} y_i \tag{A.4}$$

$$\overline{x} = \frac{1}{n} \sum_{i=1}^{n} x_i \tag{A.5}$$

The expected value $\widehat{y}_i$ for any given value x_i can then be calculated according to Equation A.6.

$$\widehat{y}_i = a + b \cdot x_i \tag{A.6}$$

As a measure to evaluate how well the calculated fit replicates the measured data, the coefficient of determination R^2 is determined using the residual sum of squares RSS and the total sum of squares TSS.

$$R^2 = 1 - \frac{RSS}{TSS} \tag{A.7}$$

$$RSS = \sum_{i=1}^{n} (y_i - \widehat{y}_i)^2 \tag{A.8}$$

$$TSS = \sum_{i=1}^{n} (y_i - \overline{y})^2 \tag{A.9}$$

The variance $\widehat{\sigma}^2$ and the standard error $\widehat{\sigma}$ are calculated according to Equation A.10 and Equation A.11 respectively.

$$\widehat{\sigma}^2 = \frac{1}{n-2} \sum_{i=1}^{n} (y_i - a - b \cdot x_i)^2 \tag{A.10}$$

$$\widehat{\sigma} = \sqrt{\widehat{\sigma}^2} \tag{A.11}$$

The variance and standard error of the slope b and intercept a are then calculated using the following equations.

$$\widehat{\sigma}_a^2 = \widehat{\sigma}^2 \frac{\sum_{i=1}^{n} x_i^2}{n \sum_{i=1}^{n} (x_i - \overline{x})^2} \tag{A.12}$$

$$\widehat{\sigma}_a = \sqrt{\widehat{\sigma}_a^2} \tag{A.13}$$

$$\widehat{\sigma}_b^2 = \widehat{\sigma}^2 \frac{1}{\sum_{i=1}^{n} (x_i - \overline{x})^2} \tag{A.14}$$

$$\widehat{\sigma}_b = \sqrt{\widehat{\sigma}_b^2} \tag{A.15}$$

Confidence intervals of the slope Δb and the intercept Δb are calculated using the $t_{n-2,\alpha}$ quantile of Student's t-distribution with $n-2$ degrees of freedom and a level of significance $\alpha = 0.05$.

$$\Delta a = \pm t_{n-2,\alpha} \widehat{\sigma}_a \tag{A.16}$$

$$\Delta b = \pm t_{n-2,\alpha} \widehat{\sigma}_b \tag{A.17}$$

The 95 % confidence band is finally calculated according to Equation A.18.

$$\Delta y_K(x) = \pm t_{n-2,\alpha} \widehat{\sigma} \sqrt{\frac{1}{n} + \frac{(x - \overline{x})^2}{\sum_{i=1}^{n} (x_i - \overline{x})^2}} \tag{A.18}$$

On the following pages the remaining linear regression plots of the MS calibration for the species NO, NO_2 and N_2O are shown.

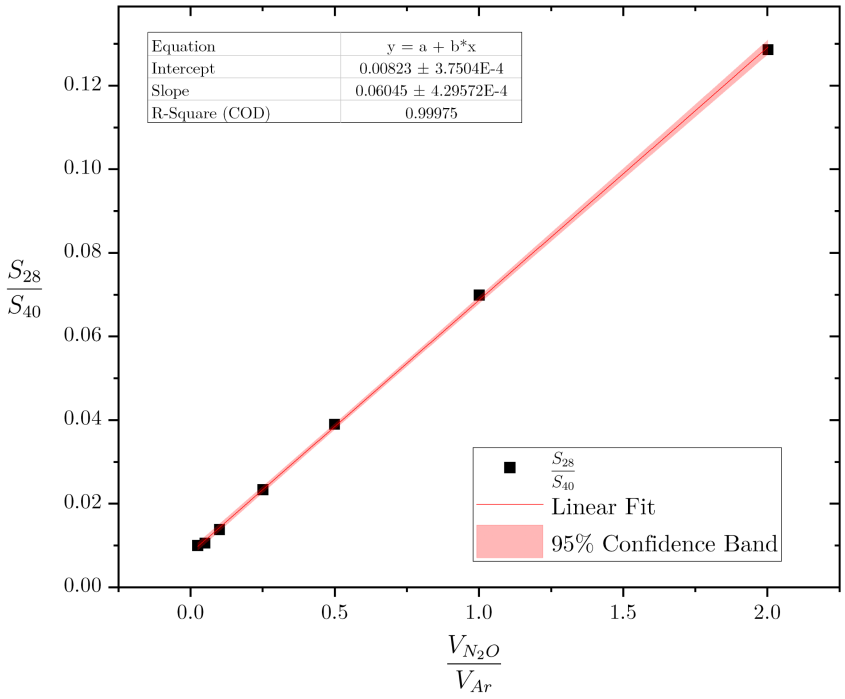

Figure A.1: Regression plot for m/z = 28 of N_2O for the second MS parameter set

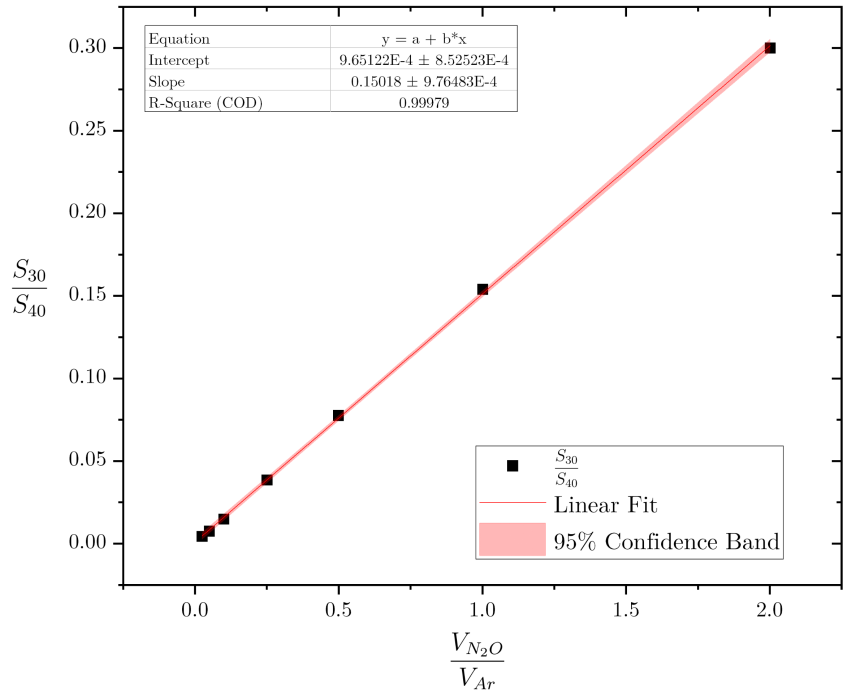

Figure A.2: Regression plot for m/z = 30 of N_2O for the second MS parameter set

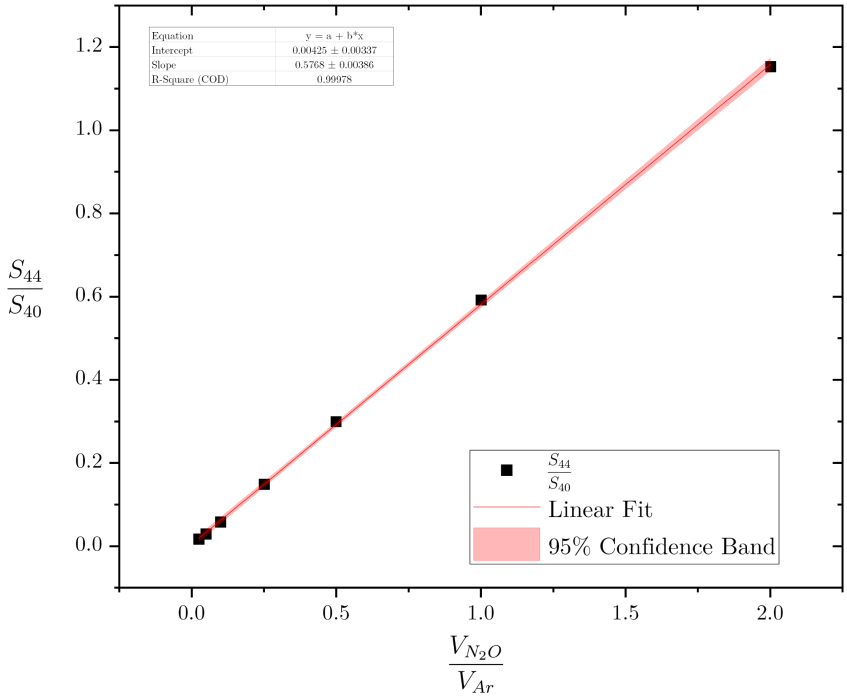

Figure A.3: Regression plot for m/z = 44 of N_2O for the second MS parameter set

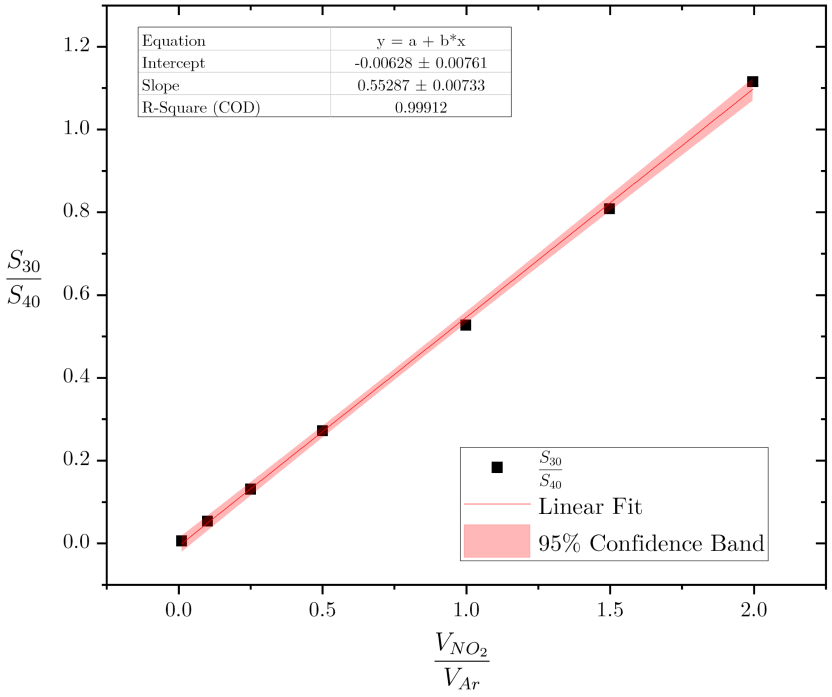

Figure A.4: Regression plot for m/z = 30 of NO_2 for the second MS parameter set

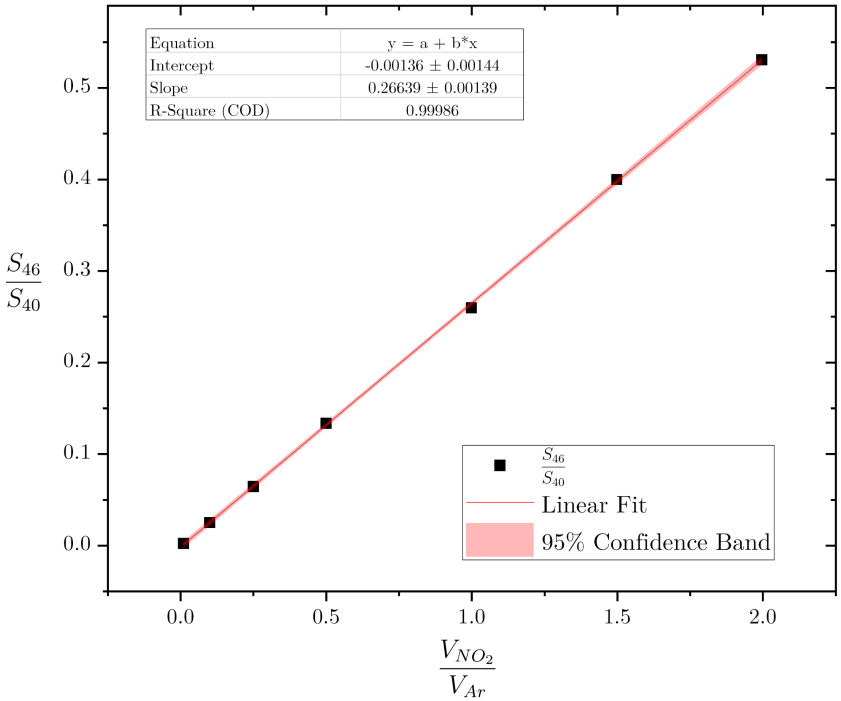

Figure A.5: Regression plot for m/z = 46 of NO_2 for the second MS parameter set

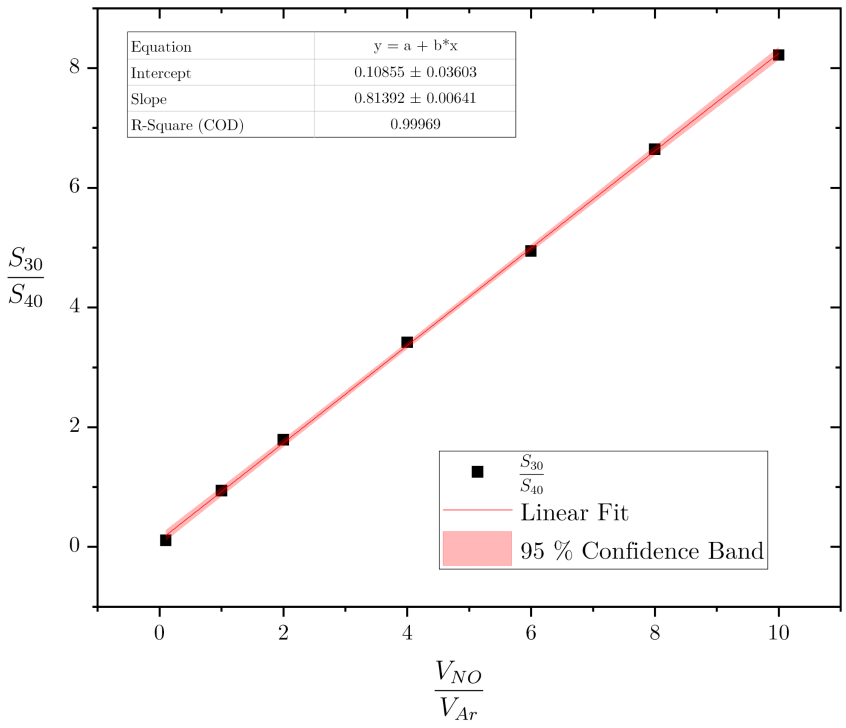

Figure A.6: Regression plot for m/z = 30 of NO for the first MS parameter set

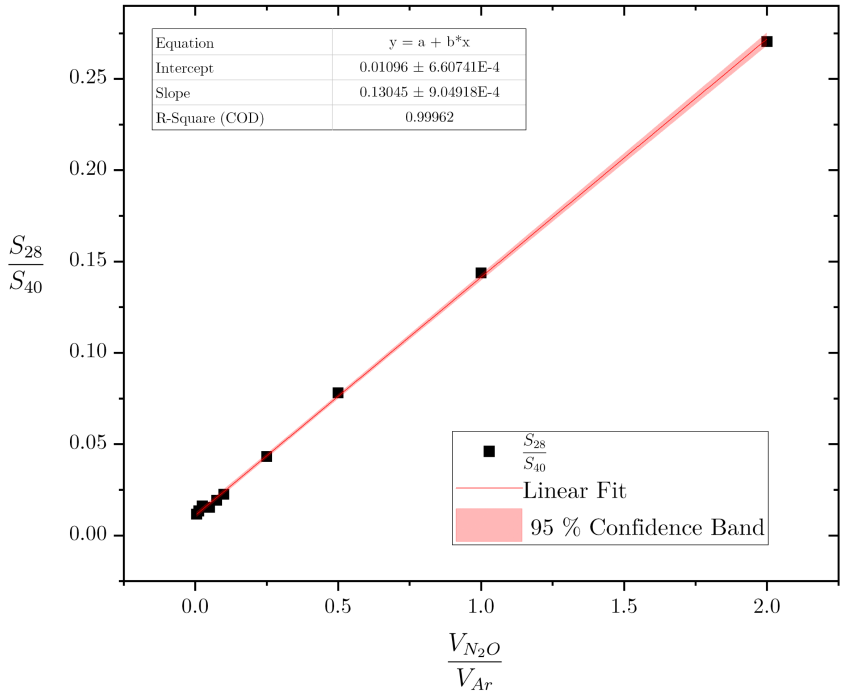

Figure A.7: Regression plot for m/z = 28 of N_2O for the first MS parameter set

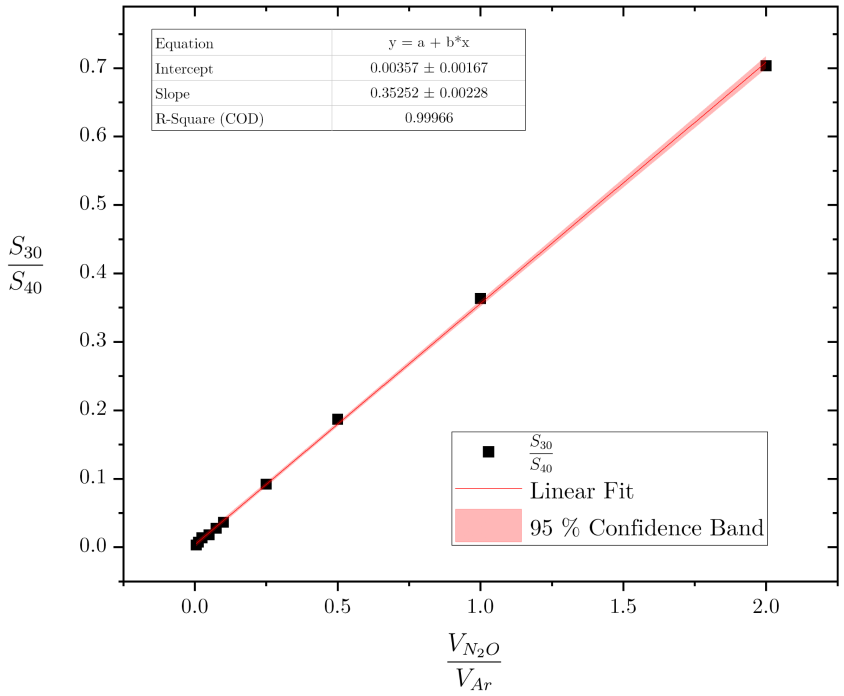

Figure A.8: Regression plot for m/z = 30 of N_2O for the first MS parameter set

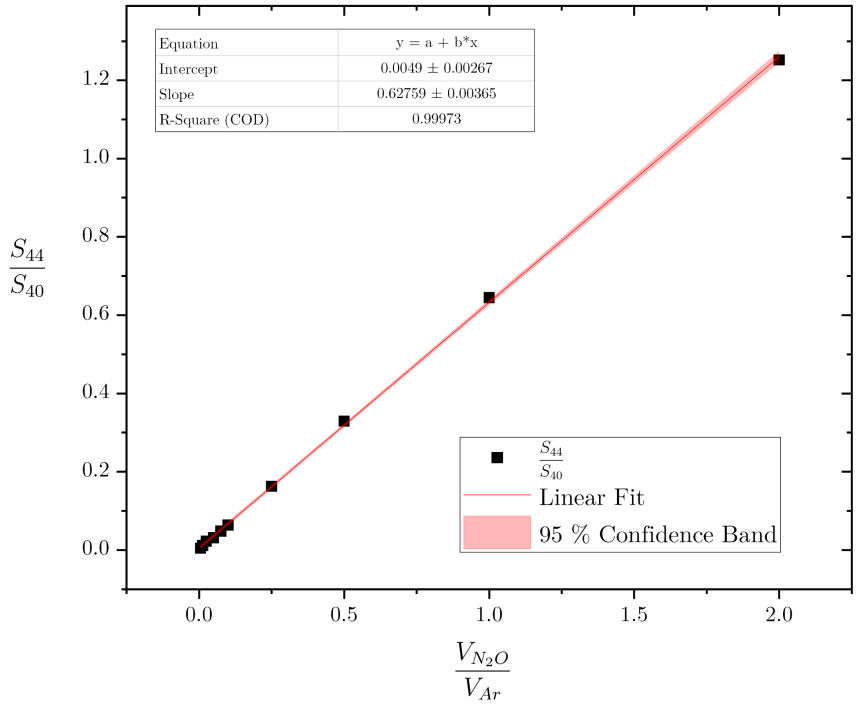

Figure A.9: Regression plot for m/z = 44 of N_2O for the first MS parameter set

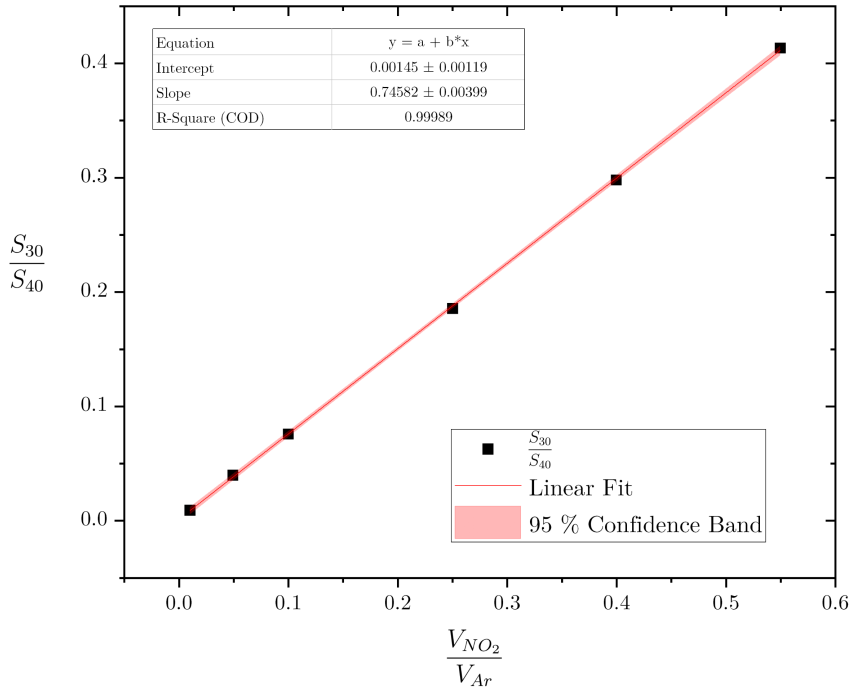

Figure A.10: Regression plot for m/z = 30 of NO_2 for the first MS parameter set

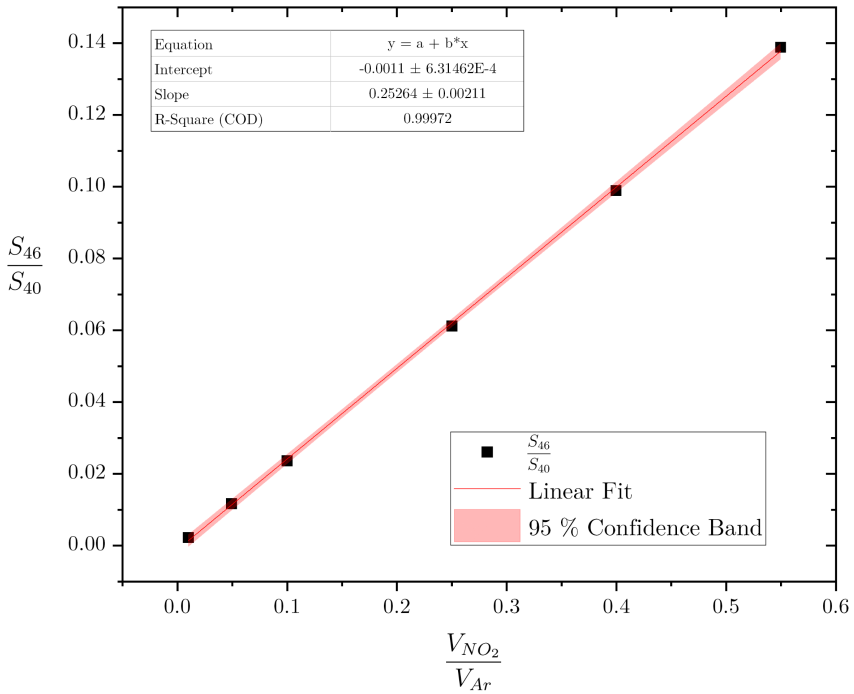

Figure A.11: Regression plot for m/z = 46 of NO_2 for the first MS parameter set

A.2 Gas Phase Physical Properties

Table A.1: Physical Properties of the gas phase species used in CFD simulations with the interpenetrating wire model

Species	M $[\frac{kg}{mol}]$	$H_{\text{ref}}(298.15\ \text{K})$ $[\frac{kJ}{mol}]$	ε [Å]	σ [K]
ammonia	17.03052	-45.9	481	2.92
oxygen	31.9988	$-0.85 \cdot 10^{-3}$	107.4	3.458
water	18.01528	-242	572.4	2.605
nitric oxide	30.0061	90.3	97.53	3.621
nitrous oxide	44.0128	82.1	232.4	3.828
nitrogen	28.0134	$1.43 \cdot 10^{-3}$	97.53	3.621

List of Figures

List of Tables

List of Abbreviations

BOI	bodies of influence
CFD	Computational Fluid Dynamics
DC	direct current
DFT	Density Functional Theory
HPLC	high-performance liquid chromatography
MBMS	molecular beam mass spectrometer
MFC	mass flow controllers
MS	mass spectrometer
PDE	partial differential equations
RF	radio frequency
SCR	selective catalytic reduction
SEM	scanning electron microscopy
Spaci-MS	spatially resolved capillary-inlet mass spectrometer
TAP	Temporal Analysis of Products
UHV	Ultra-high Vacuum

List of Symbols

Latin symbols:

Variable	Meaning	Unit
a_x	Dimensionless parameter in the Mathieu equation	$-$
A_1	factor in polynomial function to calculate specific heat capacities	$\frac{J}{kg\ K}$
A_2	factor in polynomial function to calculate specific heat capacities	$\frac{J}{kg\ K^2}$
A_3	factor in polynomial function to calculate specific heat capacities	$\frac{J}{kg\ K^3}$
A_4	factor in polynomial function to calculate specific heat capacities	$\frac{J}{kg\ K^4}$
A_5	factor in polynomial function to calculate specific heat capacities	$\frac{J}{kg\ K^5}$
A_k	pre-exponential factor in Arrhenius equation of reaction k	$\frac{1}{s}\left(\frac{m^2}{mol}\right)^{n-1}\left(\frac{1}{K}\right)^{-\beta_k}$
c	molar concentration	$\frac{mol}{m^3}$
c_p	heat capacity	$\frac{J}{kg\ K}$
$c_{s,t}$	surface concentration of a species t	$\frac{mol}{m^2}$
C	conversion	$-$
$CF_{s,m/z}$	calibration factor of species s at a given m/z ratio	$-$
d	diameter	m
$D_{\mathrm{T},s}$	thermal diffusion coefficient	$\frac{kg}{m^2\ s}$
$D_{m,s}$	diffusion coefficient of a species s in a gas mixture m	$\frac{m^2}{s}$

D_{st}	binary diffusion coefficient	$\frac{m^2}{s}$
e	elementary charge	$1.602176634 \cdot 10^{-19}\ C$
E_a	activation energy	$\frac{J}{mol}$
$E_{\lambda,b}(T)$	spectral radiation energy	$\frac{W}{m^3}$
f	external force	N
G	superficial volumetric flow rate	$\frac{kg}{dm^2}$
h	enthalpy	J
h_r	reactor height	m
HS	Heat transported by further heat sources	$\frac{J\ kg}{m^3\ s}$
$I_{s,m/z}$	MS peak intensity of species s at a given m/z ratio	$counts$
$I_\lambda(T)$	signal intensity measured with pyrometer	$\frac{W}{m^3}$
$j_{D,\gamma}$	Chilton-Colburn j-factor	$-$
$\vec{j}_{s,j}$	diffusion mass flux of species s in direction j	$\frac{kg}{m^2\ s}$
k_{f_k}	forward reaction rate constant of reaction k	$\frac{1}{s}\left(\frac{m^2}{mol}\right)^{n-1}$
$k_{g,s}$	mass transport coefficient of a species	$\frac{m}{s}$
K	pyrometer constant	$W\ m^2$
Kn	Knudsen number	$-$
K_s	number of surface reactions	$-$
$\bar{l}$	mean free path length	m
m	ion mass	amu
M	molar mass	$\frac{g}{mol}$
$\dot{n}$	molar flow rate	$\frac{mol}{s}$
$\vec{n}$	outward pointing unit vector normal to the catalyst surface	$-$
N_g	total number of gas phase species in the system	$-$
N_s	total number of surface species in the system	$-$
p	pressure	Pa
q_x	Dimensionless parameter in the Mathieu	$-$

	equation	
r_0	half distance between two quadrupole rods	m
re	resolution of a quadrupole mass filter	$-$
Re	Reynolds number	$-$
R_s^{het}	reaction rate of a species s by surface reactions	$\frac{kg}{m^2\ s}$
s	slope of the mass scan line	$-$
$\dot{s_s}$	net production rate of a species s	$\frac{mol}{m^2\ s}$
S	selectivity	$-$
Sc	Schmidt number	$-$
Sh	Sherwood number	$-$
t	time	s
T	temperature	K
u	velocity	$\frac{m}{s}$
U	DC voltage applied to quadrupole rods	V
V	RF voltage applied to quadrupole rods	V
w	mass fraction	$-$
x_i	spatial direction in Cartesian coordinates	m
x_M	mach disk location	m
X	mole fraction	$-$
Y	yield	$-$
z	ion charge	$-$

Greek Symbols:

Variable	**Meaning**	**Value**
β	temperature exponent in Arrhenius equation	$-$
γ	gauze fractional open area	$-$
Γ	total surface site density	$\frac{mol}{m^2}$
δ_{ij}	Kronecker delta	$-$
ϵ	emissivity	$-$
ε	interaction well depth	J

θ	surface coverage	$-$
κ	isentropic expansion factor	$-$
λ	wavelength	m
λ_{therm}	thermal conductivity	$\frac{W}{m\ K}$
μ	dynamic viscosity	$Pa\ s$
ν	stoichiometric coefficient	$-$
ρ	density	$\frac{kg}{m^3}$
σ	collision cross section	m^{-2}
τ	dimensionless parameter in the Mathieu equation	$-$
τ_{ij}	stress tensor	$\frac{N}{m^2}$
ϕ_{st}	parameter for the calculation of gas mixture properties	$-$
Φ_0	electric potential applied to quadrupole rods	V
$\Phi(x,y)$	electric potential between quadrupole rods	V
ω	angular frequency of the RF-voltage	$\frac{1}{s}$
Ω	collision integral	$-$

Fundamental Constants:

Constants	**Meaning**	**Value**
k_B	Boltzmann constant	$1.380649 \cdot 10^{-23}\ \frac{J}{K}$
N_A	Avogadro constant	$6.022 \cdot 10^{23}\ mol^{-1}$
R	universal gas constant	$8.31451\ \frac{J}{mol\ K}$
π	circle constant	3.1415
C_1	first Planck radiation constant	$3.74177153 \cdot 10^{-16}\ W\ m^2$
C_2	second Planck radiation constant	$1.4387770 \cdot 10^{-2}\ m\ K$

Subscripts and superscripts:

Variable	**Meaning**
c	critical ratio
cal	calibration

cap	capillary
$frag$	fragmentation peak
hps	high pressure site
i	spatial direction
in	inlet
$inner$	inner
j	spatial direction
k	surface reaction k
$main$	main peak of a species
n	nozzle
nc	nozzle chamber
$orifice$	sampling orifice
out	outer
$pzuz$	axial reactor position IN z AENDERN
r	reactor
ref	reference state
R	spectral radiance
ss	sound of speed
s	species
t	species
$thermo$	thermocouple
w	wire
$*$	reduced

Bibliography

[1] Clariant launches major climate campaign: free N2O-removal catalyst for nitric acid producers worldwide (Nov. 2021).
URL https://news.agropages.com/News/NewsDetail---41097.htm

[2] Nitric Acid, Chemical Economics Handbook, IHS Chemical, London, 2020.
URL https://ihsmarkit.com/products/nitric-acid-chemical-economics-handbook.html

[3] S. T. Hatscher, E. Wagner, H. J. Kneuper, Ammonia Oxidation, in: Handbook of heterogeneous catalysis, Vol. 5, 2008, pp. 2575–2592.

[4] M. Thiemann, E. Scheibler, K. W. Wiegand, Nitric Acid, Nitrous Acid, and Nitrogen Oxides, in: Wiley-VCH Verlag GmbH & Co. KGaA (Ed.), Ullmann's Encyclopedia of Industrial Chemistry, Wiley-VCH Verlag GmbH & Co. KGaA, Weinheim, Germany, 2000. doi:10.1002/14356007.a17_293.
URL http://doi.wiley.com/10.1002/14356007.a17_293

[5] T. H. Chilton, Strong Water. Nitric Acid: Sources, Methods of Manufacture, and Uses, MIT Press, Cambridge, 1968.

[6] L. Andrussow, Über die schnell verlaufenden katalytischen Prozesse in strömenden Gasen und die Ammoniak-Oxydation (V), European Journal of Inorganic Chemistry 60 (8) (1927) 2005–2018, number: 8.

[7] L. Andrussow, Über die katalytische Ammoniakoxydation und schnellverlaufende katalytische Prozesse, Angewandte Chemie 63 (15) (1951) 350–355, number: 15.

[8] S. Solomon, I. P. on Climate Change, I. P. on Climate Change (Eds.), Climate change 2007: the physical science basis: contribution of Working Group I to the Fourth Assessment Report of the Intergovernmental Panel on Climate Change, Cambridge University Press, Cambridge ; New York, 2007, oCLC: ocn132298563.

[9] M. Baerns, R. Imbihl, V. Kondratenko, R. Kraehnert, W. Offermans, R. Vansanten, A. Scheibe, Bridging the pressure and material gap in the catalytic ammonia oxidation: structural and catalytic properties of different platinum catalysts, Journal of Catalysis 232 (1) (2005) 226–238, number: 1. doi:10.1016/j.jcat.2005.03.002.
URL http://linkinghub.elsevier.com/retrieve/pii/S0021951705000990

[10] M. Warner, B. S. Haynes, Formation of N2 and N2O in industrial combustion of ammonia over platinum, Proceedings of the Combustion Institute 35 (2) (2015) 2215–2222, number: 2. doi:10.1016/j.proci.2014.06.110.
URL https://linkinghub.elsevier.com/retrieve/pii/S1540748914002685

[11] Wiser, Artur, Investigation of the industrial NH3 oxidation by CFD simulations including detailed surface kinetics, Ph.D. thesis, Technische Universität Darmstadt, Darmstadt, publisher: UNSPECIFIED (2020).
URL https://tuprints.ulb.tu-darmstadt.de/id/eprint/17208

[12] C. Weststrate, J. Bakker, E. Rienks, C. Vinod, A. Matveev, V. Gorodetskii, B. Nieuwenhuys, Ammonia oxidation on Pt(410), Journal of Catalysis 242 (1) (2006) 184–194. doi:10.1016/j.jcat.2006.06.011.
URL https://linkinghub.elsevier.com/retrieve/pii/S0021951706002144

[13] O. Ivashenko, N. Johansson, C. Pettersen, M. Jensen, J. Zheng, J. Schnadt, A. O. Sjåstad, How Surface Species Drive Product Distribution during Ammonia Oxidation: An STM and Operando APXPS Study, ACS Catalysis 11 (13) (2021) 8261–8273, number: 13. doi:10.1021/acscatal.1c00956.
URL https://pubs.acs.org/doi/10.1021/acscatal.1c00956

[14] T. Heydt, Untersuchung der Pt-katalysierten NH3-Oxidation unter operando Bedingungen und CFD-Simulation, Ph.D. thesis, Technische Universität Darmstadt, Darmstadt (2018).

[15] M. Klingenberger, Efficient implementation of detailed surface kinetics in advanced reactor simulations, Ph.D. thesis, Technische Universität Darmstadt (2016).

[16] H. Ma, W. F. Schneider, DFT and microkinetic comparison of Pt, Pd and Rh-catalyzed ammonia oxidation, Journal of Catalysis 383 (2020) 322–330. doi:10.1016/j.jcat.2020.01.029.
URL https://linkinghub.elsevier.com/retrieve/pii/S0021951720300300

[17] M. Warner, The Kinetics of Industrial Ammonia Combustion, Ph.D. thesis, The University of Sydney, Sydney (2013).
URL http://ses.library.usyd.edu.au/handle/2123/9426

[18] S. Jantzen, J. Neumann, A Novel Multifunctional Product Family of Umicore's MKS Concept: Beyond a Mere Solution for N2O Abatement (2006).

[19] T.-W. Nien, Multi-scale Modelling of Structured Reactors, Ph.D. thesis, University of Alberta, Alberta (2013).

[20] A. Scheibe, U. Lins, R. Imbihl, Kinetics of ammonia oxidation on stepped platinum surfaces. I. Experimental results, Surface Science 577 (1) (2005) 1–14. doi:10.1016/j.susc.2004.12.027.
URL https://linkinghub.elsevier.com/retrieve/pii/S0039602804015493

[21] A. Scheibe, Gestufte Platineinkristalloberflächen als Modellsystem für die katalytische Ammoniakoxidation mit Sauerstoff, Doktor der Naturwissenschaften, Universität Hannover, Hannover (2003).

[22] R. Imbihl, A. Scheibe, Y. F. Zeng, S. Günther, R. Kraehnert, V. A. Kondratenko, M. Baerns, W. K. Offermans, A. P. J. Jansen, R. A. van Santen, Catalytic ammonia oxidation on platinum: mechanism and catalyst restructuring at high and low pressure, Phys. Chem. Chem. Phys. 9 (27) (2007) 3522–3540, number: 27. doi:10.1039/B700866J.
URL http://xlink.rsc.org/?DOI=B700866J

[23] V. A. Kondratenko, M. Baerns, Mechanistic insights into the formation of N2O and N2 in NO reduction by NH3 over a polycrystalline platinum catalyst, Applied Catalysis B: Environmental 70 (1-4) (2007) 111–118, number: 1-4. doi:10.1016/j.apcatb.2005.11.037.
URL http://linkinghub.elsevier.com/retrieve/pii/S092633730600261X

[24] J. M. Bradley, A. Hopkinson, D. A. King, Control of a Biphasic Surface Reaction by Oxygen Coverage: The Catalytic Oxidation of Ammonia over Pt{100}, Journal of Physical Chemistry 99 (46) (1995) 17032–17042, number: 46.

[25] M. Rafti, J. L. Vicente, A. Albesa, A. Scheibe, R. Imbihl, Modeling ammonia oxidation over a Pt (533) surface, Surface Science 606 (1-2) (2012) 12–20, number: 1-2. doi:10.1016/j.susc.2011.08.014.
URL http://linkinghub.elsevier.com/retrieve/pii/S0039602811003505

[26] E. Rebrov, M. de Croon, J. Schouten, Design of a microstructured reactor with integrated heat-exchanger for optimum performance of a highly exothermic reaction, Catalysis Today 69 (1-4) (2001) 183–192. doi:10.1016/S0920-5861(01)00368-6.
URL https://linkinghub.elsevier.com/retrieve/pii/S0920586101003686

[27] E. Rebrov, S. Duinkerke, M. de Croon, J. Schouten, Optimization of heat transfer characteristics, flow distribution, and reaction processing for a microstructured reactor/heat-exchanger for optimal performance in platinum catalyzed ammonia oxidation, Chemical Engineering Journal 93 (3) (2003) 201–216. doi:10.1016/S1385-8947(02)00338-8.
URL https://linkinghub.elsevier.com/retrieve/pii/S1385894702003388

[28] A. Resta, U. Hejral, S. Blomberg, S. Albertin, A. Vlad, Y. Garreau, C. Chatelier, F. Venturini, P. Ferrer, G. Held, D. Grinter, E. Lundgren, A. Coati, Ammonia Oxidation over a Pt $_{25}$ Rh $_{75}$ (001) Model Catalyst Surface: An Operando Study, The Journal of Physical Chemistry C 124 (40) (2020) 22192–22199, number: 40. doi:10.1021/acs.jpcc.0c07128.
URL https://pubs.acs.org/doi/10.1021/acs.jpcc.0c07128

[29] J. Perez-Ramirez, E. Kondratenko, V. Kondratenko, M. Baerns, Selectivity-directing factors of ammonia oxidation over PGM gauzes in the Temporal Analysis of Products reactor: Primary interactions of NH3 and O2, Journal of Catalysis 227 (1) (2004) 90–100. doi:10.1016/j.jcat.2004.06.023.
URL https://linkinghub.elsevier.com/retrieve/pii/S0021951704003276

[30] J. Pérez-Ramírez, E. Kondratenko, V. Kondratenko, M. Baerns, Selectivity-directing factors of ammonia oxidation over PGM gauzes in the Temporal Analysis of Products reactor: Secondary interactions of NH and NO, Journal of Catalysis 229 (2) (2005) 303–313, number: 2. doi:10.1016/j.jcat.2004.09.020.
URL http://linkinghub.elsevier.com/retrieve/pii/S0021951704004634

[31] J. Pérez-Ramírez, E. Kondratenko, G. Novellleruth, J. Ricart, Mechanism of ammonia oxidation over PGM (Pt, Pd, Rh) wires by temporal analysis of products and density functional theory, Journal of Catalysis 261 (2) (2009) 217–223, number: 2. doi:10.1016/j.jcat.2008.11.018.
URL http://linkinghub.elsevier.com/retrieve/pii/S0021951708004405

[32] R. Horn, N. J. Degenstein, K. A. Williams, L. D. Schmidt, Spatial and temporal profiles in millisecond partial oxidation processes, Catalysis Letters 110 (3-4) (2006) 169–178, number: 3-4. doi:10.1007/s10562-006-0117-8.
URL http://link.springer.com/10.1007/s10562-006-0117-8

[33] R. Horn, K. Williams, N. Degenstein, L. Schmidt, Syngas by catalytic partial oxidation of methane on rhodium: Mechanistic conclusions from spatially resolved measurements and numerical simulations, Journal of Catalysis 242 (1) (2006) 92–102, number: 1. doi:10.1016/j.jcat.2006.05.008.
URL https://linkinghub.elsevier.com/retrieve/pii/S002195170600176X

[34] R. Horn, O. Korup, M. Geske, U. Zavyalova, I. Oprea, R. Schlögl, Reactor for in situ measurements of spatially resolved kinetic data in heterogeneous catalysis, Review of Scientific Instruments 81 (6) (2010) 064102, number: 6. doi:10.1063/1.3428727.

URL http://scitation.aip.org/content/aip/journal/rsi/81/6/10.1063/1.3428727

[35] B. C. Michael, D. N. Nare, L. D. Schmidt, Catalytic partial oxidation of ethane to ethylene and syngas over Rh and Pt coated monoliths: Spatial profiles of temperature and composition, Chemical Engineering Science 65 (12) (2010) 3893–3902, number: 12. doi:10.1016/j.ces.2010.03.033.
URL https://linkinghub.elsevier.com/retrieve/pii/S0009250910001818

[36] O. Korup, S. Mavlyankariev, M. Geske, C. F. Goldsmith, R. Horn, Measurement and analysis of spatial reactor profiles in high temperature catalysis research, Chemical Engineering and Processing: Process Intensification 50 (10) (2011) 998–1009, number: 10. doi:10.1016/j.cep.2011.05.024.
URL https://linkinghub.elsevier.com/retrieve/pii/S025527011100136X

[37] J.-Y. Luo, X. Hou, P. Wijayakoon, S. J. Schmieg, W. Li, W. S. Epling, Spatially resolving SCR reactions over a Fe/zeolite catalyst, Applied Catalysis B: Environmental 102 (1-2) (2011) 110–119, number: 1-2. doi:10.1016/j.apcatb.2010.11.031.
URL https://linkinghub.elsevier.com/retrieve/pii/S0926337310005199

[38] H. Schwarz, Y. Dong, R. Horn, Catalytic Methane Combustion on a Pt Gauze: Laser-Induced Fluorescence Spectroscopy, Species Profiles, and Simulations, Chemical Engineering & Technology 39 (11) (2016) 2011–2019, number: 11. doi:10.1002/ceat.201600286.
URL https://onlinelibrary.wiley.com/doi/10.1002/ceat.201600286

[39] K. Morgan, J. Touitou, J.-S. Choi, C. Coney, C. Hardacre, J. A. Pihl, C. E. Stere, M.-Y. Kim, C. Stewart, A. Goguet, W. P. Partridge, Evolution and Enabling Capabilities of Spatially Resolved Techniques for the Characterization of Heterogeneously Catalyzed Reactions, ACS Catalysis 6 (2) (2016) 1356–1381, number: 2. doi:10.1021/acscatal.5b02602.
URL https://pubs.acs.org/doi/10.1021/acscatal.5b02602

[40] B. Sosna, O. Korup, R. Horn, Probing local diffusion and reaction in a porous catalyst pellet, Journal of Catalysis 381 (2020) 285–294. doi:10.1016/j.jcat.2019.11.005.
URL https://linkinghub.elsevier.com/retrieve/pii/S0021951719305524

[41] R. Kraehnert, M. Baerns, Kinetics of ammonia oxidation over Pt foil studied in a microstructured quartz-reactor, Chemical Engineering Journal 137 (2) (2008) 361–375. doi:10.1016/j.cej.2007.05.005.
URL https://linkinghub.elsevier.com/retrieve/pii/S1385894707003397

[42] I. Brunborg, P. B. Holmesland, The History of Nitric Acid, in: Nitric Acid and Fertilizer Nitrates, Vol. 4, Marcel Dekker, New York, 1985, pp. 1–17.

[43] G. Martin, W. Barbour, Industrial Nitrogen Compounds and Explosives, Crosby Lockwood and Son, London, 1915.

[44] La Sociéte Norvégienne de l'azote 1905-1955, edition francaise Edition, Norsk Hydro, Paris, 1957.

[45] L. B. Hunt, The ammonia oxidation process for nitric acid manufacture, Platinum Metals Review 2 (4) (1958) 129–134, number: 4.
URL http://www.ingentaconnect.com/content/matthey/pmr/1958/00000002/00000004/art00008

[46] W. Henry, On the Action of Finely Divided Platinum on Gaseous Mixtures, and Its Application to Their Analysis, Philosophical Transactions of the Royal Society of London 114 (1824) 266–289.

[47] F. Kuhlmann, Abhandlung über die Salpeterbildung. Neue Erzeugung von Salpetersäure und Ammoniak, Annalen der Pharmacie 29 (1839) 272–279.

[48] W. Ostwald, Process of Manufacturing Nitric Acid, inventors: _:n1563 Issue: US858904 (1907).

[49] T. Baumann, Giftgas und Salpeter. Chemische Industrie, Naturwissenschaft und Militär von 1906 bis zum ersten Munitionsprogramm 1914/15, Ph.D. thesis, Heinrich-Heine-Universität, Düsseldorf (2008).

[50] J. R. Partington, The Oxidation of Ammonia, Journal of the Society of Chemical Industry 37 (17) (1918) 337–338, number: 17.

[51] W. W. Scott, Researches in catalysis with special reference to the fixation of nitrogen and the oxidation of ammonia to nitric acid, Ph.D. thesis, Colorado School of Mines, Colorado (1923).

[52] W. S. Landis, The oxidation of Ammonia, Chemical and Metallurgical Engineering 20 (9) (1919) 470–483, number: 9.

[53] A. Mittasch, Salpetersäure aus Ammoniak. Geschichtliche Entwicklung der Ammoniakoxydation bis 1920., Weinheim: Verlag Chemie, 1953.

[54] K. Kaiser, German Patent DRP 271517, inventors: _:n1719 Issue: DRP 271517 (1909).

[55] G. Fauser, Concentrated nitric acid directly attained in pressure synthesis, Chemical and Metallurgical Engineering 35 (8) (1928) 474–478, number: 8.

[56] G. Fauser, Nitric acid produced from ammonia by modified pressure system, Chemical and Metallurgical Engineering 37 (10) (1930) 604–608, number: 10.

[57] G. Fauser, Concentrated nitric acid by direct synthesis avoids absorption, Chemical and Metallurgical Engineering 39 (1932) 430–432.

[58] A. E. van Nieuwenhuyse, Production of Ammonium Nitrate and Calcium Ammonium Nitrate, European Fertilizer Manufacturers' Association, Booklet (6) (2000) 12, number: 6.
URL http://www.fertilizerseurope.com/fileadmin/user_upload/publications/tecnical_publications/guidence_techn_documentation/EFMABATCAN.pdf

[59] H. Connor, The Manufacture of Nitric Acid, Platinum Metals Review 11 (2) (1967) 60–69, number: 2.

[60] G. D. Honti, Various Processes for the Production of Commercial-Grade Nitric Acid, in: Nitric Acid and Fertilizer Nitrates, Vol. 4, Marcel Dekker, New York, 1985, pp. 61–98.

[61] H. Holzmann, Über die katalytische Oxidation von Ammoniak bei der industriellen Salpetersäure-Herstellung, Chemie Ingenieur Technik 39 (2) (1967) 89–95, number: 2.

[62] S. P. S. Andrew, The absorption and oxidation system, in: Nitric Acid and Fertilizer Nitrates, Vol. 4, Marcel Dekker, New York, 1985, pp. 41–59.

[63] P. Hoftyzer, F. Kwanten, Gas Purification Process for Air Pollution Control, 1972.

[64] F. D. Miles, Nitric acid, manufacture and uses, 1961.

[65] R. A. Searles, Pollution from Nitric Acid Plants, Platinum Metals Review 17 (2) (1973) 57–63, number: 2.
URL http://www.ingentaconnect.com/content/matthey/pmr/1973/00000017/00000002/art00005

[66] T. Kopperud, Nitrous Oxide Greenhouse Gas Abatement Catalyst, Platinum Metals Review 50 (2) (2006) 103–103, number: 2. doi:10.1595/147106706X113878.
URL http://openurl.ingenta.com/content/xref?genre=article&issn=0032-1400&volume=50&issue=2&spage=103

[67] J. Pérez-Ramırez, F. Kapteijn, K. Schöffel, J. A. Moulijn, Formation and control of N2O in nitric acid production: where do we stand today?, Applied Catalysis B: Environmental 44 (2) (2003) 117–151, number: 2.

[68] A. R. Ravishankara, J. S. Daniel, R. W. Portmann, Nitrous Oxide (N2O): The Dominant Ozone-Depleting Substance Emitted in the 21st Century, Science 326 (5949) (2009) 123–125, number: 5949. doi:10.1126/science.1176985.
URL http://www.sciencemag.org/cgi/doi/10.1126/science.1176985

[69] G. Kongshaug, L. Hjørnevik, E. Fareid, O. Nirisen, Method for the reduction of nitrogen oxide, inventors: _:n1604 Issue: US4973457A (Nov. 1990).

[70] K. M. Åbø, Investigation of the Yara 58-Y1 nitrous oxide decomposition catalyst, Ph.D. thesis, NTNU (2014).
URL https://brage.bibsys.no/xmlui/handle/11250/2351725

[71] L. Hannevold, O. Nilsen, A. Kjekshus, H. Fjellvåg, Reconstruction of platinum–rhodium catalysts during oxidation of ammonia, Applied Catalysis A: General 284 (1-2) (2005) 163–176, number: 1-2. doi:10.1016/j.apcata.2005.01.033.
URL http://linkinghub.elsevier.com/retrieve/pii/S0926860X05000669

[72] J. D. Gonzalez, M. Warner, B. S. Haynes, A. Montoya, N2O formation and dissociation during ammonia combustion: A combined DFT and experimental study, Proceedings of the Combustion Institute 36 (1) (2017) 637–644, number: 1. doi:10.1016/j.proci.2016.05.004.
URL http://linkinghub.elsevier.com/retrieve/pii/S1540748916300049

[73] S. Wang, B. Temel, J. Shen, G. Jones, L. C. Grabow, F. Studt, T. Bligaard, F. Abild-Pedersen, C. H. Christensen, J. K. Nørskov, Universal Brønsted-Evans-Polanyi Relations for C–C, C–O, C–N, N–O, N–N, and O–O Dissociation Reactions, Catalysis Letters 141 (3) (2011) 370–373. doi:10.1007/s10562-010-0477-y.
URL http://link.springer.com/10.1007/s10562-010-0477-y

[74] H. Ma, W. F. Schneider, Structure- and Temperature-Dependence of Pt-Catalyzed Ammonia Oxidation Rates and Selectivities, ACS Catalysis 9 (3) (2019) 2407–2414, number: 3. doi:10.1021/acscatal.8b04251.
URL https://pubs.acs.org/doi/10.1021/acscatal.8b04251

[75] Y. M. Fogel, B. T. Nadykto, V. F. Rybalko, V. I. Shvachko, I. E. Korobchanskaya, Use of secondary ion emission to study the catalytic oxidation of ammonia on platinum, Kinetika i Kataliz 5 (3) (1964) 496–504, number: 3.

[76] T. Pignet, L. D. Schmidt, Kinetics of NH3 oxidation on Pt, Rh, and Pd, Journal of Catalysis 40 (2) (1975) 212–225, number: 2.
URL http://www.sciencedirect.com/science/article/pii/0021951775902493

[77] P. R. Norton, An investigation of the adsorption of oxygen and oxygen containing species on platinum by photoelectron spectroscopy, Surface Science 47 (1) (1975) 98–114, number: 1.

[78] M. Asscher, W. L. Guthrie, T. H. Lin, G. A. Somorjai, A molecular beam surface scattering study of ammonia oxidation on the platinum (111) crystal face, The Journal of Physical Chemistry 88 (15) (1984) 3233–3238, number: 15.
URL http://pubs.acs.org/doi/pdf/10.1021/j150659a020

[79] J. M. Bradley, A. Hopkinson, D. A. King, A molecular beam study of ammonia adsorption on Pt {100}, Surface science 371 (2-3) (1997) 255–263, number: 2-3.
URL http://www.sciencedirect.com/science/article/pii/S0039602896010187

[80] J. Pérez-Ramírez, E. V. Kondratenko, Evidences of the origin of N2O in the high-temperature NH3 oxidation over Pt–Rh gauze, Chem. Commun. (4) (2004) 376–377, number: 4. doi:10.1039/B312685D.
URL http://xlink.rsc.org/?DOI=B312685D

[81] E. V. Kondratenko, J. Pérez-Ramírez, Transient studies on the effect of oxygen on the high-temperature NO reduction by NH3 over Pt–Rh gauze, Applied Catalysis A: General 289 (1) (2005) 97–103. doi:10.1016/j.apcata.2005.04.017.
URL https://linkinghub.elsevier.com/retrieve/pii/S0926860X05002644

[82] L. Andrussow, Über die katalytische Ammoniakoxydation, Angewandte Chemie 39 (9) (1926) 321–332, number: 9.

[83] F. Raschig, Über die Ammoniakverbrennung, Angewandte Chemie 40 (42) (1927) 1183–1185, number: 42.

[84] M. Bodenstein, Der Mechanismus der katalytischen Ammoniakverbrennung, Angewandte Chemie 48 (22) (1935) 327, number: 22.

[85] N. I. Il'chenko, Catalytic oxidation of ammonia, Russian Chemical Reviews 45 (12) (1976) 1119–1134, number: 12.
URL http://www.turpion.org/php/paper.phtml?journal_id=rc&paper_id=2765

[86] X. Traversac, Experimental and microkinetic modelling study of ammonia oxidation over platinum, Ph.D. thesis, The University of Sydney, Sydney (2007).

[87] D. C. Ford, Y. Xu, M. Mavrikakis, Atomic and molecular adsorption on Pt(111), Surface Science 587 (3) (2005) 159–174, number: 3. doi:10.1016/j.susc.2005.04.028.
URL http://linkinghub.elsevier.com/retrieve/pii/S0039602805004310

[88] M. Garcıa-Hernández, N. Lopez, I. De PR Moreira, J. C. Paniagua, F. Illas, Ab initio cluster model approach to the chemisorption of NH 3 on Pt (111), Surface science 430 (1) (1999) 18–28, number: 1.
URL http://www.sciencedirect.com/science/article/pii/S0039602899003532

[89] J. M. Gohndrone, C. W. Olsen, A. L. Backman, T. R. Gow, E. Yagasaki, R. I. Masel, Ammonia adsorption and decomposition on several faces of platinum, Journal of Vacuum Science & Technology A: Vacuum, Surfaces, and Films 7 (3) (1989) 1986–1990, number: 3. doi:10.1116/1.575998.
URL http://avs.scitation.org/doi/10.1116/1.575998

[90] J. L. Gland, V. N. Korchak, The adsorption of oxygen on a stepped platinum single crystal surface, Surface Science 75 (4) (1978) 733–750, number: 4.
URL http://www.sciencedirect.com/science/article/pii/0039602878901905

[91] J. L. Gland, B. A. Sexton, G. B. Fisher, Oxygen interactions with the Pt (111) surface, Surface Science 95 (2-3) (1980) 587–602, number: 2-3.
URL http://www.sciencedirect.com/science/article/pii/0039602880901971

[92] J. L. Gland, Molecular and atomic adsorption of oxygen on the Pt (111) and Pt (S)-12 (111)×(111) surfaces, Surface Science 93 (2) (1980) 487–514, number: 2.

[93] K. Griffiths, T. E. Jackman, J. A. Davies, P. R. Norton, Interaction of O2 with Pt(100): I. Equilibrium measurements, Surface Science 138 (1) (1984) 113–124. doi:https://doi.org/10.1016/0039-6028(84)90499-0.

[94] A. Michaelides, P. Hu, A density functional theory study of hydroxyl and the intermediate in the water formation reaction on Pt, The Journal of Chemical Physics 114 (1) (2001) 513, number: 1. doi:10.1063/1.1328746.
URL http://scitation.aip.org/content/aip/journal/jcp/114/1/10.1063/1.1328746

[95] G. Novell-Leruth, A. Valcárcel, J. Pérez-Ramírez, J. M. Ricart, Ammonia Dehydrogenation over Platinum-Group Metal Surfaces. Structure, Stability, and Reactivity of Adsorbed NH Species, The Journal of Physical Chemistry C 111 (2) (2007) 860–868, number: 2. doi:10.1021/jp064742b.
URL http://pubs.acs.org/doi/abs/10.1021/jp064742b

[96] W. Offermans, A. Jansen, R. van Santen, Ammonia activation on platinum {111}: A density functional theory study, Surface Science 600 (9) (2006) 1714–1734, number: 9. doi:10.1016/j.susc.2006.01.031.
URL http://linkinghub.elsevier.com/retrieve/pii/S0039602806000665

[97] W. D. Mieher, W. Ho, Thermally activated oxidation of NHs on Pt (111): intermediate species and reaction mechanisms, Surface science 322 (1-3) (1995) 151–167, number: 1-3.
URL http://www.sciencedirect.com/science/article/pii/0039602895900268

[98] M. Warner, B. S. Haynes, Formation of N 2 and N 2 O in industrial combustion of ammonia over platinum, Proceedings of the Combustion Institute 35 (2) (2015) 2215–2222, number: 2. doi:10.1016/j.proci.2014.06.110.
URL http://linkinghub.elsevier.com/retrieve/pii/S1540748914002685

[99] E. Kondratenko, R. Kraehnert, J. Radnik, M. Baerns, J. Pérez-Ramırez, Distinct activity and time-on-stream behavior of pure Pt and Rh metals and Pt–Rh alloys in the high-temperature NO decomposition, Applied Catalysis A: General 298 (2006) 73–79. doi:10.1016/j.apcata.2005.09.022.
URL http://linkinghub.elsevier.com/retrieve/pii/S0926860X05007192

[100] R. Burch, S. T. Daniells, P. Hu, N2O and NO2 formation on Pt(111): A density functional theory study, The Journal of Chemical Physics 117 (6) (2002) 2902–2908, number: 6. doi:10.1063/1.1490338.
URL http://aip.scitation.org/doi/10.1063/1.1490338

[101] R. Burch, S. T. Daniells, P. Hu, The mechanism of N[sub 2]O formation via the (NO)[sub 2] dimer: A density functional theory study, The Journal of Chemical Physics 121 (6) (2004) 2737, number: 6. doi:10.1063/1.1767153.

URL http://scitation.aip.org/content/aip/journal/jcp/121/6/10.1063/1.1767153

[102] A. Bogicevic, K. C. Hass, NO pairing and transformation to N 2 O on Cu (111) and Pt (111) from first principles, Surface science 506 (1) (2002) L237–L242, number: 1.
URL http://www.sciencedirect.com/science/article/pii/S0039602802014917

[103] H. Hirano, T. Yamada, K. I. Tanaka, J. Siera, P. Cobden, B. E. Nieuwenhuys, Mechanisms of the various nitric oxide reduction reactions on a platinum-rhodium (100) alloy single crystal surface, Surface Science 262 (1-2) (1992) 97–112, number: 1-2.

[104] L. Apelbaum, M. Temkin, OKISLENIE AMMIAKA NA PLATINE PRI NIZKIKH DAVLENIYAKH, DOKLADY AKADEMII NAUK SSSR 74 (5) (1950) 1963–1966, number: 5.

[105] L. Apelbaum, M. Temkin, OKISLENIE AMMIAKA NA SETKAKH IZ PLATINY I PLATINO-RODIEVOGO SPLAVA. 1, ZHURNAL FIZICHESKOI KHIMII 22 (2) (1948) 179–194, number: 2.

[106] V. A. Sadykov, L. A. Isupova, I. A. Zolotarskii, L. N. Bobrova, A. S. Noskov, V. N. Parmon, E. A. Brushtein, T. V. Telyatnikova, V. I. Chernyshev, V. V. Lunin, Oxide catalysts for ammonia oxidation in nitric acid production: properties and perspectives, Applied Catalysis A: General 204 (1) (2000) 59–87, number: 1.
URL http://www.sciencedirect.com/science/article/pii/S0926860X00005068

[107] R. J. Gorte, L. D. Schmidt, J. L. Gland, Binding states and decomposition of NO on single crystal planes of Pt, Surface Science 109 (2) (1981) 367–380, number: 2.
URL http://www.sciencedirect.com/science/article/pii/0039602881904945

[108] J. M. Gohndrone, R. I. Masel, A TPD study of nitric oxide decomposition on Pt (100), Pt (411) and Pt (211), Surface Science 209 (1-2) (1989) 44–56, number: 1-2.
URL http://www.sciencedirect.com/science/article/pii/0039602889900575

[109] R. B. Getman, W. F. Schneider, DFT-Based Characterization of the Multiple Adsorption Modes of Nitrogen Oxides on Pt(111), The Journal of Physical Chemistry C 111 (1) (2007) 389–397, number: 1. doi:10.1021/jp064841p.
URL http://pubs.acs.org/doi/abs/10.1021/jp064841p

[110] G. I. Golodets, The Oxidation of Nitrogen-Containing Inorganic Compounds, in: Heterogeneous Catalytic Reactions Involving Molecular Oxygen, no. 15 in Studies in Surface Science and Catalysis, 1983, pp. 312–364.

[111] C. W. Nutt, S. Kapur, Mechanism of Oxidation of Ammonia on Platinum, Nature 220 (5168) (1968) 697–698, number: 5168.

[112] C. W. Nutt, S. Kapur, Oxidation of ammonia on platinum, Nature 224 (5215) (1969) 169–169, number: 5215.

[113] H. Falsig, J. Shen, T. S. Khan, W. Guo, G. Jones, S. Dahl, T. Bligaard, On the Structure Sensitivity of Direct NO Decomposition over Low-Index Transition Metal Facets, Topics in Catalysis 57 (1-4) (2014) 80–88, number: 1-4. doi:10.1007/s11244-013-0164-5.
URL http://link.springer.com/10.1007/s11244-013-0164-5

[114] J. D. Gonzalez, Molecular and kinetic modelling of the ammonia oxidation on platinum, Ph.D. thesis, University of Sydney, Sydney (Mar. 2017).

[115] E. V. Rebrov, M. H. J. M. De Croon, J. C. Schouten, Development of the kinetic model of platinum catalyzed ammonia oxidation in a microreactor, Chemical Engineering Journal 90 (1) (2002) 61–67, number: 1.

[116] E. V. Rebrov, M. De Croon, J. C. Schouten, A kinetic study of ammonia oxidation on a Pt catalyst in the explosive region in a microstructured reactor/heat-exchanger, Chemical Engineering Research and Design 81 (7) (2003) 744–752, number: 7.
URL http://www.sciencedirect.com/science/article/pii/S0263876203723636

[117] R. Krähnert, Ammonia Oxidation over Polycrystalline Platinum: Surface Morphology and Kinetics at Atmospheric Pressure, Ph.D. thesis, TU Berlin (2005).

[118] A. Scheuer, M. Votsmeier, A. Schuler, J. Gieshoff, A. Drochner, H. Vogel, NH3-Slip Catalysts: Experiments Versus Mechanistic Modelling, Topics in Catalysis 52 (13-20) (2009) 1847–1851. doi:10.1007/s11244-009-9351-9.
URL http://link.springer.com/10.1007/s11244-009-9351-9

[119] A. Scheibe, M. Hinz, R. Imbihl, Kinetics of ammonia oxidation on stepped platinum surfaces, Surface Science 576 (1-3) (2005) 131–144, number: 1-3. doi:10.1016/j.susc.2004.12.007.
URL http://linkinghub.elsevier.com/retrieve/pii/S0039602804015481

[120] A. Scheibe, Selectivity changes due to restructuring of the Pt(533) surface in the NH3 þ O2 reaction, Catalysis Letters (86) (2003) 5.

[121] G. Novell-Leruth, J. M. Ricart, J. Pérez-Ramírez, Pt(100)-Catalyzed Ammonia Oxidation Studied by DFT: Mechanism and Microkinetics, The Journal of Physical Chemistry C 112 (35) (2008) 13554–13562, number: 35. doi:10.1021/jp802489y.
URL http://pubs.acs.org/doi/abs/10.1021/jp802489y

[122] G. Novell-Leruth, A. Valcárcel, A. Clotet, J. M. Ricart, J. Pérez-Ramírez, DFT Characterization of Adsorbed NH $_x$ Species on Pt(100) and Pt(111) Surfaces, The Journal of Physical Chemistry B 109 (38) (2005) 18061–18069. doi:10.1021/jp0516821.
URL https://pubs.acs.org/doi/10.1021/jp0516821

[123] E. J. Nowak, Catalytic oxidation of ammonia on platinum, Chemical Engineering Science 21 (1) (1966) 19–27, number: 1.

[124] I. A. Oele, Technological aspects of the catalytic combustion of ammonia with platinum gauze elements, Chemical Engineering Science 8 (1-2) (1958) 146–157, number: 1-2.
URL http://www.sciencedirect.com/science/article/pii/0009250958800457

[125] D. Roberts, G. R. Gillespie, Estimation of Platinum Catalyst Requirement for Ammonia Oxidation, in: H. M. Hulburt (Ed.), Chemical Reaction Engineering—II, Vol. 133, AMERICAN CHEMICAL SOCIETY, WASHINGTON, D. C., 1974, pp. 600–611. doi:10.1021/ba-1974-0133.ch045.
URL http://pubs.acs.org/doi/abs/10.1021/ba-1974-0133.ch045

[126] D. G. Löffler, L. D. Schmidt, Catalytic activity and selectivity on heterogeneous surfaces with mass transfer, AIChE Journal 21 (4) (1975) 786–791, number: 4.
URL http://onlinelibrary.wiley.com/doi/10.1002/aic.690210422/full

[127] M. Flytzani-Stephanopoulos, L. D. Schmidt, Evaporation rates and surface profiles on heterogeneous surfaces with mass transfer and surface reaction, Chemical Engineering Science 34 (3) (1979) 365–372, number: 3.

[128] S. P. S. Andrew, The Oxidation of Ammonia, in: Nitric Acid and Fertilizer Nitrates, Vol. 4, Marcel Dekker, New York, 1985, pp. 31–40.

[129] D. A. Hickman, L. D. Schmidt, The role of boundary layer mass transfer in partial oxidation selectivity, Journal of catalysis 136 (2) (1992) 300–308, number: 2.
URL http://www.sciencedirect.com/science/article/pii/002195179290063N

[130] C. W. Nutt, S. Kapur, A. Majeed, Rate of Oxidation of Ammonia on Platinum Wires, Ribbons, and Gauzes, in: J. Wei, C. Georgakis (Eds.), Chemical Reaction Engineering—Boston, Vol. 196, AMERICAN CHEMICAL SOCIETY, WASHINGTON, D.C., 1982, pp. 261–270. doi:10.1021/bk-1982-0196.ch022.
URL http://pubs.acs.org/doi/abs/10.1021/bk-1982-0196.ch022

[131] M. A. Shah, Mass transfer on stacked wire gauzes, Doctor of Philosophy, The University of Birmingham (1970).

[132] C. N. Satterfield, D. H. Cortez, Mass transfer characteristics of woven-wire screen catalysts, Industrial & Engineering Chemistry Fundamentals 9 (4) (1970) 613–620, number: 4.

[133] M. A. Shah, D. Roberts, Mass Transfer Characteristics of Stacked Metal Screens, in: H. M. Hulburt (Ed.), Chemical Reaction Engineering—II, Vol. 133, AMERICAN CHEMICAL SOCIETY, WASHINGTON, D. C., 1974, pp. 259–270. doi:10.1021/ba-1974-0133.ch020.
URL http://pubs.acs.org/doi/abs/10.1021/ba-1974-0133.ch020

[134] R. M. Heck, J. C. Bonacci, W. R. Hatfield, T. H. Hsiung, A new research pilot plant unit for ammonia oxidation processes and some gauze data comparisons for nitric acid process, Industrial & Engineering Chemistry Process Design and Development 21 (1) (1982) 73–79, number: 1.

[135] G. Nettesheim, Zündgrenzen des Systems NH3/N2/O2 bis 130 atü, Chemie Ingenieur Technik 41 (13) (1969) 773–775, number: 13.
URL http://onlinelibrary.wiley.com/doi/10.1002/cite.330411307/full

[136] M. Appl, Ammonia, Ullmann's encyclopedia of industrial chemistry (2006).
URL http://onlinelibrary.wiley.com/doi/10.1002/14356007.a02_143.pub2/full

[137] R. Kraehnert, M. Baerns, Morphology changes of Pt-foil catalyst induced by temperature-controlled ammonia oxidation near atmospheric pressure, Applied Catalysis A: General 327 (1) (2007) 73–81, number: 1. doi:10.1016/j.apcata.2007.04.031.
URL http://linkinghub.elsevier.com/retrieve/pii/S0926860X07002797

[138] E. Bergene, O. Tronstad, A. Holmen, Surface areas of Pt–Rh catalyst gauzes used for ammonia oxidation, Journal of Catalysis 160 (2) (1996) 141–147, number: 2.
URL http://www.sciencedirect.com/science/article/pii/S0021951796901335

[139] O. Nilsen, A. Kjekshus, H. Fjellv\a ag, Reconstruction and loss of platinum catalyst during oxidation of ammonia, Applied Catalysis A: General 207 (1) (2001) 43–54, number: 1.
URL http://www.sciencedirect.com/science/article/pii/S0926860X00006153

[140] T.-C. Wei, J. Phillips, Thermal and catalytic etching: mechanisms of metal catalyst reconstruction, Advances in catalysis 41 (1996) 359–421.

[141] R. T. K. Baker, R. B. Thomas, J. H. F. Notton, The Behaviour of Platinum Catalysts for Ammonia Oxidation, Platinum Metals Review 18 (4) (1974) 130–136, number: 4.
URL http://www.ingentaconnect.com/content/matthey/pmr/1974/00000018/00000004/art00003

[142] R. W. McCabe, T. Pignet, L. D. Schmidt, Catalytic etching of platinum in NH3 oxidation, Journal of Catalysis 32 (1) (1974) 114–126, number: 1.

[143] S. L. Handforth, J. N. Tilley, Catalysts for Oxidation of Ammonia to Oxides of Nitrogen, Industrial & Engineering Chemistry 26 (12) (1934) 1287–1292, number: 12.

[144] B. T. Horner, Knitted gauze for ammonia oxidation, Platinum Metals Rev 35 (2) (1991) 58–64, number: 2.
URL http://www.platinummetalsreview.com/pdf/pmr-v35-i2-058-124.pdf

[145] B. T. Horner, New fabric precious metal gauzes, Nitrogen 193 (1991) 32–37.

[146] B. T. Horner, Knitted Platinum Alloy Gauzes, Platinum Metals Review 37 (2) (1993) 76–85, number: 2.

[147] R. J. Farrauto, H. C. Lee, Ammonia oxidation catalysts with enhanced activity, Industrial & engineering chemistry research 29 (7) (1990) 1125–1129, number: 7.

[148] M. Flytzani-Stephanopoulos, S. Wong, L. D. Schmidt, Surface morphology of platinum catalysts, Journal of Catalysis 49 (1) (1977) 51–82, number: 1.
URL http://www.sciencedirect.com/science/article/pii/0021951777902391

[149] F. Sperner, W. Hohmann, Rhodium-platinum gauzes for ammonia oxidation, Platinum Metals Review 20 (1) (1976) 12–20, number: 1.
URL http://www.ingentaconnect.com/content/matthey/pmr/1976/00000020/00000001/art00007

[150] R. W. Bartlett, Platinum Oxidation Kinetics with Convective Diffusion and Surface Reaction, Journal of the Electrochemical Society 114 (6) (1967) 547–550, number: 6.

[151] L. Hannevold, O. Nilsen, A. Kjekshus, H. Fjellvåg, Chemical vapor transport of platinum and rhodium with oxygen as transport agent, Journal of Crystal Growth 279 (1-2) (2005) 206–212, number: 1-2. doi:10.1016/j.jcrysgro.2005.02.024.
URL http://linkinghub.elsevier.com/retrieve/pii/S0022024805002034

[152] A. R. McCabe, G. D. W. Smith, A. S. Pratt, The mechanism of reconstruction of rhodium-platinum catalyst gauzes, Platinum Metals Review 30 (2) (1986) 54–62, number: 2.
URL http://www.ingentaconnect.com/content/matthey/pmr/1986/00000030/00000002/art00001

[153] E. J. Nowak, Prediction of platinum losses during ammonia oxidation, Chemical Engineering Science 24 (2) (1969) 421–423, number: 2.
URL http://www.sciencedirect.com/science/article/pii/0009250969800527

[154] G. C. Fryburg, H. M. Petrus, Kinetics of the Oxidation of Platinum, Journal of the Electrochemical Society 108 (6), number: 6 (1961).

[155] M. R. Lyubovsky, V. V. Barelko, Formation of "Metal Wool" Structures and Dynamics of Catalytic Etching of Platinum Surfaces during Ammonia Oxidation, Journal of catalysis 149 (1) (1994) 23–35, number: 1.

[156] N. L. Wu, J. Phillips, Sintering of silica-supported platinum catalysts during ethylene oxidation, Journal of Catalysis 113 (1) (1988) 129–143, number: 1.
URL http://www.sciencedirect.com/science/article/pii/0021951788902436

[157] J. M. Hess, J. Phillips, Catalytic etching of Pt/Rh gauzes, Journal of Catalysis 136 (1) (1992) 149–160, number: 1.
URL http://www.sciencedirect.com/science/article/pii/002195179290114W

[158] V. W. Dean, M. Frenklach, J. Phillips, Catalytic etching of platinum foils and thin films in hydrogen-oxygen mixtures, The Journal of Physical Chemistry 92 (20) (1988) 5731–5738, number: 20.

[159] J. W. Mitchell, R. C. DeVries, R. W. Roberts, P. Cannon, REACTIVITY OF SOLIDS. Proceedings of the 6th International Symposium, Wiley-VCH Verlag GmbH & Co. KGaA, Schenectady, 1969.

[160] J. A. Busby, A. G. Knapton, A. E. R. Budd, Catalytic Processes in Nitric Acid Manufacture, Proceedings of the International Fertilizer Society 169 (1978).

[161] D. R. Anderson, Catalytic etching of platinum alloy gauzes, Journal of Catalysis 113 (2) (1988) 475–489, number: 2.
URL http://www.sciencedirect.com/science/article/pii/0021951788902734

[162] J. Pielaszek, The Catalytic Etching of Platinum and Rhodium-Platinum Gauzes, Platinum Metals Review 28 (3) (1984) 109–114, number: 3.
URL http://www.ingentaconnect.com/content/matthey/pmr/1984/00000028/00000003/art00005

[163] N. G. Schmahl, E. Minzl, Zeitschrift für Physikalische Chemie 41 (1964).

[164] H. Holzmann, Platin-Rückgewinnung bei der NH3-Verbrennung an Platin/Rhodium-Netzkatalysatoren, Chemie Ingenieur Technik 40 (24) (1968) 1229–1237, number: 24.
URL http://onlinelibrary.wiley.com/doi/10.1002/cite.330402408/full

[165] Lentia GmbH, German Patent DBP 1 088 033, inventors: _:n2259 Issue: DBP 1 088 033 (Jun. 1957).

[166] J. Pura, P. Wieciński, P. Kwaśniak, M. Zwolińska, H. Garbacz, J. Zdunek, Z. Laskowski, M. Gierej, Investigation of the degradation mechanism of catalytic wires during oxidation of ammonia process, Applied Surface Science 388 (2016) 670–677. doi:10.1016/j.apsusc.2016.05.071.
URL http://linkinghub.elsevier.com/retrieve/pii/S0169433216310790

[167] W. R. Hatfield, R. M. Heck, T. H. Hsiung, Method for Recovering Platinum in a Nitric Acid Plant, inventors: _:n1616 Issue: US4412859A (Nov. 1983).

[168] G. R. Gillespie, Process for ammonia oxidation, inventors: _:n1584 Issue: US3660024A (May 1972).

[169] L. E. James, L. Crescentini, W. B. Fisher, Process for making a cobalt oxide catalyst, Google Patents, 1983.
URL http://www.google.com/patents/US4389339

[170] W.-K. Fung, L. Ledwaba, N. Modiba, M. Claeys, E. van Steen, Choosing a suitable support for Co3O4 as an NH3 oxidation catalyst, Catalysis Science & Technology 3 (8) (2013) 1905. doi:10.1039/c3cy00041a.
URL http://xlink.rsc.org/?DOI=c3cy00041a

[171] K. Shojaee, B. S. Haynes, A. Montoya, The role of oxygen during the catalytic oxidation of ammonia on Co 3 O 4 (1 0 0), Applied Surface Science 316 (2014) 355–365. doi:10.1016/j.apsusc.2014.08.021.
URL https://linkinghub.elsevier.com/retrieve/pii/S016943321401753X

[172] M. M. Karavayev, A. P. Zasorin, N. F. Kleshchev, Catalytic oxidation of ammonia, Khimia (1983).

[173] D. A. Epstein, N. Tkachenko, M. Miniovich, N. Dobrovolskaia, A 2-Stage Catalyst for Oxidation of Ammonia, Doklady Akademii Nauk SSSR 122 (5) (1958) 874–877, number: 5.

[174] M. M. Karavaev, A. Y. Kantor, Y. V. Semenov, Oxidation of ammonia on a catalyst system with a nonplatinum oxide catalyst, Soviet Chemical Industry 22 (11) (1990) 51–55, number: 11.

[175] BASF AG, Katalysator für die katalytische Überführung von Ammoniak in Stickoxyde, German Patent DE 337568, inventors: _:n1789 Issue: DE 337568 (1916).

[176] E. F. Sutormina, L. A. Isupova, A. N. Nadeev, V. A. Rogov, V. P. Ivanov, E. B. Burgina, A. A. Budneva, Effect of the reaction medium on the physicochemical properties of the oxide monolith catalyst IK-42-1 for ammonia oxidation, Kinetics and Catalysis 50 (6) (2009) 892–898, number: 6. doi:10.1134/S0023158409060160.
URL http://link.springer.com/10.1134/S0023158409060160

[177] V. I. Chernyshov, I. M. Kisil, Platinum metals catalytic systems in nitric acid production, Platinum Metals Review 37 (3) (1993) 136–143, number: 3.
URL http://www.ingentaconnect.com/content/matthey/pmr/1993/00000037/00000003/art00002

[178] J. Pérez-Ramírez, B. Vigeland, Perovskite Membranes in Ammonia Oxidation: Towards Process Intensification in Nitric Acid Manufacture, Angewandte Chemie International Edition 44 (7) (2005) 1112–1115, number: 7. doi:10.1002/anie.200462024.
URL http://doi.wiley.com/10.1002/anie.200462024

[179] Z. Cao, H. Jiang, H. Luo, S. Baumann, W. A. Meulenberg, H. Voss, J. Caro, An Efficient Oxygen Activation Route for Improved Ammonia Oxidation through an Oxygen-Permeable Catalytic Membrane, ChemCatChem (2014) n/a–n/adoi:10.1002/cctc.201400048.
URL https://onlinelibrary.wiley.com/doi/10.1002/cctc.201400048

[180] C. Ruan, X. Wang, C. Wang, L. Li, J. Lin, X. Y. Liu, F. Li, X. Wang, Selective catalytic oxidation of ammonia to nitric oxide via chemical looping, preprint, In Review (Apr. 2021). doi:10.21203/rs.3.rs-350833/v1.
URL https://www.researchsquare.com/article/rs-350833/v1

[181] W. P. Partridge, J. M. E. Storey, S. A. Lewis, R. W. Smithwick, G. L. Devault, M. J. Cunningham, N. W. Currier, T. M. Yonushonis, Time-Resolved Measurements of Emission Transients By Mass Spectrometry, 2000, pp. 2000–01–2952. doi:10.4271/2000-01-2952.
URL https://www.sae.org/content/2000-01-2952/

[182] W. Partridge, T. Toops, J. Green, T. Armstrong, Intra-fuel cell stack measurements of transient concentration distributions, Journal of Power Sources 160 (1) (2006) 454–461, number: 1. doi:10.1016/j.jpowsour.2006.01.016.
URL https://linkinghub.elsevier.com/retrieve/pii/S0378775306000929

[183] W. P. Partridge, J.-S. Choi, NH3 formation and utilization in regeneration of Pt/Ba/Al2O3 NOx storage-reduction catalyst with H2, Applied Catalysis B: Environmental 91 (1-2) (2009) 144–151, number: 1-2. doi:10.1016/j.apcatb.2009.05.017.
URL https://linkinghub.elsevier.com/retrieve/pii/S0926337309001970

[184] J. Sá, D. L. A. Fernandes, F. Aiouache, A. Goguet, C. Hardacre, D. Lundie, W. Naeem, W. P. Partridge, C. Stere, SpaciMS: spatial and temporal operando resolution of reactions within catalytic monoliths, The Analyst 135 (9) (2010) 2260, number: 9. doi:10.1039/c0an00303d.
URL http://xlink.rsc.org/?DOI=c0an00303d

[185] R. Horn, K. Williams, N. Degenstein, A. Bitschlarsen, D. Dallenogare, S. Tupy, L. Schmidt, Methane catalytic partial oxidation on autothermal Rh and Pt foam catalysts: Oxidation and reforming zones, transport effects, and approach to thermodynamic equilibrium, Journal of Catalysis 249 (2) (2007) 380–393, number: 2. doi:10.1016/j.jcat.2007.05.011.
URL https://linkinghub.elsevier.com/retrieve/pii/S0021951707001753

[186] A. Bitsch-Larsen, R. Horn, L. Schmidt, Catalytic partial oxidation of methane on rhodium and platinum: Spatial profiles at elevated pressure, Applied Catalysis A: General 348 (2) (2008) 165–172, number: 2. doi:10.1016/j.apcata.2008.06.036.
URL https://linkinghub.elsevier.com/retrieve/pii/S0926860X08003918

[187] J. H. Gross, Massenspektrometer, in: Massenspektrometrie, Springer Berlin Heidelberg, Berlin, Heidelberg, 2013, book Authors: _:n2269. doi:10.1007/978-3-8274-2981-0_4.
URL http://link.springer.com/10.1007/978-3-8274-2981-0_4

[188] C. Dass, Fundamentals of Contemporary Mass Spectrometry, John Wiley & Sons, Inc., Hoboken, NJ, USA, 2007. doi:10.1002/0470118490.
URL http://doi.wiley.com/10.1002/0470118490

[189] M. Linscheid, Mass Spectrometry, in: H. Gnzler, A. Williams (Eds.), Handbook of Analytical Techniques, Wiley-VCH Verlag GmbH, Weinheim, Germany, 2001, pp. 579–626. doi:10.1002/9783527618323.ch20.
URL http://doi.wiley.com/10.1002/9783527618323.ch20

[190] G. Scoles, Atomic and Molecular Beam Methods - Volume 1, 1st Edition, Oxford University Press, Oxford, 1988.

[191] M. Wutz, H. Adam, W. Walcher, Handbuch Vakuumtechnik, Springer Vieweg, Braunschweig, 2000.

[192] D. Lide, CRC Handbook of Chemistry and Physics, CRC Press, Boac Raton, 2003.

[193] A. K. Rebrov, Free jets in vacuum technologies, Journal of Vacuum Science & Technology A: Vacuum, Surfaces, and Films 19 (4) (2001) 1679–1687. doi:10.1116/1.1382649.
URL http://avs.scitation.org/doi/10.1116/1.1382649

[194] R. Campargue, Progress in overexpanded supersonic jets and skimmed molecular beams in free-jet zones of silence, The Journal of Physical Chemistry 88 (20) (1984) 4466–4474. doi:10.1021/j150664a004.
URL https://pubs.acs.org/doi/10.1021/j150664a004

[195] H. Dun, B. Mattes, The Gas Dynamics of a Conical Nozzle Molecular Beam Sampling System, Chem. Phys. (38) (1979) 161–172.

[196] J. Morrison, J. Traeger, Ionization and dissociation by electron impact II. NH3 and PH3, International Journal of Mass Spectrometry and Ion Physics 11 (3) (1973) 277–288.

[197] G. Reiser, W. Habenicht, K. Müller-Dethlefs, Zero kinetic energy (ZEKE) photoelectron spectroscopy of ammonia by nonresonant two-photon ionization from the neutral ground state, The Journal of Chemical Physics 98 (11) (1993) 8462–8468. doi:10.1063/1.464505.
URL http://aip.scitation.org/doi/10.1063/1.464505

[198] J. Morrison, J. Traeger, Ionization and dissociation by electron impact: I. H2O and H2S, International Journal of Mass Spectrometry and Ion Physics 11 (2) (1973) 77–88. doi:https://doi.org/10.1016/0020-7381(73)80001-4.

[199] S. N. Foner, R. L. Hudson, Ionization Potential of the OH Free Radical by Mass Spectrometry, The Journal of Chemical Physics 25 (3) (1956) 602–603. doi:10.1063/1.1743001.
URL http://aip.scitation.org/doi/10.1063/1.1743001

[200] H. A. Ldt., EPIC and IDP Analysers; Operation Manual, 1998.

[201] J. Campana, Elementary theory of the quadrupole mass filter, International Jounal of Mass Spectrometry and Ion Physics 33 (1980) 101–117.

[202] B. Müller, U. Renz, Development of a fast fiber-optic two-color pyrometer for the temperature measurement of surfaces with varying emissivities, Review of Scientific Instruments 72 (8) (2001) 3366–3374. doi:10.1063/1.1384448.
URL http://aip.scitation.org/doi/10.1063/1.1384448

[203] V. M. Janardhanan, O. Deutschmann, Computational Fluid Dynamics of Catalytic Reactors, in: O. Deutschmann (Ed.), Modeling and Simulation of Heterogeneous Catalytic Reactions, Wiley-VCH Verlag GmbH & Co. KGaA, Weinheim, Germany, 2011, pp. 251–282. doi:10.1002/9783527639878.ch8.
URL https://onlinelibrary.wiley.com/doi/10.1002/9783527639878.ch8

[204] J. Hirschfelder, C. Curtiss, R. Bird, Molecular theory of gases and liquids, Wiley, New York, 1964.

[205] GRI-Mech 3.0, http://combustion.berkeley.edu/gri-mech/version30/text30.html (Nov. 2021).

[206] C. Hirsch, Numerical computation of internal and external flows: fundamentals of computational fluid dynamics, 2nd Edition, Elsevier/Butterworth-Heinemann, Oxford ; Burlington, MA, 2007, oCLC: ocn148277909.

[207] J. Pottbacker, S. Jakobtorweihen, A. S. Behnecke, A. Abdullah, M. Özdemir, M. Warner, M. Menon, J. M. Bujalski, D. Waller, O. Korup, R. Horn, Resolving gradients in an ammonia oxidation reactor under industrial conditions: A combined experimental and simulation study, Chemical Engineering Journal 439 (Jul. 2022). doi:10.1016/j.cej.2022.135350.
URL https://linkinghub.elsevier.com/retrieve/pii/S1385894722008531

[208] A.-S. Behnecke, CFD-simulation of capillary sampling in a catalytic profile reactor for the ammonia oxidation on platinum gauzes (2019) 108.

[209] N. Jurtz, M. Kraume, G. D. Wehinger, Advances in fixed-bed reactor modeling using particle-resolved computational fluid dynamics (CFD), Rev. Chem. Eng. 35 (2) (2019) 139–190. doi:10.1515/revce-2017-0059.
URL https://www.degruyter.com/document/doi/10.1515/revce-2017-0059/html

[210] Properties of fused silica, https://www.heraeus.com/en/hca/fused_silica_quartz_\knowledges_base_1/properties_1/properties_hca.html (Aug. 2019).

[211] C.W.C., Thermophysical Data on Platinum Resistivity and Conductivity Values Recommended, Platinum Met. Rev. 28 (4) (1984) 164–165.
URL https://www.technology.matthey.com/article/28/4/164-165/

[212] J. Speight, Lange's Handbook of Chemistry, sixteenth edition Edition, 2005.

[213] S. Brauer, Dimensioning and Design of an NOx Absorber, Bachelor Thesis (2018) 142.

[214] K. Jousten (Ed.), Handbook of vacuum technology, second, completely revised and updated edition Edition, Wiley-VCH, Weinheim, Germany, 2016. doi:10.1002/9783527688265.
URL http://onlinelibrary.wiley.com/book/10.1002/9783527688265

[215] B. Wollak, D. Doronkin, D. Espinoza, T. Sheppard, O. Korup, M. Schmidt, S. Alizadefanaloo, F. Rosowski, C. Schroer, J.-D. Grunwaldt, R. Horn, Exploring catalyst dynamics in a fixed bed reactor by correlative operando spatially-resolved structure-activity profiling, Journal of Catalysis (2021) S0021951721003316doi:10.1016/j.jcat.2021.08.029.
URL https://linkinghub.elsevier.com/retrieve/pii/S0021951721003316

[216] M. Wolf, N. Raman, N. Taccardi, R. Horn, M. Haumann, P. Wasserscheid, Capturing spatially resolved kinetic data and coking of Ga–Pt supported catalytically active liquid metal solutions during propane dehydrogenation *in situ*, Faraday Discussions 229 (2021) 359–377. doi:10.1039/D0FD00010H.
URL http://xlink.rsc.org/?DOI=D0FD00010H

[217] J. Touitou, R. Burch, C. Hardacre, C. McManus, K. Morgan, J. Sá, A. Goguet, An in situ spatially resolved analytical technique to simultaneously probe gas phase reactions and temperature within the packed bed of a plug flow reactor, The Analyst 138 (10) (2013) 2858. doi:10.1039/c3an00250k.
URL http://xlink.rsc.org/?DOI=c3an00250k

[218] B. Sosna, Spatially resolved probing of diffusion and reaction in porous catalyst pellets, Ph.D. thesis, Technische Universität Hamburg, Hamburg (2019).

[219] R. Bird, W. Stewart, E. Lightfoot, Transport Phenomena, Wiley & Sons, New York, 1960.